A STUDY OF NUCLEATE BOILING IN A LIQUID FLOWING THROUGH A VERTICAL TUBE

A thesis submitted for the

Diploma of the Imperial College

of Science and Technology

and the

Ph.D. Degree of the University of London

in the Faculty of Engineering

by

DAVID EDWARD MINNS B.Sc. (Eng.), A.C.G.I.

Department of Chemical Engineering,

Imperial College of Science and Technology,

London, S.W.7.

February 1969

ABSTRACT

A survey of the literature reveals large deficiencies in the knowledge of nucleate boiling in forced convection. A new boiling theory applicable to flowing liquids is formulated from a critical assessment of this literature and verified using published water data. From this theory a mechanism for the onset of film boiling is developed which is shown from water data to be applicable to low quality and subcooled boiling conditions and to be characterised by the value of the local heat flux at the 'burnout' point. The wider application of this approach is demonstrated by 'burnout' data obtained for 112-trichlorotrifluoroethane in an electrically heated vertical copper tube, of 13 millimetres internal diameter and 1,830 millimetres long. The 'burnout' data demonstrates the effects of variations of upstream heat flux levels at a system pressure of 2.0 bars and with a subcooled inlet temperature of 50 ^{o}C. Data is presented in the range of total flowrates of 0.037 - 0.112 Kg/s and of inlet qualities to the burnout section of 0% - 50%. Existing correlations developed for water are shown not to represent these results but, using entrainment and pressure measurements made in the boiler tube, the new 'burnout' mechanism is shown to be applicable to the majority of the data. The tube wall temperatures at the 'burnout' point are successfully predicted by this model. A new factor, the heat flux gradient at the burnout point, is observed to influence the critical heat flux for both the test liquid and water under conditions of non-uniform heat flux distribution in the range of burnout qualities from 0% - 50%.

ACKNOWLEDGEMENTS

The author would like to express his gratitude to Mr. G.H.Anderson, who supervised the project, for the great interest he has shown in every aspect of the investigation and for his many helpful suggestions.

Members of the technical staff have provided invaluable assistance in particular Messrs. J.S. Oakley and D.P. Roch.

S.R.C. provided financial assistance for the first three years and a Bursary was granted by Professor R. Sargent for the last months.

The author would also like to thank his wife, Rosemary, for her continued encouragement and great help throughout the project.

CONTENTS

Chapter	Section	Description	Page
		Nomenclature	7
		Glossary	11
ONE		Introduction	12
	1.1	The project	12
	1.2	Flow regimes in vertical upwards two-phase flow	13
	1.3	The scope of this thesis	13
	1.4	The choice of liquid	13
TWO		Critical Heat Flux - Literature Survey	16
	2.1	Introduction	16
	2.2	Effect of external parameters on the critical heat flux	18
	2.3	Correlation of critical heat flux	18
	2.4	Observation of critical heat flux mechanisms	25
	2.4.1	Sub-cooled boiling	25
	2.4.2	Saturated boiling	26
	2.5	General conclusions from correlations and observations	26
	2.6	Models presented to describe the mechanism for the onset of the critical condition	28
	2.6.1	Film dry-out models	28
	2.6.11	Droplet diffusion models	28
	2.6.12	Film stability models	29
	2.6.2	Nucleate boiling models	29
	2.7	Conclusions	33
THREE		Nucleation In Forced Flow Systems	38
	3.1	Introduction	38
	3.2	Heat transfer to bubbles in pool boiling	38
	3.3	The incipience of nucleation in forced convection	41
	3.4	Dynamics of vapour bubbles in forced convection	46
	3.4.1	Bubble departure	51
	3.4.11	Theory of Koumoutsos, Moissis and Spyridonos	51
	3.4.12	Theory of Levy	54
	3.5	On the relationship between bubble growth and bubble shape	56
FOUR		Bubble Growth In Forced Convection Boiling-Theory	61
	4.1	Introduction	61

Chapter	Section	Description	Page
	4.2	Inertia force acting on growing bubble in forced convection	61
	4.2.1	Pressure distribution about bubble	62
	4.2.2	Derivation of inertia forces from pressure distribution	68
	4.3	Heat transfer to bubbles in forced convection boiling	69
	4.3.1	Evaporation of the microlayer	69
	4.4	Bubble departure	77
	4.5	The onset of the critical condition	86
	4.5.1	The critical condition for systems with constant wall temperatures	87
	4.5.2	The critical condition for systems with constant heat fluxes	88
	4.6	Non-uniform heat flux distribution - the effect of sliding bubbles	89
	4.7	Conclusions	94
FIVE		Description of Apparatus And Experimental Procedure	97
	5.1	Introduction	97
	5.2	Description of apparatus	98
	5.2.1	The flow diagram	98
	5.2.2	Test section	101
	5.2.21	Test column	101
	5.2.22	Control and measurement of heat input	102
	5.2.23	Measurement of tube wall temperature	105
	5.2.3	Measurement of fluid temperature in test column	106
	5.2.4	Measurement and control of system pressure	106
	5.3	Experimental procedure	110
	5.3.1	Setting of experimental conditions	110
SIX		The Entrained Mass Flowrate	117
	6.1	Introduction	117
	6.2	Literature survey	117
	6.3	The technique chosen for entrainment measurement	120
	6.4	Description of apparatus	122
	6.5	Experimental technique	125
	6.5.1	Measurement of Impact pressure	125
	6.5.2	Measurement of entrainment	126
	6.6	Results	126
	6.6.1	Accuracy and reproducibility	127
	6.6.11	Sampling rates	127
	6.6.12	Impact pressures	127

Chapter	Section	Description	Page
	6.6.13	Local liquid mass velocity	128
	6.7	Discussion	129
SEVEN		The Critical Heat Flux	138
	7.1	Introduction	138
	7.2	Results	138
	7.3	Discussion of results	138
	7.3.1	Total entrainment mechanism	138
	7.3.2	Nucleate boiling	138
	7.4	Earlier correlations	139
	7.5	Prediction of tube wall temperature at burnout	143
	7.6	A new factor affecting critical heat fluxes with non-uniform distributions of heat flux	147
	7.7	Conclusions	154
EIGHT		Conclusions	161
		Appendices	
Experimental	E1	Calibration of tube wall thermocouples	166
	E1.1	Error in estimate of wall temperature	167
	E2	Calibration of travelling thermocouple	167
	E3	Heat losses	168
	E4	Physical properties of Isceon 113	170
	E5	Analysis of Entrainment flowrate	173
	E5.1	Test of constant gradient for line AB	173
	E5.2	Test of constant gradient for line BC	179
	E5.3	Conclusion of analyses	179
Theoretical	T1	Mantzouranis film thickness analysis	181
	T2	Sliding velocity of bubble	185
Computational	C1	Analysis of experimental data	189
	C2	Analysis of growth rate	189
	C2.1	Sub-routine DUBINT	190
	C2.2	Sub-routine SIMP	190
References			219

NOMENCLATURE

SI units are used throughout unless otherwise stated in the text.

Symbol		Units
A	bubble growth rate parameter or area	$m/s^{\frac{1}{2}}$
A_{HT}	heat transfer area	m^2
A_{XT}	cross sectional area	m^2
C'	function defined by equation (2.21)	m^{-1}
C_P	specific heat at constant pressure	J/Kg^oC
C_B	constant relating to buoyancy force	-
C_S	constant relating to surface tension force	-
C_F	constant relating to friction force	-
C_D	drag coefficient	-
D	diameter	m
E_r	ratio defined by equation (6.3)	-
F	function defined by Tong equation (2.20)	-
F_B	buoyancy force	N
F_D	drag force	N
F_S	surface tension force	N
F_{IH}	horizontal inertia force	N
F_{IV}	vertical inertia force	N
F_I	inertial force	N
F_M	momentum force	N
G	mass velocity	Kg/m^2s
g	gravitational acceleration	m/s^2

Symbol		Units
g_0	force convertion factor	N/Kg F
h	Heat transfer coefficient	W/m^2
k	thermal conductivity	W/m^oC
K	proportionality constant, subscripted and superscripted as defined in the text	various
L	length	m
L_{DNB}	distance from onset of boiling to burnout point	m
m	exponent	-
n	exponent	-
p	pressure	N/m^2
q	heat flux	W/m^2
r	polar co-ordinate	m
R	radius	m
R'	universal gas constant	$J/Kg\ mole^oK$
R_c	critical radius of nucleation site for onset of boiling	m
R_L	liquid phase hold-up	-
R_G	gas phase hold-up	-
S	ratio of entrained drop velocity to vapour velocity	-
t	time	s
T	temperature	^oC
U	velocity	m/s
u*	Von Karman friction velocity	m/s

Symbol		Units
V	velocity	m/s
W	mass flowrate	Kg/s
X	quality	-
x_V	group defined by equation (T1.6)	-
(x,y,z)	cartesian co-ordinate	m
y_i	liquid film thickness	m
y_b	distance from heating surface to bubble apex	m

Greek Symbols

α	constant associated with s and defined by equation (T1.6)	-
β	contact angle	degrees
δ	micro-layer thickness	m
δ_{TB}	thermal boundary layer thickness	m
Δ	difference operator	-
ϵ	empirical constant in equation (3.18)	s/m
θ	angle co-ordinate	degrees
λ	latent heat of evaporation	J/Kg
μ	viscosity	Kg/ms
ν	kinematic viscosity	m^2/s
ρ	density	Kg/m^3
σ	surface tension	N/m
ζ	shear stress	N/m^2
ϕ	velocity potential	s^{-1}
ψ	angle co-ordinate	degrees

Dimensionless Groups

Re	Reynolds Number; ratio $\frac{\text{inertia}}{\text{viscous}}$ force
Pr	Prandtl Number, $\mu C_p / k$
We	Weber Number ratio $\frac{\text{inertia}}{\text{surface tension}}$ force
We_Σ	critical Weber number for liquid entrainment used in equation (6.1)
We_b	Weber number governing bubble shape defined by equation (4.48)
$We_{b\ crit}$	Weber number for bubble departure; equals 5
u^+	Von Karman velocity; U/u^*
y^+	Von Karman length; $\rho y u^* / \mu$
Re*	Reynolds number based on friction velocity; $\rho_L u^* r_W / \mu_L$
W^+	liquid flow parameter; $W_L / (2 \pi r_W \mu_L)$

Superscripts

-	mean value

Subscripts

a	acceleration
b	bubble
b_o	burnout
c	critical or contact
d	departure
DNB	departure from nucleate boiling
e	entrainment
f	frictional
GT	Guerrieri-Talty
H	hydrodynamic mean

Subscripts

h	hemispherical
HT	heat transfer
i	initiation of nucleation or inlet
I	impact
L	liquid
lam	laminar boundary layer
N	normal
o	inlet
S	saturation
s	spherical
sub	subcooled
T	total
TP	two-phase
V	vapour
W	wall

Glossary

'critical point' represent the location of the onset of burnout.

CHAPTER ONE

INTRODUCTION

1.1 The Project

This thesis is concerned with nucleate boiling in a liquid flowing through a vertical tube, a phenomenon which has wide industrial application to a great variety of liquid systems. Straight tube reboilers are used in the distillation of petroleum products and a nuclear reactor, with vertical boiler tubes, which uses an organic liquid as the primary coolant has been developed in Canada. Boiling heat transfer also occurs in refrigeration systems using, for example, ammonia of Freon-12.

Despite these many applications, the major part of the very large research effort centered on the various aspects of boiling heat transfer has concentrated on the study of steam/water systems. Although it has produced many useful correlations for this particular system, these are not generally applicable to other liquid systems and there still exists a lack of understanding of the fundamental mechanisms underlying many of the phenomena. Before universally applicable theories can be formulated, more work must be conducted on systems other than water so that a more thorough investigation of these basic mechanisms can be made.

This thesis presents data for an organic liquid, 112-trichloro-trifluoroethane, and uses these, together with published water data, to investigate nucleate boiling, and 'burnout' in a forced flow system. Mechanisms for these two phenomena are presented and their inter-relationship discussed with reference to both uniform and non-uniform heat flux distributions.

1.2 Flow Regimes In Vertical Upward Two-Phase Flow

A number of different flow regimes have been observed and several of these may be present in a boiler tube at any one time. Detailed descriptions have been presented by many workers and good examples with diagrams are given by GRIFFITH (38). Nucleate boiling has been observed in all the regimes where the heating surface is covered by liquid.

1.3 The Scope Of This Thesis

The objectives of this thesis are concerned with a thorough investigation of the mechanisms underlying nucleate boiling in forced flow systems and the importance of boiling in the precipitation of burnout under these conditions.

To achieve this, a critical assessment of the literature is made to ascertain the known facts and trends and also to investigate the occurrence of burnout associated with nucleate boiling. With this background, a new boiling mechanism is developed which is tested against published data and extended to describe the precipitation of burnout. A series of experiments were performed to confirm this new theory and to clarify some of the points arising from the theory's development and the literature discussion. Entrainment measurements were made to determine the burnout mechanism for the experimental data. A careful analysis of this data is made to confirm earlier trends and to recognise new ones.

1.4 Choice Of Liquid

The choice of liquid on which to conduct these investigations was governed by the desire to obtain burnout data for a large range of nucleation rates and also that the liquid should be stable at the high temperatures

generated at the 'burnout' point.

These conditions were satisfied by using 112-trichlorotrifluoroethane as the test liquid. The liquid's low latent heat and boiling point allowed the required experimental data to be readily observed and its inertness reduced laboratory hazards in its use.

The liquid was supplied by Imperial Smelting Co. Ltd., by whom it is termed ISCEON 113. It is manufactured to the following purity specification:

Maximum Water Content (p.p.m. by wt.)	10
Maximum Boiling Range (deg.C, 5% - 85%)	0.25
Maximum High Boiling Residue (Vol %)	0.01
Chlorides	Not Detectable
Appearance	Clear and Water White

There exists a considerable difference between many of the values of the physical properties of Isceon and water as shown in Table 1.1.

TABLE 1.1

Physical Properties at 1 Atmosphere

	Isceon 113	Water	
Boiling point	49.8	100	^{o}C
Density of liquid at sat.	1504.	988	Kg/m^3
Density of vapour at sat.	7.7	0.605	Kg/m^3
Surface tension at 20°C	0.023	0.072	N/m
Viscosity of liquid at sat.	0.49×10^{-3}	$.28 \times 10^{-3}$	Ns/m^2
Latent heat of vaporisation	1.46×10^{5}	22.7×10^{5}	J/Kg
Thermal conductivity of liquid, 30°C	.066	0.62	$W/m^{o}C$

The experimental data presented in this thesis therefore provides valuable evidence, when used in conjunction with the many available water data, for assessing the validity of mechanisms in the formulation of universal theories.

CHAPTER TWO

CRITICAL HEAT FLUX - LITERATURE SURVEY

2.1 Introduction.

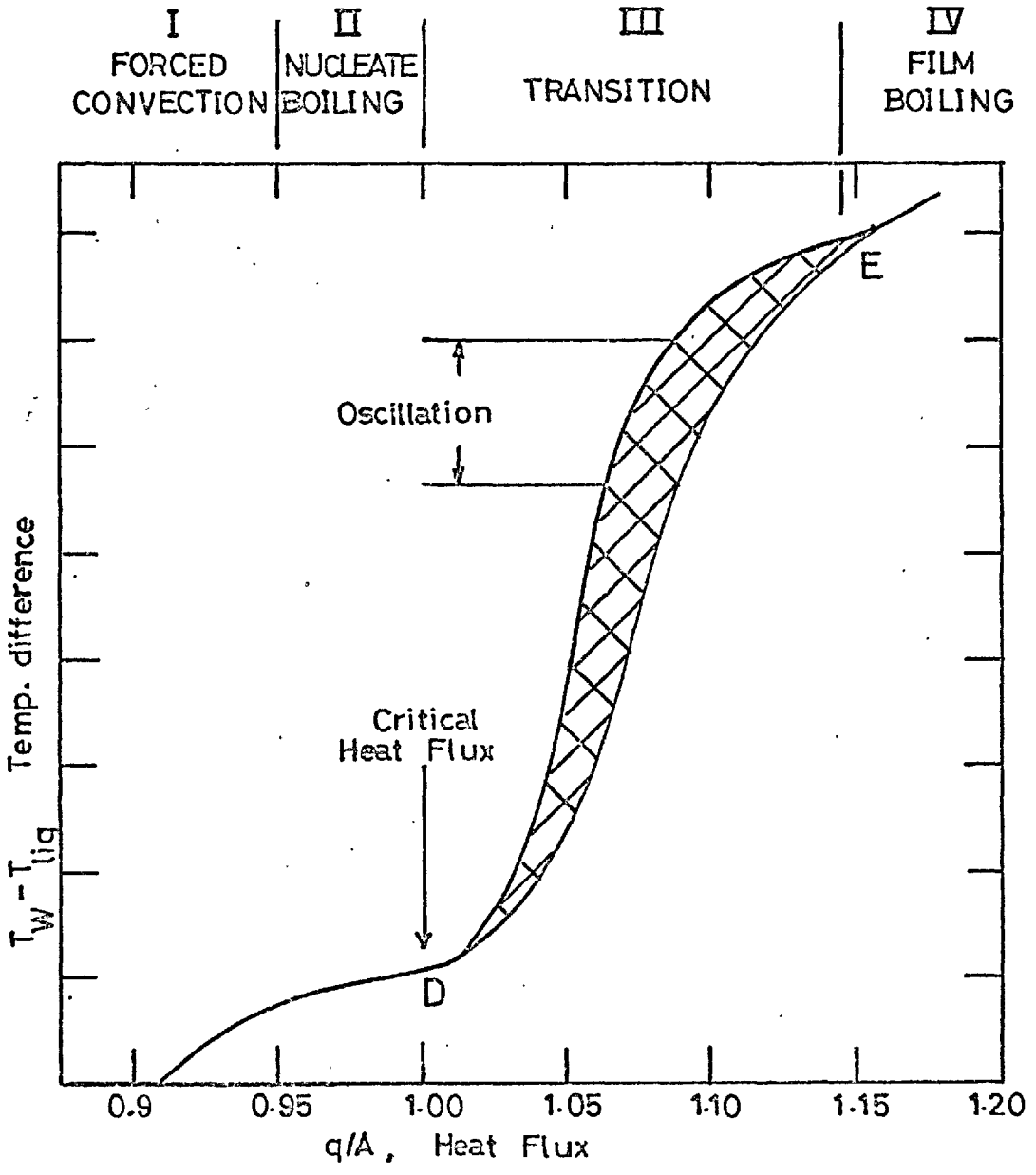
Typical of test results in the vicinity of burnout is the curve shown in Fig. 2.1 where four regions of heat transfer are identified. Point D represents the heat flux which is associated with a sharp reduction in the ability to transfer heat from the surface. The value of the heat flux at D has been variously termed the point of departure from nucleate boiling (DNB), the critical heat flux, the critical condition and the burnout point or burnout heat flux.

The expression DNB particularly refers to pool boiling and sub-cooled forced convection boiling but as will be shown later, cannot accurately be applied to saturated forced convection boiling although some authors have done so.

The burnout heat flux is literally the heat flux at which a self heated element - an electrically heated one for instance, or a fuel element in a nuclear reactor - will burn out because of the heat flux. It may fail because it melts or in the case of an internally pressurised element because of rupture aided by a rise in temperature. The burnout heat flux cannot therefore, be related uniquely to any particular point in the boiling curve and may occur anywhere on the curve depending upon the metal and the conditions of the experiment.

Of the terms used the critical heat flux and critical condition are the best since they imply neither a mechanism for the change in heat transfer rate nor the necessity for tube failure. These expressions are

FIG 2.1 A Typical Temperature History During Burnout (3)



used as far as possible for the point D in the following chapters but the term 'burnout' is also used on occasions and may be regarded as synonymous with critical heat flux.

In annular flow nucleate boiling may not occur if the film is very thin and point D may be reached without Region II of Fig. 2.1 ever being obtained. Point E is called both the point of minimum heat flux and the Liedenfrost point and both these terms are used in the following discussion.

2.2 Effect Of External Parameters On The Critical Heat Flux.

The results of BELL (4) for the upward flow of water in a rectangular channel at 2000 p.s.i.a. show that at a fixed quality the critical heat flux decreases with increasing mass velocity at qualities greater than saturation and increases with increasing mass velocity under subcooled burnout conditions; this suggests a change of burnout mechanism at zero quality. Whereas for subcooled boiling BERGLES (5) shows no L/D effect for L/D greater than 40, LOWDERMILK et al (6) and TIPPETTS (7) show the existence of a very strong L/D effect at high qualities again indicating a change in mechanism from the subcooled condition.

The importance of the inlet conditions has been disclosed by MACBETH (10) who demonstrated that data obtained from experiments having inlet qualities greater than zero showed a considerable scatter. Results obtained under subcooled inlet conditions were more consistent and amenable to correlation.

2.3 Correlations Of Critical Heat Flux

Many correlations for forced convection critical heat fluxes are presented in the literature and they fall broadly into three categories;

a) correlations developed for one set of data only,

b) correlations which are derived by a statistical analysis of a large number of data,

c) semi-empirical correlations based on an attempt to define a criterion for the onset of the critical condition.

Category (a).

The early work of GUNTHER (11) affords a good example of a correlation in this category. He produced critical heat flux data for sub-cooled water flowing in a channel of rectangular cross section 3/16"x1/2"x6", with an electrically heated metal strip $\frac{1}{8}$" wide suspended lengthwise to divide the channel into two flow passages. He correlated his own water data by the expression

$$q_{burnout} = 0.0135V^{0.5}\Delta T_{sub} \quad . \quad . \quad . \quad . \quad . \quad . \quad (2.1)$$

Category (b)

This type may be represented by the correlations of MACBETH (10), LOWDERMILK et al (5) and VON GLAHN (12). Macbeth formulated an expression which correlated a large number of the published water data upto 1964. He recognised a low and a high flow regime for burnout and produced a correlation for each as follows:

Low velocity regime: Pressure range 560 - 2000 p.s.i.a.

$$q_{bo}x10^{-6} = \frac{(Gx10^{-6})(\lambda+\Delta h_i)}{158.D^{0.1}(Gx10^{-6})^{0.49}+4L/D} \quad . \quad . \quad . \quad . \quad . \quad (2.2)$$

High velocity regime:

$$q_{bo}x10^{-6} = \frac{A'-\frac{1}{4}D(Gx10^{-6})X_c\lambda}{C'} \quad . \quad . \quad . \quad . \quad . \quad (2.3)$$

where

$$A' = Y_o D^{Y_1}(Gx10^{-6})^{Y_2}(1+Y_3 D+Y_4(Gx10^{-6})+Y_5 D(Gx10^{-6}))\ldots \quad (2.4)$$

and

$$C' = Y_6 D^{Y_7}(Gx10^{-6})^{Y_8}(1+Y_9 D\, Y_{10}(Gx10^{-6})+Y_{11} D(Gx10^{-6})) \quad (2.5)$$

The twelve constants of Y are tabulated for different pressures in reference (10).

Lowdermilk et al (6) produced a correlation for water data. Two regions of burnout were observed, a low velocity, high exit quality region for which the critical heat flux was correlated by the expression

$$q_{bo} D^{0.2}(L/D)^{0.85} = 270 \times G^{0.85} \quad (2.6)$$

for

$G/(L/D)^2$ less than 150

and a high velocity low exit quality region where

$$q_{bo} D^{0.2}(L/D)^{0.15} = 1400\, G^{0.5} \quad (2.7)$$

for

$G/(L/D)^2$ greater than 150.

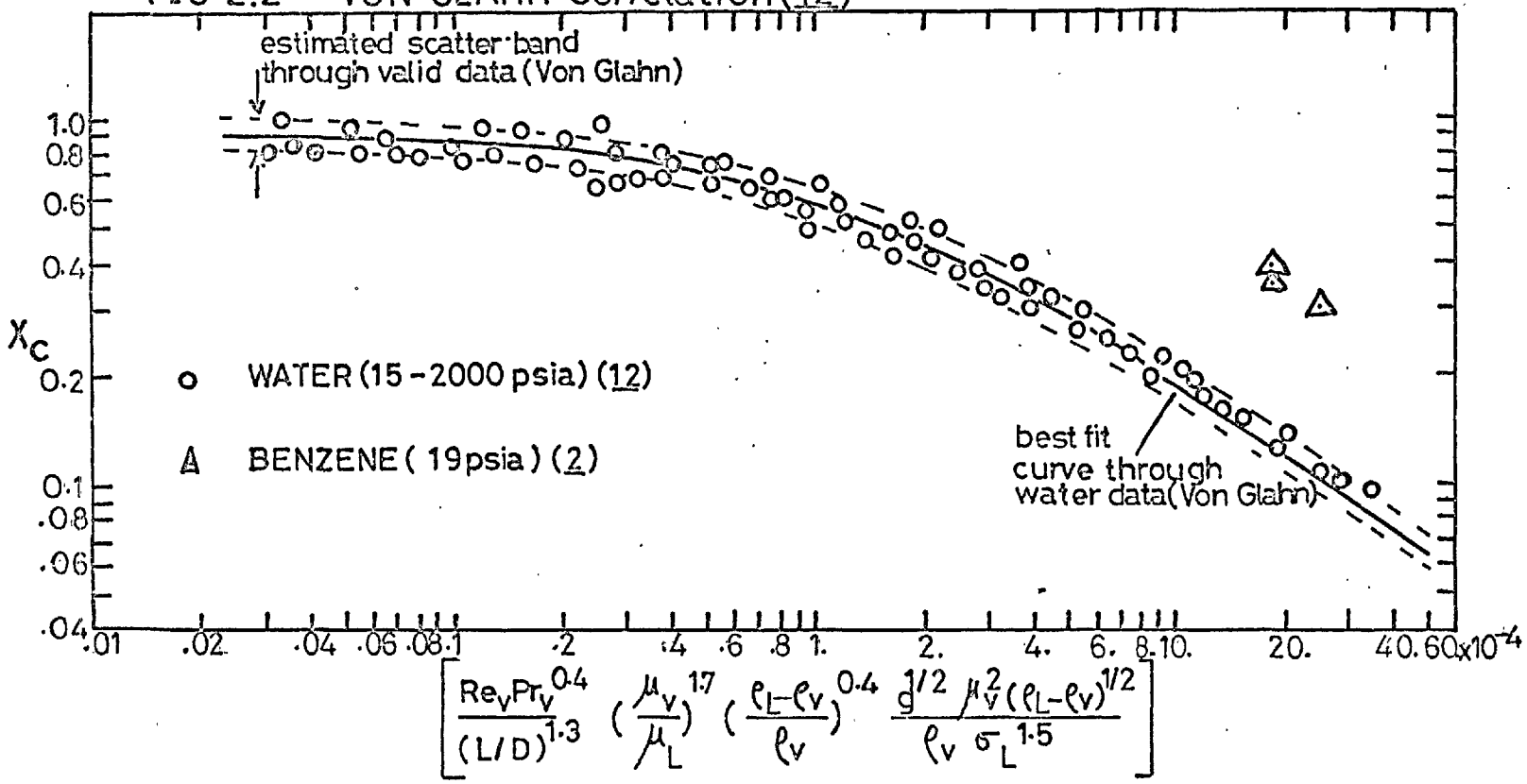
These workers noted that at the limiting value of $G/(L/D)^2$ of 150 the exit quality varied from 40 to 60%.

Von Glahn (12) used the water data of Lowdermilk, and further data for hydrogen and nitrogen to produce a more general correlation,

$$\frac{\frac{q_c L}{G D}}{\left(\frac{4}{\lambda + WC_p \Delta T_i}\right)} = f\left(\frac{Re_V^{0.4} Pr_V}{(L/D)^{1.3}} \left(\frac{\mu_V}{\mu_L}\right)^{1.7} \left(\frac{\rho_L - \rho_V}{\rho_V}\right)^{0.4} \left(\frac{g^{\frac{1}{2}} \mu_V^2 (\rho_L - \rho_V)^{\frac{1}{2}}}{\rho_V \sigma_L^{1.5}}\right)\right) \quad (2.8)$$

The application of this correlation to the benzene data of Backhurst (2) is shown in Fig. 2.2. Clearly the benzene data is not so well correlated as other data and this failure to represent data for systems

FIG 2.2 VON GLAHN Correlation (12)



other than those considered in its original preparation is typical of many such correlations.

Category (c)

This third category may be represented by the correlations of GAMBILL (13) and SONNEMANN (14).

Gambill produced a correlation to predict the forced convection subcooled burnout heat flux for a variety of liquids based on the premise that boiling and convective heat flux terms can be independently formulated and added to yield the total heat flux at the critical condition.

The pool boiling contribution under saturated conditions was calculated from the expression

$$(q_{bo})_{pool,sat} = \frac{K' \lambda \rho_V (\sigma g \Delta\rho)^{\frac{1}{4}}}{(\rho_V^2)} \quad . \quad . \quad . \quad . \quad . \quad (2.9)$$

Heat fluxes for subcooled conditions were derived from the saturated value by multiplying by F_{sub}, a function of the fluid physical properties and subcooled temperature difference.

The forced convection contribution was obtained from

$$(q_{bo})_{nb} = h_{nb}(T_W - T_L)_{bo} \quad . \quad . \quad . \quad . \quad . \quad (2.10)$$

where $(T_W - T_L)_{bo}$ was calculated from the Bernath correlation (32) and the heat transfer coefficient, h_{nb}, was presented in the general form

$$h_{nb} = K'' \ (k_L/D) \ Re^m Pr^n \quad . \quad . \quad . \quad . \quad . \quad (2.11)$$

Summation of equation (2.9) - (2.10) enabled the forced convection critical heat flux to be obtained. He emphasised that this method is not applicable to forced convection bulk boiling burnout but he successfully correlated four

points occuring under these conditions using the Guerrieri-Talty multiplying factor (15).

Gambill obtains his correlation by choosing suitable values for K' (in the range 0.12 to 0.29) and K" (in the range 0.018 to 0.027) but does not indicate how values for K' and K" can be chosen for his approach to be used as a prediction method in the absence of experimental data. A random choice for K' and K" is used for the data of Table 2.1 where the benzene data of BACKHURST (2) is compared with predicted critical heat fluxes using Gambill's technique, with the values for K' and K" chosen as the approximate mid-values in their respective ranges. Under these conditions the experimental values are shown to be considerably overpredicted.

TABLE 2.1

Analysis Of Benzene Data (2) By Gambill Summation Method

K' = 0.18 (Rohsenow (16))

K" = 0.023 (Dittus-Boetter (15))

Predicted heat flux W/m^2	Experimental heat flux W/m^2	X_{bo}
0.81×10^6	0.26×10^6	0.45
0.91×10^6	0.26×10^6	0.43
0.90×10^6	0.317×10^6	0.37

SONNEMANN (14) earlier presented a correlation for water at 2000 p.s.i.a. based on the premise that the burnout heat flux is equal to the sum of the flux required to initiate nucleate boiling (q_{nu}) plus an incremental flux required to bring about what he called incipient film boiling (q^*).

This leads to the equation

$$q_{bo} = q_{nu} + q^* \qquad (2.12)$$

where q_{nu} was given by JENS and LOTTES (26) equation

$$T_W - T_S = \frac{60(q_{nu}/10^6)0.25}{e^{P/900}} \qquad (2.13)$$

q* was derived from Sonnemann's own data for water. His approach showed quite good agreement with the new subcooled boiling data he tested but there was a considerable spread at qualities above saturation.

Despite all the research effort on the critical condition aspect of heat transfer there still exists a considerable lack of universality in the application of the correlations which have been derived. This has resulted since 1961 in an increased effort to investigate the mechanism of the onset of the critical condition and the majority of the more recent works have been concerned with this.

2.4 Observations of Critical Heat Flux Mechanisms

2.41 Subcooled Boiling

Several attempts have been made to observe and photograph the phenomenon of burnout under subcooled conditions but no consistent mechanism has been revealed. GUNTHER (11) observed clumping of bubbles into local vapour films at conditions near the burnout limit and thus associated bubble coalescence with instability and incipient burnout. KIRBY et al (17) noted that the heater was covered alternately by a thin water film under large bubbles and a thick water layer between bubbles, but were unable to distinguish under which the burnout was initiated. FIORI and BERGLES (9) found a similar difficulty in describing the mechanism from photographs but supported

the view of KIRBY et al.

However, although no clear mechanism has been revealed by these observations it appears that subcooled burnout is related to bubble behaviour in the vicinity of the heating surface.

2.42 Saturated Boiling

Film flowrate measurements using water made by HEWITT et al (8) and later by BENNETT et al (18) show that burnout in annular flow can occur at the point where, as a result of evaporation and entrainment the film flow rate falls to zero. Nucleation was occasionally observed in the film but there was no evidence to suggest that this initiated the critical condition. Backhurst's entrainment data (2) for benzene and benzene/toluene mixtures lend support to this film dry-out mechanism for the majority of his critical heat flux measurements, but he presents three values, one for benzene at 40% quality, and two for benzene/toluene mixtures at 42% and 50% quality, which indicate that a substantial liquid film flowrate remained at the burnout point. No attempt was made by Backhurst to present a mechanistic account of this phenomenon though he did describe these burnouts as 'film boiling' indicating the posibility of a nucleation mechanism.

2.5 General Conclusions From Correlations And Observations

For uniform heat flux distributions, a dependency on the overall conditions would give at constant inlet subcooling and burnout quality

$$q_{bo}LD \propto W_T$$

or $$q_{bo}LD \propto G_T D^2$$

and $$q_{bo} \propto G_T(D/L) \qquad (2.14)$$

This may be closely compared with the correlation of Lowdermilk et al for the low velocity, high exit quality region where

$$q_{bo} \propto G^{0.85} D^{0.65}/L^{0.85} \quad . \quad . \quad . \quad . \quad . \quad . \quad . \quad (2.15)$$

The application of this correlation to only high exit quality conditions corresponds precisely with the conditions of the observation of the 'film dry-out' mechanism of HEWITT (8) so that data obtained for uniform and non-uniform heat flux distributions which are correlated by a total heat input or mean heat flux approach can be expected to have resulted from this mechanism.

GUNTHER (11) however showed that for subcooled burnout precipitated by nucleation

$$q_{bo} \propto \overline{U}_L^{\frac{1}{2}} \quad . \quad . \quad . \quad . \quad . \quad . \quad . \quad (2.16)$$

or since $\overline{U}_L = G_T/\rho_L$

$$q_{bo} \propto G_T^{\frac{1}{2}} \quad . \quad . \quad . \quad . \quad . \quad . \quad . \quad (2.17)$$

This compares with the Lowdermilk correlation for high velocity, low exit quality region where

$$q_{bo} \propto G_T^{0.5}/(L^{0.15} D^{0.05}) \quad . \quad . \quad . \quad . \quad . \quad . \quad (2.18)$$

This suggests that burnouts in low quality regions as well as subcooled regions may be precipitated by nucleation and the small dependency of q on L and D in equation (2.18) indicates that the local heat flux rather than the overall heat input is the criterion for burnout. This nucleation mechanism for burnout in saturated boiling has not been directly observed but the measurements by BACKHURST (2) described in Section 2.4 afford indirect confirmation.

2.6 Models Presented To Describe The Mechanism For The Onset Of The Critical Condition

Several attempts have been made to produce a correlation to describe the critical heat flux data, derived from a mechanistic approach. These may broadly be divided into the two categories described in Section 2.4 of liquid deficient or film dry-out mechanisms and nucleate boiling mechanisms.

2.61 Film Dry-Out Models

With high steam qualities fog flow occurs in the channel. The bulk of the fluid then consists of saturated vapour with a dispersion of small liquid droplets and the wall is covered by a thin film of liquid. It is for this region that dry-out mechanisms have been proposed.

2.61.1 Droplet Diffusion Models

The model of ISBIN et al (19) assumed that liquid is lost from the film by vaporisation and by entrainment of liquid droplets into the vapour core; liquid is also returned to the film by a droplet diffusion from the vapour core. Burnout occurs when the quantity of liquid removed from the heating surface exceeds the liquid deposition sufficiently to reduce the liquid film flow rate to zero.

A complex analysis of this model is presented in (19) resulting in a correlation involving six empirical constants, three of which take different values for every set of data correlated making use of their model for prediction difficult.

The model of GOLDMANN et al (20) assumed the same mechanism for heat transfer as described by Isbin. A flow of vapour normal to the

heating surface is postulated opposing droplet diffusion and also causing some droplets to evaporate before reaching the heating surface. Knowledge of the physical factors in the model, the eddy diffusion of droplets for example, are limited and attempts to fit this model to experimental data have not been successful. TOPPER (21) presented a model described by STEIN (22) which is identical to that of Goldmann et al, but their derived correlation systematically overpredicts by more than 30%. Work being conducted at Harwell by COUSINS and HEWITT (23)concerning droplet deposition may help in the further investigation of the validity of these diffusion models.

2.61.2 Film Instability Models

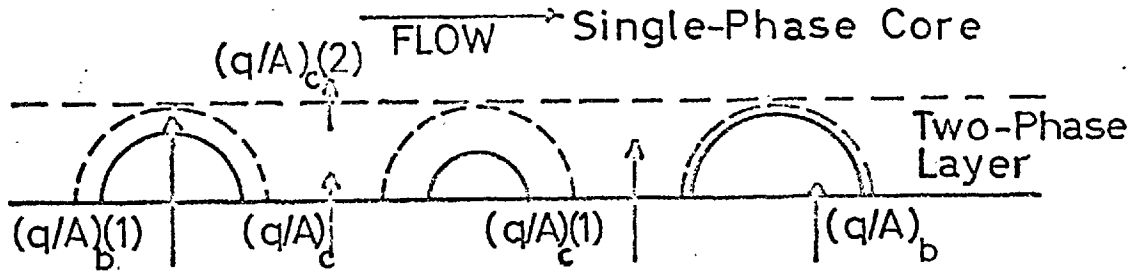
BECKER (24) and TIPPETS (25)have both presented models which suggest that breakdown of the liquid film is caused by the amplitude of waves on the film surface exceeding the liquid film thickness causing formation of a stable dry spot which precipitates the burnout condition. Observations of HEWITT and LACEY (27), however show that spontaneous breakdown of the film does not occur until the liquid film flowrate is very close to zero so that it is difficult to distinguish between a disruption of the film by wave action and straight forward evaporation.

2.62 Nucleate Boiling Models

The earliest presented nucleation model was the Sequential Rate Process of BANKOFF (28) based on the work of GUNTHER (11). His model is shown in Fig.2.3 and he described the heat transfer process in 3 phases:

1) Heat transfer to two phase layer.

2) Heat transfer through two phase layer.



$(q/A)_c(2)$ = the convective heat flux from the outer portion of the two phase wall layer to the turbulent core.

$(q/A)_b(1)$ = the heat flux due to vaporisation of liquid at the inner portion of the wall layer and condensation at the outer portion.

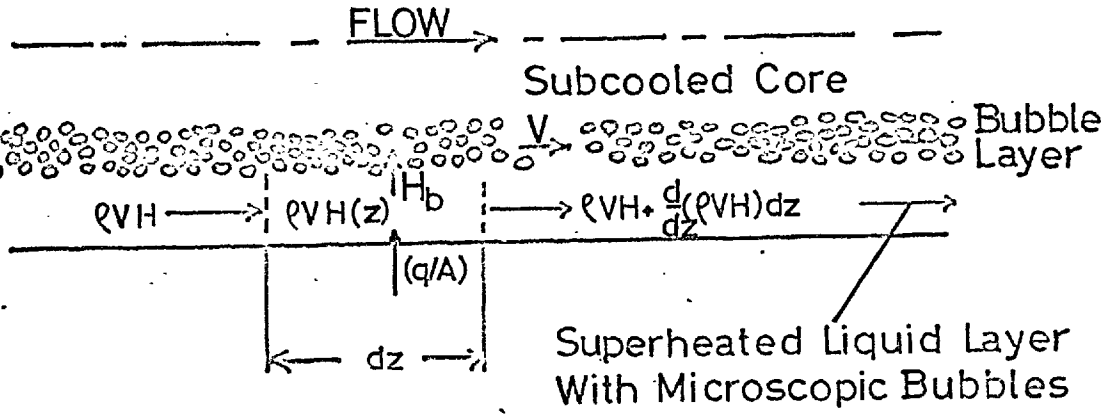
$(q/A)_c(1)$ = the convective heat transport through the liquid between the bubbles.

$(q/A)_c$ = the convective heat flux from the surface between the bubbles at any instant.

$(q/A)_b$ = the heat flux from the surface beneath the bubbles.

$$(q/A)_c(2) = (q/A)_b(1) + (q/A)_c(1) = (q/A)_b + (q/A)_c$$

FIG 2.3A BANKOFF'S Sequential Rate Process Model



The superheat of the superheated layer and the local heat flux determine the temperature of the wall and thus critical heat flux conditions.

FIG 2.3B TONG'S Subcooled Burnout Model

3) Heat transfer away from two phase layer.

His work was basically concerned with predicting the rate of heat transfer in subcooled nucleate boiling but he did suggest that the critical heat flux would be reached when heat was transferred through the two phase layer faster than it could be removed by the single phase layer. No attempt was made to use this as a prediction method.

More recently ROHSENOW and TODREAS (29) attempted to explain upstream burnout data obtained for non-uniform heat flux distributions and some uniform heat flux distributions (30) by disruption of the liquid film by bubbles causing the formation of a stable dry-spot. They assumed that the greater the liquid film flow rate the greater would the nucleation rate need to be to disrupt the film and they anticipated a burnout curve of the form shown in Fig.2.4. They made no attempt to measure the film flowrate at the critical point so the only support they have for their mechanism is that their results follow similar trends to those of Fig.2.4. However, the results of HEWITT (8) also show the same trend and these were shown to be caused by total evaporation of the liquid film.

If film dry-out does account for the results of Rohsenow and Todreas then they should be correlated by a total heat input approach. Fig. 2.5 demonstrates that the majority of their results for the flowrate 0.5×10^6 lb/ft^{2}hr are in fact correlated to $\pm$ 10% by this approach. However several points at qualities less than 50% (Fig.2.6) clearly could not be explained on this basis and it may be that the model of Todreas and Rohsenow is applicable to this lower quality regime.

TONG (33) attempted to derive a multiplying factor to predict the

local non-uniform burnout heat flux from knowledge of the uniform value so that

$$(q_{bo})_{\text{non-uniform}} = F \times (q_{bo})_{\text{uniform}} \quad . \quad . \quad . \quad (2.19)$$

His model is shown in Fig.2.3 and he proposes that burnout occurs when the enthalpy of the superheated layer reaches some constant but undefined value. From this he developed the following expression for F :

$$F = \frac{C' \int_{o}^{L_{DNB}} q(Z) e^{-C'(L_{DNB}-Z)}\, dZ}{q_{\text{mean loc}}(1-e^{-C'L_{DNB}})} \quad . \quad . \quad . \quad (2.20)$$

where

$$C' = \frac{h_{TP}}{\rho_L U_L Y_i C_P} \quad . \quad . \quad . \quad (2.21)$$

and L_{DNB}= distance from onset of nucleation to burnout point.

Tong suggested that for water data

$$C' = \frac{0.44(1-X_{bo})^{7.9}}{(G_T/10^6)^{1.72}} \quad \text{in}^{-1} \quad . \quad . \quad . \quad (2.22)$$

This approach proves quite successful with the results he presents but this may be deceptive support for his model since equation (2.22) is derived empirically.

Very recently FIORI and BERGLES (9) have presented a nucleation theory for burnout in subcooled systems. Their model is shown in Fig.2.7 and assumes that the vapour volume at the critical point is sufficiently large for slug flow to occur; an assumption which is supported by their own photographic evidence. Bubbles growing in the thin layer of liquid between a vapour slug and the tube wall cause this liquid film to breakdown in a similar manner to that suggested by Rohsenow - Todreas. The wall temp-

erature under the dry spot thus formed commences to rise but is quenched again by a liquid slug once the vapour slug has passed.

Burnout is said to occur when ΔT_{rise} with dry spot exceeds ΔT_{Quench} This temperature oscillation is shown to occur by their own measurements and is also supported by the data of Fig.2.1. Attempts to observe the breakdown of the liquid film in this manner were unsuccessful so that it is not known whether the liquid film flowrate would be sufficiently small to support a dry spot in the manner which they desire.

2.7 Conclusions

At least two mechanisms describe burnout in forced convection boiling, a nucleation initiated mechanism in subcooled boiling and low quality saturated boiling, and a film dry-out mechanism in high quality saturated boiling.

Burnout induced by nucleation depends on the local conditions at the critical point but film dry-out, since it involves total evaporation of the liquid film, is characterised by its dependency on the total heat input to the test section.

The film dry-out mechanism is well described although the physical model is not easily analysed because of the problems involved in the prediction of the proportion of the liquid flow entrained in the vapour stream. Many differing models have been presented in an effort to predict nucleate boiling burnout with little success and it is this aspect of forced convection heat transfer which this thesis discusses in the following chapters.

FIG 2.4 Burnout Prediction Of TODREAS And ROHSENOW

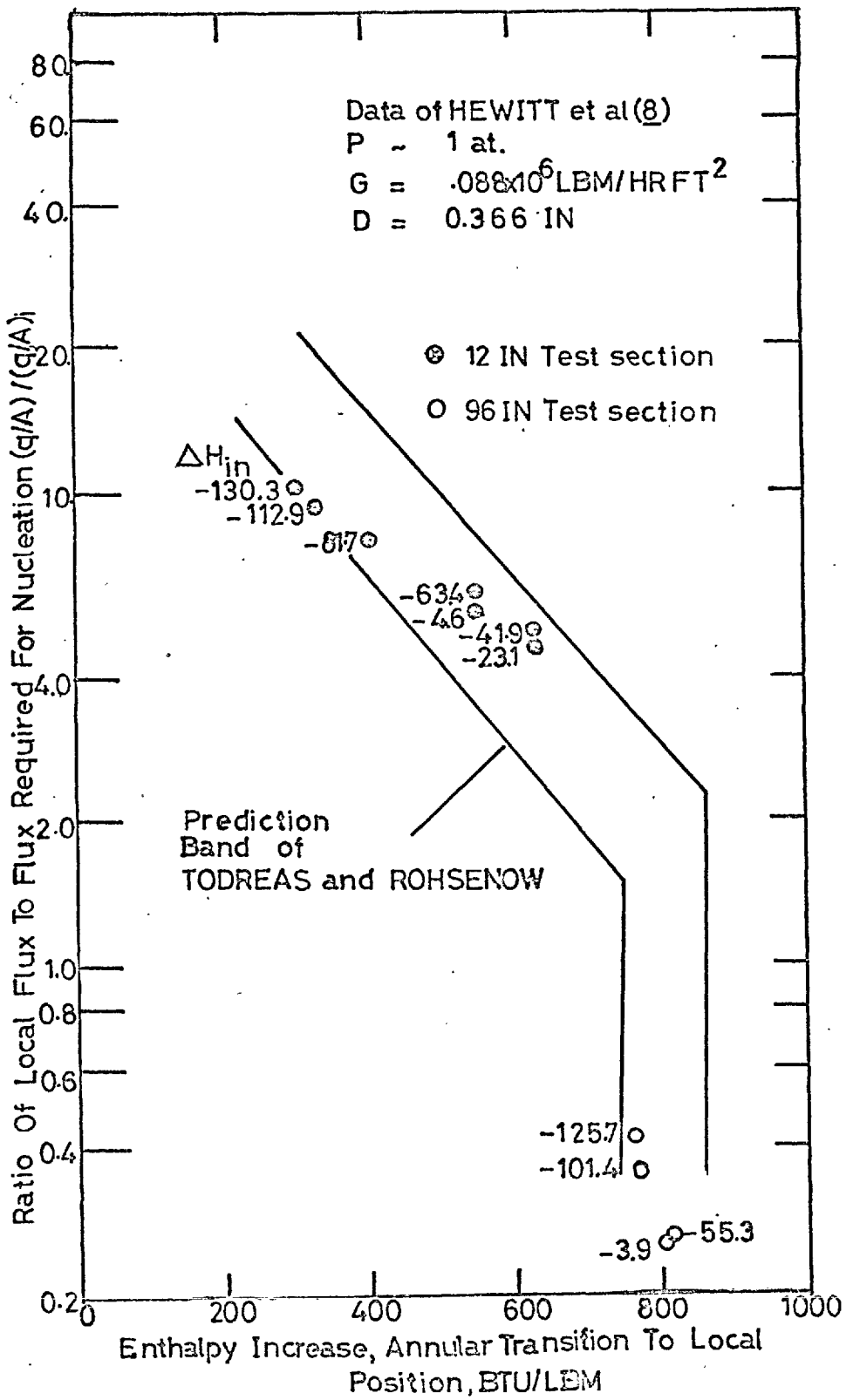


FIG 2.5 Total Heat Input As Correlating Factor

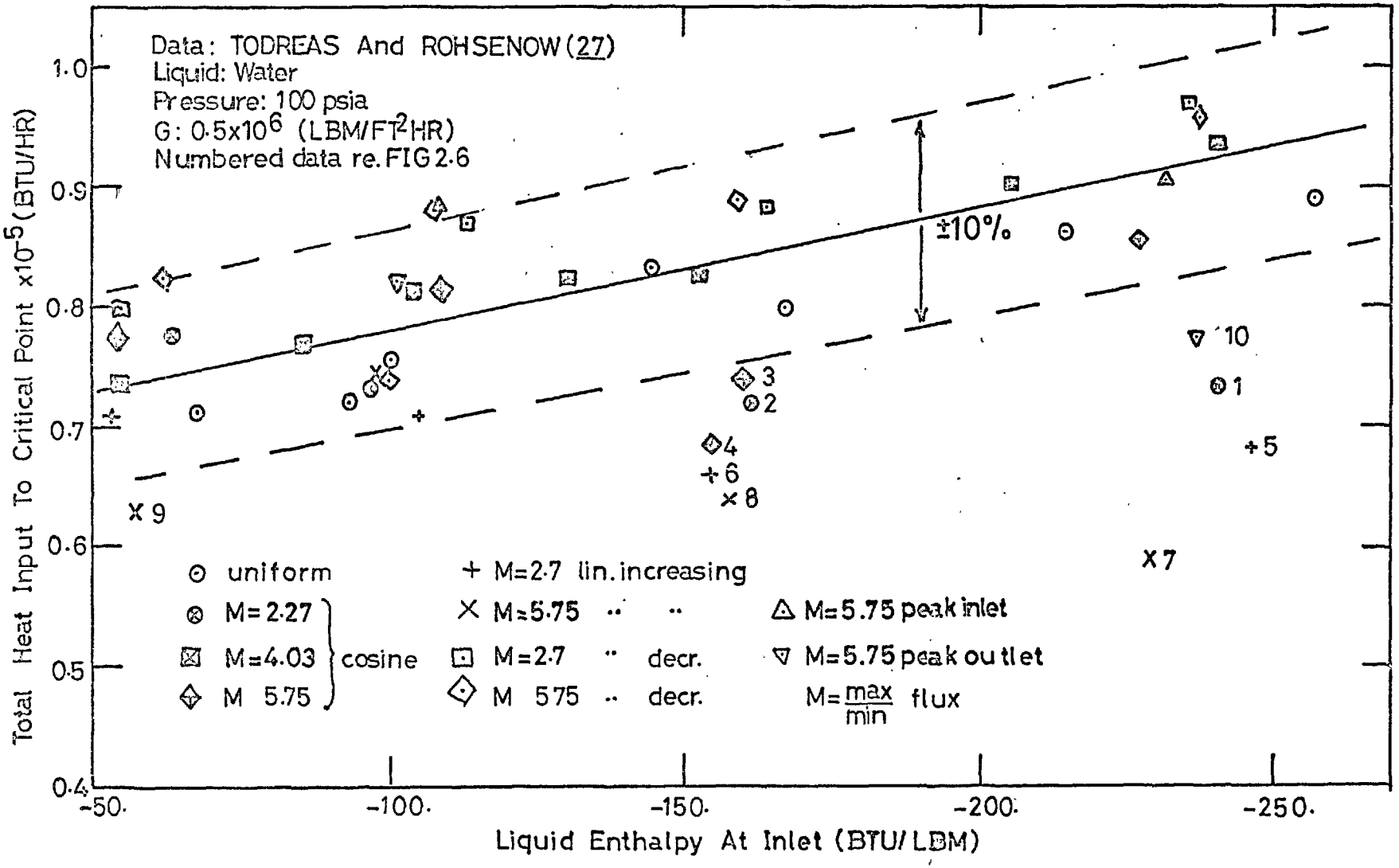


FIG 2.6 Local Burnout Heat Flux As Correlating Factor

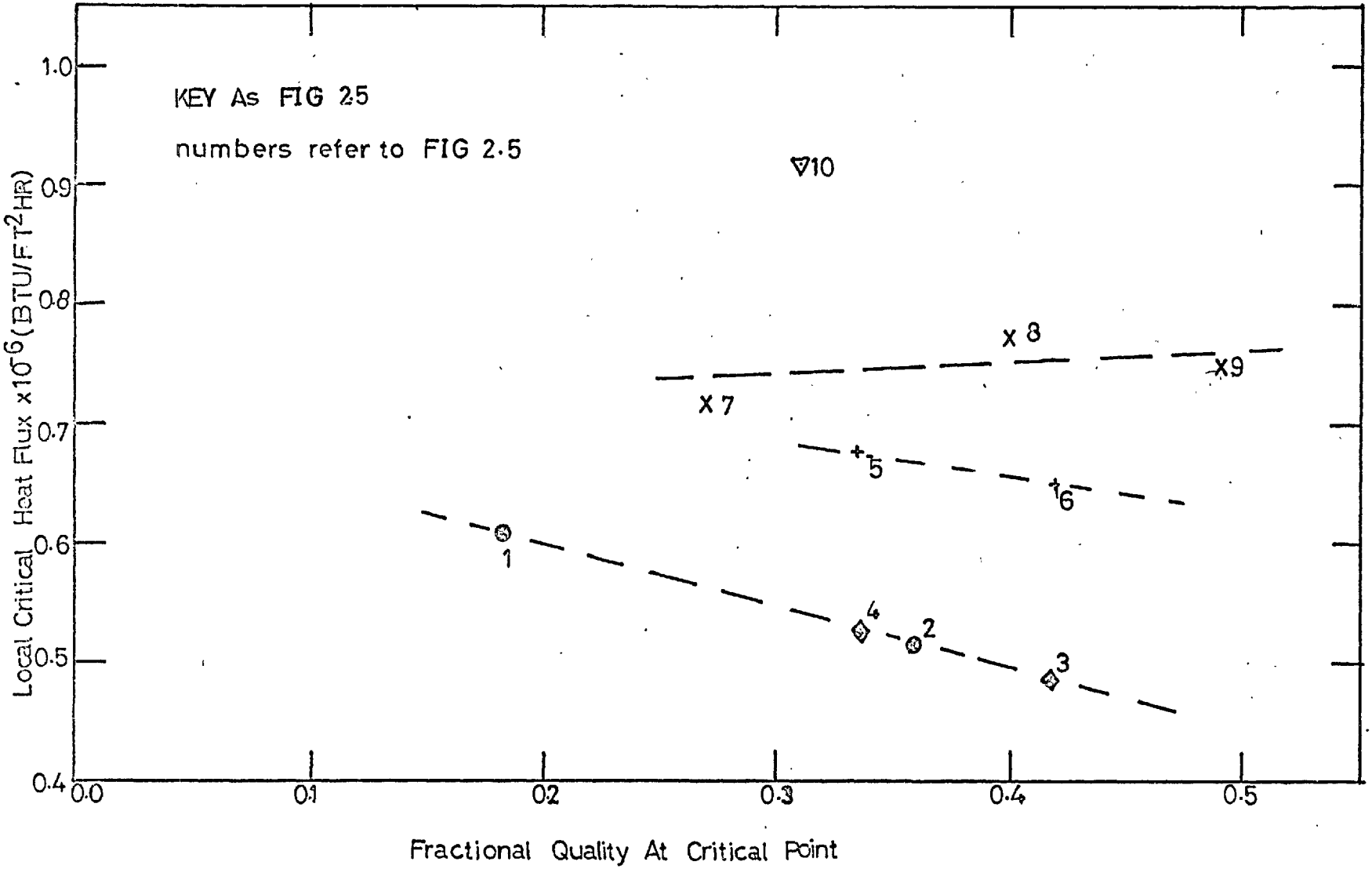
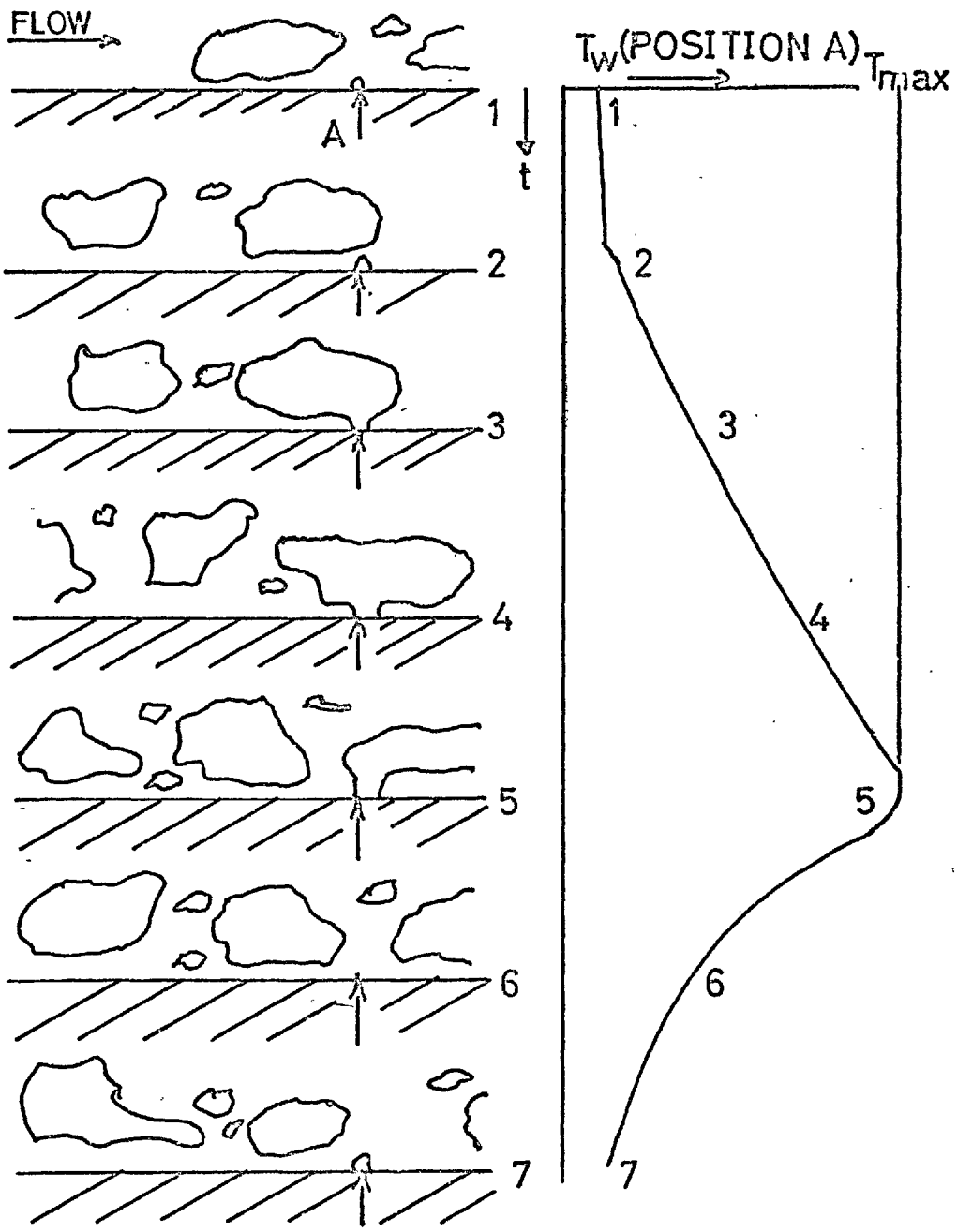


FIG 2.7 Burnout Model Of FIORI And BERGLES



$$T_{max} - T_W = \Delta T_{rise}$$

Burnout : $\Delta T_{rise} > \Delta T_{quench}$

CHAPTER THREE

NUCLEATION IN FORCED FLOW SYSTEMS

3.1 Introduction

A clear quantitative picture of nucleation with forced flow is not available in the literature. This chapter therefore attempts to combine the results of pool boiling with the few qualitative descriptions of forced convection boiling to develop a suitable model for analysis.

3.2 Heat Transfer To Bubbles In Pool Boiling

It has been shown by STRENGE et al (34) and others that the growth of a bubble from the time it can be observed to the time of its departure from the heating surface may be expressed in a general form by the equation

$$R_b = \text{constant} \times t^n \qquad \ldots\ldots\ldots\ldots \quad (3.1)$$

The foundation of many of the theoretical attempts to derive this relationship was laid by PLESSET and ZWICK (35) and FORSTER and ZUBER (36) on the growth of spherical bubbles in an infinite, initially superheated liquid. They treated the problem as one of transient heat conduction from the liquid to the bubble and derived a value of $\frac{1}{2}$ for the exponent n.

The observations of JAKOB and FRITZ (37) of a superheated liquid layer close to the surface of a hot plate in boiling water led to an extension of the transient heat conduction theory to bubbles growing on a heating surface. The general model developed from this analogy is presented in Fig.3.1A. The model assumes that the bubble grows from heat lost by conduction from the superheated boundary layer, δ, which is then pushed away from the heating surface as the bubble expands.

Many workers, (39, 40, 41, 42) for example, have used this

FIG 3.1 Heat Transfer To Bubbles

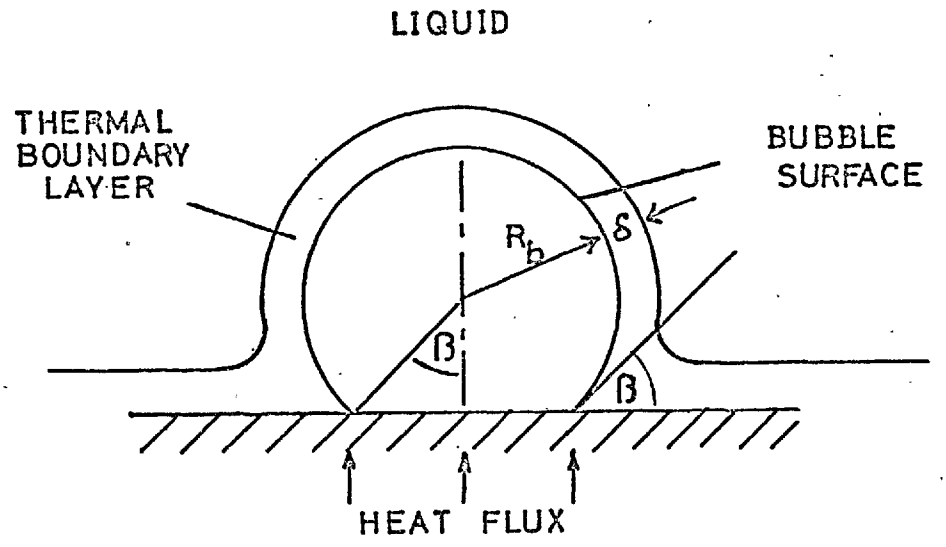


FIG 3.1A Superheated Boundary Layer Theory

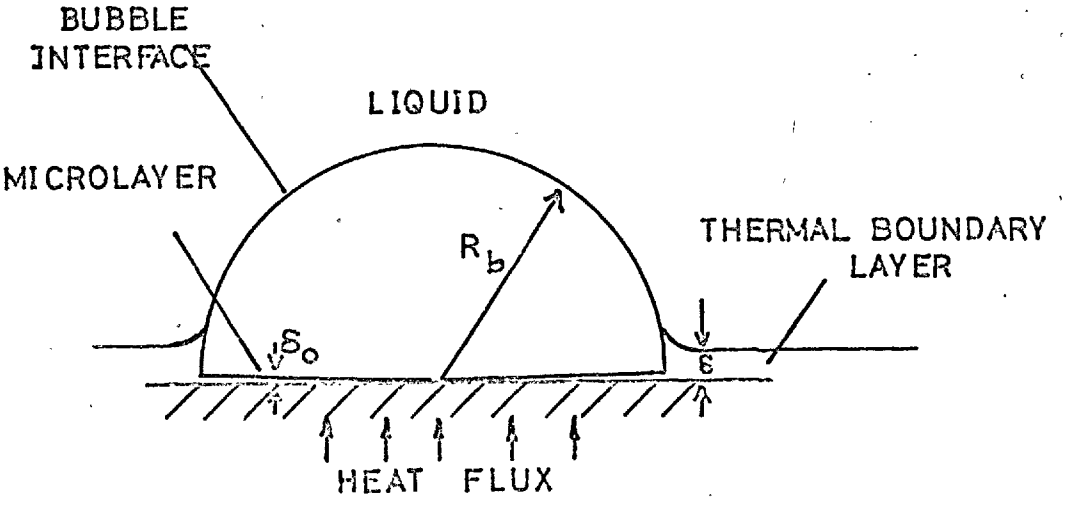


FIG 3.1 B Microlayer Theory

approach with some success to derive expressions for bubble growth and their solutions may be generalised into the form of equation (3.1) as

$$R_b = f(\text{physical properties}, \Delta T) \times t^{\frac{1}{2}} \quad . \quad . \quad (3.2)$$

The form of the function f depends on the particular boundary conditions employed to obtain the solution.

A second model, shown in Fig.3.1B, has been presented by LLOYD (47) suggesting that, at high bubble growth rates, heat transfer does not occur in the manner just described but by the evaporation of a thin film, or micro-layer of liquid existing at the bubble base.

It is related in (46) that the suggestion for such a mechanism was first made by SNYDER (44) and EDWARDS (45) who noted that this mode of heat transfer would probably be accompanied by a very rapid drop in wall temperature. Later measurements by MOORE and MESLER (43) of heater surface temperatures during pool boiling demonstrated that large drops in temperature did occur during nucleation but, unfortunately, the experimental design did not enable the temperature fluctuations to be related to the growth of individual bubbles. HENDRICKS and SHARP (46) and LLOYD (47) succeeded in matching surface temperature measurements with photographic evidence and noted that a rapid drop in temperature occurred when the perimeter of the bubble base passed over the point of temperature measurement thus providing strong evidence in support of the microlayer theory.

This approach does not lend itself readily to the analysis of bubble growth, but an attempt by LLOYD (47) using a numerical technique predicted a value of $\frac{1}{2}$ for the exponent in equation (3.1).

The majority of the attempts to derive a theoretical expression

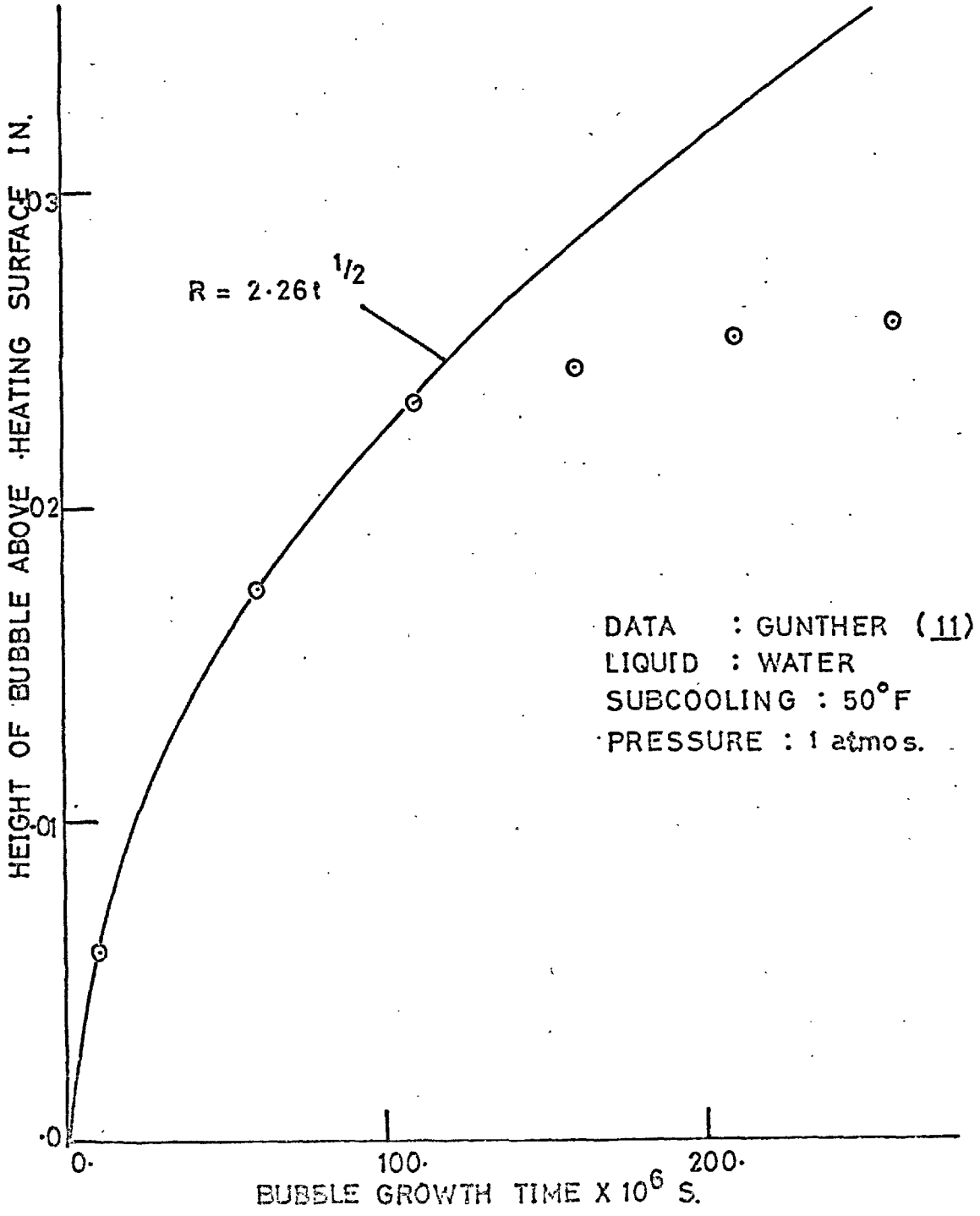
for bubble growth have assumed that the total expansion of the bubble is equal to the total evaporation at the bubble interface. BANKOFF and MASON (48)measured heat transfer coefficients from a steam bubble to subcooled water in forced convection and the results suggested to BANKOFF (49) that latent heat may be transferred through a bubble by evaporation at the base and condensation at the pole so that the bubble growth would be slower than predicted from theory. This can be shown by applying Lloyd's conclusion, $R_b \propto t^{\frac{1}{2}}$, to the data of GUNTHER (11) for growth of hemispherical bubbles in forced convection subcooled boiling. As shown in Fig.3.2, agreement between theory and experiment is obtained upto a bubble radius of .023in. but then a sharp drop in growth rate occurs as the condensation rate becomes significant and the bubble starts to collapse. However the close agreement obtained in the early stages of the bubble growth does suggest that under saturated conditions, when condensation can be expected to be less important, the growth of hemispherical bubbles can be closely approximated by Lloyd's expression

$$R_b \propto t^{\frac{1}{2}} \qquad \ldots\ldots\ldots \quad (3.3)$$

3.3 The Incipience Of Nucleation In Forced Convection

To establish the range of validity of a theory for nucleation in forced convection it is important to be able to estimate the conditions for the incipience or suppression of the boiling. It is now widely accepted that nucleation occurs from pits or scratches in the heating surface where vapour becomes trapped and forms the nucleus from which a bubble grows. This argument was first presented by BANKOFF (65) and has subsequently received considerable support from the photographic studies of CLARK,

FIG 3.2 Growth Of A Hemispherical Bubble



STRENGE and WESTWATER (66) and others.

On this basis BERGLES and ROHSENOW (50) adapted the approach of HAN and GRIFFITH (51) to develop a criterion for the onset of nucleate boiling for a system with a wide range of nucleation sites. They postulated that a hemispherical nucleus will grow if the liquid temperature at a distance $y = R_c$ from the wall is greater than the equilibrium vapour temperature.

For laminar flow at the heating surface the temperature distribution in the liquid close to the wall was approximated by

$$T_L = T_W - qy/K_L \qquad . \quad . \quad . \quad . \quad . \quad . \quad . \quad (3.4)$$

The bubble temperature was derived from the Clausius-Clapeyron equation

$$\left(\frac{dP}{dT}\right)_s = \frac{\lambda P}{R' T^2} \qquad . \quad . \quad . \quad . \quad . \quad . \quad . \quad (3.5)$$

by application of a force balance at the bubble interface of

$$P_b - P_s = \frac{2\sigma}{R_b} \qquad . \quad . \quad . \quad . \quad . \quad . \quad . \quad (3.6)$$

Combination of (3.6) with the integration of (3.5) gave the bubble temperature in the form

$$T_b - T_s = \frac{T_b T_s R'}{\lambda} \ln\left(1 + \frac{2\sigma}{R_b \rho_s}\right) \qquad . \quad . \quad . \quad (3.7)$$

Fig.3.3A shows that the cavity size which is activated is given by the value for R_c at which equation (3.4) becomes a tangent to equation (3.7)

Using this last criterion Bergles and Rohsenow developed a design equation for the heat flux required to initiate nucleate boiling in water :

$$q_i = 15.6\, P^{1.156} (T_W - T_s)^{(2.30/P^{0.0234})} \qquad . \quad . \quad (3.8)$$

INITIATION OF BOILING

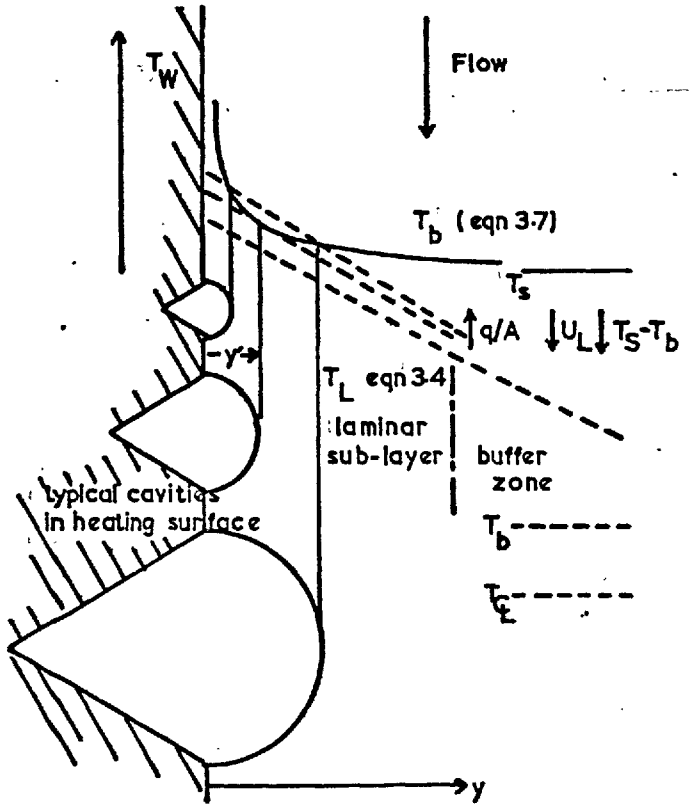


FIG 3.3A

INITIATION OF BOILING

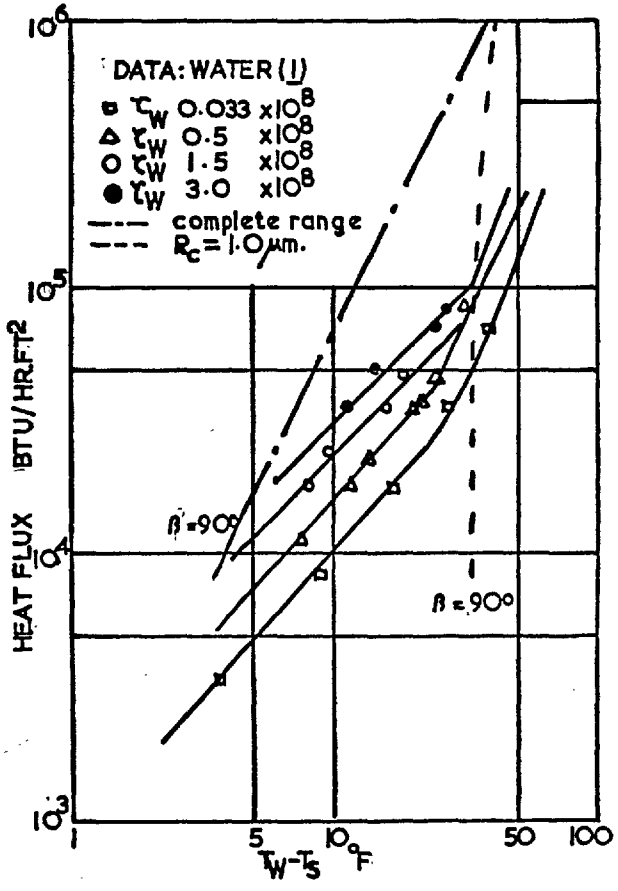


FIG 3.3B

In theory, a nucleation site will be activated if the rate of evaporation into the vapour nucleus exceeds the rate of condensation. The assumption of Bergles and Rohsenow thus represents an upper limit for the criterion.

I KENNING and COOPER (52) suggested that the correct criterion for the onset of boiling was a function of the height of the bubble and the liquid flow past the bubble. They developed an empirical correlation using this criterion and the assumptions of the Bergles and Rohsenow theory, but their analysis predicts wall superheats that are considerably lower than those predicted by the former analysis.

SATO and MATSUMURA (53) also used a derivation similar to Bergles and Rohsenow but assumed a spherical bubble with the critical stream temperature occurring at a distance from the wall equal to the bubble radius. They obtained the following expression for the heat flux required to initiate boiling

$$q_i = \frac{k_L \lambda \rho_V}{8 \cdot T_s} (T_W - T_s)^2 \qquad \cdots \qquad (3.9)$$

All these derivations assume that a wide range of cavity sizes exist on the heating surface, an assumption which is unlikely to be true for polished surfaces. DAVIS and ANDERSON (54) extended the work of Bergles and Rohsenow to deal with surfaces having only a limited cavity size. They assumed the bubble to be a truncated sphere having a contact angle β with the surface.

Thus

$$y_b = R_b (1 + \cos \beta) \qquad \cdots \qquad (3.10)$$

and equation (3.7) becomes

$$T_b - T_s = \frac{R'T_bT_s}{\lambda} \ln\left(1 + \frac{2(1+\cos\beta)\sigma}{y_b P_s}\right) \quad \cdot \cdot \quad (3.11)$$

Using the tangent criterion of Fig.3.2, the following expression was derived for the wall superheat at the onset of boiling

$$T_W - T_s = \frac{\frac{R'T_s^2}{\lambda} \ln(1+\xi')}{1 - \frac{R'T_s}{\lambda}(1+\xi')} + \frac{q_i y'}{K_L} \quad \cdot \cdot \quad (3.12)$$

where

$$\xi' = \frac{2\sigma(1+\cos\beta)}{P_s y'} \quad \cdot \cdot \quad (3.13)$$

and

$$y' = \frac{(1+\cos\beta)\sigma}{P_L} + \left(\left(\frac{(1+\cos\beta)\sigma}{\rho_L}\right)^2 + \frac{2(1+\cos\beta)K_L\sigma T_s}{q_{Wi}\lambda\rho_V}\right)^{\frac{1}{2}}$$

$$\cdot \cdot \quad (3.14)$$

When equation (3.12) is applied to data of MANTZOURANIS (1) for water boiling at 20 lb/in^{2}abs., Fig3.3, the value for q_{Wi} is considerably overpredicted for any given value for ΔT.

An electron micrograph of the surface of the heating tube used by Mantzouranis revealed a maximum cavity size of only 2×10^{-6}M. This means that a higher superheat would be needed to initiate boiling than suggested by (3.12) which is derived for a wider distribution of sites. Fig 3.3B shows that if the constraint of a maximum cavity radius of one micron is applied to equation (3.12) an excellent agreement with experiment is obtained.

3.4 Dynamics Of Vapour Bubbles In Forced Convection

Studies of the dynamics of vapour bubbles in forced convection

boiling are very few and are mostly of a qualitative nature. Photographic studies of subcooled boiling by GUNTHER (11) in horizontal flow and by TIPPETS (7) and KIRBY, STANIFORTH and KINNIER (17)in vertical upward flow showed that after initiation, hemispherical bubbles formed which tended to slide along the heating surface in the direction of the liquid flow before either departing into the liquid stream or collapsing on the wall. KIRBY et al noted, though, that if the applied heat flux was reduced to less than 1/10 of the critical value for burnout, the bubbles did not slide but departed into the bulk liquid from their point of initiation. No attempt has been made to measure the velocity of the sliding bubbles but Gunther estimated it to be of the order of 8/10 of the mean stream velocity increasing slightly with bubble size. SULLIVAN, HARDY and HOLLAND (59) studied the formation of air bubbles at orifices submerged beneath a variety of liquids with a range of flowrates between 0.34 and 2.5 cm./s. The bubbles formed under these conditions were always spherical and showed no tendency to slide.

Kirby, Staniforth and Kinneir qualitatively discussed the forces acting on a spherical bubble growing in vertical forced convective flow, see Fig 3.4A. They developed an expression for bubble inertia forces assuming that the virtual mass of a stationary spherical bubble growing in a liquid of uniform velocity is equal to $\frac{1}{2}$ x the mass of the displaced liquid. This is the same as the value given for spheres moving with a constant acceleration through a stationary liquid (60). Assuming the bubble to be spherical and using an expression for the inertia force as equal to d/dt (virtual mass x velocity), they derived the force in the direction parallel to the heater

surface as

$$\frac{d}{dt}\left(\frac{2}{3}\pi R_b^3 \rho_L U_L\right) = 2\pi R_b^2 \rho_L \frac{dR_b}{dt} U_L \quad . \quad . \quad (3.15)$$

and in the direction normal to the heating surface as

$$\frac{d}{dt}\left(\frac{2}{3}\pi R_b^3 \rho_L \frac{dR_b}{dt}\right) = \frac{2}{3}\pi R_b^3 \rho_L \frac{d^2R_b}{dt^2} + 2\pi R_b^2 \rho_L \left(\frac{dR_b}{dt}\right)^2 \quad (3.16)$$

Equation (3.16) describes a force tending to flatten the bubble against the heating surface and Kirby et al conclude that the bubble will be hemispherical provided this inertia force is greater than the surface tension force, $2\pi R_b \sigma$, tending to make the bubble spherical. On this basis they suggested a physical model for the growth of a large bubble and this is reproduced in Fig. 3.4B.

The importance of the inertial force in governing the shape of a growing bubble is also shown by the work of JOHNSON, JAVIER de la PENA, and MESLER (61) in pool boiling. They recognised three bubble shapes - spherical oblate and hemispherical - and produced graphs comparing the inertial and surface tension forces for each of the bubble types. Fig.3.5 shows, from their data, how the ratio of inertial to surface tension force varies throughout the bubble growth time indicating that

1) for a spherical bubble; surface tension force is greater than inertial force,
2) for an oblate bubble; surface tension force is approximately equal to inertial force, and
3) for a hemispherical bubble; surface tension force is less than inertial force.

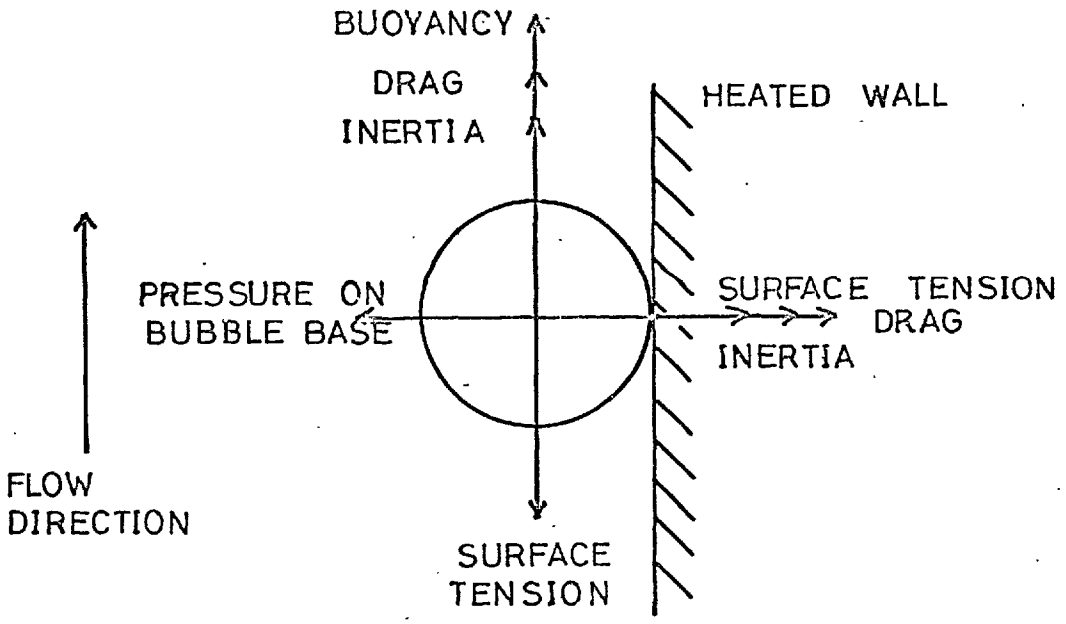


FIG 3·4A Forces Acting On A Growing Bubble

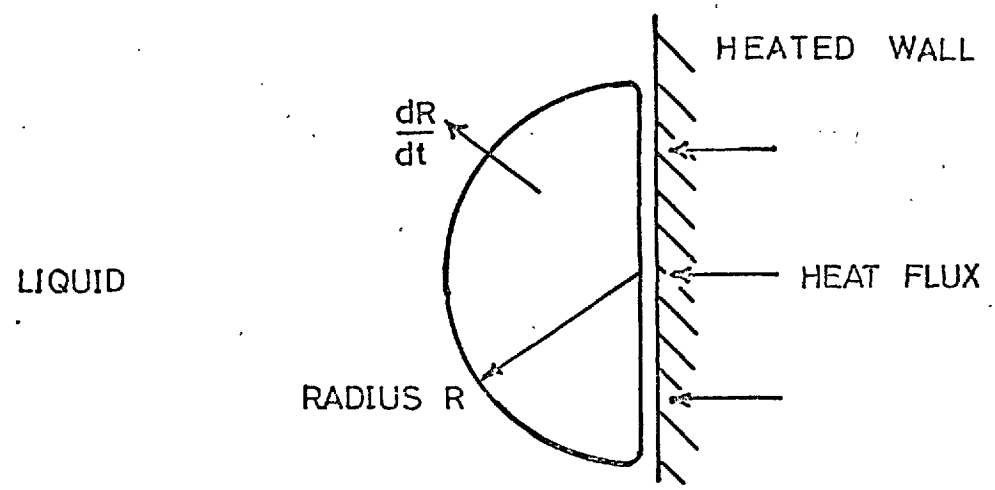
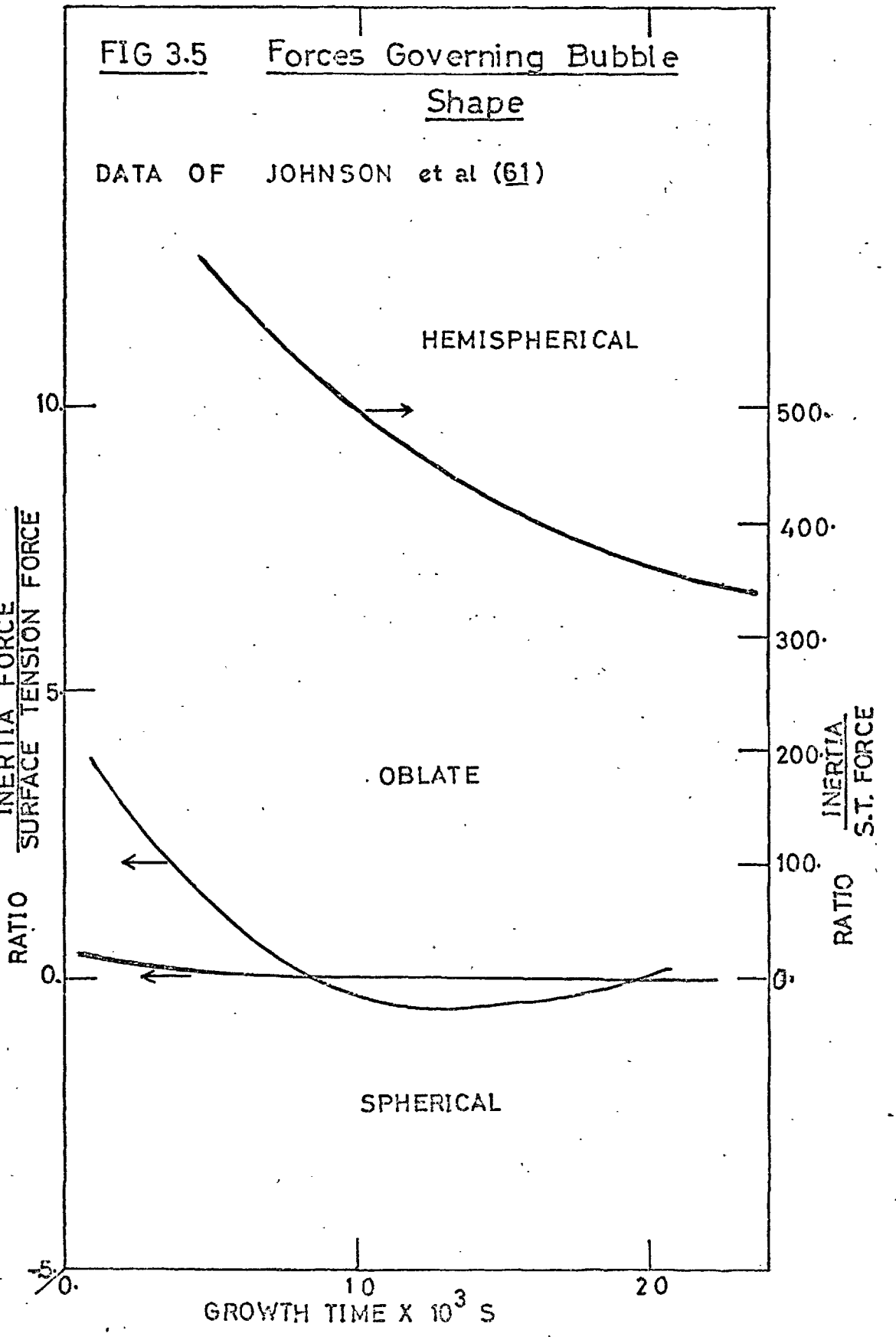


FIG 3·4B Idealised Model Of Large Bubble

FIG 3.4 A Model Of Bubble Dynamics Presented By KIRBY, STANIFORTH And KINNIER

FIG 3.5 Forces Governing Bubble Shape



3.41 Bubble Departure

The only aspect of bubble dynamics in forced flow systems which has received any quantitative theoretical treatment is that of bubble departure. Two attempts have been made and these are presented in detail.

3.41.1 Theory Of KOUMOUTSOS, MOISSIS and SPYRIDONOS (62)

These workers photographed the growth and departure of bubbles from a horizontal heating surface in saturated water at flowrates from 3.63 to 35.8 cm/s. Their observations showed the bubbles to be ellipsoidal in shape and to slide along the heater surface before departing if the flow velocity was increased beyond 15 cm/s.

From their photographs they developed a model for the bubble shape at departure and by consideration of the forces acting on this bubble, attempted a theoretical prediction of the bubble departure radius. Their model and the equations describing the forces are presented in Fig.3.6.

In the derivation inertial forces are neglected and it is proposed that the bubble will depart when the resultant of the drag force F_D, surface tension force, F_S, and buoyancy force F_B, equals zero. That is

$$F_S^2 = F_B^2 + F_D^2 \qquad (3.17)$$

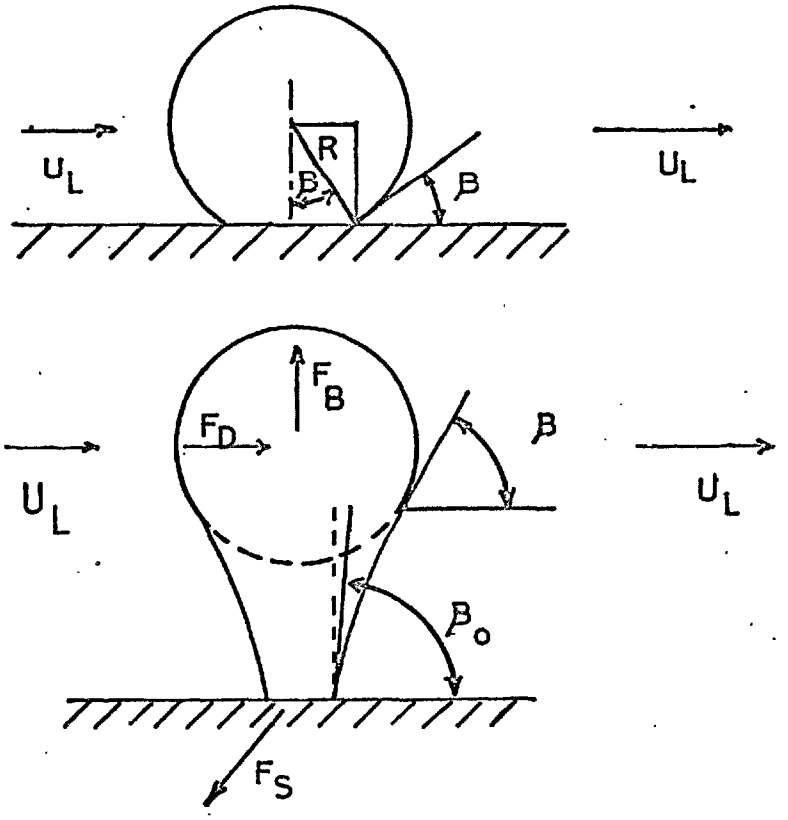
Expressions for the three forces are then derived (see Fig.3.6) and substituted into equation (3.16) to give an expression for the departure radius

$$\frac{R_d}{B} = \left(\left(\frac{R_d}{B}\right)_{U_L=0}\left(\frac{C}{0.36}\right)^2 + N^4 f^4(\beta)\right)^{\frac{1}{2}} - N^2 f^2(\beta) \qquad (3.18)$$

where

$$B = \frac{2g_o\sigma}{g\rho_L}$$

FIG 3.6 A Model For Bubble Departure By KOUMOUTSOS, MOISSIS And SPYRIDONOS



The forces acting on the bubble are given as:

$$F_S = C_S \, 2\pi R \sin^2\beta$$

$$F_D = 0{\cdot}398 \, \rho_L \frac{U_L^2}{2g_o} R^2 \left(\frac{\nu_L}{U_L L}\right)^{1/4} (\pi - \beta + \sin\beta\cos\beta)$$

$$F_B = C_B \, \frac{\pi R^3}{3} (1+\cos\beta)(2-\cos\beta) \rho_L g / g_o$$

$$C_S = 0{\cdot}36 \left(1 - \frac{\epsilon \rho_V U_L \nu_L}{g_o \sigma}\right)^n$$

where

ϵ, n, C_S, C_B are constants

$$C = 0.36\left(1 - \frac{\epsilon \rho_V U_L \nu}{g_o}\right)^n$$

$$N = \frac{0.423}{g B}\frac{U_L^2}{}\left(\frac{\nu}{U_L L}\right)^{\frac{1}{4}}$$

and

$$f(\beta) = \frac{(\pi - \beta + \sin\beta \cos\beta)}{(1 + \cos\beta)^2 (2 - \cos\beta)}$$

Subsequent analysis showed that the effect of N on the departure radius was negligibly small and equation (3.18) was simplified to

$$\frac{R_d}{R_{(U_L=0)}} = \left(1 - \frac{\epsilon \rho_V U_L \nu_L}{g_o \sigma}\right)^{n/2} \quad . \quad . \quad (3.19)$$

which correlated the results to + 25% and - 10% with $\frac{\epsilon \rho_V \nu_L}{g_o} = 0.015$ s/cm and n = 4.

Examination of equation (3.19) shows that as the stream velocity increases, the predicted bubble departure radius decreases and finally becomes negative. The authors suggested that there must be an upper limit of velocity for the validity of (3.19) occurring at the change from the regime of single bubble growth to that of continuous vapour columns, a regime not covered by the proposed model. This conclusion, however, can only be applied if it assumed that increasing the flow velocity also increases the nucleation rate. This is entirely opposed to previous observations which indicate that an increase in velocity in fact inhibits nucleation (1). KOUMOUTSOS et al collected their data at a constant heater temperature of 115°C so that another explanation may be that the stream velocity at $R_d = 0$ is the velocity at which nucleation is suppressed at this particular wall superheat.

In their experiments the bubbles were observed to be ellipsoidal indicating that the inertial forces were likely to be significant and should not have been excluded from the derivation. The success of the correlation in spite of this omission probably arises from the maintenance of a constant heater temperature which would keep the inertia forces approximately constant.

Equation (3.19) derives directly from the equation

$$F_B = F_S \qquad \ldots\ldots\ldots \quad (3.20)$$

by substitution of the appropriate expressions for F_B and F_S suggesting this to be the force relationship describing bubble departure rather than the equation (3.17) suggested by KOUMOUTSOS et al. This indicates either that the drag force acting on the bubble at its time of departure is zero, a condition not discussed by KOUMOUTSOS, or that their model does not accurately represent the physical nature of bubble departure.

3.41.2 Theory Of LEVY (63)

LEVY presented a model to predict the bubble departure radius in vertical forced convection subcooled boiling. This model is reproduced in Fig.3.7 with the expressions for the forces acting on the bubble.

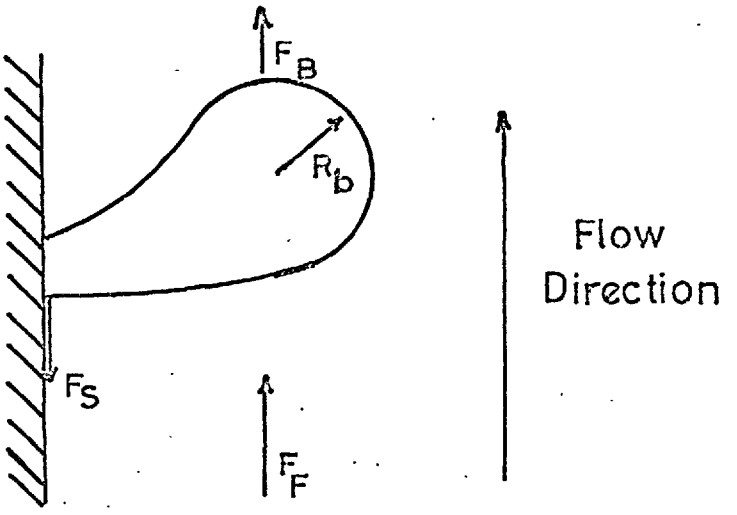
Inertial forces were neglected in the derivation but the effect of flow velocity was included by defining a friction force acting on the bubble which is related to the wall shear stress, τ_W. The departure criterion is defined by the force balance :

$$F_S = F_B + F_F \qquad \ldots\ldots\ldots \quad (3.21)$$

and from this, the following expression for the bubble departure radius is derived :

$$R_d = \left(\frac{g_o C_S \sigma}{C_B g (\rho_L - \rho_V) - C_F g_o \frac{\tau_W}{D_H}} \right)^{\frac{1}{2}} \qquad \ldots \quad (3.22)$$

FIG 3.7 A Model For Bubble Departure By LEVY



The forces acting on the bubble are:

$$F_B = C_B R_b^3 (\rho_L - \rho_V) g/g_o$$

$$F_S = C_S R_b \sigma$$

$$F_F = C_F \frac{\tau_W}{D_H} R_b^3$$

$$D_H = \frac{4 \times A_{XT}}{\text{wetted perimeter}}$$

The Levy model is developed for non-sliding and therefore spherical bubbles. Section 3.41 describes how spherical bubbles are formed when the inertial forces are small compared with the surface tension forces suggesting that Levy's decision to neglect inertia in his derivation is probably justified. This does, however, limit the application of the solution since KIRBY et al (17) could only form spherical bubbles at heat fluxes less than 1/10 of the critical value.

No data has been produced to test the theory but it seems likely that it would only be valid for conditions close to the onset of nucleation.

3.5 The Relationship Between Bubble Growth And Bubble Shape

Both the heat transfer mechanisms presented in Section 3.2 suggest that bubble growth rate will increase with an increase in the heater temperature, T_W, so that bubbles may be expected to be spherical at wall temperatures close to the onset of nucleation but to become hemispherical as burnout conditions are approached.

This tendency is supported by the 'contact angle' measurements of CORTY and FOUST (64) for pool boiling Freon 113 on a nickel surface. They found that at a temperature difference, $T_W - T_S$, of 55°F, the 'contact angle' was 45° but that an increase in ΔT to 65°F increased the 'contact angle' to 60°.

STRENGE, ORELL and WESTWATER (34) obtained values of the constant and exponent of equation (3.1) for pool boiling at several wall superheats. A plot of their results for the exponent as a function of temperature difference with the standard deviation from the mean indicated, is presented in Fig.3.8. This reveals a significant change in the value of n from about $\frac{1}{2}$

at $T = 10$ deg.F to approximately $\frac{1}{4}$ at $\Delta T = 35$ deg.F. The value of the constant, however, is nearly independent of ΔT.

It would be expected from the earlier argument that $n = \frac{1}{4}$, occurring at the higher wall superheats, applies to the growth of hemispherical bubbles. However, Fig.3.9 shows how an overall bubble growth rate of $R \propto t^{\frac{1}{4}}$ may be obtained from two growth periods of $R \propto t^{\frac{1}{2}}$ if the constant of proportionality of the first growth period is considerably larger than that of the second period.

JOHNSON et al (61) have shown that the growth of a hemispherical bubble is very much faster than that of either an oblate or a spherical bubble, suggesting that a difference may exist between the mechanisms of heat transfer. The microlayer theory can only apply to hemispherical growth and this mechanism could account for the observed high growth rates, the superheated boundary layer theory applying to the slower growth of oblate and spherical shapes.

At high wall superheats the bubble grows fast enough to become hemispherical soon after its initiation but as the bubble approaches departure it will become oblate and finally spherical. When the bubble changes from a hemisphere to a sphere the heat transfer mechanism will change from the evaporation of the microlayer to heat conduction from the superheated liquid boundary layer and the bubble will grow more slowly. Thus although the results of Strenge et al suggest that for hemispherical bubble growth, $R_b \propto t^{\frac{1}{4}}$, probably the true relationship for this bubble shape is

$$R_b = \text{constant} \times t^{\frac{1}{2}}$$

as originally described by Lloyd (see Section 3.2), the constant, however,

being considerably greater than the constant for spherical growth at the same superheat. (Fig.3.9).

FIG 3.8 Variation Of The Bubble Growth Exponent, n, With Wall Superheat

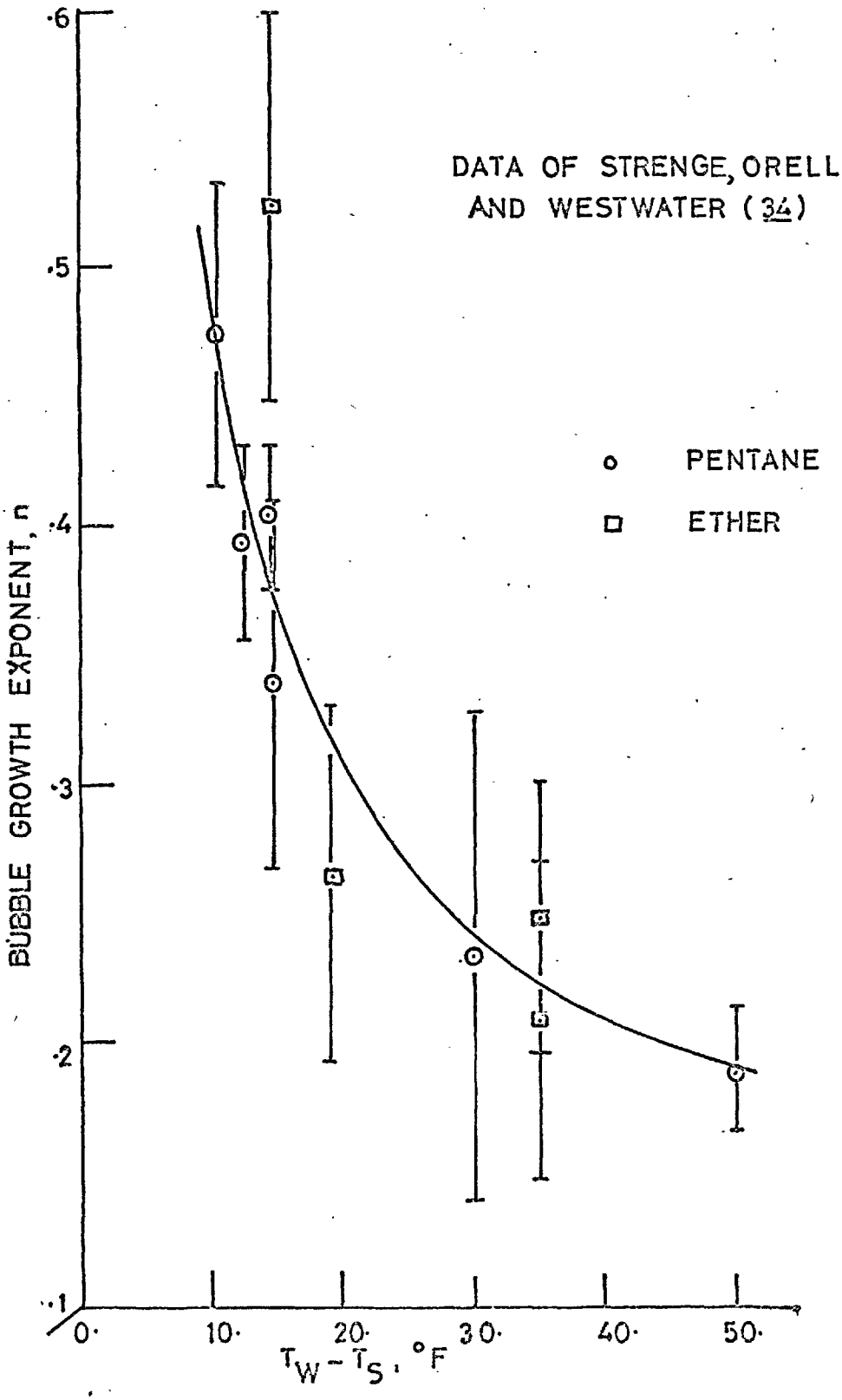
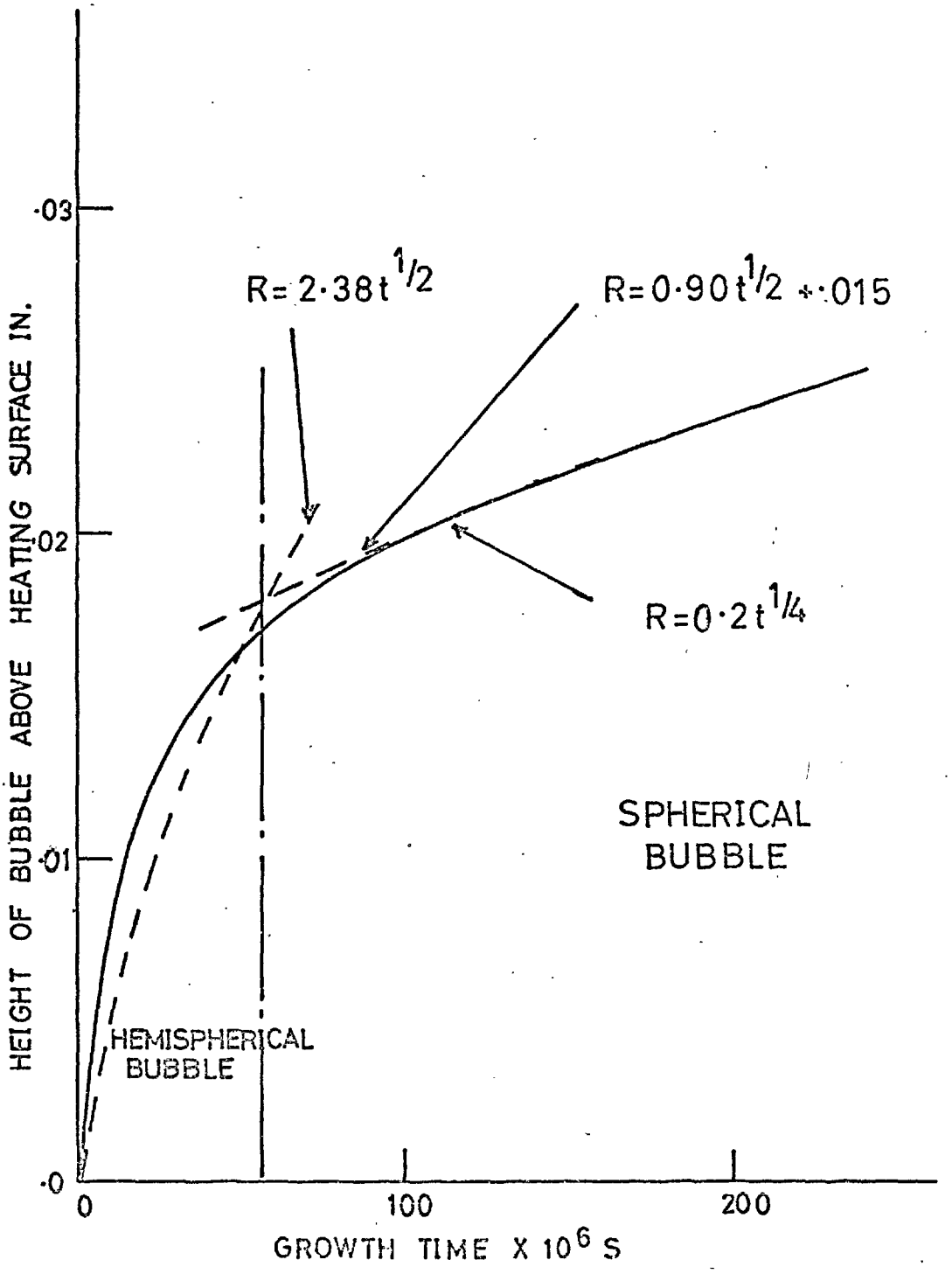


FIG 3.9 The Relationship Between Bubble Shape And Bubble Growth



CHAPTER FOUR

BUBBLE GROWTH IN FORCED CONVECTION BOILING - THEORY

4.1 Introduction

Chapter three has presented the details of bubble growth as given in the literature and from these has attempted to develop a model to describe bubble growth in forced convection with high heat fluxes. This chapter presents a new theory giving a quantitative description of bubble dynamics and growth and develops an explanation for the precipitation of burnout in forced convection.

4.2 Inertia Force Acting On Growing Bubble In Forced Convection

Section 3.4 describes how KIRBY et al (17) developed an expression for the inertia forces acting on a stationary spherical bubble growing in a flowing liquid using the concept of'virtual mass'. This term originates from the study of the non-uniform motion of bodies in fluids where it is observed that the general effect of the liquid is to increase the mass of the body by an amount proportional to the mass of the liquid displaced, the increase in mass being termed the 'virtual mass'. For inviscid fluids, the resistance to the motion of the body caused by the 'virtual mass' may be related directly to the pressure distribution about the body due to its motion. The evaluation of this pressure distribution is used in the following derivation in preference to the concept of virtual mass because it is considered to give a clearer physical picture of the origin of the inertia forces.

In the analysis the flow is considered to be inviscid. This is thought to be a reasonable approximation since, in the absence of surfactants

the shear stress at the bubble interface will be close to zero. The bubble is not assumed to be stationary relative to the heating surface but to have a velocity $U_b(t)$ in the direction of liquid flow to represent the sliding effect already described in Chapter Three.

The bubble model to be analysed is shown in Fig.4.1. The expression for the pressure distribution about a hemispherical bubble growing on a heating surface can be obtained by considering pressures on one side only of the dividing streamline for flow about a spherical bubble as shown in Fig.4.2.

4.21 Pressure Distribution About Bubble

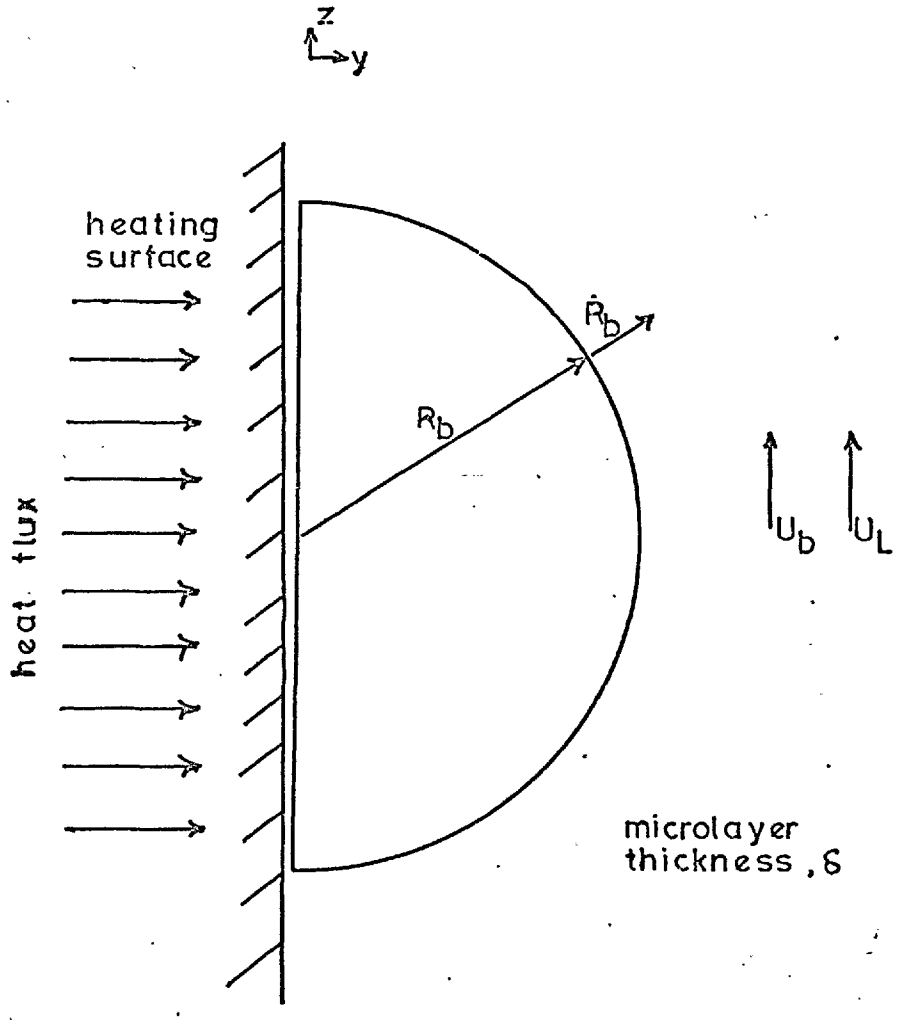
The following assumptions are made concerning the bubble and fluid motion in the analysis. Referring to Fig.4.2;

1) the bubble has radius $R_b = R_b(t)$,
2) the bubble has velocity $U_b = U_b(t)$ in direction z,
3) the liquid has a uniform velocity $U_L = U_L(t)$ in direction z,
4) the bubble is assumed to be spherical and the resultant flow to have axisymmetry about the plane yz,
5) the liquid boundary is at infinity,
6) the motion is irrotational.

The pressure at any point in the liquid relative to the pressure at infinity can be calculated for inviscid, irrotational motion from Bernoulli's equation (72)

$$\frac{P_L}{\rho_L} = \frac{\partial \phi}{\partial t} - \tfrac{1}{2}u^2 \qquad \ldots\ldots\ldots \quad (4.1)$$

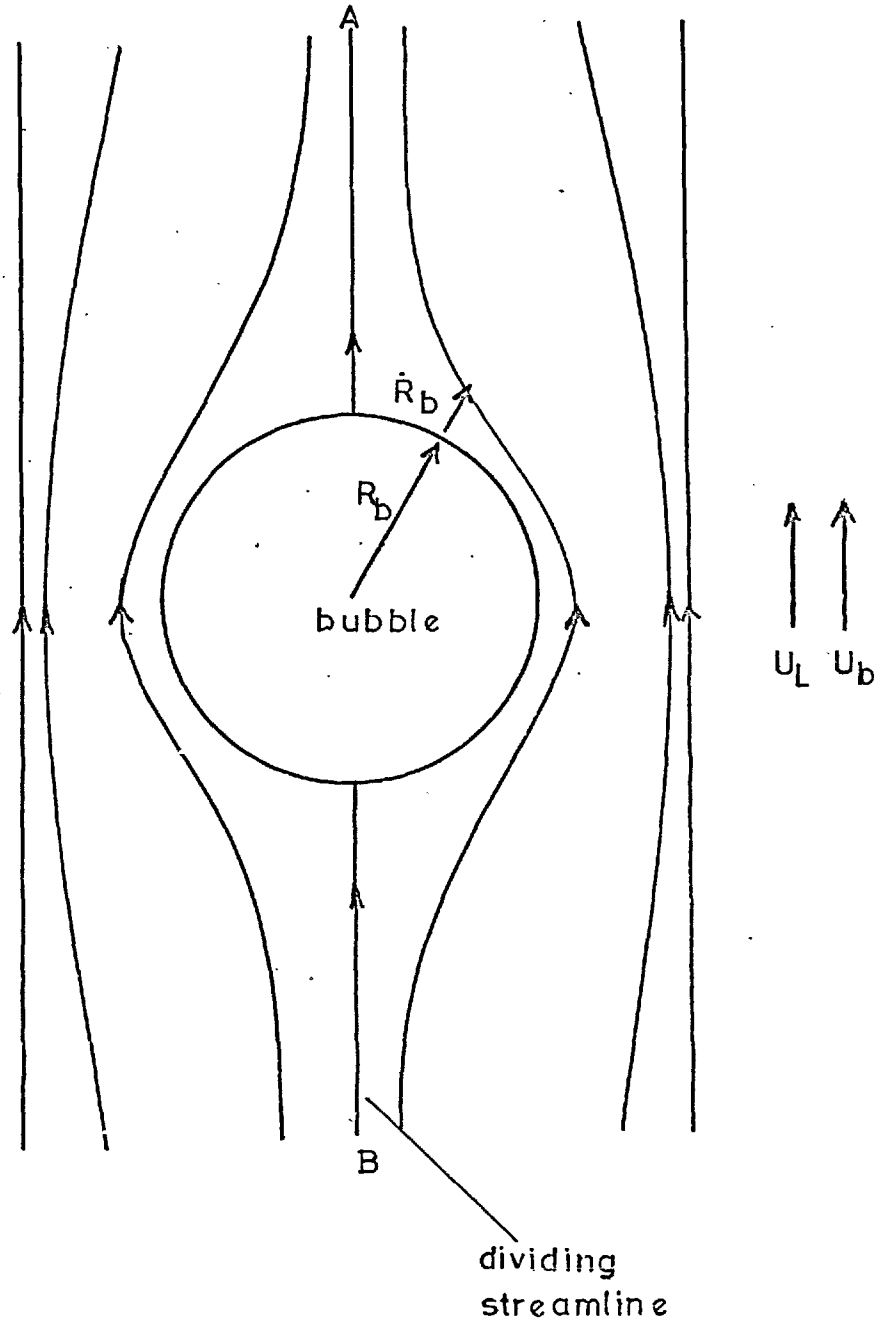
where u and ϕ are related by the expression



Model for Analysis: Bubble Dynamics and Heat Transfer

FIG 4.1

FIG 4.2



Model for Analysis of Inertial Forces

$$u = -\nabla\phi \qquad (4.2)$$

For irrotational motion, the vorticity is zero, thus

$$\nabla \times u = 0 \qquad (4.3)$$

and by combination of (4.2) and (4.3)

$$\nabla^2\phi = 0 \qquad (4.4)$$

The boundary conditions for this analysis are :

$$r = R_b, \text{ all } \theta; \quad -\frac{\partial\phi}{\partial r} = \dot{R}_b + U_b \cos\theta \qquad (4.5)$$

$$r = \infty, \text{ all } \theta; \quad -\frac{\partial\phi}{\partial r} = U_L \cos\theta \qquad (4.6)$$

The solution of (4.4), (4.5) and (4.6) for ϕ will enable the pressure distribution about the bubble to be evaluated from (4.1) and (4.2) with $r = R_b$.

The following solutions of equation (4.4) have been presented in the literature :

a) Motion of a bubble in an infinite stationary liquid (60)

$$\phi_b = U_b \frac{R_b^3}{2r^2} \cos\theta \qquad (4.7)$$

b) Motion of an infinite liquid past a stationary bubble (60)

$$\phi_L = -U_L \left(r + \frac{R_b^3}{2r^2}\right) \cos\theta \qquad (4.8)$$

c) Expansion of a bubble in an infinite stationary liquid (60)

$$\phi_{EXP} = \frac{R_b^2 \dot{R}_b}{r} \qquad (4.9)$$

Since each of these represents a solution to (4.4) then the sum must also represent a solution.

Let

$$\phi = \phi_b + \phi_L + \phi_{EXP} \qquad (4.10)$$

then

$$-\frac{\partial \phi}{\partial r})_{r=R_b} = U_b \cos\theta + \dot{R} \qquad (4.11)$$

and

$$-\frac{\partial \phi}{\partial r})_{r=\infty} = U_L \cos\theta \qquad (4.12)$$

Comparing equations (4.11) and (4.12) with (4.5) and (4.6) shows that this expression for ϕ also satisfies the required boundary conditions and therefore represents the solution of equation (4.1) to give the desired pressure distribution.

Thus

$$\phi = (U_b - U_L)\frac{R_b^3}{2r^2}\cos\theta + \frac{R^2\dot{R}}{r} - U_L r\cos\theta \qquad (4.13)$$

$$\frac{\partial \phi}{\partial t})_{r\theta} = \frac{\partial \phi}{\partial r})\frac{\partial r}{\partial t}) + \frac{\partial \phi}{\partial \theta})\frac{\partial \theta}{\partial t}) + \frac{\partial \phi}{\partial (U_b-U_L)})\frac{\partial (U_b-U_L)}{\partial t}) + \frac{\partial \phi}{\partial U_L})\frac{\partial U_L}{\partial t}) + \frac{\partial \phi}{\partial R_b})\frac{\partial R_b}{\partial t}) \qquad (4.14)$$

$$\frac{\partial \phi}{\partial r} = -(U_b-U_L)\frac{R_b^3}{r^3}\cos\theta + \frac{R_b^2\dot{R}_b}{r^2} - U_L\cos\theta \qquad (4.15)$$

$$\frac{\partial \phi}{\partial \theta} = -(U_b-U_L)\frac{R_b^3}{2r^2}\sin\theta + U_L r\sin\theta \qquad (4.16)$$

$$\frac{\partial \phi}{\partial (U_b-U_L)} = \frac{R^3}{2r^2}\cos\theta \qquad (4.17)$$

$$\frac{\partial \phi}{\partial U_L} = -\dot{r}\cos\theta \qquad (4.18)$$

and

$$\frac{\partial \phi}{\partial R_b} = \frac{2R\dot{R}}{r} + \frac{R^2}{r}\frac{\ddot{R}}{\dot{R}} + \frac{3}{2}(U_b - U_L)\frac{R^2}{r^2}\cos\theta \qquad (4.19)$$

The origin is taken to be the centre of the bubble and is therefore in motion so that,

$$\frac{\partial r}{\partial t}) = - U_b \cos \theta \qquad . \quad . \quad . \quad . \quad . \quad (4.20)$$

and

$$\frac{\partial \theta}{\partial t}) = \frac{U_b}{r} \sin \theta \qquad . \quad . \quad . \quad . \quad . \quad (4.21)$$

Substitution of equations (4.15) to (4.21) into (4.14) yields, after some simplification

$$\frac{\partial \phi}{\partial t})_{r=R_b} = U_b^2 \left(\cos^2\theta - \frac{\sin^2\theta}{2}\right) + \frac{3}{2} U_b U_L \sin^2\theta + \frac{5}{2} U_b \dot{R} \cos \theta$$

$$+ \dot{U}_b \frac{R}{2} \cos \theta + 2\dot{R}^2 + R\ddot{R} - \frac{3}{2} \dot{U}_L R \cos \theta - \frac{3}{2} U_L \dot{R} \cos \theta \qquad . \quad (4.22)$$

For axial symmetry

$$u^2 = \left(\frac{\partial \phi}{\partial r}\right)^2 + \frac{1}{r^2} \left(\frac{\partial \phi}{\partial \theta}\right)^2 \qquad . \quad . \quad . \quad . \quad . \quad (4.23)$$

Where $\frac{\partial \phi}{\partial r}$ is given by equation (4.15) and $\frac{\partial \phi}{\partial \theta})$ by equation (4.16).

Thus, when $r = R_b$

$$u^2)_{r=R_b} = \dot{R}_b^2 + U_b^2 \left(\cos^2\theta + \frac{\sin^2\theta}{4}\right) + 2U_b \cos \theta \dot{R}_b + \frac{9}{4} U_L^2 \sin^2\theta$$

$$- \frac{6}{4} U_b U_L \sin^2\theta \qquad . \quad . \quad . \quad . \quad . \quad (4.24)$$

The pressure distribution at the bubble interface is obtained by the substitution of (4.24) and (4.22) into equation (4.1) giving

$$\frac{P_L}{\rho_L} = U_b^2 \left(\frac{\cos^2\theta}{2} - \frac{5 \sin^2\theta}{8}\right) + \frac{9}{4} U_b U_L \sin^2\theta + \frac{3}{2} \dot{R}_b^2 + R_b \ddot{R} + \frac{3}{2} U_b \dot{R}_b \cos \theta$$

$$- \frac{9}{8} U_L^2 \sin^2\theta + \dot{U}_b \frac{R_b}{2} \cos \theta - \frac{3}{2} \dot{U}_L R_b \cos \theta - \frac{3}{2} U_L \dot{R}_b \cos \theta \qquad . \quad (4.25)$$

4.2.2 Derivation Of Inertia Forces From Pressure Distribution

As stated in the previous section, the inertia forces acting in the horizontal and vertical direction for a hemispherical bubble growing on solid surface may be derived from equation (4.25) by assuming that the solid surface acts along the dividing stream line of the flow.

The direction of the inertial forces and the co-ordinate system used in their derivation are shown in Fig.4.3.

The normal force at the bubble interface is given by

$$dF_N = - P_L dA$$
$$= - P_L R_b^2 \sin\theta \, d\theta \, d\psi \qquad . \quad . \quad . \quad . \quad . \quad (4.26)$$

Therefore,

$$F_{IV} = \iint_A -dF_N \cos\theta \qquad . \quad . \quad . \quad . \quad . \quad (4.27)$$

and

$$F_{IH} = \iint_A -dF_N \sin\theta \cos\psi \qquad . \quad . \quad . \quad . \quad . \quad (4.28)$$

Substitution of (4.26) into (4.27) and (4.28) gives

$$F_{IV} = \int_{\psi=-\frac{\pi}{2}}^{\psi=\frac{\pi}{2}} \int_{\theta=0}^{\theta=\pi} R_b^2 P_L \sin\theta \cos\theta \, d\theta \, d\psi \qquad . \quad . \quad (4.29)$$

and

$$F_{IH} = \int_{\psi=-\frac{\pi}{2}}^{\psi=\frac{\pi}{2}} \int_{\theta=0}^{\theta=\pi} R_b^2 P_L \sin^2\theta \cos\psi \, d\theta \, d\psi \qquad . \quad . \quad (4.30)$$

Integration of equations (4.29) and (4.30) with respect to and θ after

substitution for P_L from equation (4.25) gives the following values for the inertia forces

$$F_{IV} = \pi R_b^2 \rho_L \left(U_b \dot{R}_b + \dot{U}_b \frac{R_b}{3} - \dot{U}_L R_b - U_L \dot{R}\right) \quad \ldots \quad (4.31)$$

and

$$F_{IH} = 2\pi R_b^2 \rho_L \left(\frac{27}{32} U_b U_L - \frac{11}{64} U_b^2 - \frac{27}{64} U_L^2 + \frac{3}{4} \dot{R}_b^2 + \frac{R_b}{2} \ddot{R}_b\right) \quad (4.32)$$

4.3 Heat Transfer To Bubbles In Forced Convection Boiling

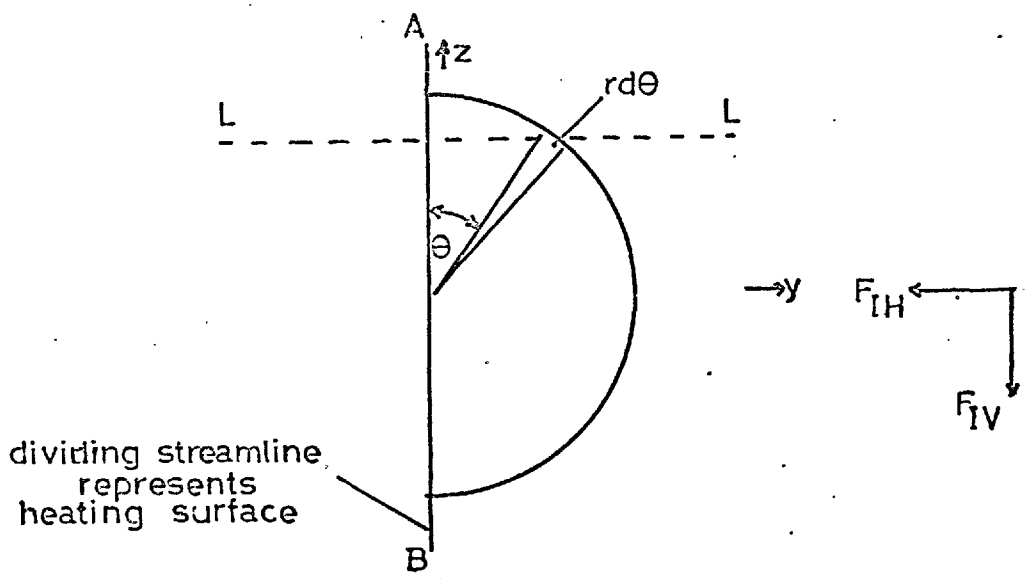
It is concluded in Section 3.6 that the growth of hemispherical bubbles occurs by evaporation from a thin layer of liquid called a microlayer between the bubble and the heater surface. The model for pool boiling suggested by LLOYD (47), presented in Fig.3.1A assumes that the liquid film is not continuous but that a dry patch exists around the nucleation site.

This model may also apply to bubbles growing in forced flow systems whilst they are stationary on the heating surface. However, once the bubbles start to slide as described in Section 3.4, it is suggested that the microlayer becomes continuous as shown in Fig.4.1 and it is this model of the bubble sliding over a thin continuous liquid film which is used in the following heat transfer analysis.

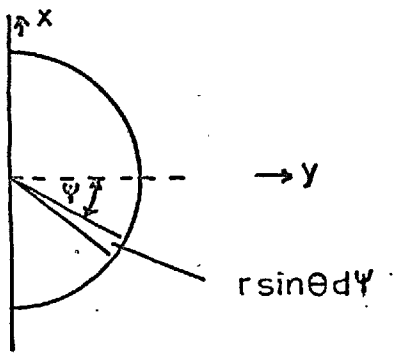
4.3.1 Evaporation Of The Microlayer

Consider a small element of the microlayer of area $r dr d\psi$ and thickness δ, as shown in Fig.4.4B. The rate of evaporation from this element into the bubble must equal the rate of supply of heat to the liquid / vapour interface through the liquid film.

The value of the Rayleigh number for the microlayer was estimated to be approximately 1. No convection is possible below a Rayleigh number



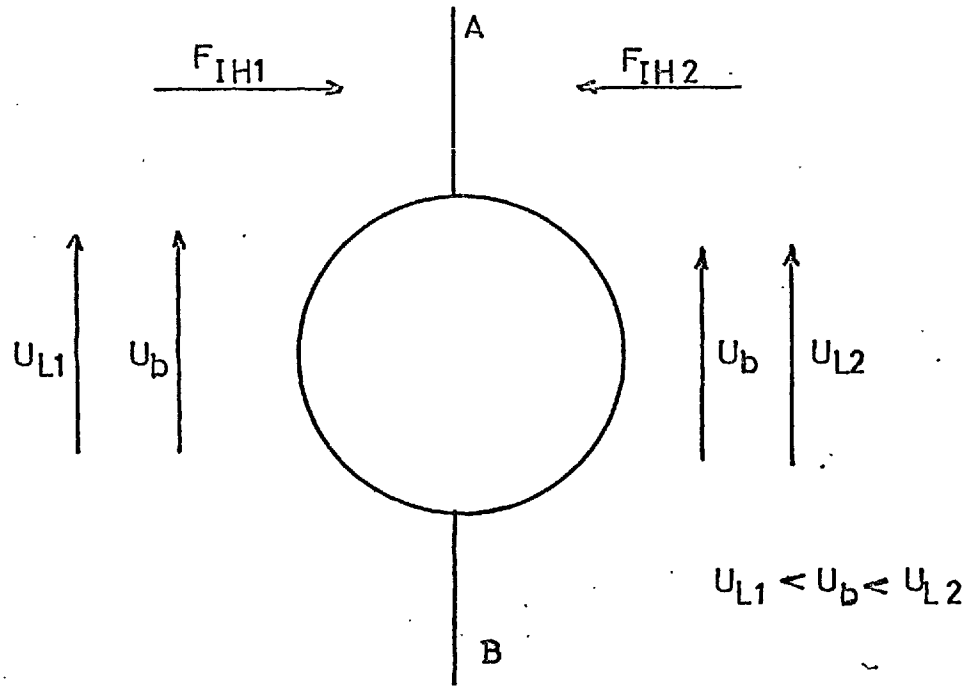
Co-ordinate system - yz plane



section LL

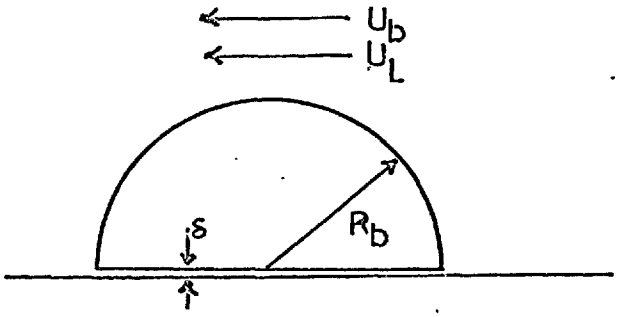
Co-ordinate system -xy plane

FIG 4.3

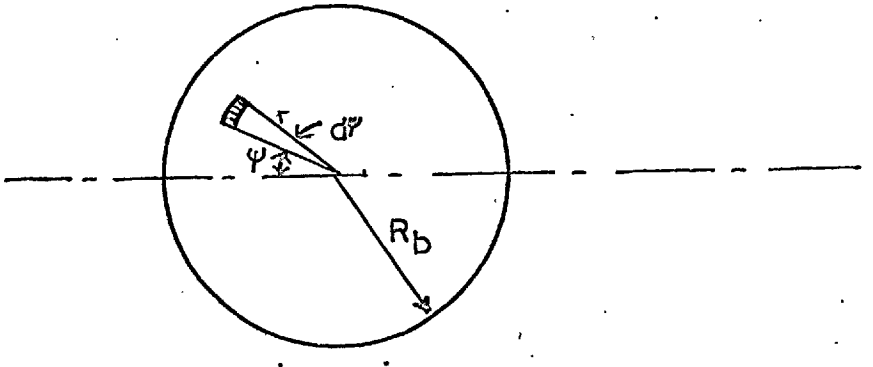


Motion of a Bubble in a Velocity Gradient

FIG 4.4A



side view



plan view

Evaporation of the Microlayer : Co-ordinate System

FIG 4.4 B

of 1100, (35) so that heat transfer through the film will be by conduction only. Therefore

Heat supply to vapour/liquid interface $= \frac{k_L}{\delta}(T_W - T_b)\, r dr d\psi$ (4.33)

and

Heat loss by evaporation from an element of microlayer $= -\rho_L \lambda\, r dr d\psi \frac{d\delta}{dt}$ . . (4.34)

Equating equations (4.33) and (4.34) gives

$$\frac{k_L}{\delta}(T_W - T_b) = -\lambda \rho_L \frac{d\delta}{dt} \quad . \; . \; . \; . \; . \quad (4.35)$$

An expression for $\delta(r, \psi, t)$ may be obtained by integration of equation (4.35) as

$$\delta^2 = \delta_o^2 - \int_{t-t_c}^{t} \frac{2k_L}{\rho_L \lambda}(T_W - T_b)dt \quad . \; . \; . \; . \; . \quad (4.36)$$

where

t_c = contact time of point (r, ψ, t) with bubble

δ_o = initial thickness of microlayer at time, $(t - t_c)$

and

t =time from initiation of the bubble.

The contact time, t_c, of a point (r, ψ) may be derived from the integral equation

$$R_{(t-t_c)}\left(1 - \frac{r^2}{R^2_{(t-t_c)}} \sin^2\psi\right)^{\frac{1}{2}} - r\cos\psi = \int_{t-t_c}^{t_c} U_b\, dt \quad (4.37)$$

The solution of this equation, however, presumes a knowledge of the radius of the bubble at time $(t - t_c)$, $R_{(t - t_c)}$, and also a knowledge of the variation of the bubble velocity during time t_c as a function of time.

Equations (4.33) and (4.34) may also be used to derive the following expressions for the mean heat flux, $q(t)$, through the bubble base at any time during the bubble growth. From equation (4.33)

$$q(t) = \frac{1}{\pi R_b^2} \int_0^{\pi} \int_0^{R_b} \frac{k_L}{\delta} (T_W - T_b)\, r dr d\psi \qquad (4.38)$$

and from equation (4.34)

$$q(t) = \frac{1}{\pi R_b^2} \int_0^{2\pi} \int_0^{R_b} \rho_L \lambda \frac{d\delta}{dt}\, r dr d\psi \qquad (4.39)$$

Equation (4.38) gives an expression for the mean heat flux through the microlayer. A further expression may be derived from the growth of the bubble if it is assumed that heat transfer to the bubble by conduction from the superheated boundary layer and heat losses by condensation at the pole of the bubble are either negligible or equal.

Thus

$$q(t) = \frac{\rho_V \lambda}{\pi R_b^2} \left(\frac{dV}{dt}\right) \qquad (4.40)$$

$$= 2 \rho_V \lambda \dot{R} \qquad (4.41)$$

Equating (4.41) and (4.38)

$$\dot{R} = \frac{k_L (T_W - T_b)}{2\pi \rho_V \lambda R_b^2} \int_0^{\pi} \int_0^{R_b} \frac{r dr d\psi}{\delta} \qquad (4.42)$$

where it is assumed $T_b \neq T_b(r, \psi)$

But since

$$R = At^{\frac{1}{2}} \qquad (3.3)$$

then

$$\dot{R} = \frac{A^2}{2R} \qquad (4.43)$$

An expression for $\delta(t)$ is presented in (4.36) but to facilitate the solution of equations (4.42) and (4.43) for A, some simplifications can be made in this expression.

Assume t_c sufficiently small that $(T_W - T_b)$ remains constant. Equation (4.44) may then be integrated to yield

$$\delta^2 = \delta_0^2 - \frac{2k_L}{\rho\lambda}(T_W - T_b)\, t_c \qquad (4.44)$$

An estimate for T_b may be derived using the Clausius-Clapeyron equation (3.5) so that

$$\frac{1}{T_b + 273} = \frac{1}{(T_s + 273)} - \frac{R'}{\lambda} \ln\left(1 + \frac{P_b}{P_s}\right) \qquad (4.45)$$

where

$$P_b = \frac{2\sigma}{R_b}(1 + We_b) \qquad (4.46)$$

and We_b is defined by equation (4.48).

With t_c assumed to be small, to a first approximation

$$R_{b(t-t_c)} = R_{bt}$$

and $$U_b = \text{constant}$$

Thus equation (4.37) becomes

$$R_b\left(1 - \frac{r^2 \sin^2\Psi}{R_b^2}\right)^{\frac{1}{2}} - r\cos\Psi = U_b\, t_c \qquad (4.47)$$

Equations (4.42), (4.43), (4.44) and (4.47) may be solved to obtain A

No published data are available which provide all the necessary information to solve these equations but an approximate analysis can be made using the water data of GUNTHER (11). The derivation of the growth rate

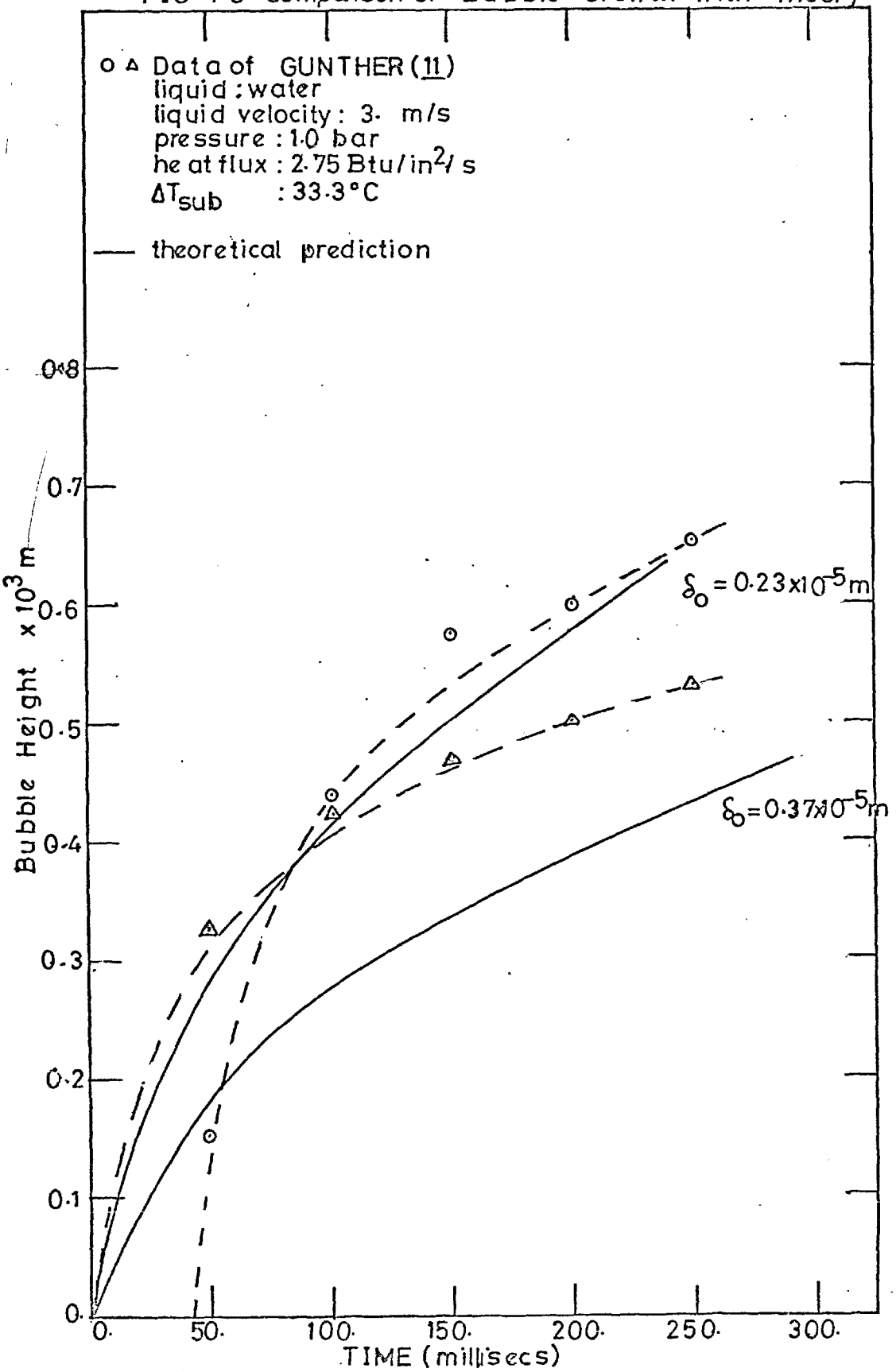
parameter, A, for comparison with these data depends on a knowledge of the value of the microlayer thickness, δ_o. The microlayer might be considered as a region where viscous forces exceed inertial forces created by the bubble and liquid motion and thus to be related to the thickness of the laminar sub-layer, δ_{lam}, in the region into which the bubble is sliding. The value of δ_{lam} may therefore provide an initial order of magnitude estimate for δ_o for the derivation of A.

An estimate for δ_{lam} of 0.8×10^{-5}m is obtained for Gunther's data by assuming the laminar sub-layer thickness to be equivalent to $y^+ = 5$ in the Von Karman velocity profile (Appendix T1) deriving the wall shear stress for the solution of y^+ from standard friction factor curves assuming that the total flow through the test section consisted only of liquid phase. The theoretical solution for A (see Appendix C2) are shown in Fig. 4.5. The two solutions were obtained assuming that $(T_W - T_S)$ equalled 20^oC; Gunther does not give this information.

Fig. 4.5 reveals that if δ_o equals 0.23×10^{-5}m close agreement is obtained between theoretical and experimental growth rate. This value for δ_o is smaller than the estimated value for δ_{lam} but this might be expected since the moving bubble accelerates liquid close to the surface into the region where δ_{lam} already exists.

The value for δ_o estimated by LLOYD (47) for pool boiling water is 0.25×10^{-5}m which agrees very closely with the estimated value for Gunther's data and provides good confirmatory evidence for the validity of this micro-layer heat transfer mechanism for bubble growth in forced convective flow.

FIG 4.5 Comparison of Bubble Growth with Theory



4.4 Bubble Departure

The importance of inertia forces in governing the shape of a bubble has been emphasised in Section 3.4. For vertical motion, the inertia force acting on a hemispherical bubble in the horizontal direction is described by equation (4.32) and provided this force is greater than the surface tension force, tending to make this bubble spherical, the bubble will remain attached to the heating surface since there exists no force to remove it.

The ratio of this inertia force to the surface tension force may be described as a bubble Weber number, We_b, in the form

$$We_b = \frac{2\pi R_b^2 \rho_L \left(\frac{27}{32} U_b U_L - \frac{11}{64} U_b^2 - \frac{27}{64} U_L^2 + \frac{3}{4} \dot{R}_b^2 + \frac{R_b \ddot{R}_b}{2}\right)}{2\pi R_b \sigma} \qquad (4.48)$$

where the surface tension force is arbitrarily represented by $2\pi R_b \sigma$. Appendix T2 describes how the sliding velocity of the bubble, U_b, may be expressed in terms of U_L, and it has already been shown in Section 3.5 that the growth of a hemispherical bubble can be expressed in the form

$$R_b = \text{constant} \times t^{\frac{1}{2}} \qquad . \quad . \quad . \quad . \quad . \quad . \quad (3.3)$$

Use of these two equations enable We_b to be evaluated for any value of t during the bubble growth.

Inspection of equation (4.48) shows that We_b will be very large immediately after bubble inception but will fall during the growth of the bubble. The bubble shape will change immediately We_b drops below the critical value, shown by Fig.3.5 to lie between 5 and 0 for pool boiling data.

In the preceding analysis of the pressure distribution about a

bubble presented in Section 4.22 it was assumed that the liquid velocity was uniform. Although this assumption is approximately valid for a hemispherical bubble growing on a heating surface, since the majority of its curved surface lies in the turbulent liquid stream, it cannot be satisfactorily applied to a spherical bubble in the vicinity of the wall since, in this case, a large part of its curved surface lies in the region of low liquid velocity adjacent to the heating surface.

If a velocity gradient exists across a spherical bubble the inertial pressure variation developed tends to move the bubble towards the region of higher flow velocity. This can be demonstrated by the simple model shown in Fig.4.4A where the liquid velocity to the left of the dividing streamline is uniform and equal to U_{L1}, and to the right is also uniform but equal to U_{L2}. The forces on each side of AB are therefore defined by equation (4.32). Referring to Fig.4.4A the bubble will move towards the region of higher velocity if

$$F_{IH1} > F_{IH2} \qquad (4.49)$$

Substitution of equation (4.32) into (4.49) gives

$$2U_b U_{L1} - U_{L1}^2 > 2U_b U_{L2} - U_{L2}^2 \qquad (4.50)$$

From the model

$$U_{L1} < U_b < U_{L2} \qquad (4.51)$$

Equation (4.50) simplifies to

$$2U_b(U_{L1} - U_{L2}) > (U_{L1} - U_{L2})(U_{L1} + U_{L2}) \qquad (4.52)$$

which further reduces to

$$2U_b < U_{L1} + U_{L2} \qquad (4.53)$$

Using equation (4.51)

$$2U_{L1} < U_{L1} + U_{L2} \quad . \quad . \quad . \quad . \quad . \quad . \quad . \quad (4.54)$$

or

$$U_{L1} < U_{L2} \quad . \quad . \quad . \quad . \quad . \quad . \quad . \quad (4.55)$$

Equation (4.55), derived from equation (4.49), demonstrates the truth of the original premise.

A velocity gradient always exists in a liquid flowing over a rigid boundary so that as soon as a spherical bubble forms on the heating surface it receives a force from the flowing liquid tending to move the bubble away from the surface and into the main stream. Other forces may act in opposition to this inertial force but it might be expected that these would be small compared with the pressure force on a bubble immediately adjacent to a solid surface where very steep velocity gradients exist. The theory also suggests that a further quite large force, enhancing this inertial effect, can develop from the abrupt drop in growth rate and radius which occurs when the bubble shape changes (see Sections 3.5 and 4.22).

The change in bubble shape brought about when We_b falls below its critical value can thus be regarded as a departure criterion for a bubble growing in a flowing liquid. To predict bubble departure it is therefore necessary to investigate the variation of We_b during the bubble growth period. Equation (4.48) for We_b may be expressed generally as

$$We_b = R_b \frac{\rho_L}{\sigma_L} \left(K_b U_L^2 + \frac{A^2}{16t}\right) \quad . \quad . \quad . \quad . \quad . \quad (4.56)$$

where K_b varies according to the ratio U_b/U_L

If U_b / U_L is less than 0.56, K_b is negative. The variation of We_b during the bubble growth time with U_b / U_L equal to 0.5 is shown in Fig.4.6 for

FIG 4.6

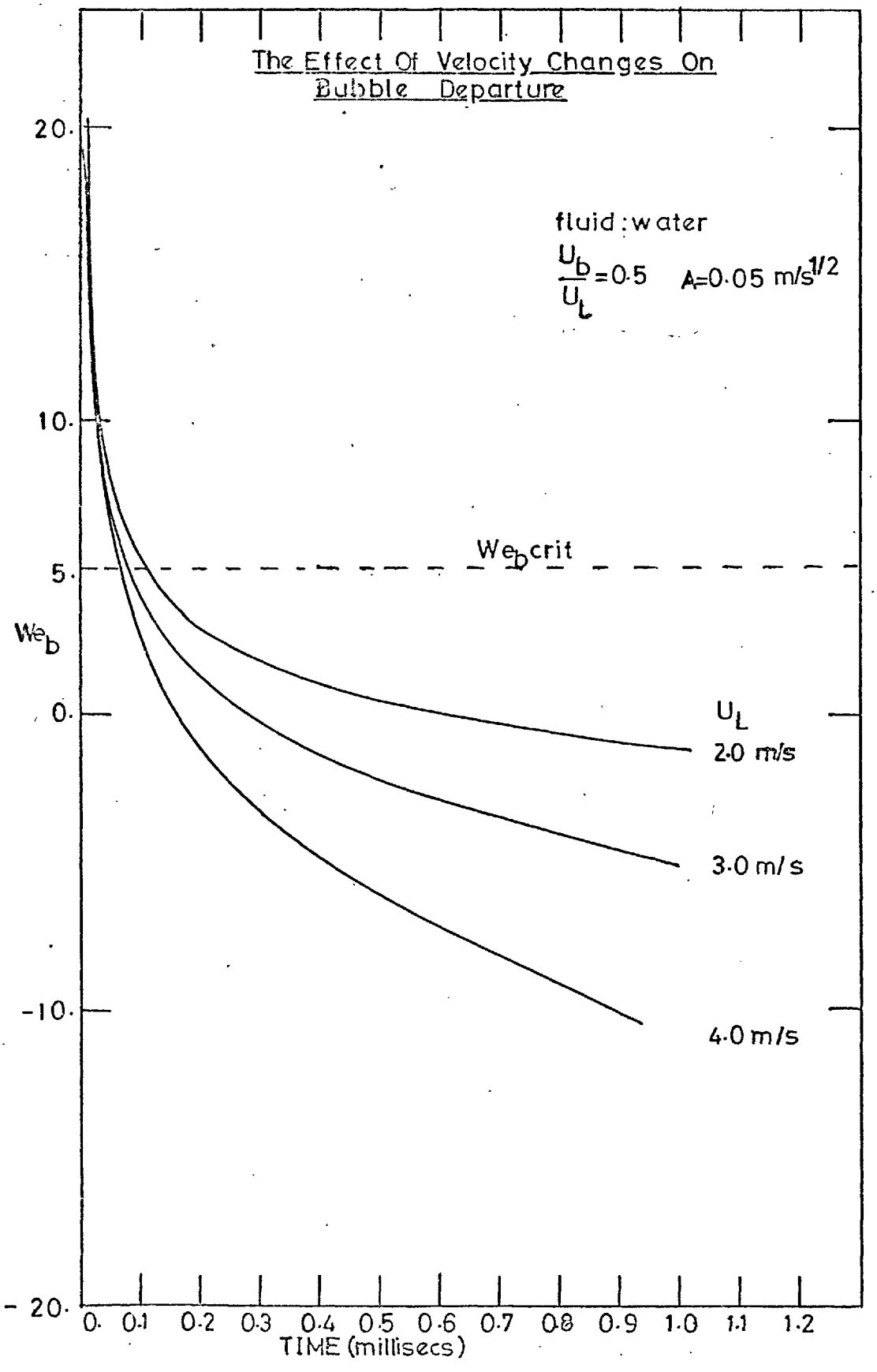

The Effect Of Velocity Changes On Bubble Departure
fluid : water
$\frac{U_b}{U_L}$ = 0.5 A = 0.05 m/s$^{1/2}$
20.
10.
5.
0.
-10.
- 20.
We_b
$We_{b\,crit}$
U_L
2.0 m/s
3.0 m/s
4.0 m/s
0. 0.1 0.2 0.3 0.4 0.5 0.6 0.7 0.8 0.9 1.0 1.1 1.2
TIME (millisecs)

FIG 4.7

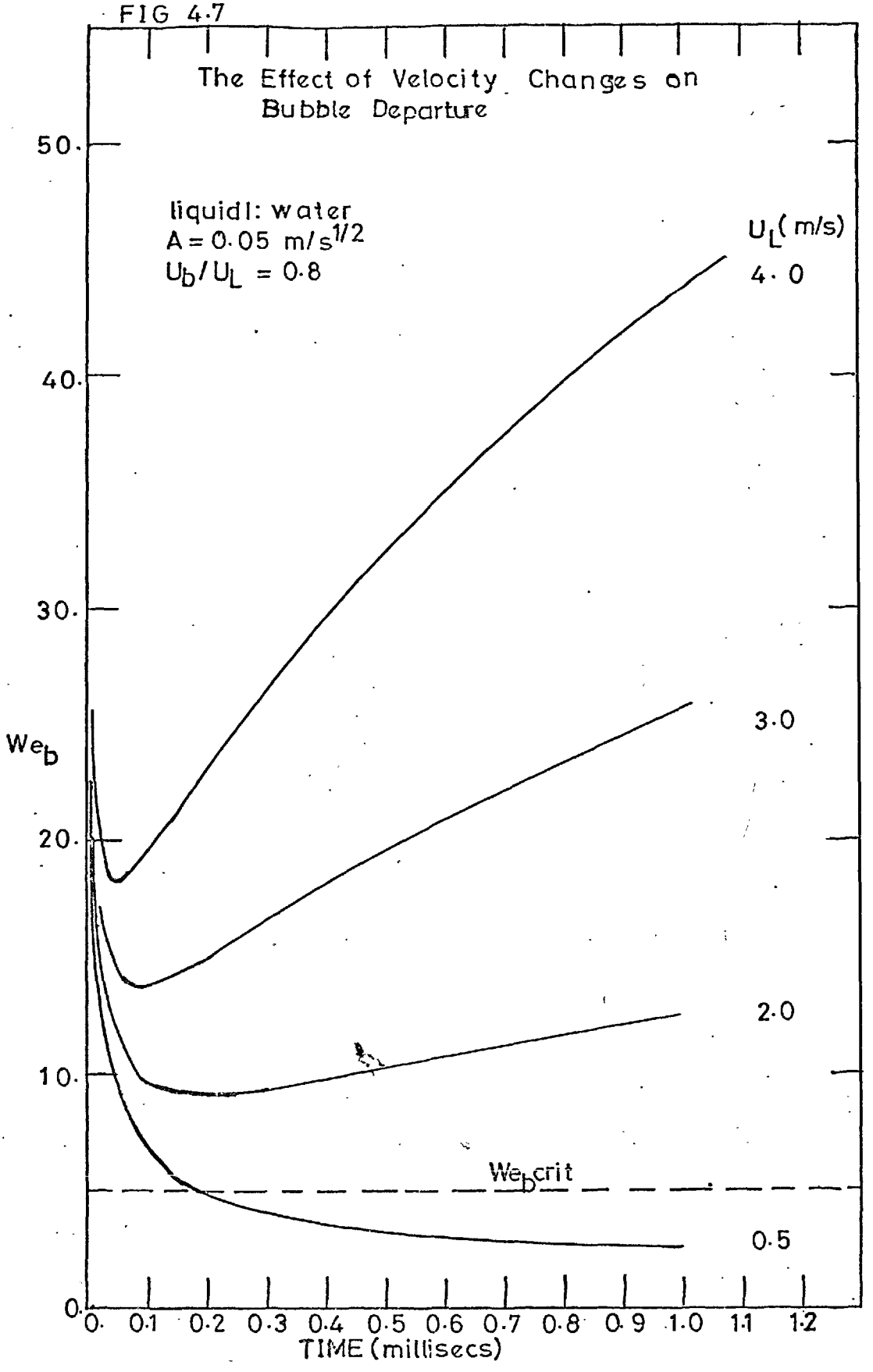
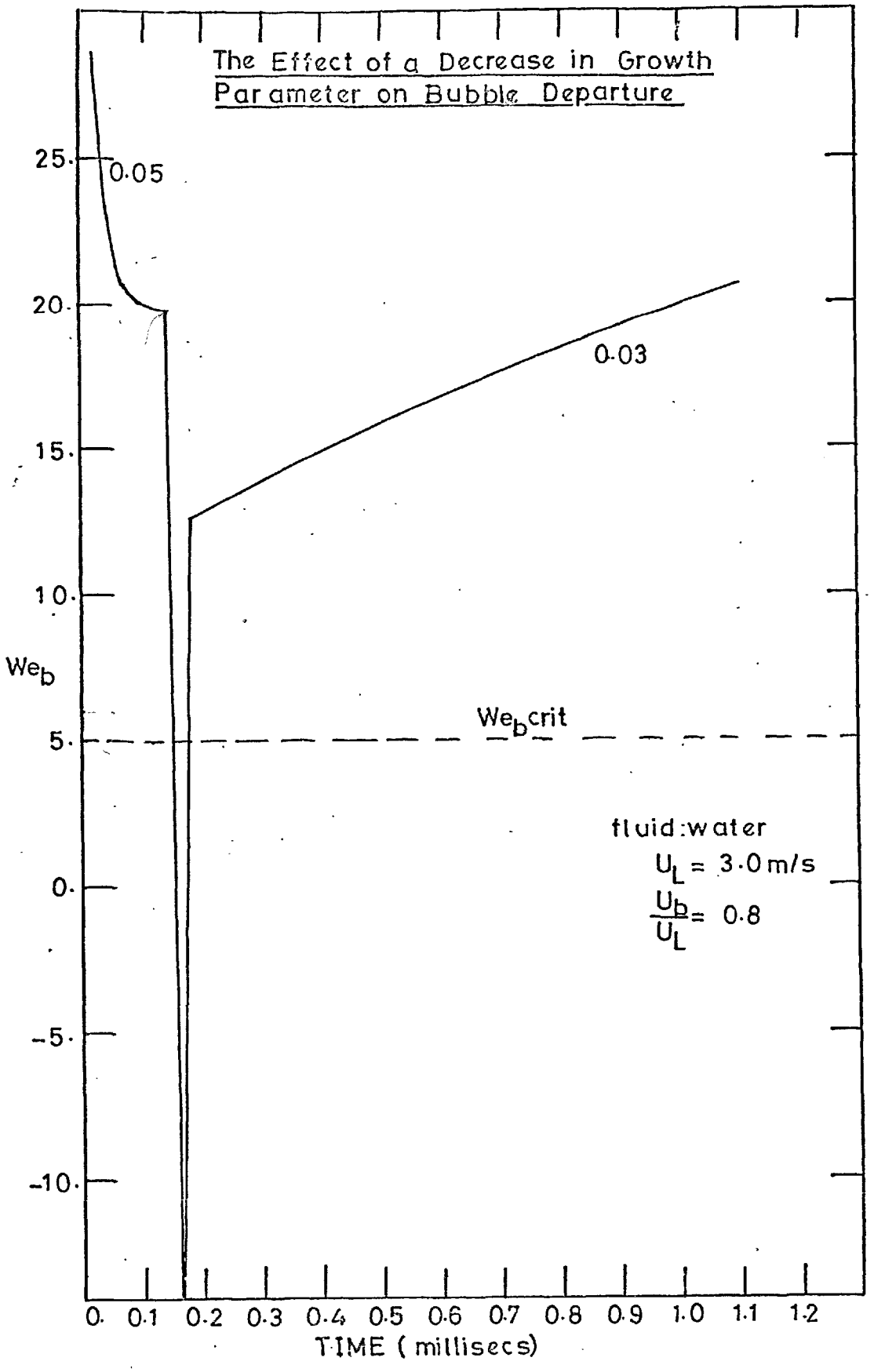

The Effect of Velocity Changes on Bubble Departure
liquid1: water
A = 0.05 m/s^1/2
Ub/UL = 0.8
UL (m/s)
4.0
3.0
2.0
0.5
Web crit
Web
50.
40.
30.
20.
10.
0.
0. 0.1 0.2 0.3 0.4 0.5 0.6 0.7 0.8 0.9 1.0 1.1 1.2
TIME (millisecs)

FIG 4.8


The Effect of a Decrease in Growth Parameter on Bubble Departure
0.05
0.03
We_b
$We_b crit$
fluid: water
U_L = 3.0 m/s
$\frac{U_b}{U_L}$ = 0.8
25
20
15
10
5
0
-5
-10
0. 0.1 0.2 0.3 0.4 0.5 0.6 0.7 0.8 0.9 1.0 1.1 1.2
TIME (millisecs)

several values of the fluid velocity. This shows that for a constant bubble growth parameter, A, the bubble departure time, that is, the time at which We_b equals We_b crit, lessens with increasing fluid velocity and is thus in qualitative agreement with the results of KOUMOUTSOS et al (62).

Gunther however, observed that $U_b / U_L = 0.8$ and a graph of We_b versus time for this ratio is given in Fig.4.7. It can be seen that a minimum occurs in the curve so that above a velocity of about 2m/s, We_b never drops below its critical value suggesting that the bubble remains hemispherical and attached to the surface until it grows to the same order of size as its container. This phenomenon was not observed by Gunther even at a velocity of 6 m/s. On the contrary he noted a decrease in the maximum bubble radius with increased fluid velocity, in agreement with Koumoutsos et al.

A probable explanation is that the curves depicted in Fig.4.7 are based on the assumption of a constant growth parameter throughout the bubble lifetime. This may be true whilst the microlayer forms a continuous film over the base of the bubble, but as the bubble grows, the contact time of the microlayer with the heating surface also increases until partial dry-out of the microlayer occurs. This forms a region of solid/vapour contact with a consequent reduction in the efficiency of heat transfer causing the bubble growth rate to drop. The effect of different bubble growth rates on We_b / t curves is shown in Fig.4.8 demonstrating how a drop in growth rate caused by the total evaporation of a section of the microlayer could precipitate bubble departure. The sharp drop in We_b is caused by the sudden change in $\ddot{R}_b$ at the change in growth rate.

The value of the bubble radius at which a dry-patch is first formed may be derived from equations (4.44) and (4.56). Microlayer contact time is greatest at the point (R_b, π) so that this element will be the first to evaporate. Thus from equation (4.47)

$$t_c(R_b, \pi) = \frac{2R_b}{U_b} \qquad (4.57)$$

Substituting this into (4.44) and putting $\delta(R_b, \pi) = 0$, the bubble radius when a dry-patch just commences to form beneath the bubble is given by

$$R_b' = \frac{\delta_0^2 \rho_L \lambda U_b}{4 k_L (T_W - T_b)} \qquad (4.58)$$

The discussion of Section 4.3 showed that δ_0 is related to the thickness of the laminar sub-layer in turbulent flow. At Re is greater than 5×10^4 τ_W is approximately proportional to U_L^2 and the Von Karman friction velocity

$$u^* \propto U_L \qquad (4.59)$$

and so

$$\delta_{lam} \propto \frac{1}{U_L} \qquad (4.60)$$

Because of the reduced bubble growth rate after the formation of the dry-patch, the bubble departure radius R_d will approximate to R_b' of equation (4.58). Hence

$$R_b' \simeq R_d = \frac{1}{U_L^2} \frac{\rho_L \lambda U_b}{4 k_L \Delta T} \qquad (4.61)$$

assuming $U_b \propto U_L$, then from equation (4.61)

$$R_d \propto \frac{1}{U_L} \qquad (4.62)$$

At $U_L = 0$, $R_d = R_{U=0}$

and therefore from (4.60)

$$\frac{R_d}{R_{U=0}} (K_b U_L + 1) = 1 \quad . \quad . \quad . \quad . \quad . \quad . \quad . \quad (4.63)$$

or

$$\frac{R_d}{R_{U=0}} = (K_b U_L + 1)^{-1} \quad . \quad . \quad . \quad . \quad . \quad . \quad . \quad (4.64)$$

$$\simeq 1 - K_b U_L + K_b^2 U_L^2 \quad . \quad . \quad . \quad . \quad . \quad (4.65)$$

This expfession compares closely with that of Koumoutsos, equation (3.19) which may be presented in an expanded form as

$$\frac{R_d}{R_{U=0}} = 1 - 2K_K U_L + K_K^2 U_L^2 \quad . \quad . \quad . \quad . \quad . \quad (4.66)$$

where

$K_K = 0.015$ s /cm

This close comparison supports the premise that the evaporation of an element of the microlayer is the prime factor leading to bubble departure in systems for which U_b / U_L exceeds 0.56. Further evidence of this mechanism is given by the theoretical prediction of bubble growth presented in Section 4.3. The estimated bubble departure radius for $\delta_0 = 0.23 \times 10^{-5}$m equals 0.625×10^{-3}m which corresponds closely with the experimental radius at which Gunther's bubble started to collapse.

The arguments presented above apply only to situations where the liquid depth exceeds the departure radius of the bubble, R_d. It is possible in annular flow conditions, however, for the liquid depth to be less than the value for R_d predicted from equation (4.58). In this case, the bubble may be expected to depart when it has grown to the size of the liquid film.

4.5 The Onset Of The Critical Condition

The mechanism proposed for bubble departure is that a section of the microlayer beneath the bubble evaporates to dryness causing the growth rate to drop and We_b to fall below its critical value. The bubble changes its shape at this point and departs under the hydrodynamic forces acting upon it. It is this period between the time, t_d, when the first dry-patch appears and the time of physical departure of the bubble which is of importance when considering the advent of the critical condition since this period represents the contact time of the dry-patch with the heating surface.

An estimate of the time for the bubble to change its shape from the hemispherical to the spherical can be made if it is assumed;

1) after t_d, the bubble growth rate is zero so that no volume change occurs, and
2) the velocity of the bubble interface, $\dot{R}$, remains constant at the value it attained at time, t_d.

Then, if

R_h = radius of hemispherical bubble at t_D and

R_s = radius of equivalent sphere,

then

$$R_s = \frac{R_h}{2^{1/3}} \qquad . \quad . \quad . \quad . \quad . \quad . \quad . \quad (4.66)$$

Time for bubble to change shape = contact time of dry-spot

$$= (2R_s - R_h)\frac{1}{\dot{R}} \qquad . \quad . \quad (4.67)$$

But

$$R_h = A\, t_d^{\frac{1}{2}} \qquad . \quad . \quad . \quad . \quad . \quad . \quad . \quad (3\,3)$$

and therefore

$$\dot{R} = \tfrac{1}{2} \frac{A}{t_d^{\frac{1}{2}}} \qquad . \quad . \quad . \quad . \quad . \quad . \quad . \quad (4.68)$$

Thus, substituting equations (4.66) and (4.68) into (4.67) and simplifying

$$\text{Contact time of dry-spot} = 1.2\, t_d \qquad . \quad . \quad . \quad . \quad . \quad (4.69)$$

If during this contact time, the dry-spot continues to expand at the same rate as at t_d, from equation (4.58)

$$\text{Length of microlayer} = \frac{\delta_\delta^2 \rho_L \lambda U_b}{2 k_L \Delta T} = \text{constant} \qquad . \quad . \quad (4.70)$$

Length of dry-spot = $2R_h$ - length of microlayer

therefore

$$\text{Rate of increase of dry-spot} = 2\dot{R} = \frac{A}{t_d^{\frac{1}{2}}} \qquad . \quad . \quad (4.71)$$

and

$$\text{Final length of dry-spot} = \frac{A}{t_d^{\frac{1}{2}}} \text{ x contact time} \qquad . \quad . \quad (4.72)$$

Substituting the contact time of the dry-patch (4.69) into equation (4.72) and using equation (3.3) to simplify :

$$\text{Final length of dry-spot} = 1.2\, R_h \qquad . \quad . \quad . \quad . \quad (4.73)$$

The poor heat transfer rates which occur across dry-patches will therefore be of large significance when considering nett heat transfer from the heating surface to the bubble since equations (4.73) and (4.69) suggest that a dry-spot may finally grow to approximately half the total contact area of the hemispherical bubble and exist for a period greater than half the total bubble contact time.

4.5.1 The Critical Condition For Systems With Constant Wall Temperatures

Examples of these systems are those using condensing steam as the

heating medium, a frequent application in evaporators. An increase of this wall temperature has two opposing effects on the nett heat transfer to the system and it is the relative size of these effects which causes a maximum or critical heat flux to be obtained.

1) A wall temperature increase may be expected to increase the number of nucleation sites and also the growth rate of each bubble. Equation (4.58) shows that the bubble radius at departure will be reduced so that more bubbles can be expected to grow and depart in any given time. These effects would tend to increase the heat flux.

2) The reduction in bubble size will reduce the size of the hydrodynamic forces acting to remove the bubble from the heating surface. The dry-patch beneath the bubble may therefore be expected to remain relatively longer on the heating surface when compared with the total bubble contact time. This would tend to decrease the heat flux.

Thus, for wall temperatures below the critical value it is suggested that effect (1) exceeds effect (2) such that an increase in wall temperature would result in an increase in the heat flux and that the reverse effect occurs for temperatures lying between the critical and the Liedenfrost temperatures. Stable film boiling occurs for wall temperatures in excess of the Liedenfrost point.

4.5.2 The Critical Condition For Systems With Constant Heat Fluxes

Examples of these systems are those using radiant and nuclear energy as the heating source, both techniques of which are widely used to produce high pressure steam for the generation of electricity. The wall

temperature varies to maintain the heat flux at a constant value so that during the period of contact of a dry-patch with the heating surface, the wall temperature must rise. This temperature rise will be quenched by the bulk liquid once the bubble has departed. However, if the rise in temperature exceeds the quenching by the liquid, then the wall temperature will increase in an oscillatory fashion similar to that presented in Fig. 2.1 until the Liedenfrost point is exceeded when stable film boiling occurs.

A series of bubbles passing over a point on the heater would precipitate 'burnout' in this manner in agreement with the observations made by KIRBY et al (17) who could discern no change in the bubble motion at the critical point, bubbles still sliding past until the onset of film boiling.

This model suggests that the rate of rise of temperature beneath a dry-patch (and hence the critical heat flux) is related to the physical properties and dimensions of the heating surface. This conclusion is supported by the results of TIPPETTS (1), shown in Fig 4.9, which show how a reduction of the thickness of the heating element from 0.01 in. to 0.006 in. reduces the critical heat flux by approximately 20%. Similar effects have also been observed by HEWITT et al (8) and by FIORI and BERGLES (9). Despite these observations in published works little effort has been made to include this clearly important effect in the development of 'burnout' correlations.

4.6 Non-Uniform Heat Flux Distributions - The Effect Of Sliding Bubbles

Tedreas' data for non-uniform heat flux distributions, Fig. 2.6, suggests that variation in the local critical heat flux is not random but is related to the axial flux distribution. This variation might be accounted for by the effect of variations in the tube wall thicknesses reported by TIPPETTS

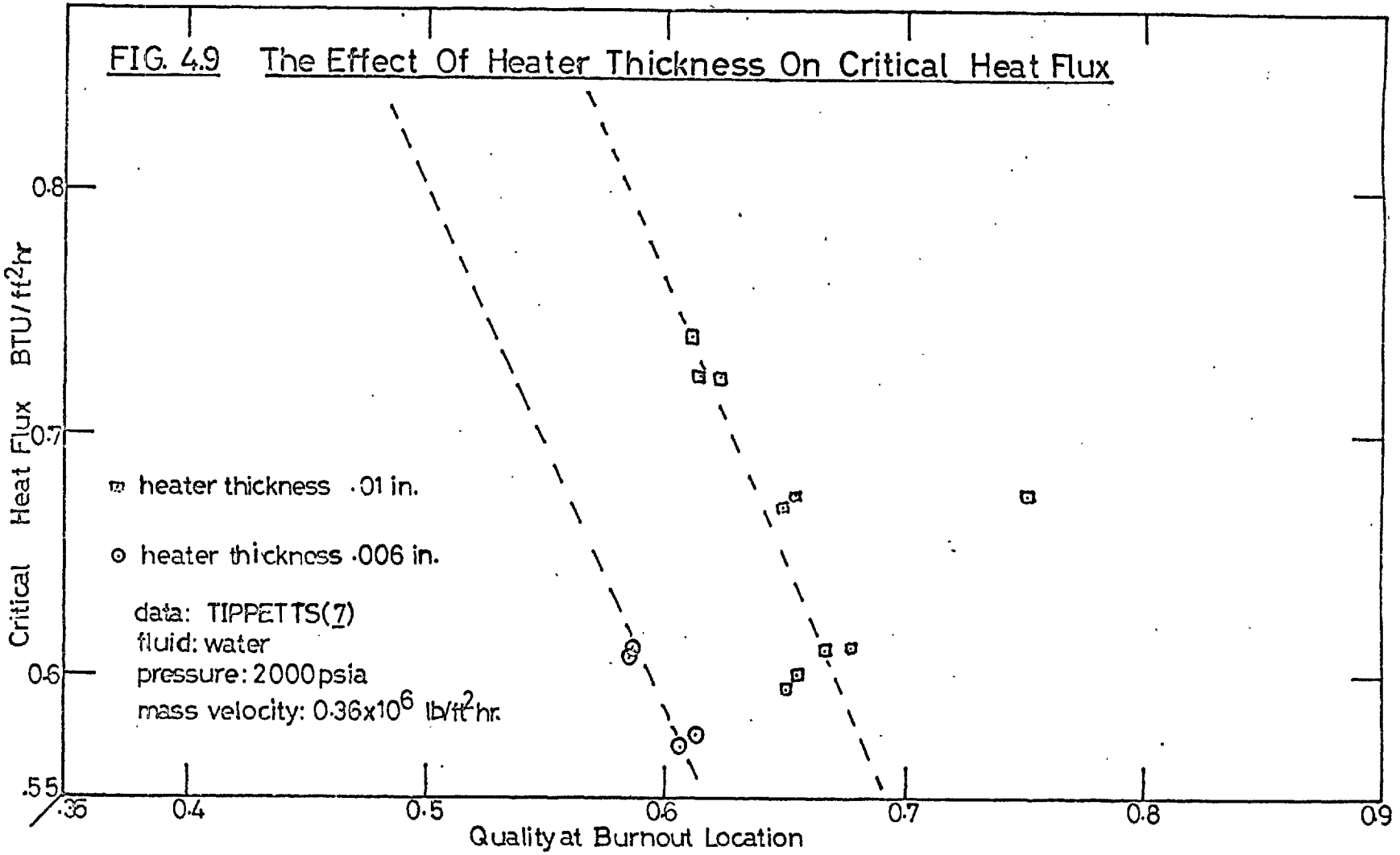
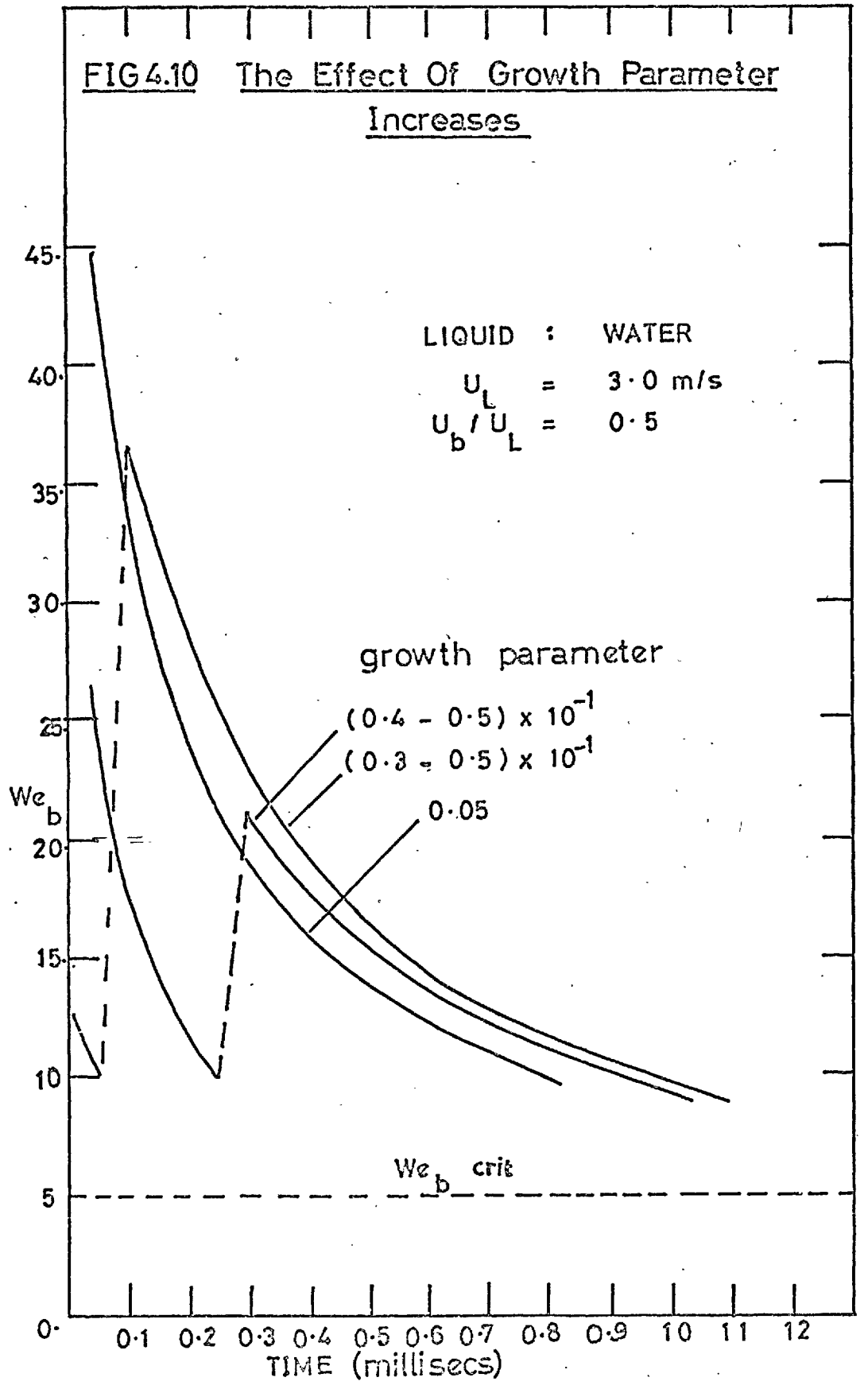

FIG. 4.9 The Effect Of Heater Thickness On Critical Heat Flux
Critical Heat Flux BTU/ft²hr
0.8
0.7
0.6
.55
heater thickness .01 in.
heater thickness .006 in.
data: TIPPETTS(7)
fluid: water
pressure: 2000 psia
mass velocity: 0.36x10⁶ lb/ft²hr.
.35
0.4
0.5
0.6
0.7
0.8
0.9
Quality at Burnout Location

FIG 4.10 The Effect Of Growth Parameter Increases



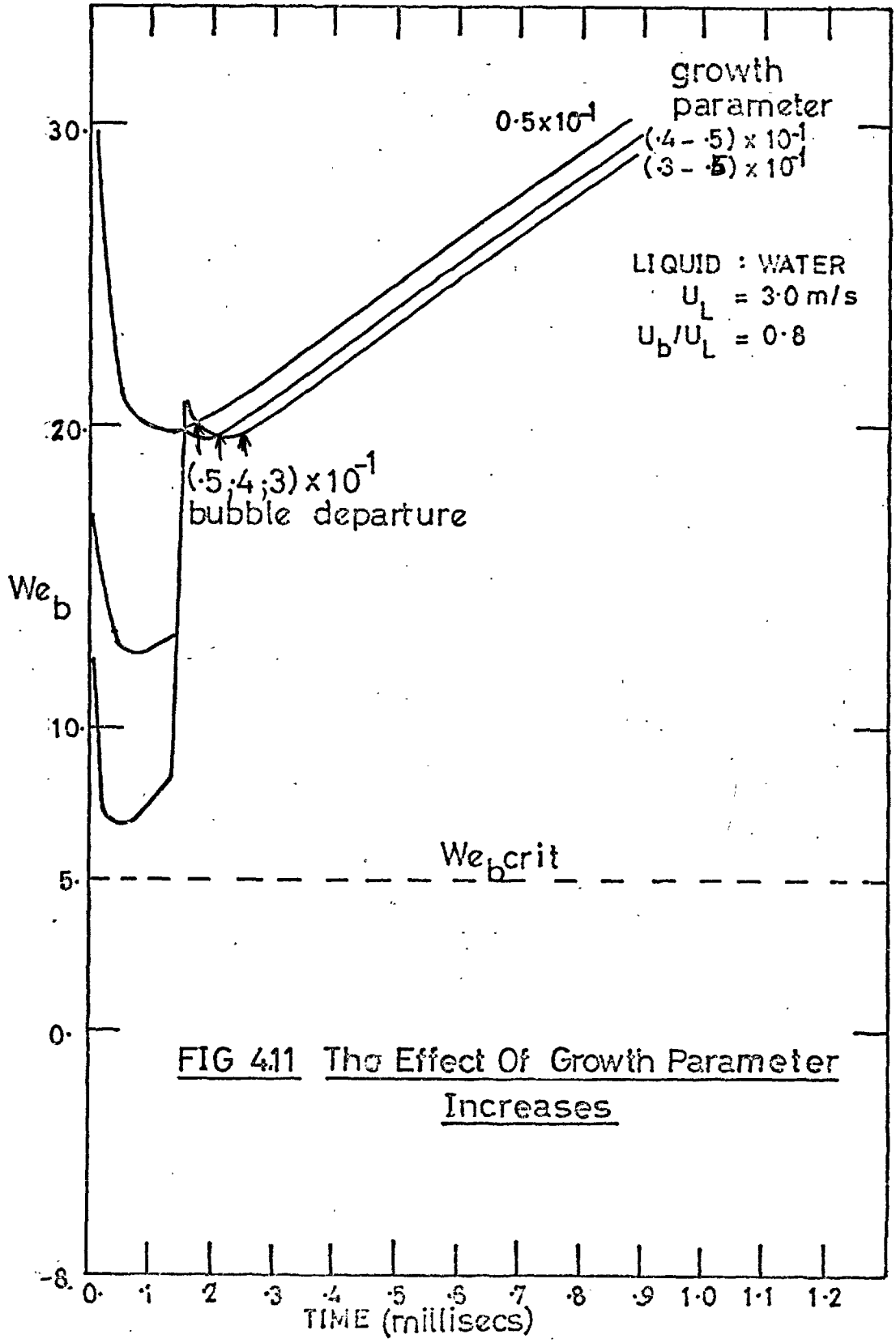


FIG 4.11 The Effect Of Growth Parameter Increases

(discussed above) but details of this are not readily obtainable from the data of Todreas. It might appear that the effect of bubbles sliding along the heater surface and undergoing changes in growth rate due to changes in the heater wall temperature could also account for this phenomenon. Fig.4.10 shows the effect of a change of growth rate parameter on the variation of We_b with time for $U_b / U_L = 0.5$. Fig.4.11 shows the same changes for $U_b / U_L = 0.8$.

The bubble radius as a function of time during the first growth period is given by

$$R_b = A_1 t^{\frac{1}{2}} \qquad (4.74)$$

and in the second growth period, starting at time t_r, by

$$R_b = A_2 (t - t_p)^{\frac{1}{2}} \qquad (4.75)$$

where

$$t_p = t_r \left(1 - \left(\frac{A_1}{A_2}\right)^2\right) \qquad (4.76)$$

Both Figs 4.10 and 4.11 demonstrate how this change in growth from A_1 to A_2 causes the bubbles to stay longer on the heating surface than if the growth rate is constant at A_2. Both figures show that bubbles with the lowest value for A_1 remain stably hemispherical for the longest period of time. As discussed in Section 4.4 if U_b / U_L is greater than 0.56 bubbles depart when partial dry-out of the microlayer occurs and the departure radius is given approximately by

$$R_d = \frac{\delta_0^2 \rho_L \lambda U_b}{4 k_L (T_W - T_b)} \qquad (4.58)$$

From (4.75) and (4.76) a further equation for R_d may be obtained;

$$R_d = A_2 \left(t_d - t_r \left(1 - \left(\frac{A_1}{A_2}\right)^2\right)\right)^{\frac{1}{2}} \quad . \quad . \quad . \quad . \quad (4.77)$$

which, on rearranging, gives

$$t_d = \frac{R_d^2}{A_2^2} + t_r \left(1 - \left(\frac{A_1}{A_2}\right)^2\right) \quad . \quad . \quad . \quad . \quad (4.78)$$

Equation (4.78) shows that t_d increases as A_1 is decreased if R_d is held constant.

However, it is not whether the total contact time, with the heating surface, t_d, is influenced which is of importance but whether the contact time of the microlayer with the bubble, t_c, is altered by these changes.

Equation (4.47) shows that t_c is a function of R_b and U_b only, so that for constant R_b, t_c can only be affected by a change of U_b. Appendix T2 evaluates an expression for U_b as a function of time and shows that an increase in t_d will slightly increase U_b, causing a reduction in t_c. Equation (4.58) shows that if U_b increases then $(T_W - T_b)$ must also increase for constant R_d suggesting that a decrease in A_1 will require a higher heat flux to cause burnout. Because this change in growth rate does not predict a reduction of the critical heat flux it follows that bubbles grown in the region of constant growth rate A_2 will reach the critical condition before those sliding into this region and thus the actual value of the critical heat flux will be unaffected by the sliding bubbles.

4.7 Conclusions

A new theory describing the motion and heat transfer to bubbles growing on a heating surface in forced flow is presented.

Analysis of the pressure distribution over the surface of a hemispherical bubble growing on a heating surface shows that the shape of the bubble is governed by the value of a Weber number defined as ;

$$We_b = \frac{2\pi R_b^2 \rho_L \left(\frac{27}{32} U_b U_L - \frac{11}{64} U_b^2 - \frac{27}{64} U_L^2 + \frac{3}{4} \dot{R}_b^2 + \frac{R_b}{2} \ddot{R}_b\right)}{2\pi R_b \sigma} \qquad (4.48)$$

The bubble remains hemispherical provided the value of We_b is greater than approximately 5 : For We_b below this value, the bubble becomes spherical.

Hemispherical bubble growth occurs by evaporation from a micro-layer which forms at the bubble base, a model which is in quantitative agreement with the results of Gunther and also compares favourably with the work of Lloyd for pool boiling.

When partial dry-out of this microlayer occurs the consequent drop in bubble growth rate causes We_b to fall below its critical value and the bubble shape to change from hemispherical to spherical. Hydrodynamic forces, which had previously held the hemispherical bubble to the heating surface, cause this spherical bubble to depart. The departure radius of the equivalent hemispherical bubble is given by

$$R_d = \frac{\delta_0^2 \rho_L \lambda U_b}{4 k_L \Delta T} \qquad . \quad . \quad . \quad . \quad . \quad . \quad . \quad (4.58)$$

The microlayer thickness, δ_0, is related to the laminar sub-layer thickness and for Gunther's data is apparently of the order of $1/3\ \delta_{lam}$.

Dry patches formed in the microlayer during bubble growth exist for approximately half the total bubble contact time and play an important role in the precipitation of the critical condition.

A qualitative description of the advent of the critical condition emphasises the importance of the physical properties and dimensions of the heating element in governing the value of the critical heat flux, a conclusion supported by some experimental evidence.

The critical heat flux data of Todreas for non-uniform heat flux distributions demonstrates that some relationship exists between the value of the critical heat flux and the upstream distribution of the heat flux, but this cannot be accounted for by variations in the growth rate of bubbles sliding into the critical region.

CHAPTER FIVE

DESCRIPTION OF APPARATUS AND EXPERIMENTAL PROCEDURE

5.1 Introduction

The following series of experiments were designed to demonstrate the existence of different burnout mechanisms and also to estimate the effects of liquid flow rate, quality and upstream heat flux distribution on the value of the critical heat flux.

The critical situation was generated under the following experimental conditions. The section numbers refer to Fig.5.1.

1) % Quality At Entrance To Section 10: 0, 10, 20, 30, 40.
2) Mass Flow Rate 0.037, 0.075, 0.112 Kg/s
3) Upstream Heat Flux Distribution: A 10% quality change was made over section 9, sections 8 and 9, or sections 7, 8 and 9.

The downstream recovery of the system from a burnout situation was also measured by setting the heat input to section 10 close to its critical value and then generating burnout conditions firstly at section 12 and then at 13.

The runs were numbered to indicate the experimental conditions.

First Number, 1 - 5, to indicate 0 - 40% quality respectively.

Second Number, 1 - 3, to indicate 0.037 - 0.112 Kg/s respectively.

Third Number, 1 - 3, to indicate if quality drop over 9-7, 8 and 9 respectively.

For example:

Run Number 521 indicates 40% quality at entrance to section 10 at a mass

flowrate of 0.075 Kg/s with a 10% quality drop across section 9.

The apparatus used for this series of experiments was basically that designed by MANTZOURANIS (1). He originally built the rig to obtain boiling data for water but it was later used by BACKHURST (2) in a redesigned form for experiments with benzene and toluene.

Isceon 113 was chosen for the experiments. It is particularly suitable for studying the critical condition because of its low latent heat and boiling point, and its stability at high temperatures enables it to be used in a recycle system.

The choice of Isceon as the test liquid necessitated several changes to the apparatus. The system was completely sealed to reduce evaporative losses and the heat exchangers were all converted to water cooled systems to enable the Isceon to be cooled to room temperature before recycling. Removal of all pipe joints and valves not essential to the experiments also reduced liquid loss by leakage.

5.2 Description Of Apparatus

5.2.1 The Flow Diagram

A flow diagram of the apparatus is shown in Fig.5.1. The feed tank was sealed and had two sight glasses in the top to enable the liquid level to be checked. The Isceon 113 was circulated by an Albany rotary gear pump, rated at 100 g.p.h. at 200 p.s.i, driven by a 2 h.p., 3 - phase motor. The pump delivered the liquid at approximately 10 bar and the pressure was dropped to the operating pressure of 2 bar across the control needle valve, V_1. This large pressure drop prevented the flowrate from being noticeably affected by small pressure fluctuations in the test section. The desired

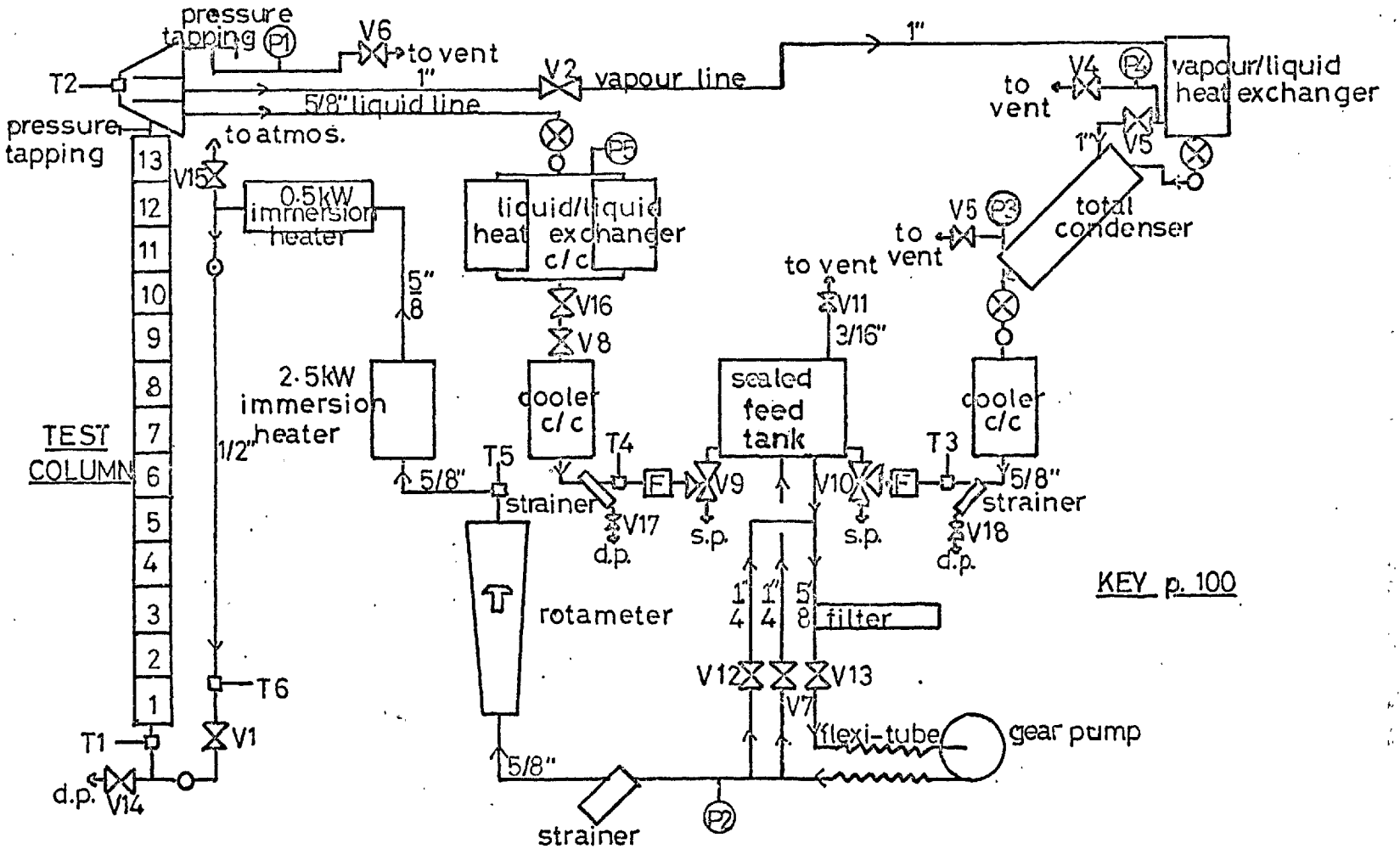


FIG 5.1 FLOW DIAGRAM OF APPARATUS

KEY TO FIG. 5.1

SYMBOLS

⊥	Thermometer or thermocouple well.
⊗	Vapour trap: Spirax-Sarco 3/4" FT 64 SLR S
⊙	Thermistor well for temperature control.
o	Sight box.
F	1/2" Kent total flowmeter.
P	Bourdon pressure gauge.
d.p	Drain point.
s.p	Sample point.
c/c	Concentric coils (see Mantzouranis (1)).

VALVES

V1	1/2" needle valve, s/s, PTFE impregnated asbestos gland packing.
V2,V3	1" needle valve, s/s, PTFE impregnated asbestos gland packing.
V4,V5	1/4" plug cock, bronze, asbestos gland packing.
V6	adjustable reducing valve set at 10 bar.
V7	adjustable reducing valve set at 15 bar.
V8	adjustable reducing valve (used fully open).
V9,V10	1/2" 3-way plug cock, bronze, PTFE gland packing.
V11	3/16" brass cock.
V12	1/4" needle valve, s/s, PTFE gland packing.
V13,V14	1/2" plug cock, bronze, PTFE gland packing.
V15	1/4" Klinger cock, brass, PTFE gland packing.
V16	1/2" Klinger cock, brass, PTFE gland packing.
V17,V18	1/8" Klinger cock, brass, PTFE gland packing.

NOTES

(1) All process lines copper.

(2) Rotameter:- Guided float insensitive to small viscosity and density changes; neoprene gland packing.

(3) Gear pump fitted with PTFE sintered bearings.

liquid flowrate was obtained by adjustment of valves V_1 and V_{12} and its steadiness and approximate magnitude were indicated by a calibrated rotameter.

The desired inlet temperature to the test section was gained by two-stage electrical preheating. The 2.5 kW first stage, manually controlled by a variac, heated the liquid to within 5 °C of the required inlet value. The temperature was then precisely controlled to ± 0.1°C by a 0.5 kW heater connected across the output from an electronic proportional controller. A thermistor placed at the exit to the preheating section acted as the temperature sensor for the controller.

The liquid and vapour leaving the test section were separated in a cyclone and returned to the feed tank by different routes. Valves V_2 and V_3 in the vapour return line were used to adjust and control the pressure in the separator. The liquid and vapour streams were cooled to room temperature by a series of water-cooled concentric-tube heat exchangers (1) before returning to the feed tank for recycling. Positive displacement meters in both the liquid and vapour return lines enabled the flow rates of the two streams to be measured to ± 2% down to the lowest tested flow rate of 12 cm^3/s.

5.2.2 Test Section

5.2.21 Test Column

The test column was a vertical copper tube of 37mm o.d. by 13mm i.d. by 1830mm long and was divided into 13 equal sections of length 130mm by grooves of depth 6mm cut in the tube surface perpendicular to its axis. These grooves reduced the conductive heat transfer along the tube and allowed the independent control of heat flow through each section into the test liquid. A slot 6mm deep by 3mm wide was cut along the length of each section

to contain thermocouples for the measurement of tube wall temperatures. A vertical cross-section through part of the tube is shown in Fig.5.2.

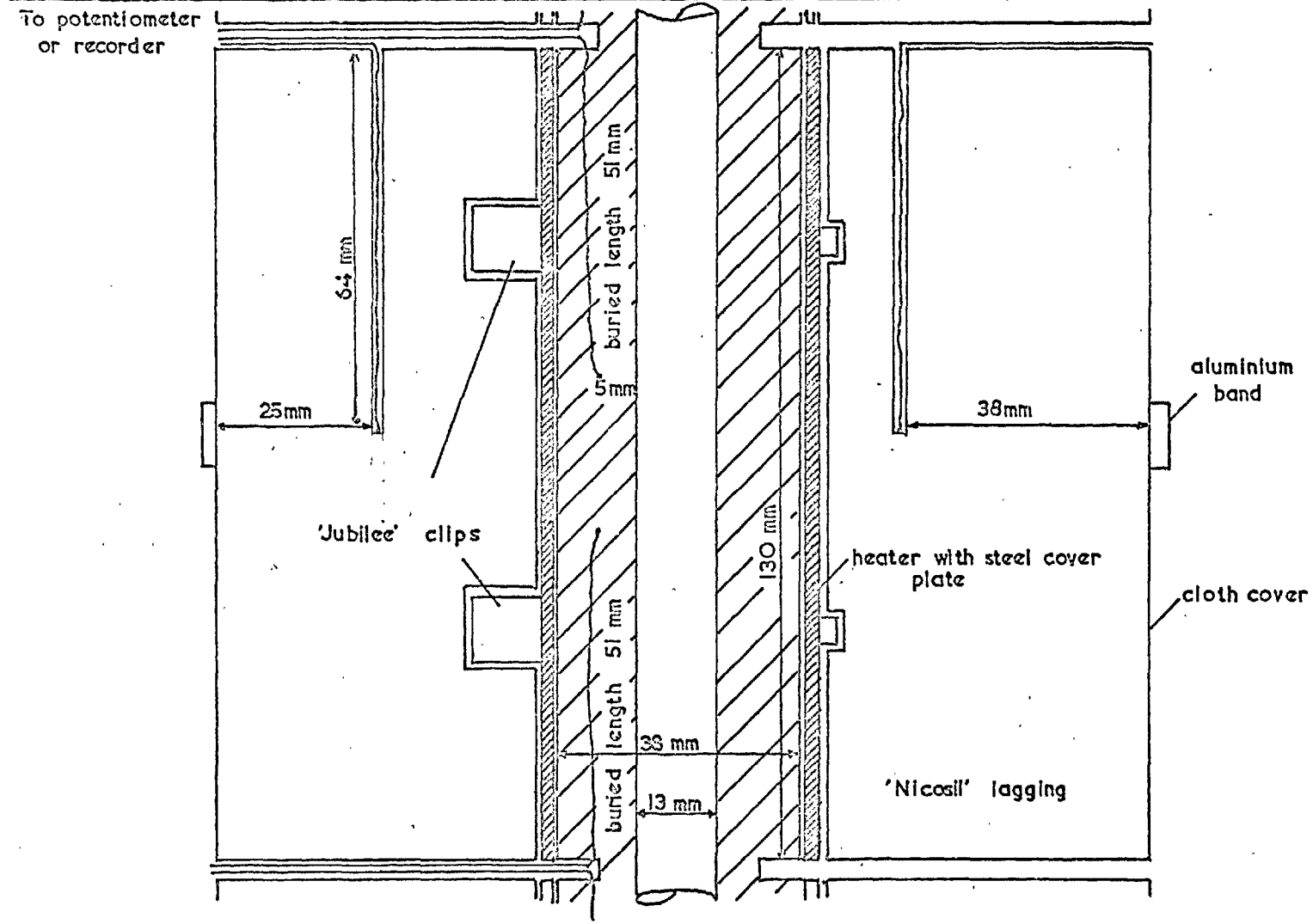
This tube had been in use for a number of years. The inner surface was cleaned with 'Starit' and when examined appeared to be covered with a smooth oxide film. DAVIS and ANDERSON (54) examined a specimen of a similar copper tube used in similar experiments under an electron microscope and reported that the only pits and cavities which they were able to find were of the order of 2μm in diameter.

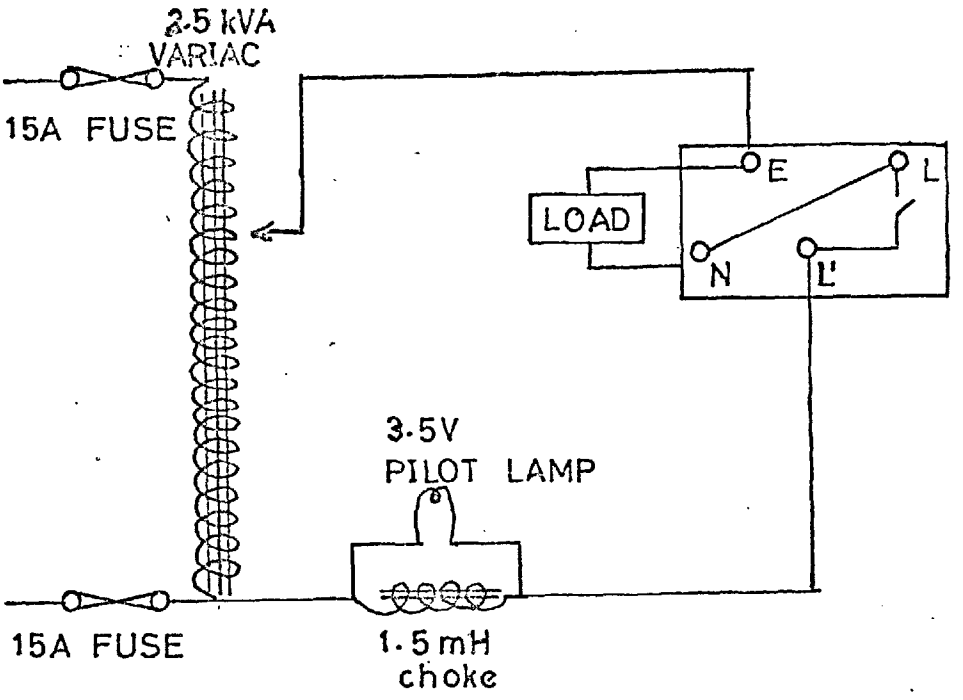
5.2.22 Control And Measurement Of Heat Input

Two 1 kW heating elements 130mm long and designed to provide an axially uniform heat flux were clamped to the outside of each section. Each heater was insulated with mica and enclosed in a copper sheath. Each pair of heaters was fitted closely around the tube by two semi-circular steel formers and held tightly in place by two 'Jubilee' clips. A watt-meter could be plugged into the circuit supplying each section (Fig.5.3) and the power input set to the desired value by adjustment of a variac. The wattmeter had three measuring ranges, 0 - 500W, 0 - 1000W and 0 - 2000W with a precision of 0.25% of full scale deflection on each scale. Two voltage regulators maintained the mains supply at 240 $\pm$ 0.6V so that the heat flux through any section remained within 0.5% of its set value.

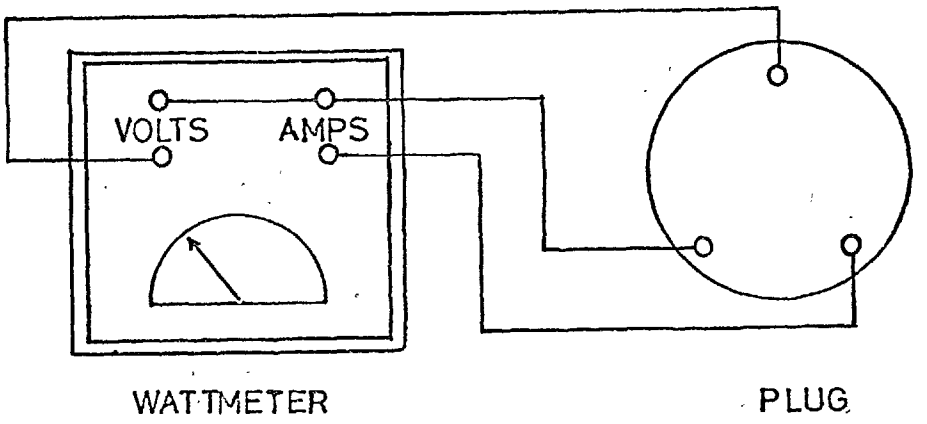
Heat losses to the atmosphere were reduced by insulating each section with a 62mm layer of 'Nicosil' lagging. The small remaining heat losses were detected by thermocouples placed in the lagging of sections 1, 9, 10 and 13 and connected to a Pye Universal Potentiometer. The heat loss calibration is presented in Appendix E3. The arrangement of the

FIG 5.2 VERTICAL CROSS SECTION THROUGH TEST COLUMN





POWER SUPPLY TO EACH SECTION OF THE TEST SECTION



WATTMETER CONNECTIONS

FIG 5.3 ELECTRICAL POWER FOR HEATING

heaters, lagging and heat-loss thermocouples is shown in Fig.5.2.

5.2.23 Measurement Of Tube Wall Temperatures

26 copper/constantan thermocouples, prepared by spot welding 32 gauge wire were used for measuring the tube wall temperatures, two being inserted in the wall of each of the 13 sections of the test column. These were laid along the bottom of the 6mm slot with the tip of one of the thermocouples 50mm from the top and the tip of the other 50mm from the bottom of the section (Fig.5.2) They were held firmly in place by a wad of asbestos fibre impregnated with 'Araldite'. Each of the thermocouples was carefully chosen so that the deviation between thermocouple readings at any given temperature never exceeded 3μV so that only one calibration curve was necessary. The liquid temperature at the inlet to the test section was used as the reference for the tube wall temperature measurements and a calibration for use with a variable reference junction was made. This is presented in Appendix E1. Only the lower thermocouple in each section was generally used for temperature measurement, the upper providing corroborating evidence when necessary. The thermocouples were monitored on a 16-point Honeywell ElectroniK 15 chart recorder with interchangeable ranges of 0 - 1mV and 0 - 5mV, and a full cycle time of 96 seconds. All the experimental readings were taken on the 0 - 5mV range and were accurate to $\pm$ 15μV. The calibration of the recorder was initially compared with that of a Pye Universal Potentiometer and was periodically checked throughout the experimental work. The air in the recorder cabinet was continuously circulated by a fan to maintain the thermocouple terminals at a uniform temperature.

For the measurement of the critical heat fluxes at sections 10, 12

and 13, the upper thermocouple in each of these sections was in turn connected to the 0 - 10mV range of a Control Instruments Hi-Speed single channel recorder against a reference junction at 0.0 °C.

5.2.3 Measurement Of Fluid Temperature In Test Section

The temperature of the fluid flowing in the tube was measured by a thermocouple which could be moved vertically along the axis of the tube, as shown in Fig.5.4. The thermocouple was of 40 gauge copper/constantan wire and was encased in a 0.80mm o.d. x 2.13m long stainless steel tube. The thermocouple tip was kept in the tube by means of a stainless steel 'spider' (see Fig.5.5). Measurements, accurate to ± 1/20 °C, were made against a reference at 0.0 °C on a Pye Universal Potentiometer. The thermocouple calibration is presented in Appendix E2.

5.2.4 Measurement And Control Of System Pressure

BACKHURST (2), using this same test column, took measurements of both the fluid temperature and pressure along the tube length. His results showed that for measurements taken in the vapour phase the values of pressure could be closely predicted from the respective temperatures assuming saturated equilibrium conditions to exist in that section of the column. An example of his results is shown in Fig.5.6. On the strength of this, saturated equilibrium conditions were assumed to exist in the presence of vapour during the present series of experiments and estimates of the system pressure were derived from measurements of the vapour temperatures.

The test pressure was taken to be the pressure existing in the cyclone separator. The vapour temperature in the separator was measured

FIG 54 Travelling Thermocouple

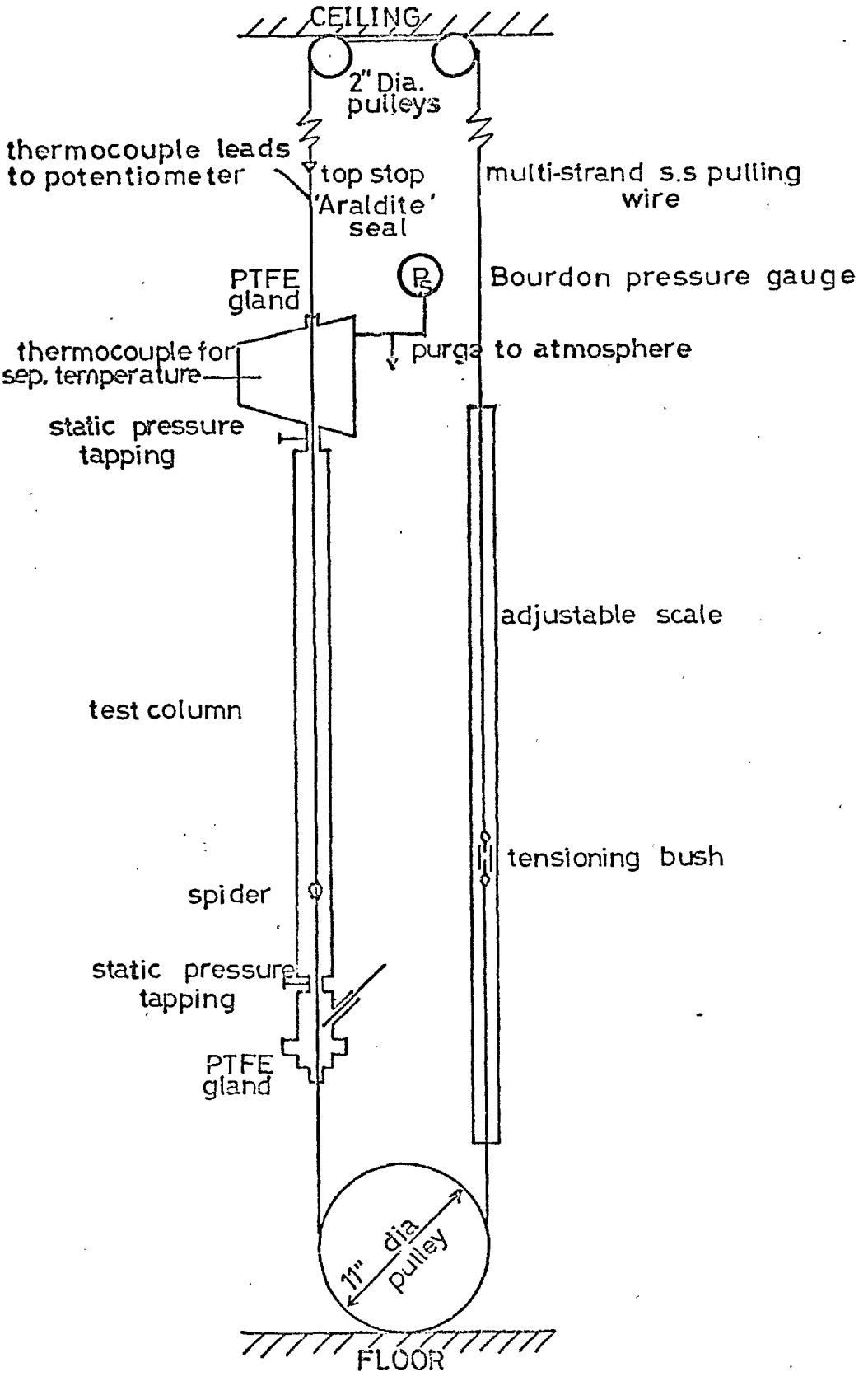
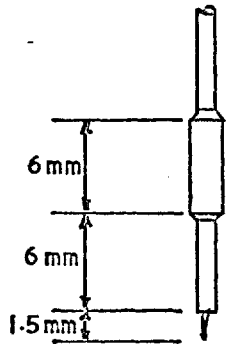


FIG 5.5

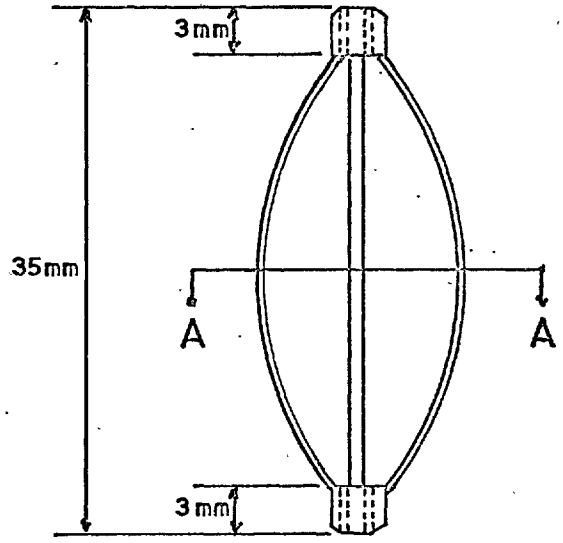


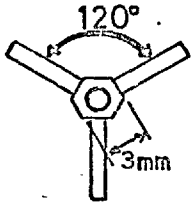
·7mm i.d. x ·8mm o.d.
ss capillary

8 BA brass, left hand thread

silver solder

thermocouple tip

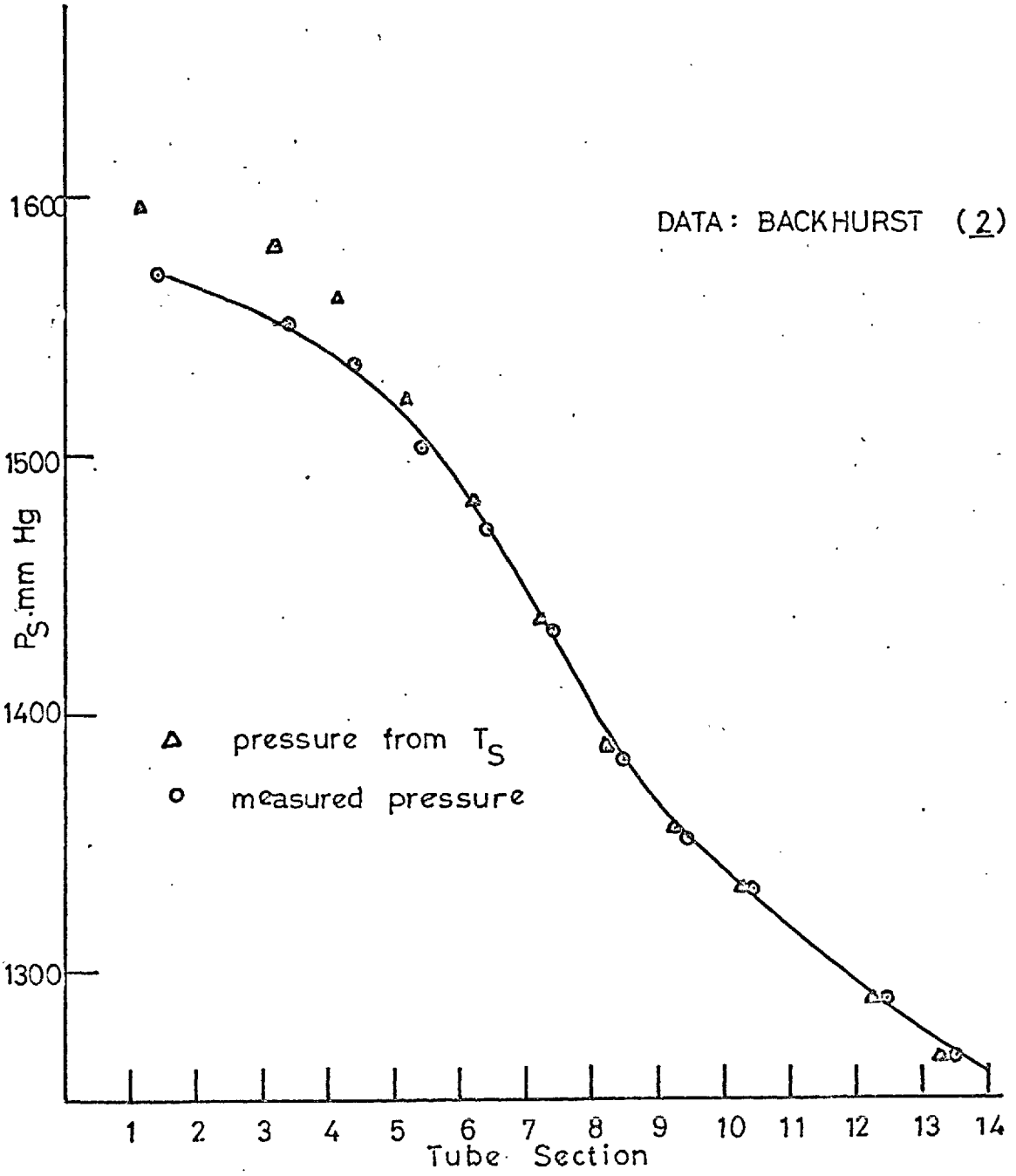




cross section AA

The Travelling Spider Arrangement

FIG 5·6 Measurement Of Vapour Pressure



with a thermocouple against a reference junction at 0.0 °C and the pressure was controlled by keeping this temperature at a fixed value. The thermocouple reading was registered on the Universal Potentiometer. The pressures at points along the test column were similarly derived from the corresponding fluid temperatures.

5.3 Experimental Procedure

The following measurements were made during each run;

(a) the liquid temperature at the inlet to the test section,

(b) the wall temperature of each of the sections of the test column,

(c) the fluid temperatures along the axis of the test column and in the separator,

(d) the heat losses through the lagging of the test section,

(e) critical heat input to sections 10, 12 and 13.

The runs were repeated to measure the entrained liquid flowrate at the critical condition of section 10. This aspect of the experimental work is dealt with in Chapter Six.

5.3.1 Setting The Experimental Conditions

At each start up air was removed from the test section by maintaining the flow rate of Isceon at its maximum value for a short while before setting the desired experimental conditions.

The values of the power inputs to sections 1 to 9 needed for the required conditions of quality and heat flux distribution were obtained by calculation. These evaluations took no account of possible heat losses so that the actual experimental values differ slightly from the nominal

conditions. Subcooled inlet conditions were used for all runs ensuring that the flow regime existing at any point in the test column was a function only of the upstream heat flux distribution. This had great importance with respect to measurements of entrainment and is considered in greater detail in Chapter Six. At the beginning of each day's experimental work, the apparatus was left for two hours to reach equilibrium once the experimental conditions had been set.

It is possible that small traces of dissolved gases remained in the liquid during measurements. No attempt was made to remove this air so that conditions obtained in industrial applications would be simulated as closely as possible.

The required experimental conditions at the entrance to section 10 were obtained by suitable adjustment of heaters 1 to 9 and the system allowed to reach steady state. Heaters 10, 11, 12 and 13 remained off during this period. The heat input to section 10 was then increased by small increments of about 20W allowing steady conditions to be re-established after each increase until a rapid rise in wall temperature was observed. At this point the critical value was taken to be the mean of this value and the steady reading immediately prior to it. Examples of the temperature variation indicated on the chart recorder during 'burnout' are shown in Figs. 5.7, 5.8, and 5.9. This experimental technique introduces a deviation of 10W in the estimation of the critical heat flux with an error in the estimate of this deviation introduced by the measuring instruments of approximately 5W, giving a total estimated experimental error of $\pm$ 15W.

FIG 5·7 mV Recording Of Burnout At Section 10

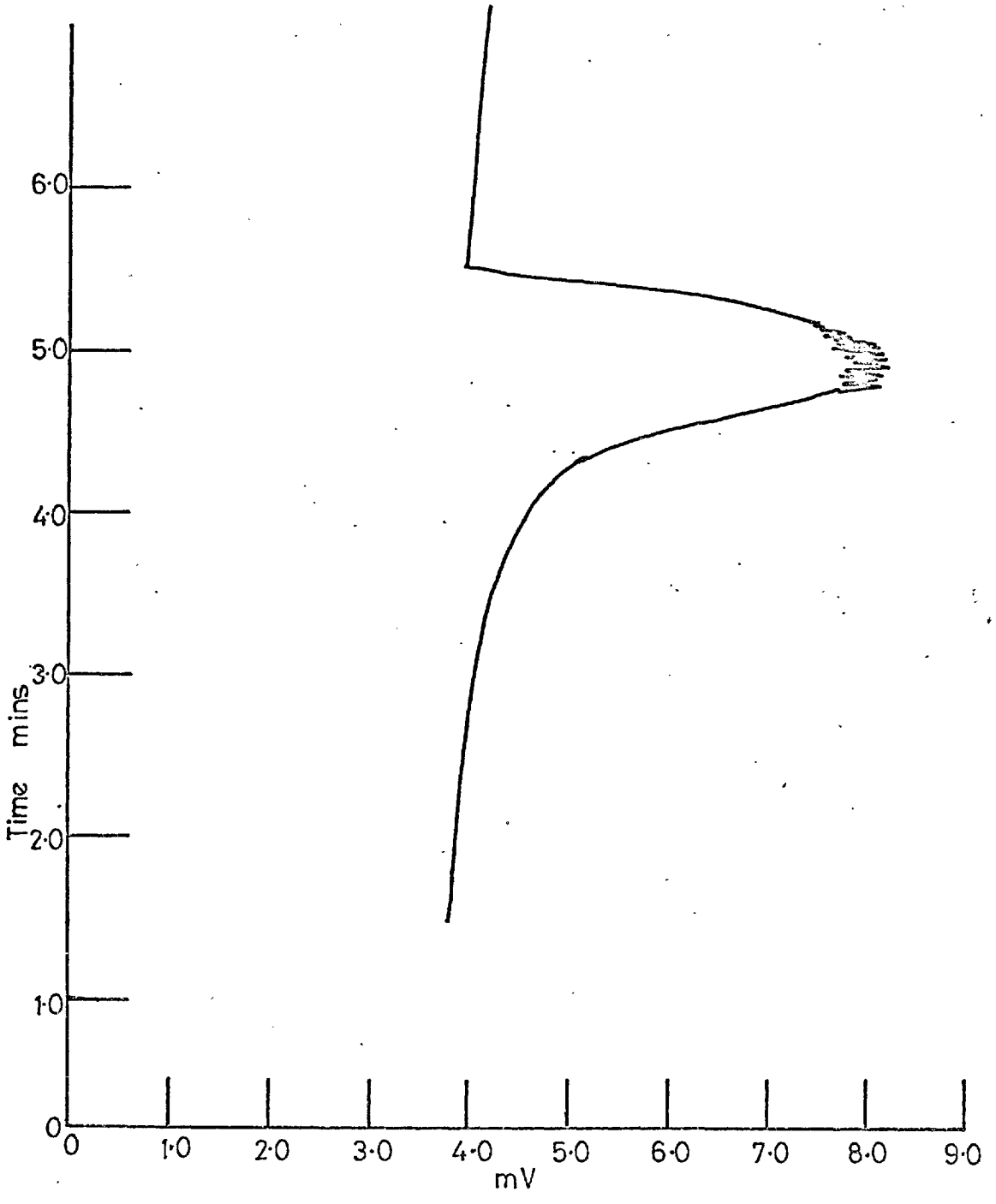
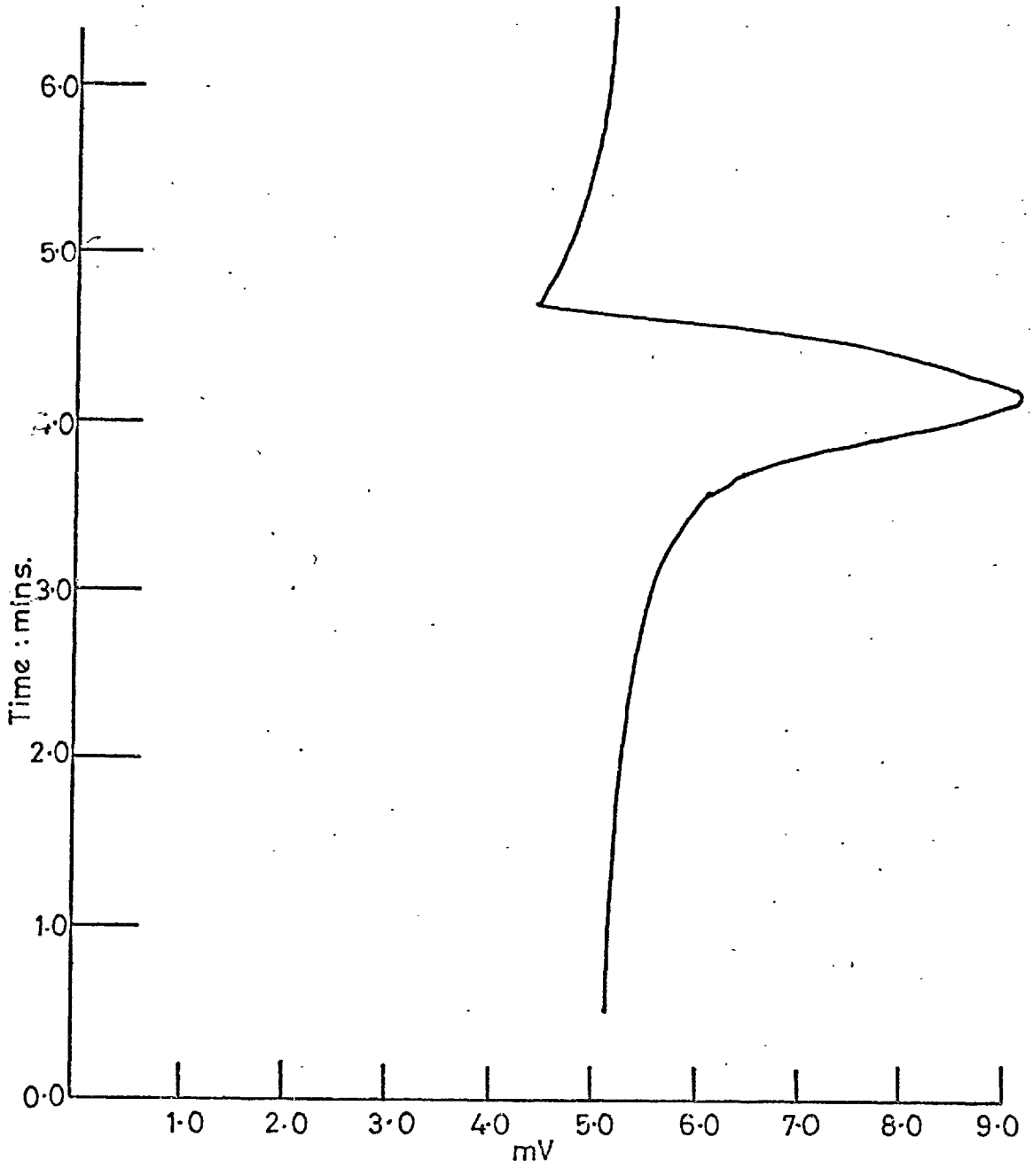
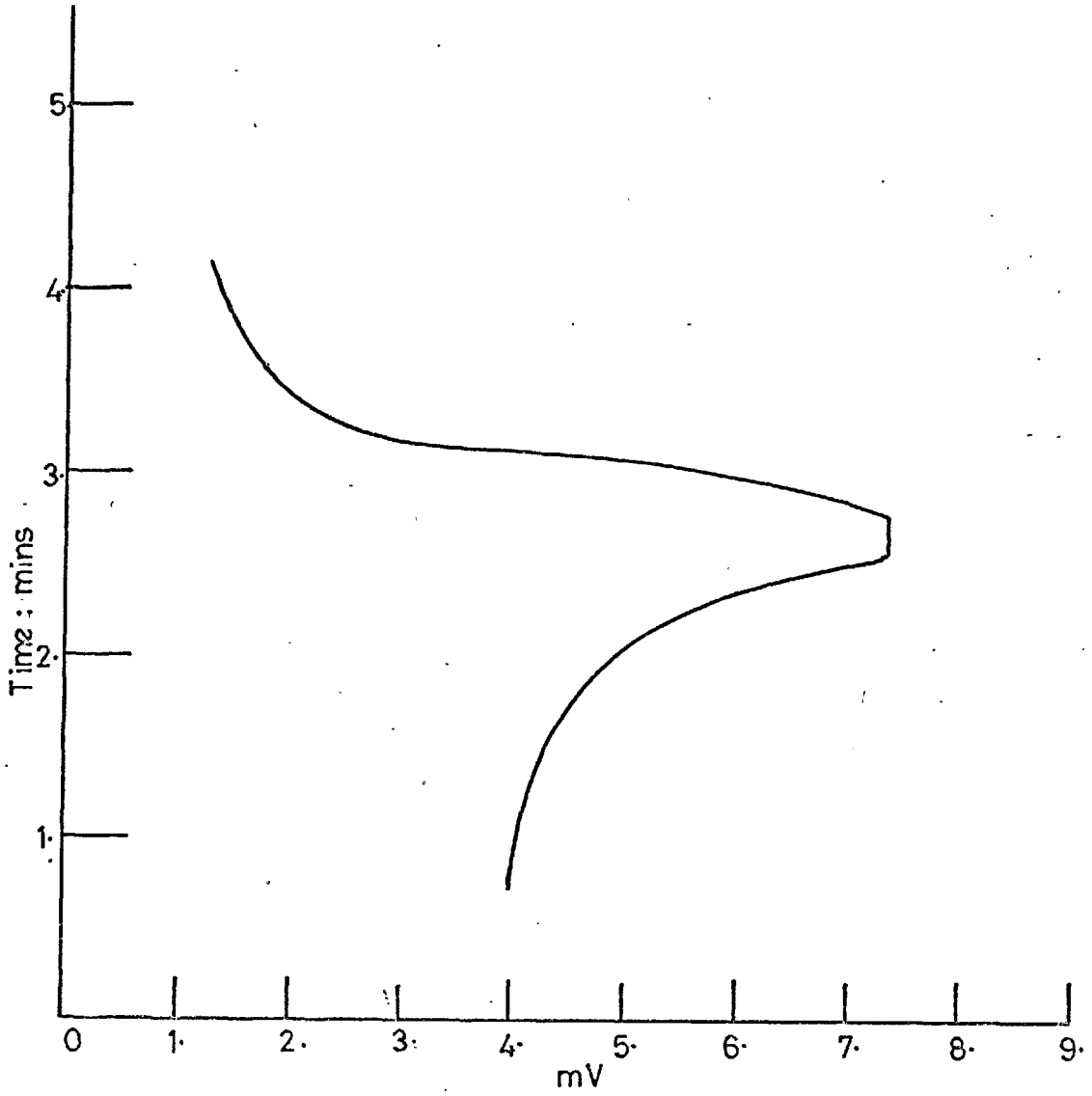


FIG 5·8



mV Recording Of Burnout At Section 10

FIG 5·9



mV Recording Of Burnout At Section 10

The heat input to 10 was now set approximately 100W lower than its critical value to avoid the precipitation of burnout conditions at this section whilst the downstream critical measurements were being carried out. The critical input to section 12 was now measured by a similar method. Once the value for section 12 had been obtained the heat supply to this section was switched off and the readings for section 13 taken.

During measurement of the critical value the pressure at the entrance to the section under test was kept constant, necessitating adjustment of the separator pressure to counteract the effect of changes in pressure gradient in the tube. Tests carried out on the tube showed that variation of the local fluid pressure caused a corresponding variation in the local wall temperature. Pressure control was therefore achieved by maintaining the wall temperatures of sections upstream of the 'burnout' point at a constant value by suitable adjustment of the separator pressure.

The long term reproducibility of the critical values was tested on four separate occasions for section 10 under run conditions 521. These gave a mean of 1050.5W with a standard deviation of 15.3W which may be favourably compared with the error involved in the experimental technique of 15W. The true critical value may thus be expected to lie within the 95% confidence limit of $\pm$ 20W of the estimated value.

An attempt was made to estimate the effect of heat conduction between sections on the critical value by raising the wall temperature of section 11 for run conditions 521. The results for section 10 gave a mean value of 1041.5W (2 results) with a standard deviation of $\pm$ 21 watts. The difference between this mean and that previously obtained was found to be

insignificant at the 5% level and the effects of heat conduction between sections were concluded to be negligibly small.

In an effort to keep the thermal dissociation of the Isceon to a small value, the wall temperatures were never allowed to exceed 200°C during these measurements. If burnout had not been observed by the time this temperature had been reached it was considered to be 'undetectable'. A similar designation was given to those points for which the critical value was greater than the maximum possible applied heat input per section.

CHAPTER SIX

THE ENTRAINED MASS FLOWRATE

6.1 Introduction

A description of the apparatus used to measure the entrained mass flowrate and the derived experimental results are presented. The measurements were made to indicate the nature of the onset of burnout; whether the critical condition for the Isceon is brought about by the total entrainment of the liquid phase or whether conditions exist for the application of the burnout model presented in Chapter Four.

6.2 Literature Survey

Most published entrainment data are for air/water systems and only a few are presented for boiler tubes. Some data for boiling water have been presented by HEWITT et al (8)and BENNETT et al (31) and also by ANDERSON, HASELDEN and MANTZOURANIS (76). Further data for boiling systems are presented by BACKHURST (2) for benzene and benzene/toluene mixtures.

Data for air-water are presented, by ALVES (56), WICKS and DUCKLER (57), GILL et al (58,69), GILL and HEWITT (68), and TRUONG QUONG MINHE and HUYGHE (71), among many others. One point has also been published for SAE-10-oil/air by ALVES (56) and a few data for ethyl alcohol/air by TRUONG QUONG MINHE and HUYGHE (71).

Attempts to correlate the data for isothermal systems have met with only partial success. The earliest correlation is presented by WICKS and DUCKLER (57) in the form

$$\left(\left(\frac{dP}{dz}\right)_L / \left(\frac{dP}{dz}\right)_V\right)^{\frac{1}{2}} = \frac{(Q_L / Q_V)\ We_c E}{\left(\frac{dP}{dz}\right)_V} \quad . \quad . \quad . \quad . \quad (6.1)$$

BACKHURST (2) correlated his boiler tube data using the approach of Wicks and Duckler to +50% and -25% but contributed this relative success mainly to the fact that the variable with the largest range, $(-\frac{dP}{dz})_V$, appeared on both sides of the equation suggesting that the correlation may not be as good as at first it may appear. Backhurst correlated his own data to +25%, -30% by

$$G_e = 2.05\ G_L^{0.30}\ G_V^{0.61} \quad \text{(f.lb.hr units)} \qquad . \quad . \quad (6.2)$$

A further correlation is presented by TRUONG QUONG MINHE and HUYGHE (71) based on the assumption that the entrained liquid flow is proportional to the mean kinetic energy of the gas stream

$$1 - E_r = f(\bar{\rho} U_V^2) \qquad . \quad . \quad . \quad . \quad . \quad . \quad . \quad (6.3)$$

where

$$E_r = \frac{W_e}{W_L}$$

and

$$\bar{\rho} = \rho_V\left(1 + E\,\frac{W_e}{W_V}\right)$$

Application of this approach to air/water and air/ethyl alcohol data (71) revealed a large physical property effect which requires further investigation.

A similar approach attempting to account for this effect of the physical properties is presented by PALEEV and FILIPPOVICH (70). They introduce the term $\left(\frac{\mu_L}{\rho_L^2 \sigma}\right)^2$ into equation (6.3) obtaining

$$1 - E_r = f\left(\bar{\rho}\, U_V^2 \left(\frac{\mu_L}{\rho_L^2 \sigma}\right)^2\right) \qquad . \quad . \quad . \quad . \quad . \quad (6.4)$$

which gave the following correlation for air/water data;

$$1 - E_r = 0.985 - 0.44 \log\left(\frac{\bar{\rho}}{\rho_L}\left(\frac{\mu_L U_V}{\sigma}\right)^2 \times 10^4\right) \quad . \quad . \quad (6.5)$$

COUSINS and HEWITT (23) using data obtained from various sources, revealed a diameter effect not accounted for by equation (6.4). Several suggestions were made by Paleev and Filippovich to explain this effect but none of these were successful in their application.

More recently LEVY (74) produced a correlation derived from Prandtl's mixing-length theory and empirical functions developed from the results of CISE, which allows the determination of the liquid film flowrate from knowledge of the pressure drop. His attempts to extend this approach to predict results obtained at Harwell show considerable deviation from the experimental results.

Very few attempts have been made to determine the mechanisms for entrainment. Work presented by HALL-TAYLOR, HEWITT and LACEY (73) demonstrates a link between large disturbance waves and entrainment in isothermal systems HEWITT et al (8) have further shown that in boiling systems, entrainment can occur from the bursting of bubbles through the surface of a liquid film.

The parametric investigation of GILL et al (58,69) for water injection through a porous section of the tube wall reveals that the entrained mass velocity is not constant across the tube but is a function of the radius. At low liquid and gas velocities, at sampling points close to the water inlet, a minimum mass velocity at the tube axis is observed, but at high liquid and gas velocities and for sampling points further than 2m from the inlet the mass velocity showed a peak at the tube axis which

sharpened as the parameters were increased. This indicates the care which must be taken when using entrainment data obtained from probe measurements only at the axis of a tube.

6.3 The Technique Chosen For Entrainment Measurement

The observations made by Gill et al presented in the last section suggest that a fixed-probe technique, taking measurements only at the axis of the tube, would lead in certain instances, to an over-estimation of the total entrained mass flowrate. However, since the present purpose of obtaining entrainment data is to ascertain whether burnout occurs by a 'film dry-out' mechanism, these errors were considered to be acceptable and a fixed probe technique was used. This decision is supported by earlier work of BACKHURST (2) who successfully differentiated between burnout mechanisms occurring in his boiler tube using entrainment data obtained by this technique.

The technique adopted was developed originally by MANTZOURANIS (1) on the experimental rig used here. Using the fixed probe, he plotted the impact pressure at the probe tip against the liquid sampling rate and obtained a curve of the form shown in Fig.6.1. This curve may be divided into two sections, depicted as AB and BC in the figure. In section AB the impact pressure, P_I, varies very little with an increase in sampling rate suggesting that only liquid is being sampled. However, at point B, a very marked decrease in P_I occurs with only a small increase in sampling rate and it is suggested that this occurs when both liquid and vapouf are being sampled. A small increase in the sampling rate would cause a large increase in vapour velocity through the probe with a consequent increase of the shear stresses, and this would result in a rapid drop in the measured impact pressure. The

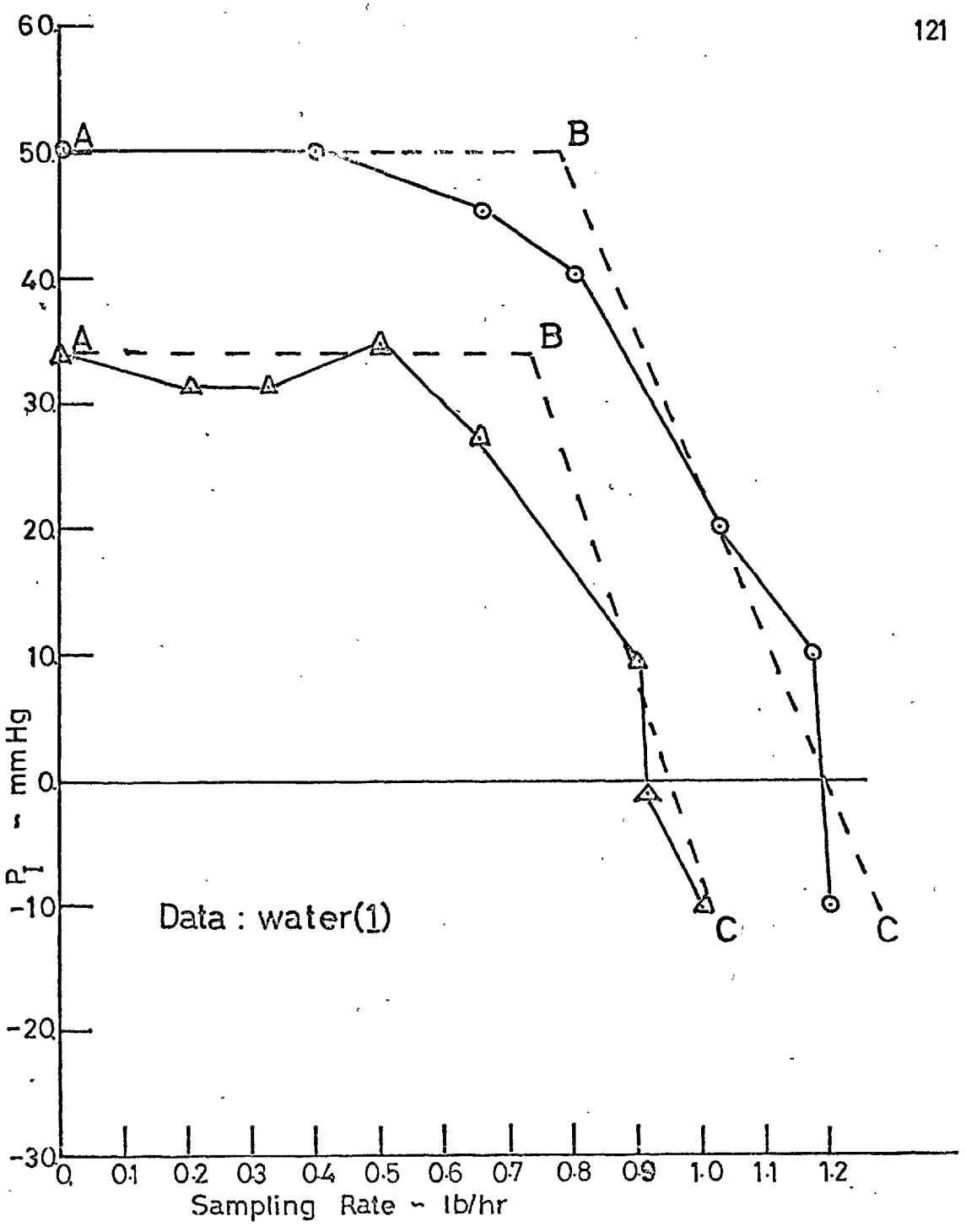


FIG 6.1 Measurement Of Entrainment

sampling rate at which the regions AB and BC intersect corresponds to the entrained mass flowrate.

6.4 Description Of Apparatus

The apparatus used for measuring the entrained liquid flowrate and impact pressures is shown in Fig.6.2 and its position in the test section in Fig.6.3. The entrainment probe was firmly held by a P.T.F.E. gland so that the probe tip was positioned opposite the static pressure tapping at the exit from the boiler tube. A brass spider attached immediately above the probe tip served to keep the tip at an axially central position in the tube.

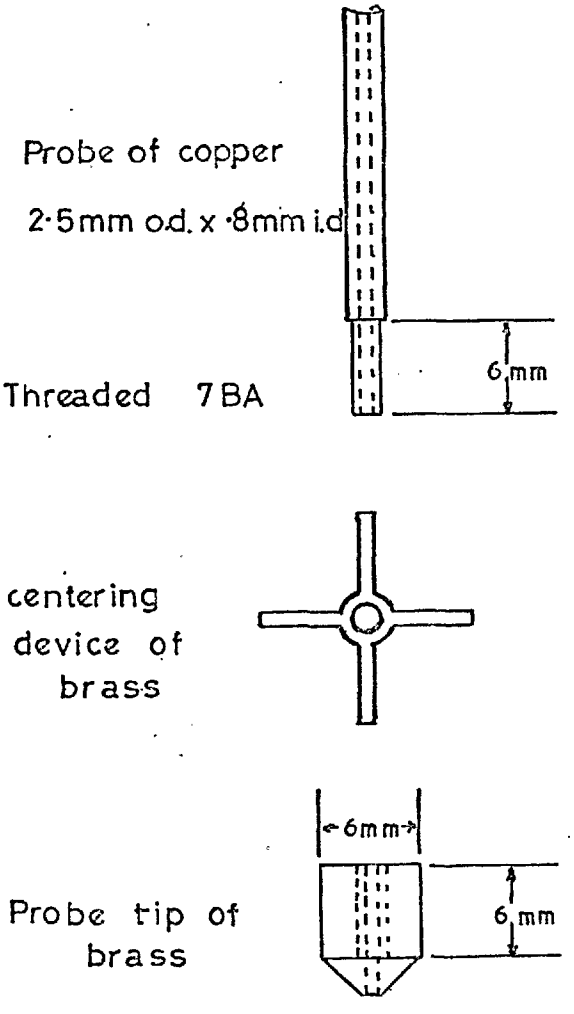
Liquid filled pressure lines led from the probe tappings to two glass bulbs and from these nitrogen filled stainless steel capillary tubes 0.36mm i.d. by 0.71mm o.d. connected with the sloping mercury manometer. The liquid levels in the two glass bulbs could be adjusted by applying nitrogen pressure from a cylinder or by opening to the atmosphere.

Liquid entering the probe was collected in a 50 ml burette and its flowrate could be sensitively adjusted by two 3 mm needle valves mounted in series. Any vapour entering the probe was condensed in the small water cooled condenser attached to the probe.

The probe was made from 2.5mm o.d. by 0.8mm i.d. copper capillary tube and the probe tip from brass, drilled 0.8mm i.d. and tapped 7B.A. This tip screwed onto the probe and held the centralising brass spider in position.

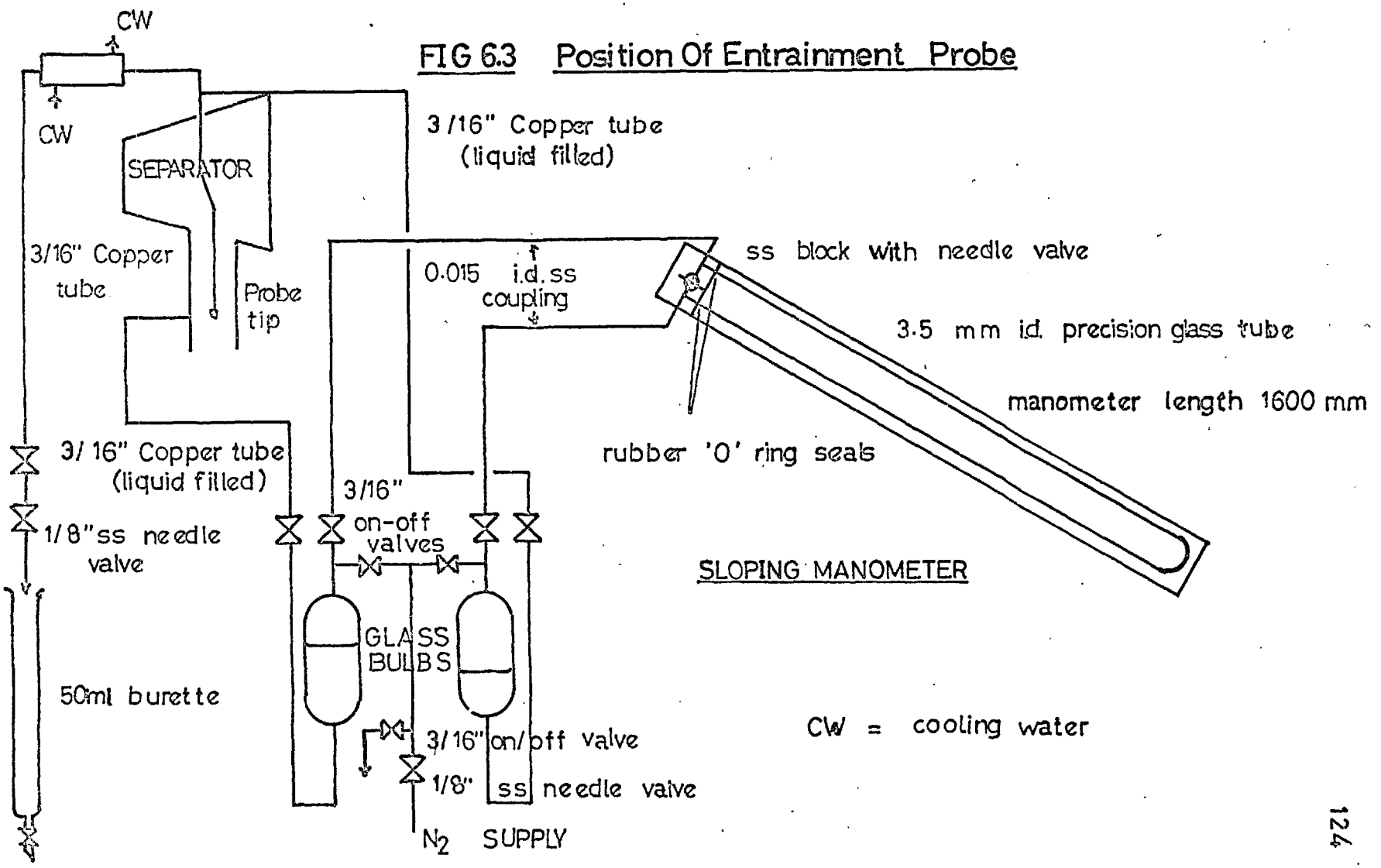
Since the probe position was fixed, the entrained flowrates for different sections of the test column were obtained by moving the tube entrance conditions. Heaters at the bottom of the tube were switched off

FIG 6·2



Entrainment Probe

FIG 6.3 Position Of Entrainment Probe



and those remaining on were adjusted to the appropriate value. Subcooled inlet temperatures were maintained for all runs so that these adjustments to the conditions would not affect the relative entrainment distribution in the tube.

6.5 Experimental Technique

6.5.1 Measurement Of Impact Pressure

Impact pressure is the difference between the pressure at the probe tip and the static pressure of the surrounding liquid at zero liquid sampling rate through the probe.

This pressure difference was measured on a sloping mercury manometer. The liquid levels in the glass bulbs were also noted so that the impact pressure could be corrected for the difference between the liquid heads in the pressure lines. The level in each arm of the manometer was read to the nearest 0.5mm. equivalent to a possible error of $\pm$ 0.18mm.Hg. in the measured pressure difference. The liquid levels in the glass bulbs were also measured to within 0.5mm increasing the possible error by $\pm$ 0.05mm.Hg. giving a total estimated experimental error in the pressure difference readings of $\pm$ 0.23mm.Hg.

To obtain reproducible results for this pressure difference it was essential to keep the probe full of liquid. Air was removed from the pressure tappings by filling the glass bulbs with liquid and then discharging them through the pressure lines. This procedure was repeated until the impact pressures were reproducible within the experimental error of $\pm$ 0.23 mm.Hg.

6.5.2 Measurement Of Entrainment

It is shown in Appendix E5 that the impact pressure variation with increase in the sampling rate is satisfactorily correlated for all runs by two straight lines of constant gradient. The curve may therefore be completely defined by two data points so only the following measurements were taken for each run condition :

(1) Impact pressure,

(2) Sampling rate through the probe at a pressure difference of between $\frac{1}{2}$ and $\frac{3}{4}$ of the impact pressure,

(3) A repeat measurement of the impact pressure to check reproducibility

To measure the sampling rate, the valve in the sampling line was slowly opened until the pressure difference, as indicated by the sloping mercury manometer, was between $\frac{1}{2}$ and $\frac{3}{4}$ of the impact pressure. The collection of a 10ml. sample in a 50ml. burette was then carefully timed with a stop-clock. This timing was repeated once and the mean value taken for the evaluation of the sampling rate. The temperature of the sampled liquid was also noted. If the two sampled flowrates differed by more than $\pm$ 0.5%, the flow was considered to be unsteady and the measurement repeated until a steady reading was obtained.

6.6 Results

The results obtained for the impact pressure and local liquid mass velocity at the axis of the tube are presented in Table 6.1. The value for the impact pressure is taken as the mean of the two recorded values and the deviation in the impact pressure as the difference between the mean value and the recorded values.

6.6.1 Accuracy and Reproducibility

6.6.11 Sampling Rates

The 10ml. sample was measured to ± 1/20ml. giving an error of ± 0.5%. An accurate assessment of the accuracy of the stop-clock was not made but it is known to be better than ±.1%. A total experimental error of ± 0.6% is thus expected in the sampling rates.

The sampling rate for each run was taken as the mean of two readings. Analysis of the deviations from this mean gives a 99% confidence limit of ± 0.5% (11 values). The close agreement between this deviation and the estimated experimental error suggests that steady sampling rates were obtained throughout the time needed for taking the experimental measurements.

6.6.12 Impact Pressures

As related in Section 6.5.1 the error introduced by the recorded measurements is estimated at ± 0.23mm.Hg. Surface tension effects at the probe tip may give a further error of upto ± 0.5mm.Hg. giving a total estimated experimental error of ± 0.73mm.Hg.

Analysis of the 'within-run' deviations of the impact pressure (Table 6.1) gives a 99% confidence limit of ± 0.4mm.Hg. (103 values). A comparison between this limit and the estimated experimental error indicates that satisfactory precautions were taken in the experimental procedure to ensure that the probe was filled with liquid before the measurements were taken.

The results for the 'between-run' reproducibility of the impact pressures are shown in Table 6.2. The deviations give a 99% confidence limit of ± 1.6mm.Hg. (9 values). This is considerably larger than might be

expected from experimental error alone and it might be suggested that this indicates that the impact pressure is sensitive to small changes in the setting of the run conditions. An 'F' test was carried out on the variances of the 'between-run' and 'within-run' results to investigate this conclusion further. No significant difference was found between these variances at the 5% level suggesting that the 'between-run' deviations could in fact be explained only by experimental error, the small sample size possibly accounting for the deceptively large confidence limit.

6.6.13 Local Liquid Mass Velocity

Only the 'between-run' reproducibility was measured and these results are presented in Table 6.2. Analysis of the deviation gives a 95% confidence limit of $\pm$ 4 Kg/m^2s or a percentage error of between $\pm$ 2% and $\pm$ 5%. The estimated experimental error is $\pm$ 2% from the evaluation of the 'constant gradients' (Appendix E5) and $\pm$ 0.6% from the sampling rates giving a total of $\pm$ 2.6%. This compares closely with the error of reproducibility suggesting that no unaccounted factors influence the entrainment.

The entrainment probe was used under non-isokinetic conditions so the capture efficiency of the probe affects the accuracy of the estimate of the local liquid mass velocity. DUSSOURD and SHAPIRO (77) present an approach to estimate this efficiency. For drop sizes of 50 μm and 100 μm, under the worst sampling conditions at which measurements were taken (0.006 Kg/s), the capture efficiency for the probe, estimated using their technique is 99% and 99.4% respectively. Hence, under the conditions used for measuring the entrainment, the capture effiency should be better than 99%. A further

error of upto ± 4% is introduced by the assumption of 'constant gradient' in the evaluation so that the true value for the local liquid mass velocity may be expected to be within ± 12 Kg/m^2s of the estimated value.

6.7 Discussion

Fig.6.4 shows the variation of entrainment with quality for run 333. A minimum occurs in the entrained mass velocity at 12% quality and the rapid increase in entrainment at qualities below this value suggests that the slug/annular transition occurs close to this minimum. A comparison with data for a benzene/toluene mixture under similar conditions (Fig.6.4) shows that entrainment for the two systems is of similar magnitude.

The Isceon entrainment data for qualities greater than 10% are correlated to +25% and -30% (Fig.6.5) by the relationship

$$G_e = 11.7\ (G_V)^{0.21}(G_L)^{0.24} \quad \text{(s.i. units)} \qquad . \quad . \quad (6.6)$$

A comparison between this equation and that derived by BACKHURST (2) for benzene and benzene/toluene mixtures,

$$G_e = K(G_V)^{0.61}(G_L)^{0.30} \qquad . \quad . \quad . \quad . \quad . \quad . \quad . \quad (6.7)$$

shows that despite the order of magnitude agreement between entrainment flow-rates shown in Fig.6.4, there exists a considerable difference in the influence of G_V and, to a lesser extent, G_L for the two liquid systems.

The entrainment data for runs 331/9, 332/9 and 333/9 (Table 6.1) indicate that the axial heat flux distribution has a considerable effect on the magnitude of entrainment in the quality region below 10%, suggesting its importance in the slug flow regime. However, at higher qualities, no definite effect of heat flux distribution is observed despite the quite high nucleation

rates which occur at some of the conditions analysed (Table A2) indicating that boiling is not a significant factor influencing entrainment in the annular flow regime.

Fig.6.6 compares the total entrained flowrate with the total liquid flowrate measured at the critical point. Only a few of the data recorded are shown to be satisfactorily explained by the 'film dry-out' mechanism for burnout (data for which all the liquid flows as entrained drops). All these 'film dry-out' data occur at the lowest flow rate investigated (0.0375 Kg/s) and then only at qualities greater than 30%. Some other mechanism for burnout must therefore be operating under the other conditions investigated.

FIG 6.4 Variation Of Entrainment At Low Quality

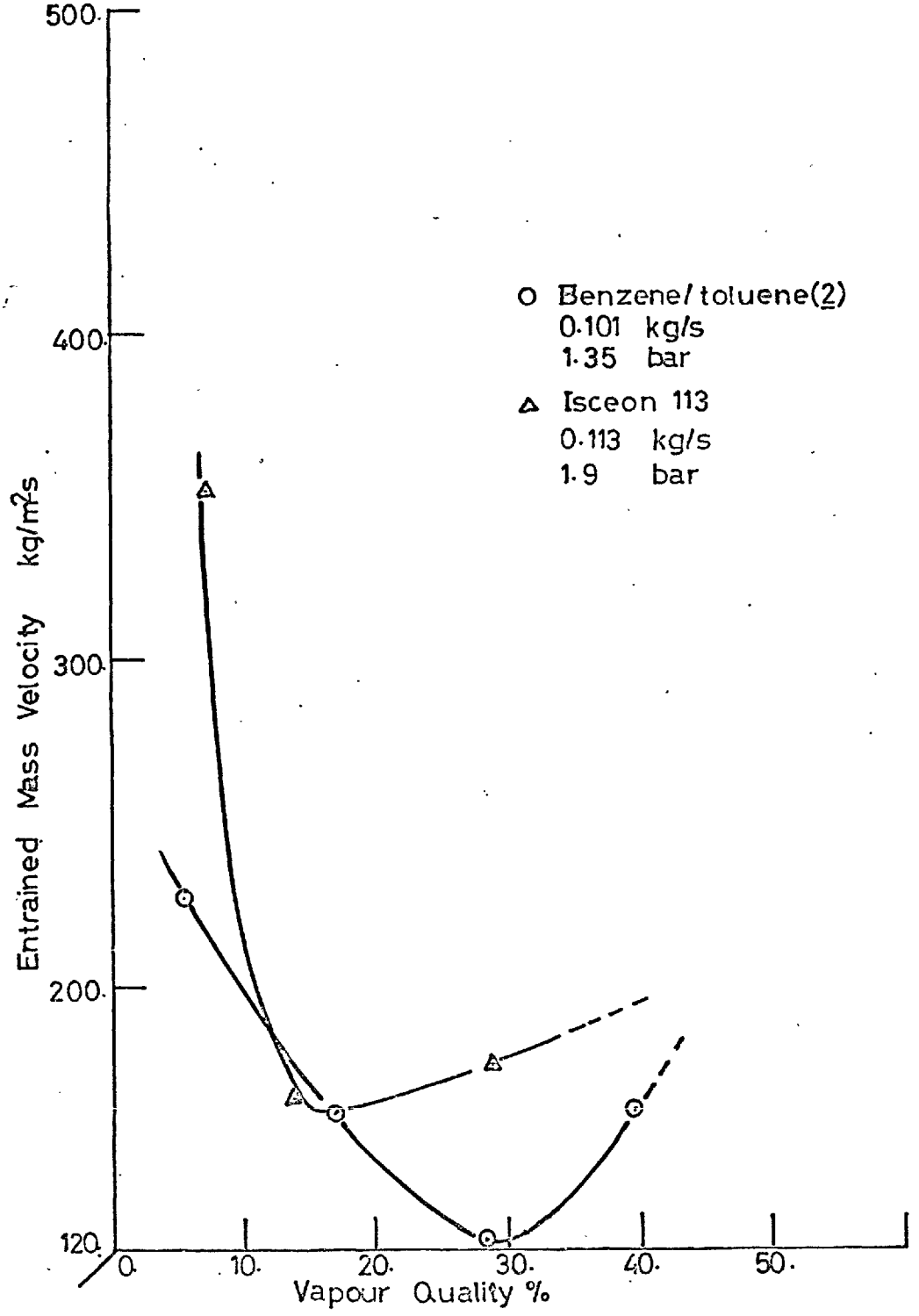


FIG 6.5 Correlation Of Entrainment

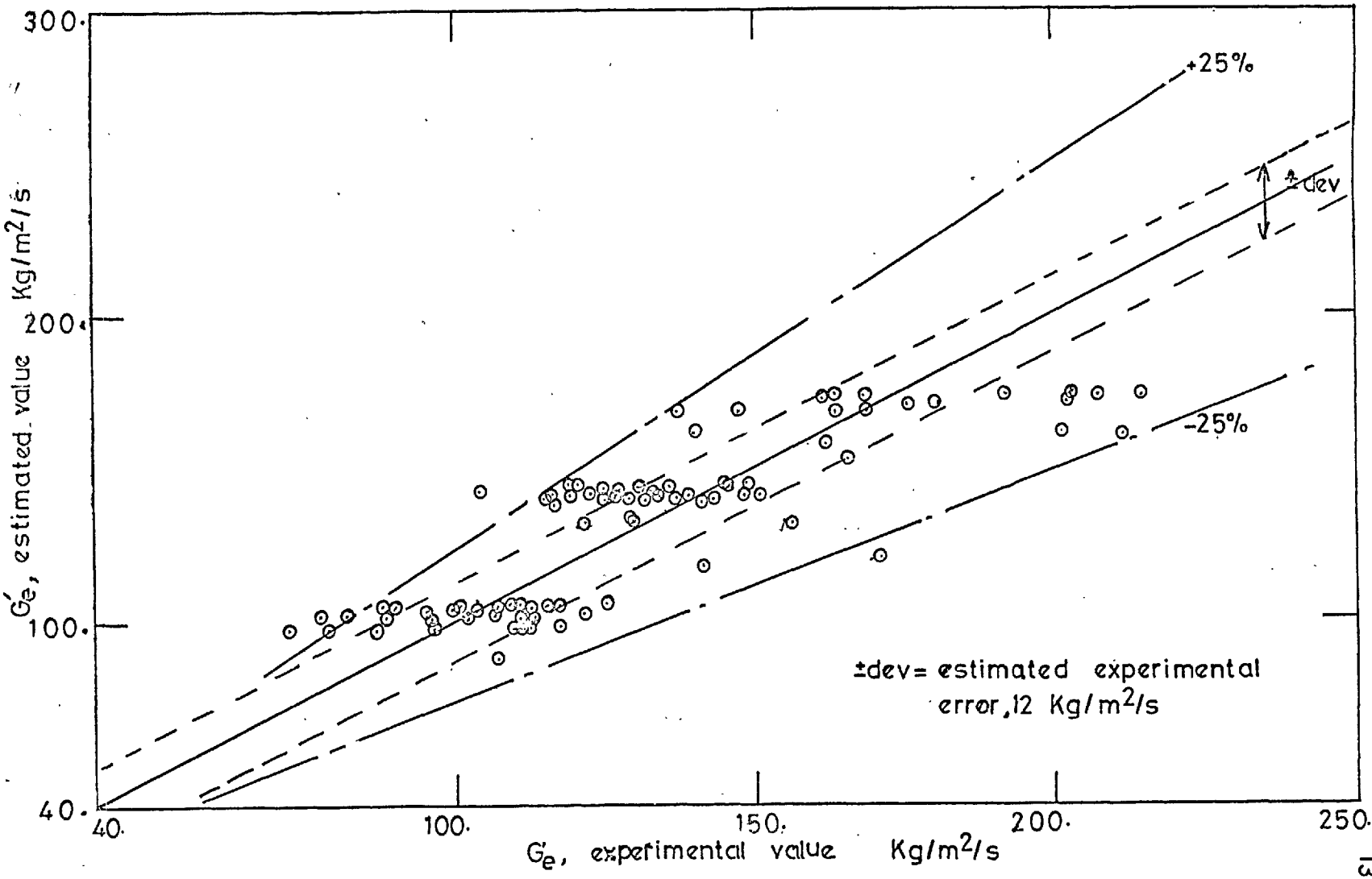


FIG 6.6 Entrained Mass Flowrate At Burnout Location

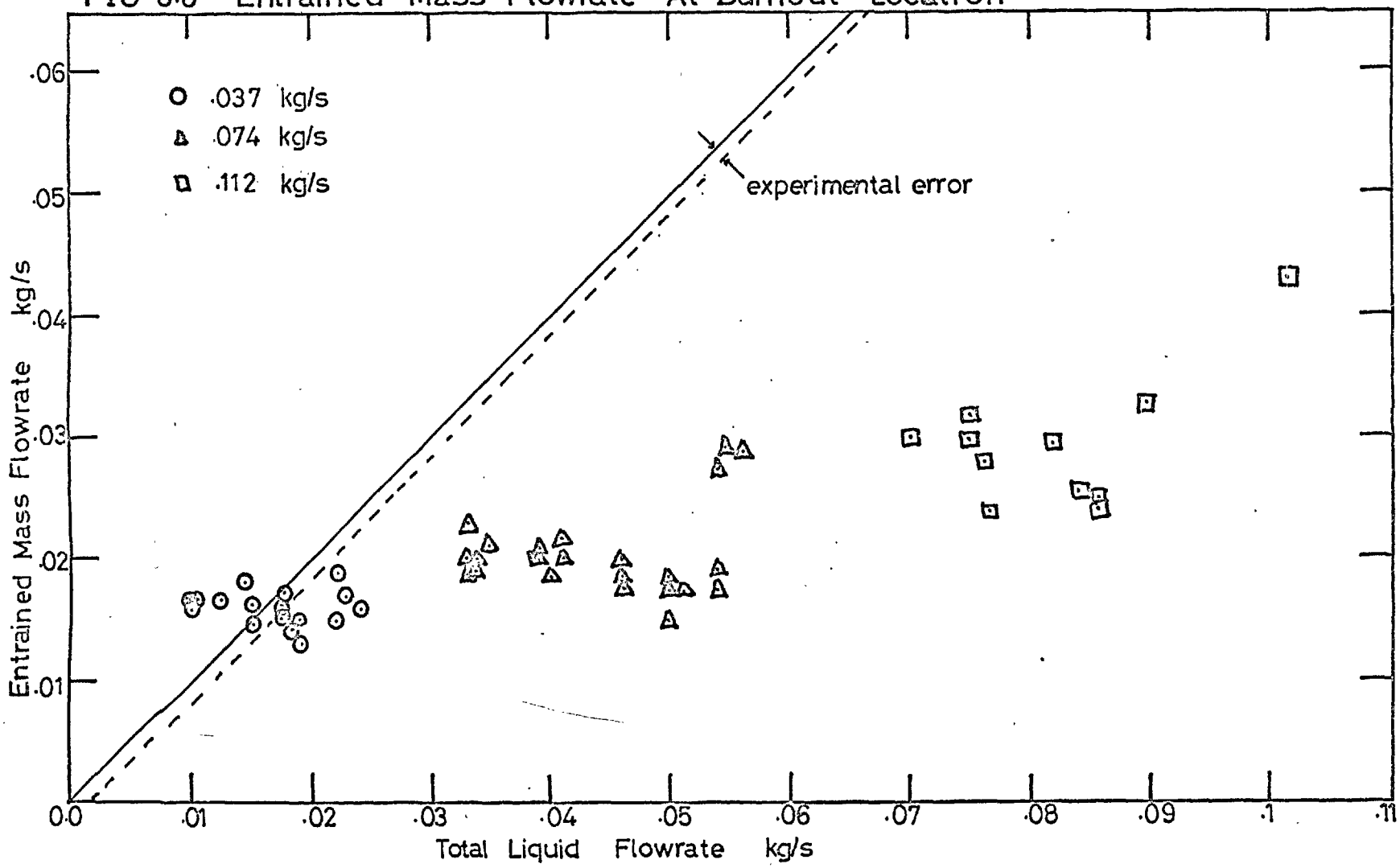


TABLE 6.1

ENTRAINMENT DATA

Run No/Sect	P_I mm Hg	dev. P_I ± mm Hg	G_e Kg/m^{2}s	W_e Kg/s
522/13	57.4	0.4	129.6	0.019
222/13	31.0	1.3	116.5	0.017
422/13	50.8	1.1	127.7	0.019
323/13	41.3	1.8	130.2	0.019
323/13	40.4	0.7	127.7	0.019
323/10	37.0	0.9	135.8	0.020
323/9	20.7	0.7	123.3	0.018
321/9	21.4	1.4	156.4	0.023
321/10	39.0	0.7	131.4	0.019
321/12	38.0	0.0	122.7	0.018
321/13	39.9	0.4	124.0	0.018
322/13	36.2	1.9	124.6	0.018
322/13	40.9	1.2	119.6	0.018
322/12	43.0	1.0	104.7	0.016
322/10	40.1	0.9	120.2	0.018
322/9	20.4	0.4	129.6	0.019
522/8	37.2	0.8	115.2	0.017
522/9	41.5	1.5	119.0	0.018
522/9	46.3	2.3	115.9	0.017
522/10	52.6	0.3	137.1	0.020
522/12	49.7	0.1	135.8	0.020
522/13	52.8	0.8	133.9	0.020
523/13	53.5	0.4	133.9	0.020
523/12	51.0	0.0	133.9	0.020
523/10	54.2	0.2	145.2	0.020
523/9	37.7	0.0	148.9	0.020
523/8	33.9	0.1	131.5	0.019
221/9	12.3	0.1	271.6	0.040
222/9	12.4	1.3	140.8	0.021
223/9	17.1	1.1	67.3	0.010
223/10	27.9	1.4	188.2	0.028
222/10	27.8	1.2	201.9	0.030
221/10	28.5	2.1	196.3	0.029
421/9	36.4	0.2	136.4	0.020
422/9	39.4	1.1	129.0	0.019
423/9	36.0	0.5	142.7	0.020
423/10	54.1	0.5	148.9	0.022
422/10	51.0	0.4	138.3	0.020
421/10	52.9	0.3	124.6	0.018
521/9	50.1	2.3	132.1	0.020
521/10	56.9	0.6	144.5	0.021

TABLE 6.1(cont.)

Run No/Sect	P_I mm Hg	dev. P_I ± mm Hg	G_e Kg/m^{2}s	W_e Kg/s
231/9	27.2	1.4	459.2	0.068
233/9	17.9	0.2	171.3	0.025
232/9	19.8	1.1	322.7	0.048
232/13	46.8	2.0	138.9	0.021
233/10	44.7	0.5	294.7	0.044
231/10	47.0	0.5	243.3	0.035
232/10	50.0	0.7	235.5	0.035
433/10	89.7	0.1	203.1	0.030
333/10	66.5	0.5	175.7	0.026
333/6	22.2	0.7	352.0	0.052
333/8	33.1	1.2	165.1	0.024
331/9	41.2	0.5	288.4	0.043
332/9	41.2	0.7	201.2	0.030
332/9	41.4	0.1	211.2	0.031
333/9	38.4	0.6	162.6	0.024
333/10	62.9	0.1	179.4	0.026
332/13	59.7	0.2	162.0	0.024
331/10	62.5	0.0	202.5	0.030
332/10	64.7	1.5	167.6	0.025
432/9	63.7	0.5	147.7	0.022
431/9	63.7	0.9	169.5	0.025
432/9	63.0	0.3	147.7	0.022
433/9	64.2	1.4	163.2	0.024
433/13	86.6	0.3	222.4	0.033
432/13	79.2	0.1	191.3	0.028
432/10	86.3	0.7	163.2	0.024
433/10	88.3	0.3	207.5	0.031
211/10	11.2	0.7	111.5	0.017
211/13	13.6	1.3	100.3	0.016
213/13	10.9	1.2	103.4	0.015
313/13	13.1	1.6	109.0	0.016
311/13	12.7	0.5	107.8	0.016
311/10	13.6	1.4	89.7	0.013
411/10	21.3	2.4	103.4	0.015
411/13	17.2	0.9	110.9	0.016
511/13	25.9	1.1	95.9	0.014
512/13	28.4	0.0	95.9	0.014
511/10	26.8	0.5	109.6	0.016
511/9	18.2	1.0	94.7	0.014
512/9	20.4	1.1	87.2	0.013
412/9	18.1	0.2	81.6	0.012
411/9	13.3	0.6	88.5	0.013
311/9	12.2	0.8	86.6	0.013
312/9	21.7	0.7	72.3	0.011

TABLE 6.1 (cont.)

Run No/Sect	P_I mm Hg	dev. P_I ± mm Hg	G_e Kg/m^2s	W_e Kg/s
212/10	11.9	1.1	117.1	0.017
312/10	13.3	1.0	115.9	0.017
412/10	26.6	3.1	106.5	0.016
413/10	21.4	2.0	102.8	0.015
313/10	19.0	0.2	112.1	0.017
313/10	17.4	0.1	105.9	0.016
213/10	11.6	0.4	125.2	0.019
213/9	10.5	2.2	106.5	0.016
313/9	17.0	0.9	78.5	0.012
413/9	21.8	1.9	77.2	0.011
513/9	16.6	1.3	99.7	0.015
513/10	27.1	1.0	110.9	0.016
513/13	17.2	0.1	112.1	0.017
513/13	20.0	0.0	117.1	0.017
413/13	13.6	0.3	121.5	0.018
512/13	20.7	1.5	112.8	0.017
522/13	59.9	0.1	142.0	0.021
522/13	57.1	0.4	150.8	0.022

TABLE 6.2

REPRODUCIBILITY OF ENTRAINMENT DATA

Date	Run No.	P_I mm Hg	G_e Kg/m^2s
5.8.68	513/13	20.0	117.1
6.8.68	513/13	17.2	112.1
7.8.68	313/10	19.0	112.1
6.8.68	313/10	17.4	105.9
5.8.68	522/13	57.1	150.8
2.8.68	522/13	57.4	138.9
24.7.68	522/13	55.5	129.6
2.8.68	322/13	41.5	130.2
1.8.68	322/13	40.4	127.7
25.7.68	522/9	41.5	117.7
24.7.68	522/9	46.3	115.9
9.8.68	332/9	41.4	201.4
12.8.68	332/9	41.2	211.2
9.8.68	333/10	62.9	176.3
12.8.68	333/10	66.7	175.7
9.8.68	433/10	88.4	207.5
12.8.68	433/10	89.7	203.1

CHAPTER SEVEN

THE CRITICAL HEAT FLUX

7.1 Introduction

In this chapter the critical heat flux data are presented and discussed, correlations and physical models of 'burnout' presented earlier in Chapter Two tested and an attempt made to predict the tube wall temperatures at the critical condition from the nucleate boiling theory presented in Chapter Four.

7.2 Results

The experimental critical heat flux data are presented in Table 7.1 and their trends are depicted graphically in Figs 7.11 - 7.13. The block diagram for the computer programme used for these derivations is presented in Appendix C1.

7.3 Discussion Of Results

7.3.1 Total Entrainment Mechanism

Analysis of this 'film dry-out' mechanism is presented earlier in Section 6.7 where this model is shown to provide an unsatisfactory explanation for the majority of the burnout data. Those data for which 'burnout' is considered to be a result of total entrainment are indicated in Table 7.1.

7.3.2 Nucleate Boiling

To test the possible application of a nucleate boiling mechanism to the burnout data, calculations were made for each run to investigate at which sections in the test column nucleate boiling was occurring.

The approach presented by DAVIS and ANDERSON (54) was used to calculate the necessary liquid superheat to initiate boiling (section 3.3).

The actual superheat existing at each section was calculated from the measured heat flux and wall temperature, and if this superheat exceeds the superheat necessary to initiate nucleation, nucleate boiling is assumed to be occurring. The results of this analysis are presented in Table A2 and show that for all run conditions nucleate boiling was occurring at the critical point during burnout suggesting that a nucleate boiling burnout mechanism may be applicable to the data obtained.

7.4 Earlier Correlations

The correlations of GAMBILL (13) and VON GLAHN (12) (Section 2.3) are investigated using the Isceon data and the results are tabulated in Table A1.

For Gambill's correlation : $k' = 0.18$, $k'' = 0.023$ and the forced convection heat transfer coefficient, h_{GT}, is obtained using the approach of Guerrieri-Talty as suggested by Gambill. Fig.7.1 reveals that this correlation provides a poor estimate of the critical heat flux, all data being overpredicted by 25% and the majority by over 50%. It might be considered that this overprediction results from an error in the prediction of the heat transfer coefficient. Fig.7.2 compares h_{GT} with the experimental heat transfer coefficient derived, for non-boiling conditions (Table A2), from the relationship

$$h_{TP} = \frac{q}{(T_W - T_S)} \qquad \cdots\cdots\cdots (7.1)$$

and shows that h_{TP} is consistently under-predicted by at least 50%. Use of h_{TP} in place of h_{GT} in Gambill's correlation would result in an even greater over-estimation of the critical heat flux.

FIG 7.1 GAMBILL Correlation

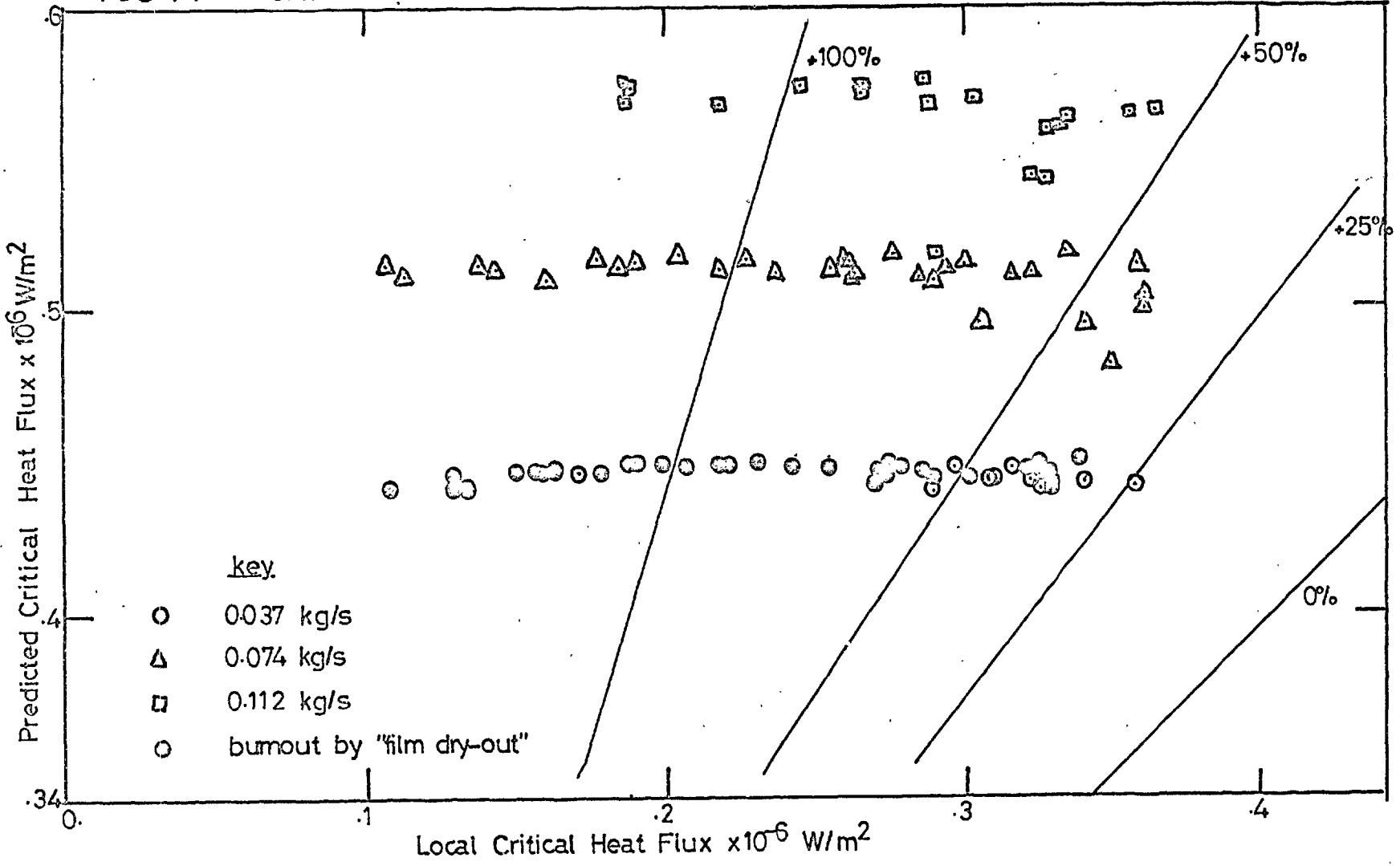
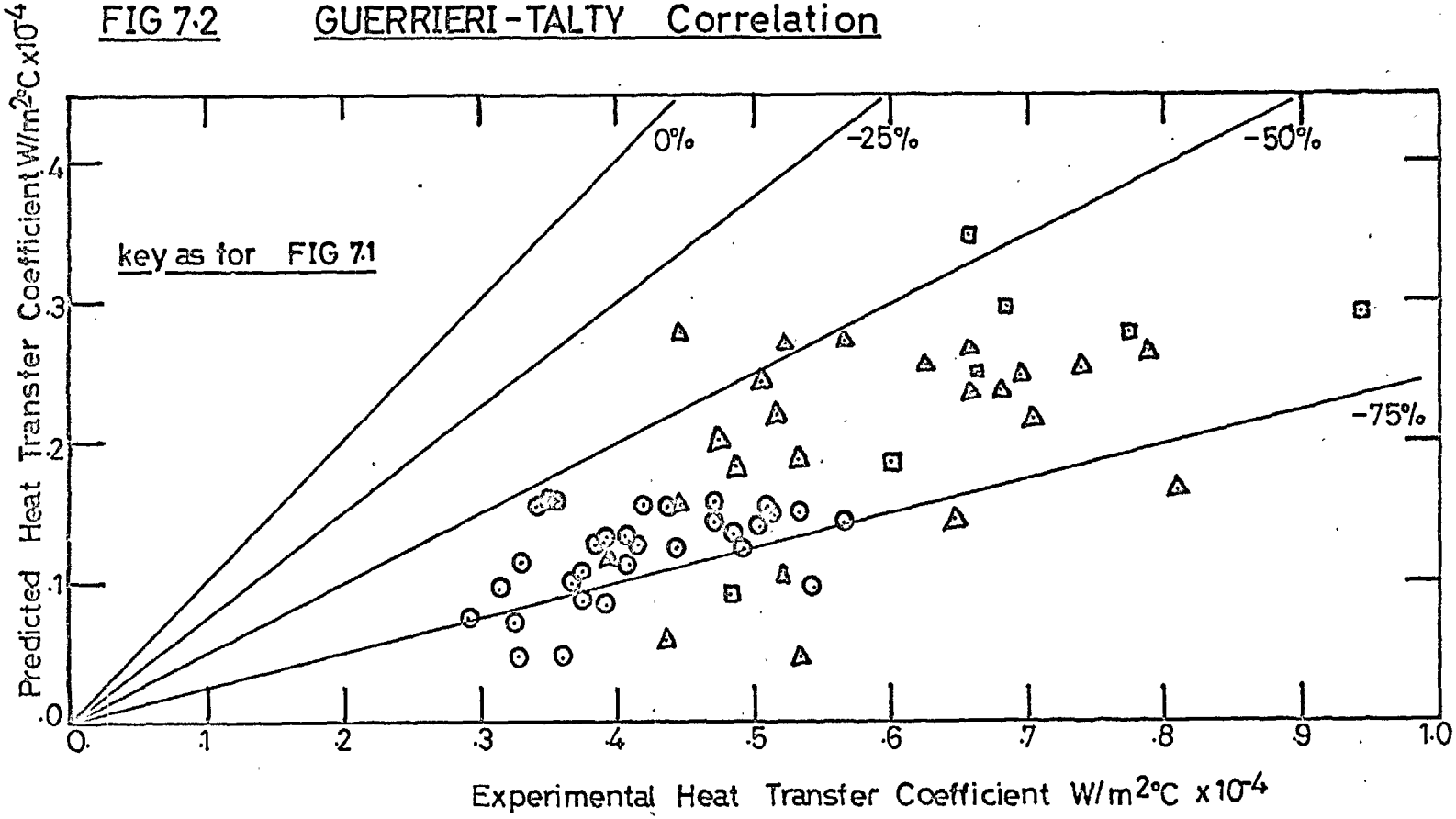


FIG 7·2 GUERRIERI-TALTY Correlation



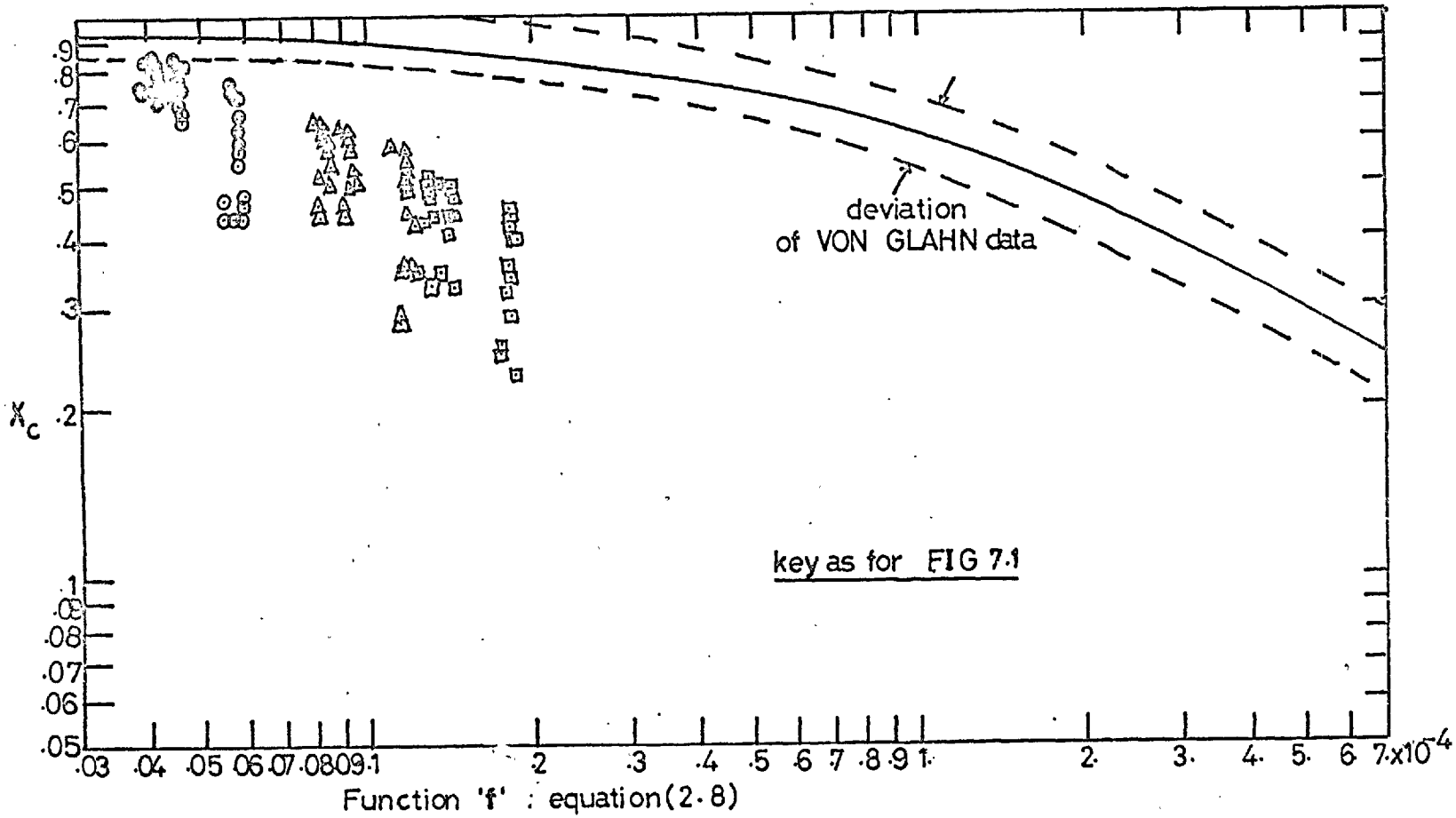


FIG 7·3 VON GLAHN Correlation

These large discrepancies confirm Gambill's expressed sceptiscism of the application of this model to saturated boiling conditions and suggest that his earlier success may have been fortuitous.

The correlation of Von Glahn is presented in Fig.7.3. A poor prediction of the experimental data is obtained and deviations from the predicted values similar those of benzene (Fig.2.3) are found, providing confirmation of the general observation that correlations are not applicable to liquids other than those for which they are developed.

7.5 Prediction Of Tube Wall Temperature At Burnout

Section 4.52 describes how the departure radius of the bubble may be approximately represented by

$$R_d = \frac{\delta_0^2 \rho_L \lambda U_b}{4 k_L \Delta T} \qquad (4.57)$$

for $U_b > 0.56\ U_L$, provided the bubble growth rate is not so small that We_b becomes less than $We_{b\ crit}$ without requiring a change of growth rate for departure.

This applies to bubbles growing in liquids whose depth is greater than R_d. However, if the liquid depth is less than R_d the bubble will depart when it grows to the size of the liquid film by bursting through the surface. This latter situation may well exist in the annular flow conditions studied here so that knowledge of the film thicknesses and liquid film velocities are necessary for a complete investigation.

To aid this an attempt was made to predict the film flow properties at the critical point from pressure gradient measurements using the approach described by MANTZOURANIS (1). His theory is presented in Appendix T1.

Not all runs could be analysed because of inaccuracies in the measured pressure gradients (see Section 5.2.4) but the data obtained are presented in Table 7.2. Using the data of run 522/9 the following procedure was adopted to determine the mode of bubble departure for the system.

(i) Determine the growth rate parameter, A, and then determine whether We_b falls below We_{crit} before any dry-spots form in the micro-layer.

(ii) Determine the bubble radius at departure by dry-spot formation (equation 4.57)

(iii) Compare this bubble radius with the film thickness.

The determination of the growth rate parameter, A, for the Isceon is identical to that used for water in Section 4.5.1. δ_0 is put equal to $\delta_{lam}/3$ corresponding to the approximate relationship found for water and the ratio U_b/U_L equal to 0.8. Under these conditions, A is found to be 0.009m/$s^{\frac{1}{2}}$.

The variation of We_b with time is shown in Fig.7.4 and shows that at no time during the constant growth rate phase does We_b drop below $We_{b\ crit}$. The estimated bubble departure time by partial microlayer dry-out is arrowed in the figure and corresponds to a bubble radius of 0.365×10^{-3}m. The film thickness is estimated to be 0.115×10^{-3}m, less than the estimated bubble radius, so that the film thickness acts as the departure criterion.

It has been proposed that burnout occurs when the temperature rise beneath a dry-spot exceeds the temperature fall by quenching (Section 4.6). With the bubble departure controlled by the film thickness, it is suggested that the heat flux required to raise the wall temperature sufficiently for a dry-patch to form before the bubble departs will also be sufficient to

FIG 7.4 Growth Of Isceon Bubble

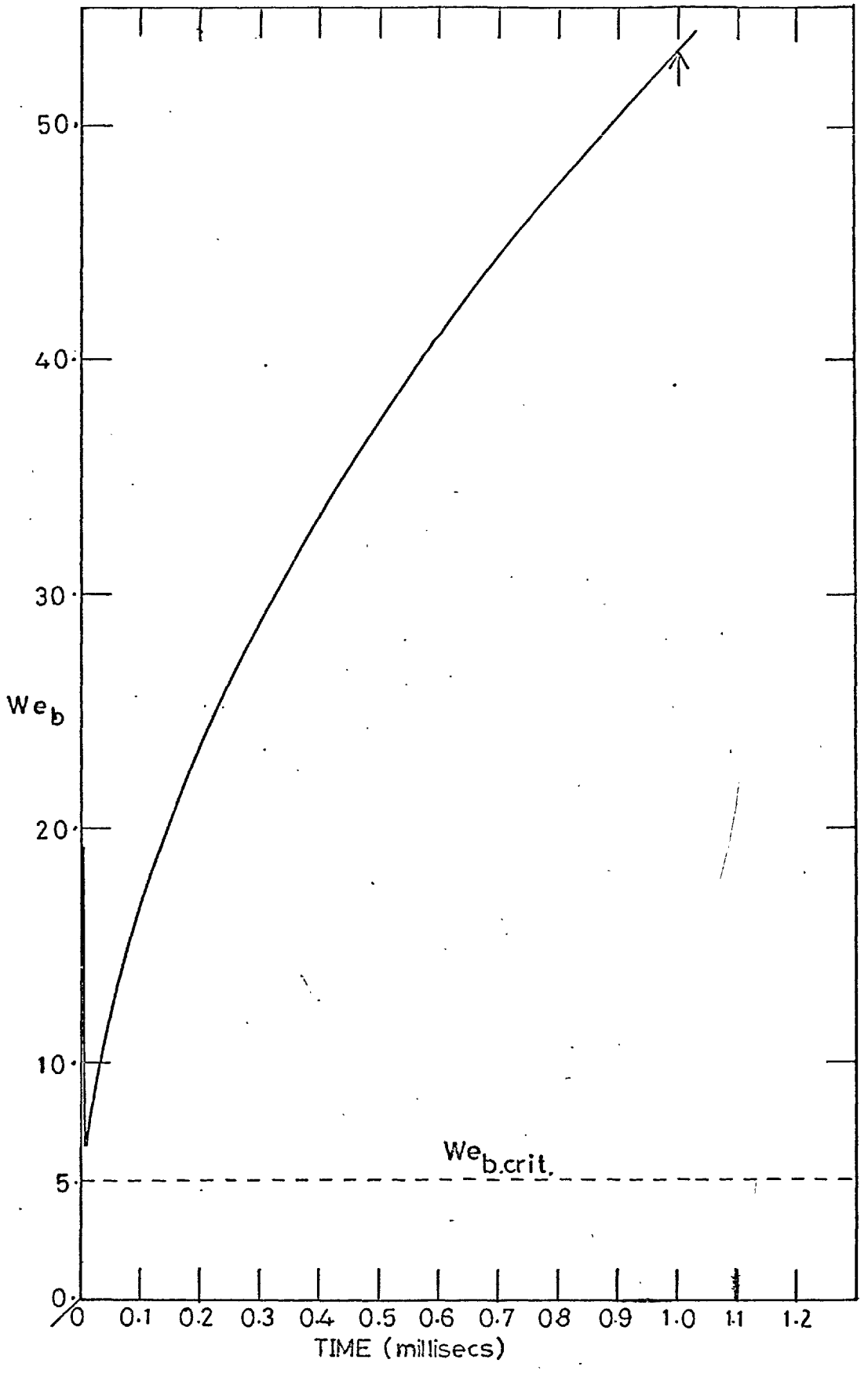
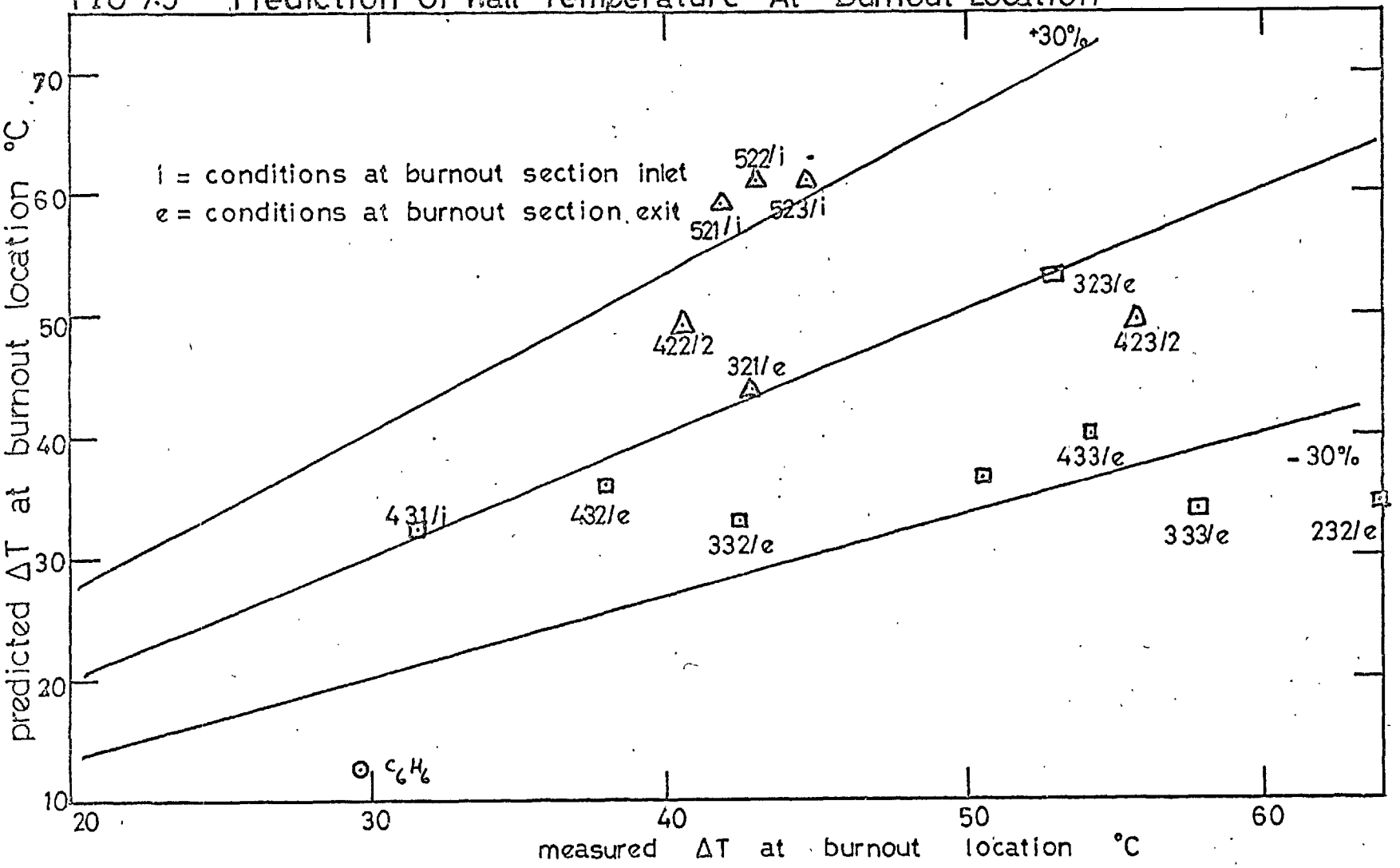


FIG 7.5 Prediction Of Wall Temperature At Burnout Location



precipitate burnout once the dry spot has been formed.

Putting $R_d = y_i$ in equation (4.57) and rearranging, the temperature difference at burnout is given by

$$\Delta T_{bo} = \frac{\delta_0^2 \rho_L \lambda U_b}{4 y_i k_L} \quad . \quad . \quad . \quad . \quad . \quad . \quad . \quad (7.2)$$

Estimates for ΔT_{bo} are obtained with $\delta_0 = \delta_{lam}/3$ and $U_b = 0.8U_L$. Because it is not known whether conditions at the inlet or exit to section 10 govern any given burnout, estimates for both conditions were obtained and the best values are presented in Fig.7.5.

Allowing for the experimental error in the measured value of ΔT of $\pm 2^{\circ}C$, all but values 333/e and 232/e are predicted to $\pm 30\%$. For these two runs the film thickness has values 0.29×10^{-3}m and 0.30×10^{-3}m respectively, the thickest films measured. It is possible that in these two instances the heat flux needed to obtain the calculated temperature difference is too small to cause burnout. The actual temperature difference would therefore be higher than the value calculated from the assumption that the film thickness is the governing departure criterion. A similar underestimate is obtained when prediction of ΔT for the single benzene film boiling value presented by BACKHURST (2) is attempted. In this instance the film thickness is even greater, 0.37×10^{-3}m.

7.6 A New Factor Affecting Critical Heat Fluxes With Non-Uniform Distributions Of Heat Fluxes

Figs. 7.7, 7.6 and 7.8 show how the critical heat flux for the Isceon data varies with the heat flux gradient, $\frac{dq}{dz}$, at the burnout point and demonstrate, for the majority of data analysed, that the critical heat flux

increases with $\frac{dq}{dz}$ at constant quality at all flowrates.

This effect has not previously been recorded but the data of ROHSENOW and TODREAS (29) provides evidence of a similar trend for water. Fig.2.7 presents their data not correlated by the total heat input approach of Fig.2.6. Reference to Fig.2.7 shows that at a constant quality, the critical heat flux for cosine distribution ($\frac{dq}{dz}$ negative) < that for linear increasing distribution ($M = 2.27$) < that for linear increasing distribution ($M = 5.75$) < that for peak at outlet distribution ($_M = 5.75$).

It is shown in Section 4.7 that these effects are not explained by the growth rate variation of bubbles sliding into the critical region. However in the last section, the critical wall temperatures for Iscoon are correlated from knowledge of the hydrodynamic properties of the liquid film and it may be the manner in which $\frac{dq}{dz}$ affects the liquid film dynamics which influences the magnitude of the local critical heat flux.

This effect can be investigated using the film thickness data presented in Table 7.2 as follows :

From Figs.7.6 - 7.8

$$q_{bo} \propto \left(\frac{dq}{dz}\right)_{bo} \quad . \quad . \quad . \quad . \quad . \quad . \quad (7.3)$$

At a fixed quality, an increase in the applied heat flux increases the wall temperature giving, as an approximation from equation (7.3)

$$\Delta T_{bo} \propto \left(\frac{dq}{dz}\right)_{bo} \quad . \quad . \quad . \quad . \quad . \quad . \quad (7.4)$$

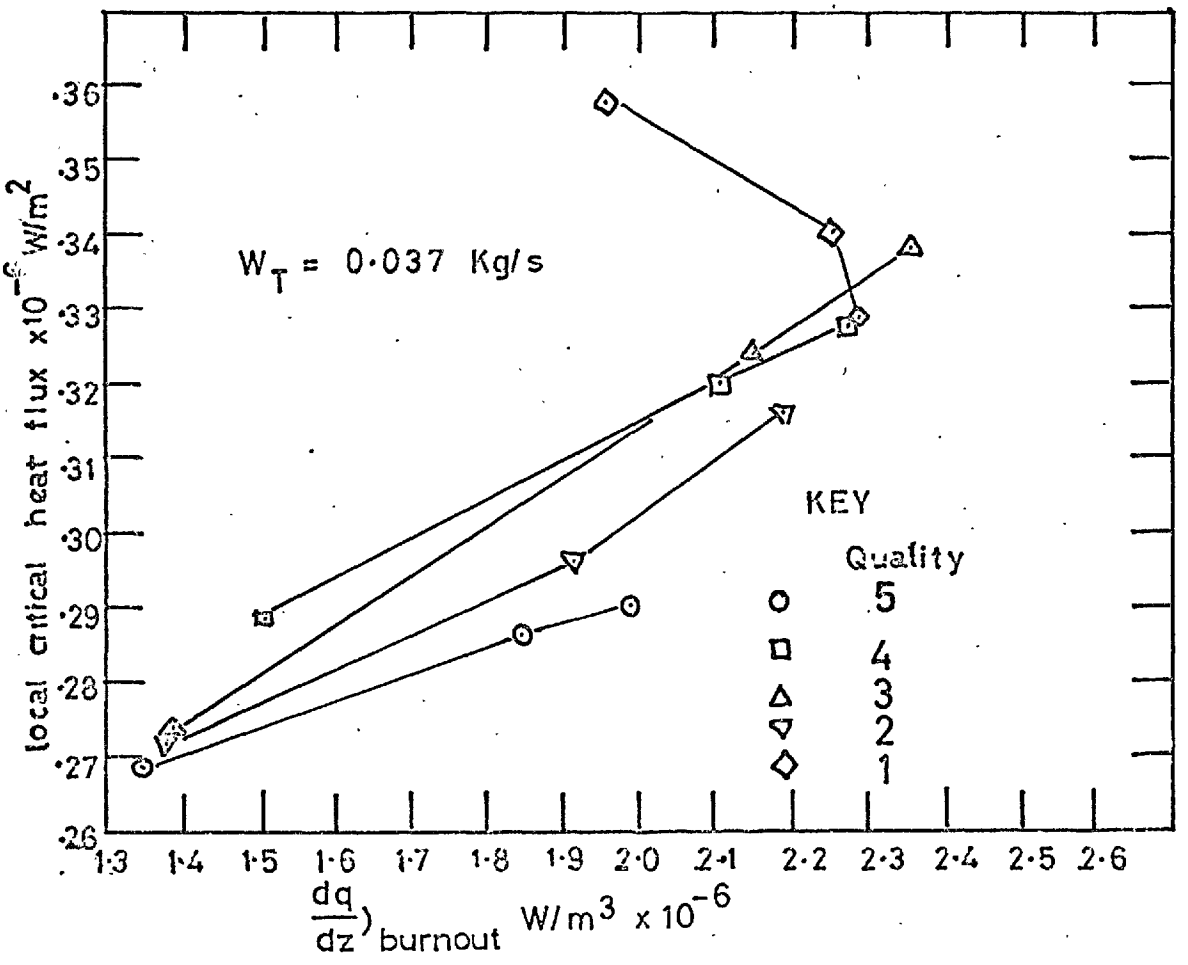
From equation (7.2)

$$\Delta T_{bo} \propto \frac{\delta_o^2 U_b}{y_i} \quad . \quad . \quad . \quad . \quad . \quad . \quad (7.5)$$

where

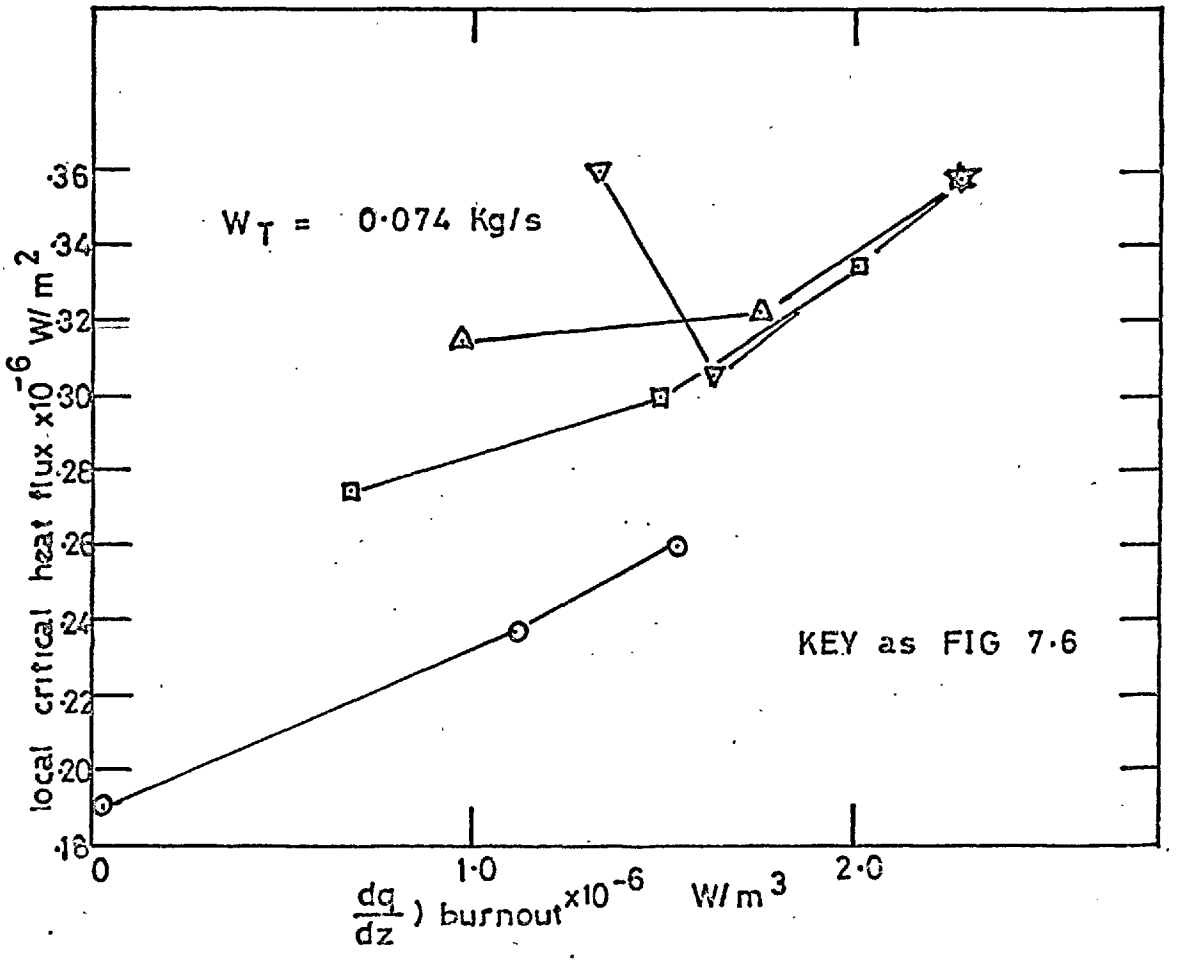
$$\delta_o \propto \delta_{lam} \quad . \quad . \quad . \quad . \quad . \quad . \quad (7.6)$$

FIG 7·6



Effect Of Heat Flux Gradient

FIG 7·7



Effect Of Heat Flux Gradient

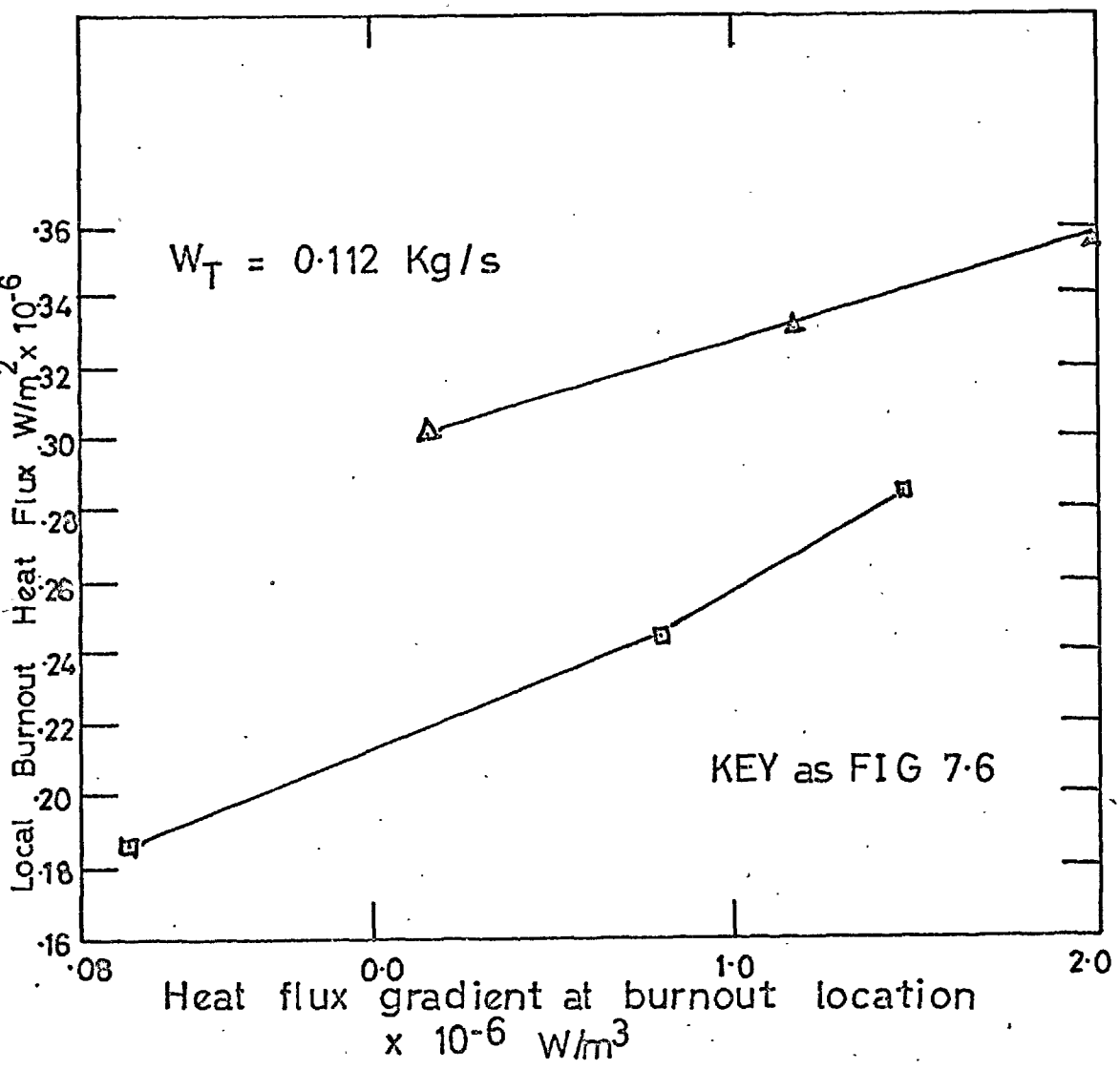
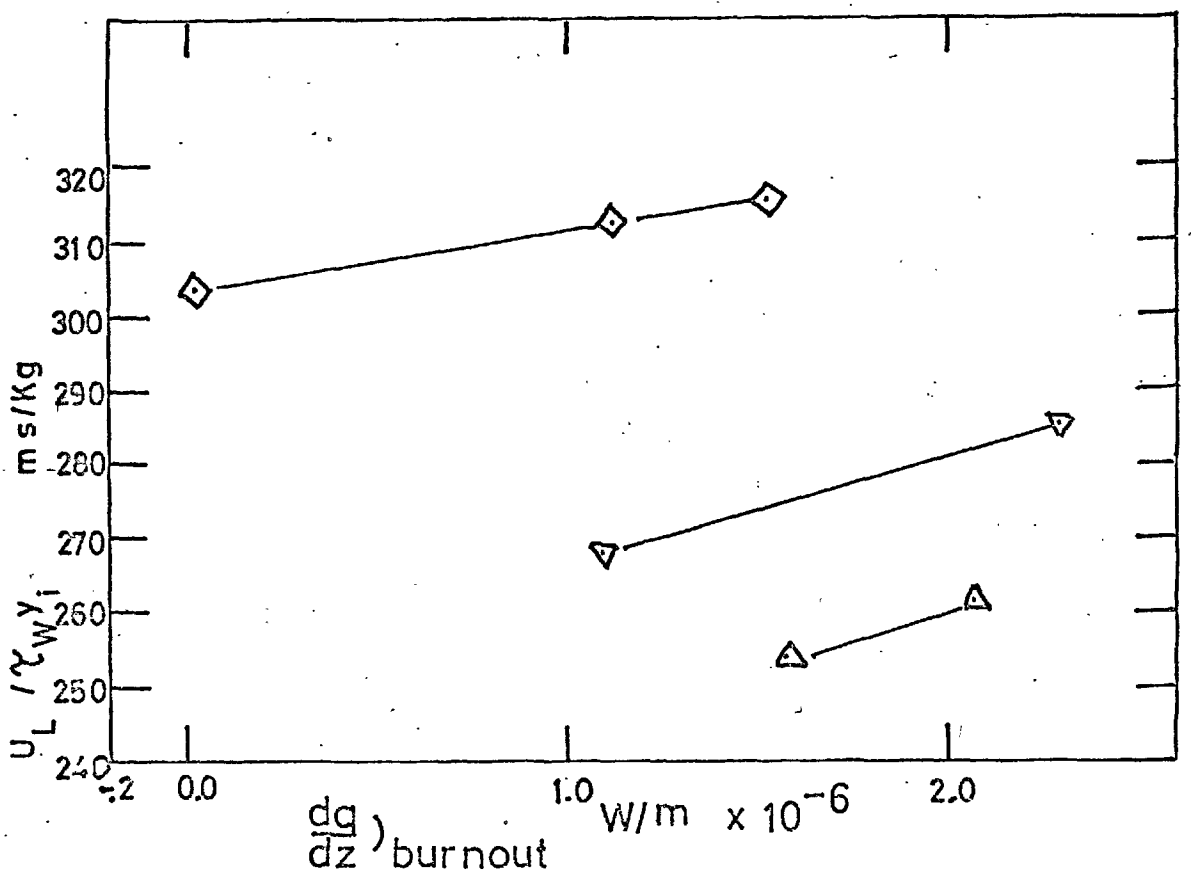


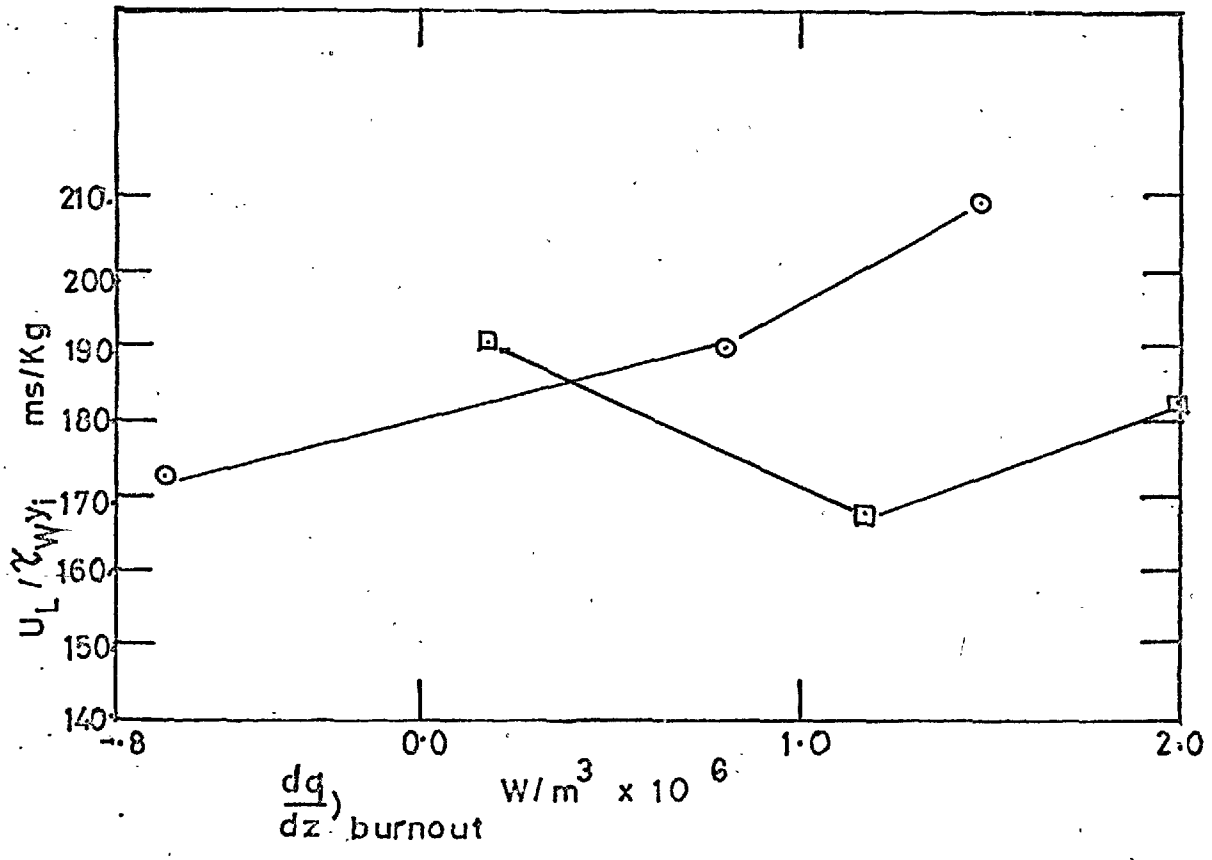
FIG 7.8 Effect Of Heat Flux Gradient

FIG 7·9



The Relationship Between $\frac{dq}{dz}$ And The Liquid Film Dynamics

FIG 7·10



The Relationship Between $\frac{dq}{dz}$ And The Liquid Film Dynamics

$$U_b \propto U_L \qquad (7.7)$$

and from Von Karman's velocity profile (Appendix T1)

$$\zeta^2_{lam} \propto \frac{1}{\tau_W} \qquad (7.8)$$

Substitution of equations (7.6) - (7.8) into (7.5) yields

$$\Delta T_{bo} \propto \frac{U_L}{\tau_W y_i}$$

or, from equation (7.4)

$$\left(\frac{dq}{dz}\right)_{bo} \propto \frac{U_L}{\tau_W y_i} \qquad (7.9)$$

Figs.7.9 and 7.10 show that this relationship holds for the Isceon data. This confirms the conclusion that the dependence of q_{bo} on $\left(\frac{dq}{dz}\right)_{bo}$ in annular flow is related to variation of the liquid film dynamics and it is suggested that this variation probably results from the influence of both q and $\frac{dq}{dz}$ on the acceleration of vapour in the core of the tube.

7.7 Conclusions

a) The correlations of Von Glahn and Gambill are inadequate to predict the critical heat flux data obtained for Isceon 113.

b) A comparison between the estimated bubble departure diameter by partial microlayer dry-out and the liquid film thickness derived from a MANTZOURANIS analysis, indicates that in the majority of the cases analysed, bubble departure is controlled by the dimensions of the liquid film.

c) The burnout wall temperatures are predicted to $\pm$ 25% for the majority of the data points using the film thickness as the departure criterion. Two points for Isceon and one for benzene are not predicted but in these

instances the film thickness has ceased to be the departure criterion.

d) For non-uniform heat flux distributions the heat flux gradient, $\frac{dq}{dz}$, at the critical point is an important factor influencing the value of the critical heat flux. The larger $\frac{dq}{dz}$ the higher is q_{bo} at a given quality. Careful analysis of the data of Todreas has revealed a similar trend for water. The effect of $\frac{dq}{dz}$ is related to its influence on the acceleration of the vapour core in annular flow which results in a variation of the dynamics of the liquid film.

FIG 7.11 Critical Heat Flux Data

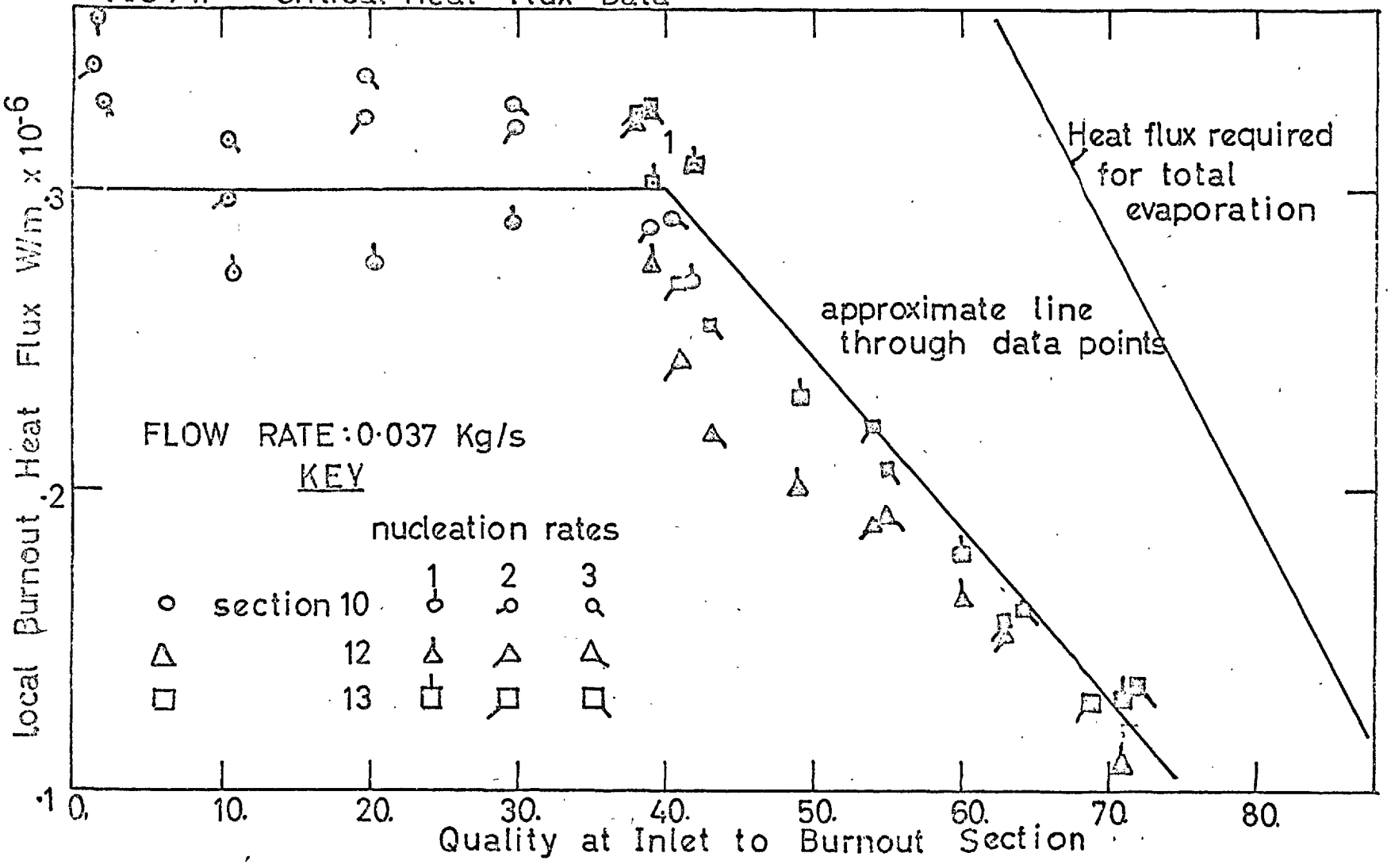


FIG 7·12 Critical Heat Flux Data

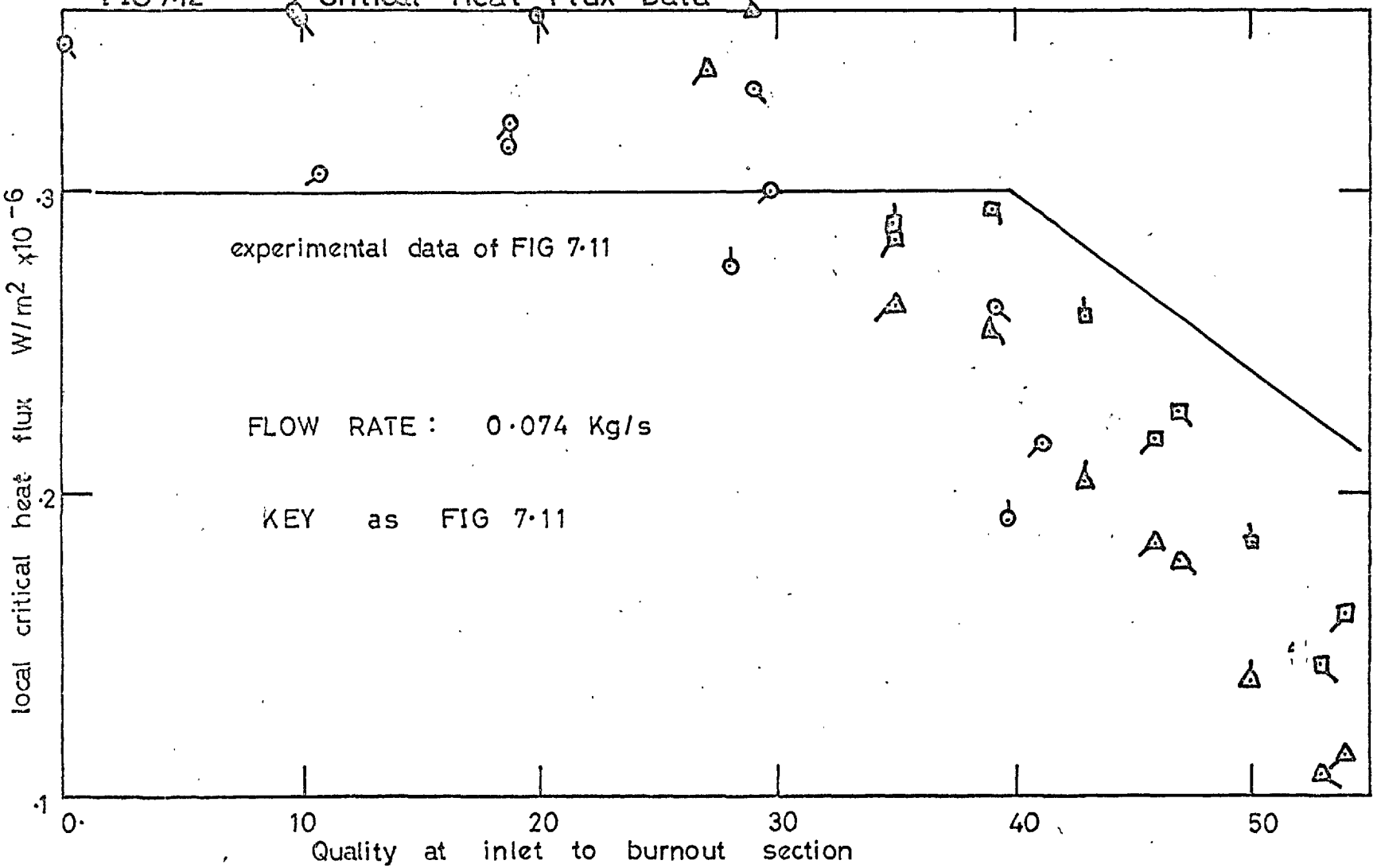


FIG 7·13 CRITICAL HEAT FLUX DATA

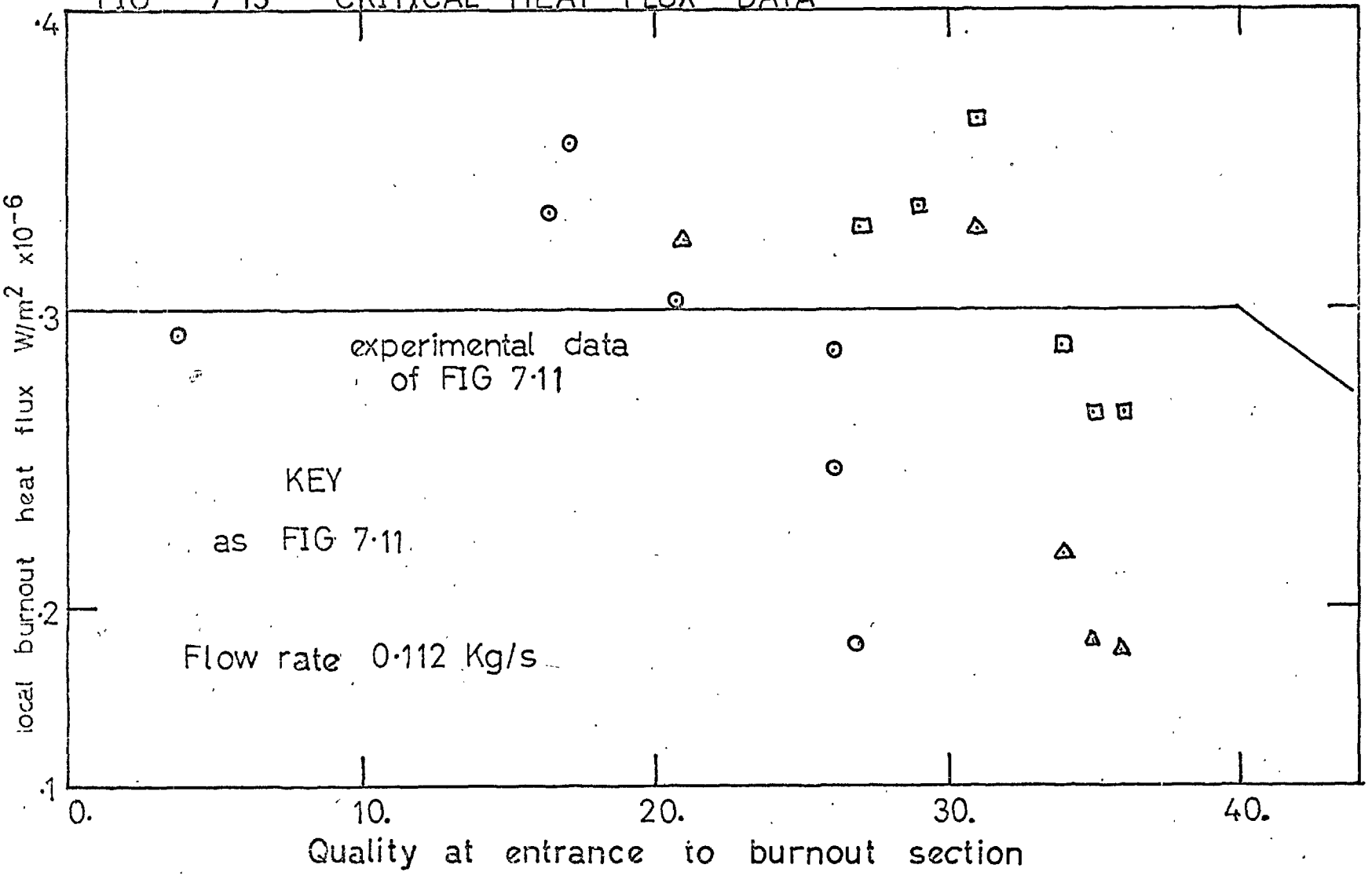


TABLE 7.1 EXPERIMENTAL BURNOUT DATA

Run No.	G_T Kg/s	INLET QUALITY SEC.10	CRITICAL HEAT FLUX $W/m^2 \times 10^{-6}$ 10	12	13	OUTLET QUALITY AT CRITICAL SECTION 10	12	13
511	0.037	0.42	0.269*	0.109*	0.131*	0.71	0.81	0.83
512	0.038	0.39	0.286*	0.130*	0.129*	0.69	0.81	0.81
513	0.037	0.41	0.290*	0.134*	0.134*	0.72	0.85	0.85
411	0.038	0.30	0.269*	0.164*	0.179*	0.60	0.76	0.77
412	0.038	0.30	0.320*	0.151*	0.157*	0.63	0.78	0.78
413	0.038	0.30	0.328*	0.159*	0.161*	0.64	0.80	0.80
311	0.038	0.20	0.274	0.200*	0.231*	0.49	0.68	0.72
312	0.038	0.20	0.324*	0.188*	0.221*	0.54	0.72	0.75
313	0.038	0.20	0.338*	0.191*	0.207*	0.55	0.73	0.75
211	0.038	0.11	0.272	0.274*	0.301*	0.39	0.65	0.68
212	0.039	0.10	0.296	0.242*	0.279*	0.41	0.64	0.68
213	0.039	0.10	0.316	0.218*	0.255*	0.43	0.64	0.67
111	0.036	0.02	0.358	0.308	0.309	0.42	0.74	0.74
112	0.037	0.01	0.340	0.322	0.325	0.38	0.70	0.70
113	0.036	0.02	0.325	0.327	0.327	0.39	0.72	0.72
521	0.076	0.40	0.190	0.138	0.184	0.50	0.56	0.59
522	0.074	0.41	0.237	0.113	0.160	0.54	0.60	0.62
523	0.076	0.39	0.261	0.107	0.143	0.53	0.58	0.60
421	0.077	0.28	0.275	0.204	0.259	0.43	0.52	0.55
422	0.076	0.30	0.300	0.184	0.218	0.46	0.55	0.56
423	0.076	0.30	0.334	0.177	0.227	0.47	0.55	0.58
321	0.078	0.19	0.315	0.262	0.289	0.35	0.47	0.49
322	0.078	0.19	0.322	0.263	0.284	0.35	0.48	0.49
323	0.075	0.20	0.358	0.255	0.294	0.39	0.52	0.54
221	0.076	0.09	0.360	0.360	undet	0.29	0.47	0.47
222	0.075	0.11	0.340	0.340	undet	0.27	0.44	0.45
223	0.076	0.10	0.358	undet	undet	0.29	0.47	0.47
121	0.075	0.01	undet	undet	undet	0.21	0.40	0.40
122	0.075	0.01	undet	undet	undet	0.21	0.40	0.40
123	0.075	0.01	0.349	undet	undet	0.20	0.38	0.38
531		No results - conditions unstable						
532		No results - conditions unstable						
533		No results - conditions unstable						
431	0.118	0.27	0.186	0.217	0.287	0.34	0.39	0.42
432	0.118	0.26	0.245	0.188	0.265	0.35	0.41	0.43
433	0.118	0.26	0.285	0.186	0.265	0.36	0.42	0.45
331	0.120	0.21	0.302	undet	0.363	0.31	0.43	0.43
332	0.230	0.16	0.331	undet	0.327	0.27	0.39	0.37
333	0.118	0.17	0.355	undet	0.334	0.29	0.41	0.40
231	0.115	0.09	undet	0.326	undet	0.31	0.33	0.34
232	0.115	0.09	undet	0.322	undet	0.21	0.32	0.34
233	0.120	0.04	0.290	undet	undet	0.13	0.25	0.25
131	0.112	0.00	undet	undet	undet	0.13	0.26	0.26
132	0.112	0.00	undet	undet	undet	0.13	0.26	0.26
133	0.112	0.00	undet	undet	undet	0.13	0.26	0.26

undet = burnout undetected or outside range of applied heat flux.
* = burnout by film dry-out.

TABLE 7.2

DATA FROM MANTZOURANIS ANALYSIS

Run No		Lam.b.l. Thickness $\times 10^5$ m	Mean Film Vel m/s	Film Thickness $\times 10^3$ m	Critical ΔT ^oC	τ_W N/m^2	$(\frac{dq}{dz})_c \times 10^{-6}$ W/m^3	Est. ΔT ^oC
522	9	0.516	3.81	0.115	43.1	106	1.108	60.5
	10	0.458	3.82	0.064		135		
521	9	0.586	3.38	0.135	41.9	82.3	.018	59.0
	10	0.553	3.32	0.091		93.1		
523	9	0.583	3.35	0.127	44.8	83.1	1.53	61.0
	10	0.467	3.80	0.067		131		
422	9	0.672	3.08	0.194	40.6	62.3	1.59	49.0
	10	0.498	3.82	0.097		114.0		
423	9	0.598	3.40	0.168	55.8	76.6	2.08	49.5
	10	0.451	4.10	0.081		136		
321	9	0.641	3.32	0.212		68.8		
	10	0.540	3.80	0.146	42.8	97.7	0.97	44.0
431	9	0.430	5.2	0.202	31.6	148.	-.67	32.5
	10	0.433	4.95	0.177		142.		
432	9	0.489	4.60	0.244		113.		
	10	0.431	5.09	0.181	37.9	147.	0.8	36.0
433	9	0.466	4.80	0.227		124.		
	10	0.387	5.54	0.142	54.1	183	1.47	40.0
331	9	0.409	5.37	0.172		164.		
	10	0.402	5.49	0.167	50.6	172.	.16	36.5
332	9	0.478	4.76	0.241		121.		
	10	0.433	5.23	0.204	42.4	150.	1.17	33.0
333	9	0.518	4.42	0.290		101.		
	10	0.413	5.37	0.185	57.9	160.	2.0	34.0
232	9	0.632	3.54	0.297		68.7		
	10	0.502	4.43	0.220	64.0	110.	1.69	34.5
323	9	0.745	2.87	0.271		49.6		
	10	0.509	3.93	0.129	53.0	107.	2.28	53.0

CHAPTER EIGHT

CONCLUSIONS

A new model describing the growth and dynamics of bubbles on a heating surface in forced flow systems is presented and is extended to include the mechanism for the onset of burnout.

The shape of a bubble growing on a surface immersed in a flowing liquid is governed by the interaction of an inertial force.

$$F_I = 2\pi R_b^2 \rho_L \left(\frac{27}{32} U_b U_L - \frac{11}{64} U_b^2 - \frac{27}{64} U_L^2 + \frac{3}{4} \dot{R}_b^2 + \frac{R_b \ddot{R}_b}{2}\right) \qquad (4.32)$$

tending to flatten the bubble against the surface, and a surface tension force, for convenience given the value $2\ R_b$, tending to form the bubble into a sphere. The ratio of these two forces, We_b, where

$$We_b = \frac{R_b \rho_L}{\sigma} \left(\frac{27}{32} U_b U_L - \frac{11}{64} U_b^2 - \frac{27}{64} U_L^2 + \frac{3}{4} \dot{R}_b^2 + \frac{R_b \ddot{R}_b}{2}\right) \qquad (4.48)$$

can be used to determine whether the bubble is spherical or hemispherical; if We_b exceeds 5 an approximately hemispherical bubble is formed. The inertial pressure force keeps hemispherical bubbles close to the surface, but acts to cause spherical bubbles to depart. Earlier observations of boiling show that hemispherical bubbles grow with applied heat fluxes greater than 1/10 of the critical value and that for bulk liquid velocities exceeding 15 cm/s, the bubbles slide along the heater surfaces at approximately 8/10 of the mean stream velocity.

Spherical bubbles grow by evaporation from the superheated boundary layer which forms close to any heating surface. Hemispherical bubbles however, grow by evaporation from a thin layer of liquid or microlayer, which forms at the bubble base. For both bubble shapes $R_b \propto t^{\frac{1}{2}}$ during the growth

period, but the constant of proportionality is much greater for hemispherical bubbles. Analysis of GUNTHER's data (11) for hemispherical bubbles shows that the microlayer thickness, is approximately a third of the laminar boundary layer thickness.

Two basic mechanisms exist for the departure of bubbles from the heating surface in boiler tubes :

1) In annular flow where thin liquid films exist, the bubbles depart when they grow to the magnitude of the film.
2) In liquids of greater depth, departure occurs under the action of hydrodynamic forces when the bubbles become spherical.

Bubbles which are hemispherical soon after their initiation become spherical later in their growth period by one of two mechanisms : Either

a) their growth rate is small so that We_b falls below its critical value or
b) their growth rate is high initially but is suddenly reduced by partial dry-out of the microlayer, again causing We_b to fall below its critical value.

Bubble departure occurs by 1) and 2b) at heat fluxes close to the burnout point.

This concept of partial micro-layer dry-out governing bubble departure correctly predicts the variations of bubble departure radius with flow velocity observed by GUNTHER (11) and KOUMOUTSOS et al (62) and results in the prediction equation

$$R_d = \frac{\delta_0^2 \rho_L \lambda \; U_b}{4 \; k_L \; (T_W - T_b)} \qquad \ldots\ldots\ldots (4.58)$$

The mechanism of the growth of hemispherical bubbles by microlayer

evaporation is readily extended to describe the onset of the critical condition in both constant heat flux and constant wall temperature systems. For systems with constant applied heat fluxes, burnout occurs when temperature increase beneath a dry spot under a bubble formed by partial dry-out of the microlayer exceeds the temperature drop by liquid quenching after bubble departure. As consecutive bubbles pass, thd wall temperature increases in an oscillatory manner by this mechanism, until the Liedenfrost temperature is exceeded, when stable film boiling occurs.

Extensive experimental data for burnout and heat transfer to 112-trichlorotrifluoroethane in a vertical boiler tube are presented to verify further this nucleate boiling mechanism for the precipitation of the critical condition and a large number of entrainment measurements confirm the presence of a liquid film at the critical point of sufficient thickness to support nucleation. The data also reveal an important new factor $\frac{dq}{dz}$, acting in the range 0 - 50% quality, which influences burnout in systems with non-uniform axial heat flux distributions, such that at a given quality an increase in $\frac{dq}{dz}$ at the burnout location increases the local critical heat flux.

A study of the hydronamics of liquid films in the boiler tube shows that $\frac{dq}{dz}$ influences the acceleration of vapour in the tube which in turn affects the dimensions of the liquid film; consequent change in the bubble dynamics is reflected in the change of the local critical heat flux.

This conclusion is confirmed by the successful prediction of wall temperatures at the critical point achieved for conditions where the bubble departure is controlled by the magnitude of the liquid film.

The burnout data presented was not predicted by earlier correlations presented by Von Glahn and Gambill.

Suggestions for Further Work

More experimental data and observations of forced convection boiling for a variety of liquid systems are required to confirm the mechanisms of bubble growth and dynamics presented in this thesis. Investigation of the influence of bubble and fluid velocities on the microlayer thickness should be attempted, possibly by an adaptation of the system presented by LLOYD (47) for pool boiling.

Direct observations and further measurement of nucleate boiling burnout in annular flow are required to verify the influence of the liquid film thickness on the critical heat flux and wall temperature. A combination of this information with an analysis of the relationship between applied heat fluxes and heater wall temperatures in boiler tubes would enable the extension of the partially qualitative burnout model presented in this thesis to a complete quantitative prediction of boiling burnout heat fluxes under all the hydrodynamic conditions in which nucleation might occur.

Two data points for stable film boiling in benzene/toluene mixtures presented by BACKHURST (2) suggest that an extensive study of binary systems with their added variables arising from concentration changes, would yield valuable confirmatory data for nucleate boiling and burnout models.

APPENDICES

APPENDIXES

Exporimental

E.1 Calibration of Tube Wall Thermocouples

These thermocouples were calibrated for use with a variable reference junction. Two vacuum flasks containing transformer oil were used for the hot and cold junction. Each oil bath was well stirred and heated by a 0.5 kW immersion heater to maintain a temperature difference of about $20^{\circ}C$ between the two junctions. A calibrated mercury thermometer indicated the temperature of the bath to $\pm 1/20^{\circ}C$ and the output from each thermocouple was recorded by a Honeywell 16-point recorder (described in Section 5.2) on the 0 - 1 mV range to an accuracy of $\pm 3\mu V$. The vacuum flasks reduced the cooling rate of each bath sufficiently not to necessitate the use of a temperature controller for the calibration.

The calibration was repeated until it was reproducible. 21 values were taken for the final calibration in the range of hot junction temperatures from $20^{\circ}C$ - $140^{\circ}C$. A linear best fit line through these values, based on the suggested relationship of MANTZOURANIS (1) gave the following calibration curve

$$\frac{\Delta E}{T_H - T_C} = 0.03954 + 4.61 \times 10^{-5} (T_H + T_C) \quad . \quad . \quad (E1.1)$$

where T_H = hot junction temperature, $^{\circ}C$.

and T_C = cold junction temperature, $^{\circ}C$.

ΔE = thermal EMF, mV

The wall temperature was corrected for the depth of the thermocouple tip below the tube surface (Fig. 5.2) by the addition of a factor,

calculated from the heat flux, $3.02 \times 10^{-4} q\ ^{\circ}C$.

E1.1 Error in Estimate of Wall Temperature

For $T_H - T_C = 20^{\circ}C$:

Error in estimate of T_H from calibration curve = $\pm$ 0.5°C (99% confidence) and error derived from temperature measurement at calibration = $\pm$ 0.1°C and therefore total error in temperature estimate = $\pm$ 0.6°C.

A further error of $\pm$ 0.25°C was introduced in the measuring system for the experimental wall temperatures by changing the range from 0 - 1mV to 0 - 5mV on the multi-point recorder, Thus the experimental wall temperatures were accurate to $\pm$ 0.85°C.

E.2 Calibration of Travelling Thermocouple

The calibration of the thermocouple was achieved using an ice-pot (0.0°C) for the cold junction and heated transformer oil in a vacuum flask as the hot junction. The oil bath was well stirred and a 0.5 kW heater, connected across a controller using a thermister as a temperature sensor, maintained the oil bath temperature to within $\pm$ 1/10°C of the set temperature. The precise temperature of the hot junction was measured to $\pm$ 1/20°C by a previously calibrated thermocouple against a reference junction in an ice-pot (0.0°C). The voltage generated by the two thermocouples were measured to $\pm$ 1 μV using a Pye Universal Potentiometer.

A linear best fit line using these measured values gave the following calibration curve.

$$\Delta E = 0.1439 + 0.0339T + 0.0001T^2$$

The confidence limit for this equation at the 97.5% level is $\pm$ 0.03°C, which with the error in the temperature measurement of $\pm$ 1/20°C, gives the total

error in the temperature estimation using the calibration as $\pm$ 0.08°C.

E.3 Heat Losses

Two thermocouples were placed in the lagging of each of sections 1, 9, 10, and 13 of the test column as shown in Fig.5.2 and were connected so that one of the thermocouples acted as the cold junction and the other as the hot junction. The voltage generated by the pair of thermocouples was measured by a Pye Universal Potentiometer. A calibration for each pair of thermocouples was made by recording their thermal EMF for a number of different measured heat losses.

To derive the heat loss calibration, liquid Isceon was pumped through the test column at a known flowrate. Once the system had reached steady state, the liquid inlet and outlet temperatures were measured using the travelling thermocouple and the output from the four pairs of thermocouples recorded. From the liquid temperatures and flowrate, the total heat loss was calculated and, assuming that this heat loss was evenly distributed along the length of the column, the heat loss through one section, corresponding to the thermocouple measurements, was calculated as 1/13 of the total.

Heat losses were measured for several different liquid temperatures and flowrates, and the following calibration accurate to $\pm$ 0.5 W was obtained

Tube Section 1

$$\text{Heat loss (W)} = 6.4\ (\Delta E) + 0.5$$

Tube Section 9

$$\text{Heat loss (W)} = 5.6\ (\Delta E) + 0.6$$

Tube Section 10

$$\text{Heat loss (W)} = 4.7\ (\Delta E) + 0.5$$

Tube Section 13

$$\text{Heat loss (W)} = 6.1\ (\Delta E) + 0.5$$

where

ΔE = Thermal E.M.F. mV.

APPENDIX E4 PHYSICAL PROPERTIES OF ISCEON 113

1. Liquid Properties

1.1 Surface Tension σ_L

$$\sigma_L = 0.023 \left(\frac{214.1 - T}{189.1}\right)^{1.2} \quad N/m$$

T = deg.C

1.2 Density ρ_L

$\rho_L \times 10^{-3}$ Kg/m^3	Temp. T^oC
1.621	0.0
1.554	30.0
1.450	71.0
1.359	93.0

1.3 Viscosity μ_L

$\mu_L \times 10^3$ Ns/m^2	Temp. T^oC
0.497	48.2
0.442	60.0
0.395	71.1
0.356	82.2
0.322	93.3
0.293	104.4
0.268	115.6

1.4 Thermal Conductivity k_L

$k_L = 0.066$ W/m^oC

1.5 Specific Heat C_{PL}

$$C_{PL} = 980.4 \quad J/Kg^{\circ}C$$

2. Vapour Properties

2.1 Density ρ_V

ρ_V Kg/m^3	Temp. $T^{\circ}C$
7.709	49.0
10.743	60.0
14.642	71.0

2.2 Viscosity μ_V

$\mu_V \times 10^3$ Ns/m^2	Temp. $T^{\circ}C$
0.0101	15.6
0.0103	26.7
0.0106	37.8
0.0108	49.0
0.0111	60.0
0.0113	71.0
0.0116	82.0
0.0118	93.0
0.0120	104.0
0.0123	116.0

2.3 Thermal Conductivity k_V

$$k_V = 4186.8 \mu_V \left(\frac{C_{PV}}{4186.8} + \frac{2.48}{(MW)}\right) \quad W/m^{\circ}C$$

2.4 Specific Heat At Constant Pressure C_{PV}

$$C_{PV} = 711.7 \quad J/Kg^{o}C$$

3.0 General Properties

Critical temperature = 214.1 ^{o}C.

Molecular weight, MW = 187.52

3.1 Latent Heat Of Evaporation

$$\lambda = 2326\ (70.67 - 0.1584T) \quad J/Kg$$

$T = {}^{o}C$

3.2 Saturated Vapour Pressure P_s

$$P_s = 133.32 \exp\left(16.100398 - \frac{2686.376}{T + 236.219}\right) \quad N/m^2$$

T = sat. temperature, ^{o}C.

1 bar = $10^5\ N/m^2$

E.5 Analysis of Entrainment Flowrate

The entrainment mass flowrate is obtained from measurements of sampling rate and impact pressure using a fixed probe technique. Examples of the variation of the measured impact pressure with the sampling rate are shown in Fig.E5.1 and E5.2 where the sampling rate at point B (Fig.E5.1) represents the entrained mass flowrate. To reduce the amount of experimental work necessary to obtain the point B, it is proposed to test the assumption that the gradients of lines AB and BC (Fig.E5.1) are constant for all runs and to ascertain the possible error introduced by such an assumption.

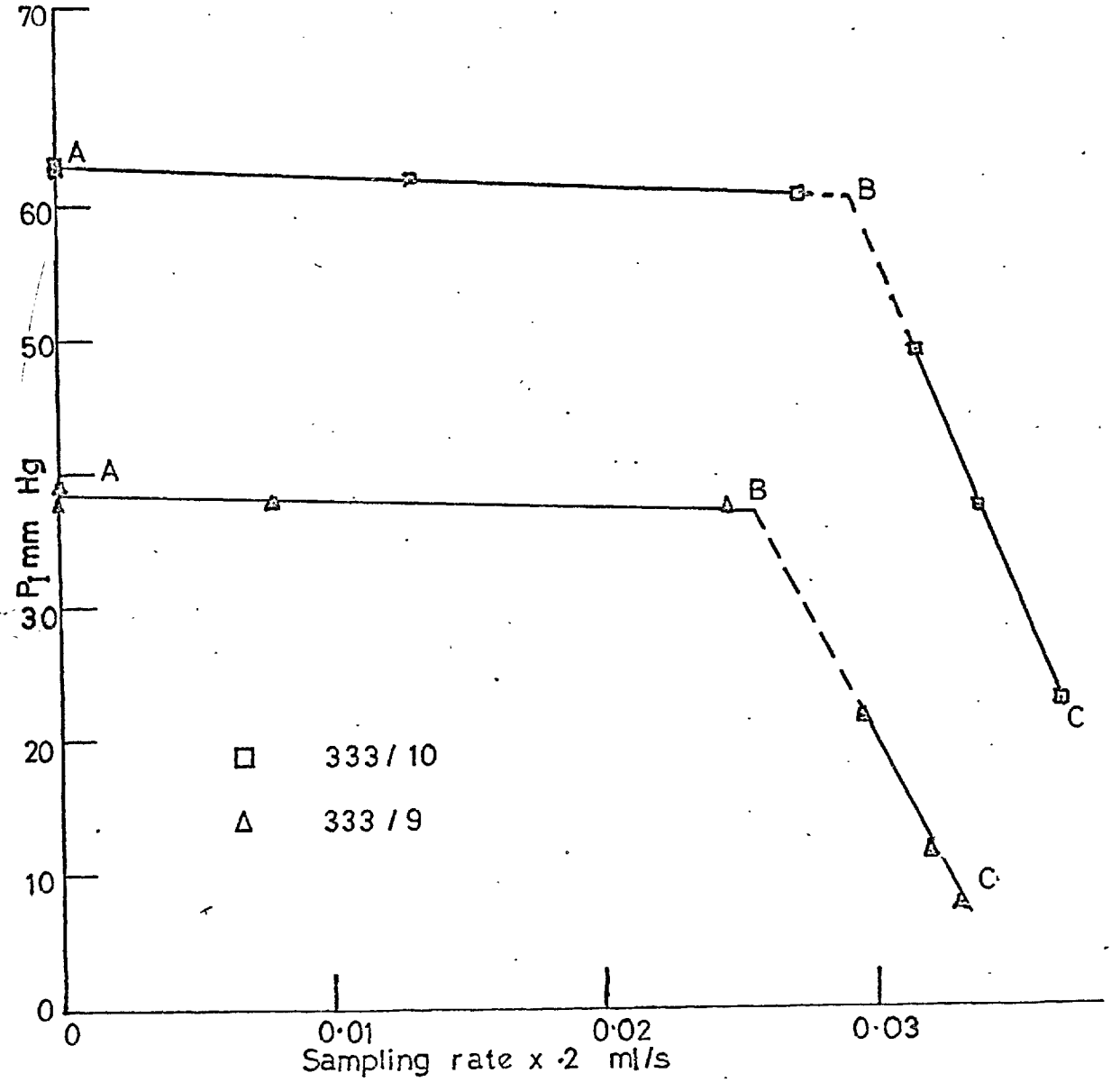
E.5.1 Test of Constant Gradient for Line AB

The main results from the statistical analysis conducted on the five runs investigated are shown in Table E 5.1 and the distribution of the gradients of the line AB about their mean is shown in graphical form in Fig.E 5.3.

The 'F' test shows that the maximum estimated error variance is not significantly greater than the population variance at the 5% level. This strongly supports the hypothesis of constant gradient and it is concluded that the distribution of the points about their mean value is due solely to experimental error and that the hypothesis for constant gradient to the line AB for five points investigated is proved within the limits imposed by experimental error.

The range of impact pressures for which this result has been obtained includes nearly all the values obtained for other run conditions and it is judged that measurement of the impact pressure is sufficient to define the line AB for all runs.

FIG E5·1



Entrainment Measurement

FIG E5·2 ENTRAINMENT MEASUREMENTS

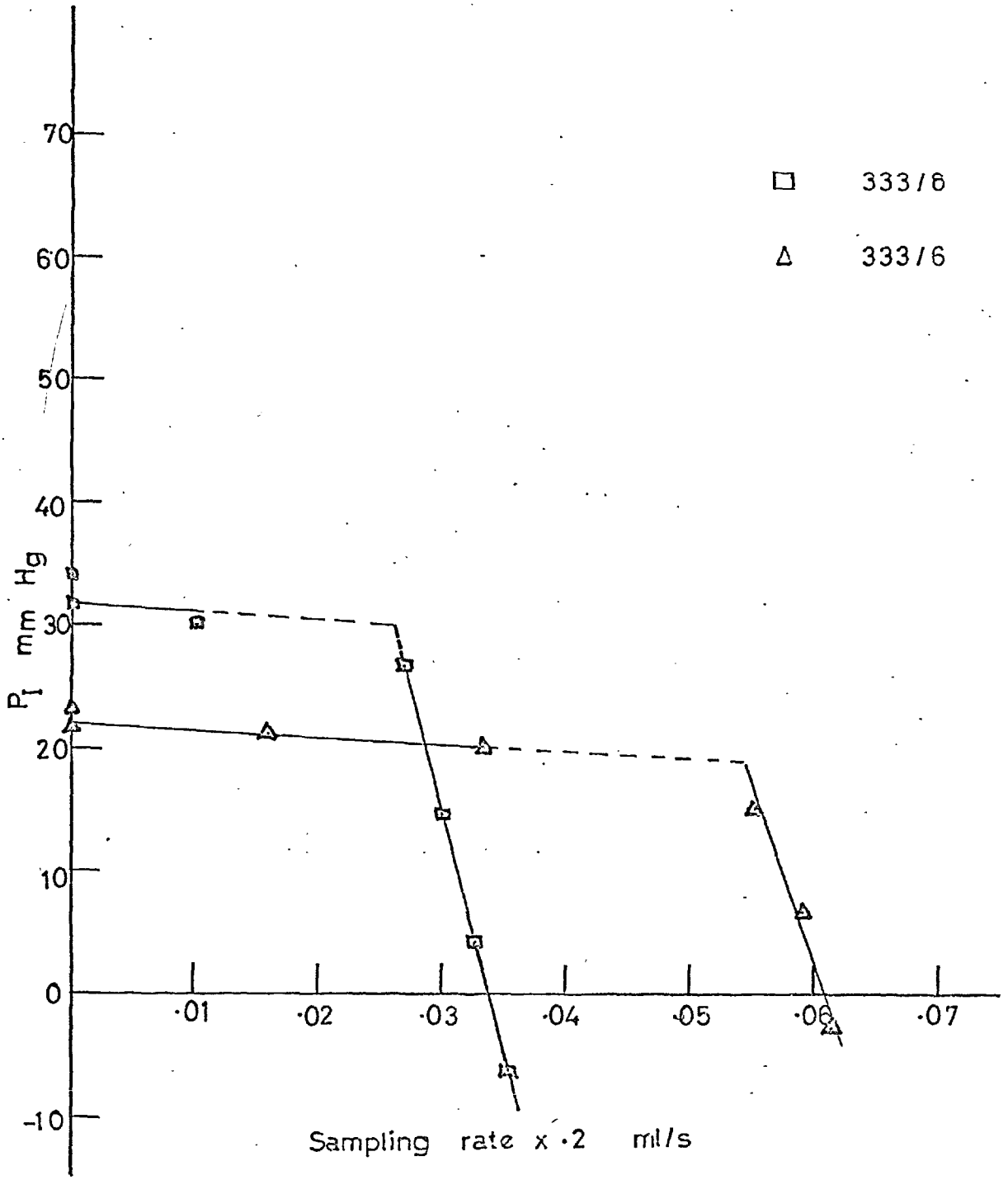
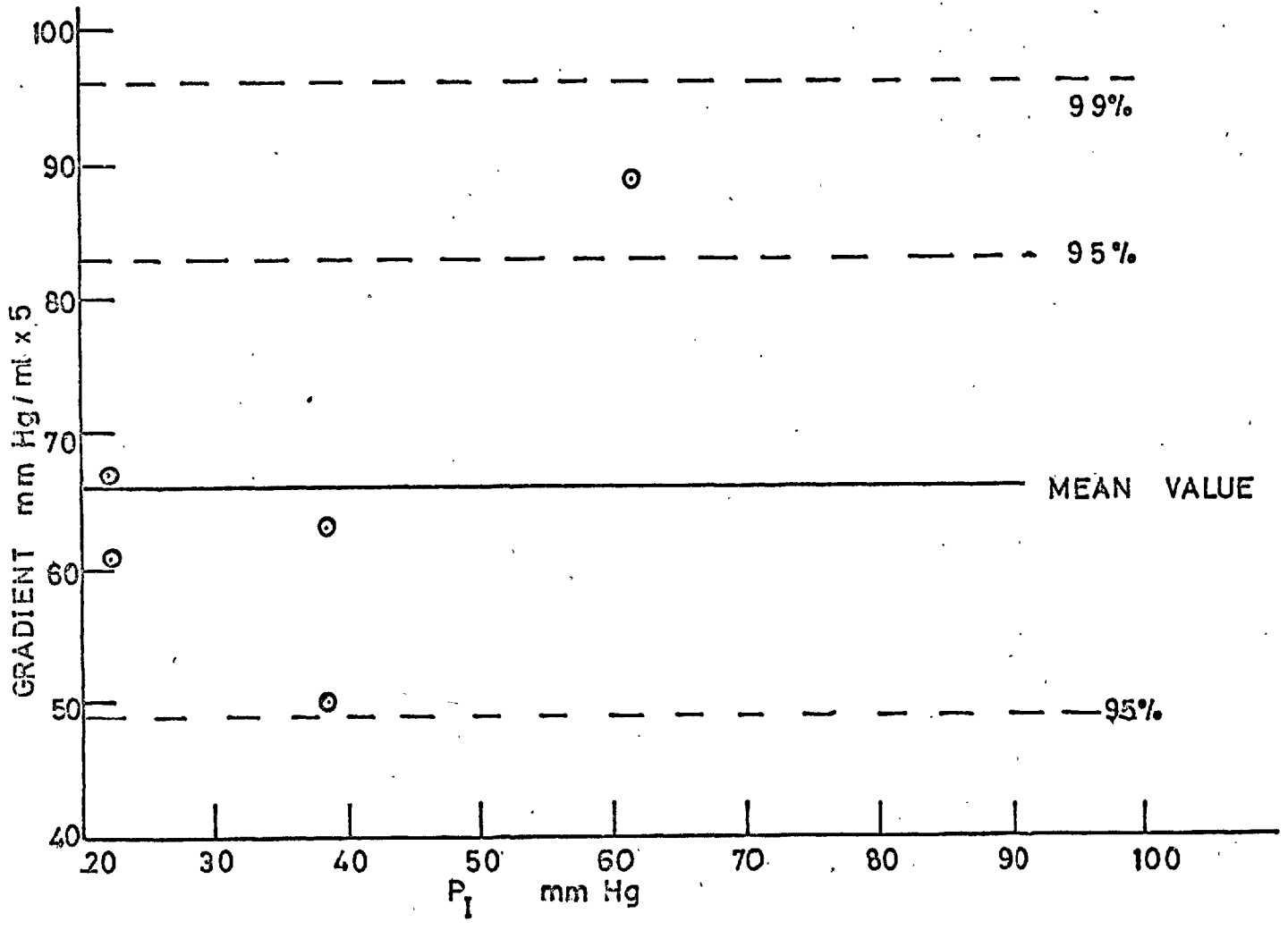


FIG E5·3 Gradient Line AB



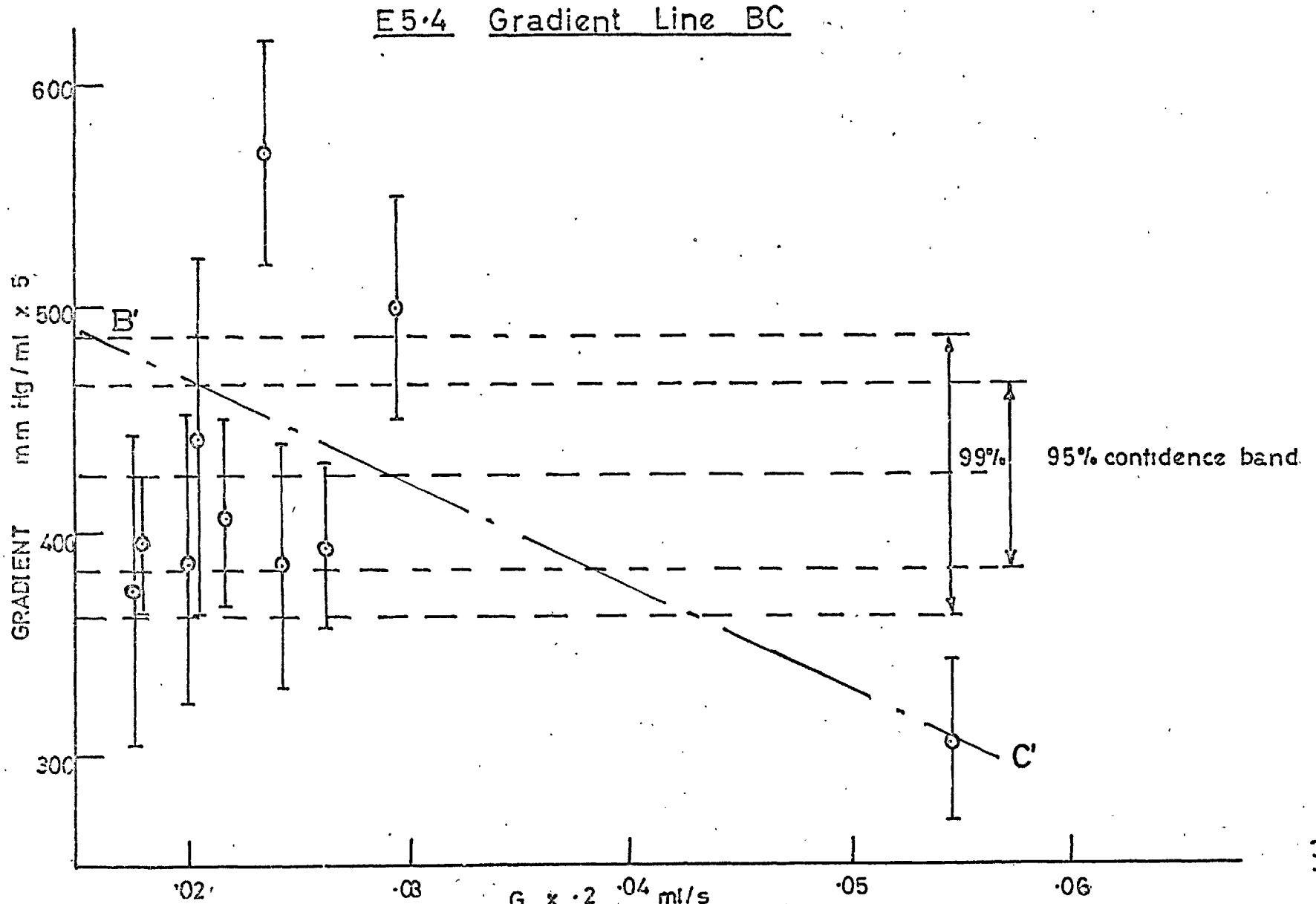

E5·4 Gradient Line BC
600
500
400
300
GRADIENT mm Hg / ml x 5
B'
C'
99%
95% confidence band
·02
·03
·04
·05
·06
G_p x ·2 ml/s

TABLE E 5.1

THE MAIN RESULTS FROM THE STATISTICAL ANALYSIS TO TEST THE CONSTANT GRADIENT HYPOTHESIS

	Test on Gradient AB	Test on Gradient BC
Mean Value of Gradient mm Hg. s./ml x 5	66	4170
Variance (σ_1^2)	255 (4)	56.39×10^4 (9)
Maximum Estimated Experimental Error Variance (σ_2^2)	1240 (4)	1.63×10^4 (9)
$\frac{\sigma_2^2}{\sigma_1^2}$ 'F' Test	4.86	34.3
Significance of 'F' Test	5% NS, 1% NS	5% S, 1% S
Confidence Limit ± 95%	17	460
Confidence Limit ± 99%	30	700

Notes : Variance; the number in brackets following the estimates of variance indicates the number of degrees of freedom on which the estimate is based

Significance; S = significant

NS = not significant

The preceding percentages indicate the level at which the significance was tested.

Fig.E 5.3 shows no obvious trend of the gradient with impact pressure so it is not considered necessary to take further readings in amplification of the conclusion of the constant gradient analysis.

E.5.2 Test of Constant Gradient for Line BC

Ten values for the gradient of line BC were used to analyse the hypothesis. The main results of the analysis are shown in Table E 5.1 and the variation of these points with the corresponding estimated sampling rate, G_e, at the intercept, B, is shown in Fig.E 5.4.

The 'F' test shows that the population variance is significantly greater than the estimated error variance at the 1% level which suggests the existence of a better correlation for the points than that proposed. The distribution of the points in Fig.E 5.4 shows that a better correlation may exist along the line B'C', shown dashed, and the maximum deviation between this correlation and that of the constant gradient hypothesis is -4%. Examination of the reproducibility of the results (Section 6.6) shows a deviation of $\pm$ 4% so that an improvement in the correlation to B'C' could have shown an improvement in the overall estimate of G_e from $\pm$ 8% to $\pm$ 4%. However, these entrainment measurements are made so that an estimate of the total entrainment can be obtained assuming a uniform mass velocity distribution across the tube. This assumption introduces further errors (Section 6.3) and the assumption of constant gradient was therefore considered to be justified despite the analysis indicating the possibility of a better correlation.

E 5.3 Conclusion of Analyses

The analyses of the previous two sections show that the variation

of pressure drop with sampling rate may be represented by two straight lines of constant gradient for all runs. Entrained flow rates could therefore be evaluated from a knowledge of the impact pressure and the sampling rate at a pressure difference of approximately one half of the impact pressure. This conclusion is used for the development of the general experimental procedure presented in Section 6.5 .

Theoretical

T 1 MANTZOURANIS' Film Thickness Analysis (1)

Mantzouranis developed the following analysis for deriving the film thickness from a measurement of the total pressure gradient in a tube. His model is shown in Fig.T 1.1.

A force balance on the liquid yields

$$\tau_W \frac{2}{r_W} = \frac{dP_T}{dz} R_L + \frac{dP_f}{dz} R_V - \frac{dP_{aL}}{dz} R_L + g \rho_L R_L \quad . \quad . \quad (T\ 1.1)$$

and for the vapour core with entrained droplets

$$\frac{dP_{aV}}{dz} + \frac{dP_{ae}}{dz} = \frac{dP_T}{dz} - \frac{dP_f}{dz} + g \bar{\rho}_V \quad . \quad . \quad (T\ 1.2)$$

where $\bar{\rho}_V$ = mean density of the vapour core, but in the use of this analysis $\bar{\rho}_V$ was assumed equal to ρ_V. The accelerational pressure gradient developed in the liquid film is given by

$$- \frac{dP_{aL}}{dz} = m_L \frac{G_L^2}{R_L^2 \rho_L} \left(2 \frac{d \ln G_L}{dz} - \frac{1}{R_L} \frac{dR_L}{dz}\right) \quad . \quad . \quad (T\ 1.3)$$

where $m_L = 1 + \frac{1.13}{(y_i^+)^{0.59}}$ assuming the universal velocity profile of Von Karman to represent the conditions in the liquid film.

The accelerational pressure gradients in the vapour core are, for the vapour stream

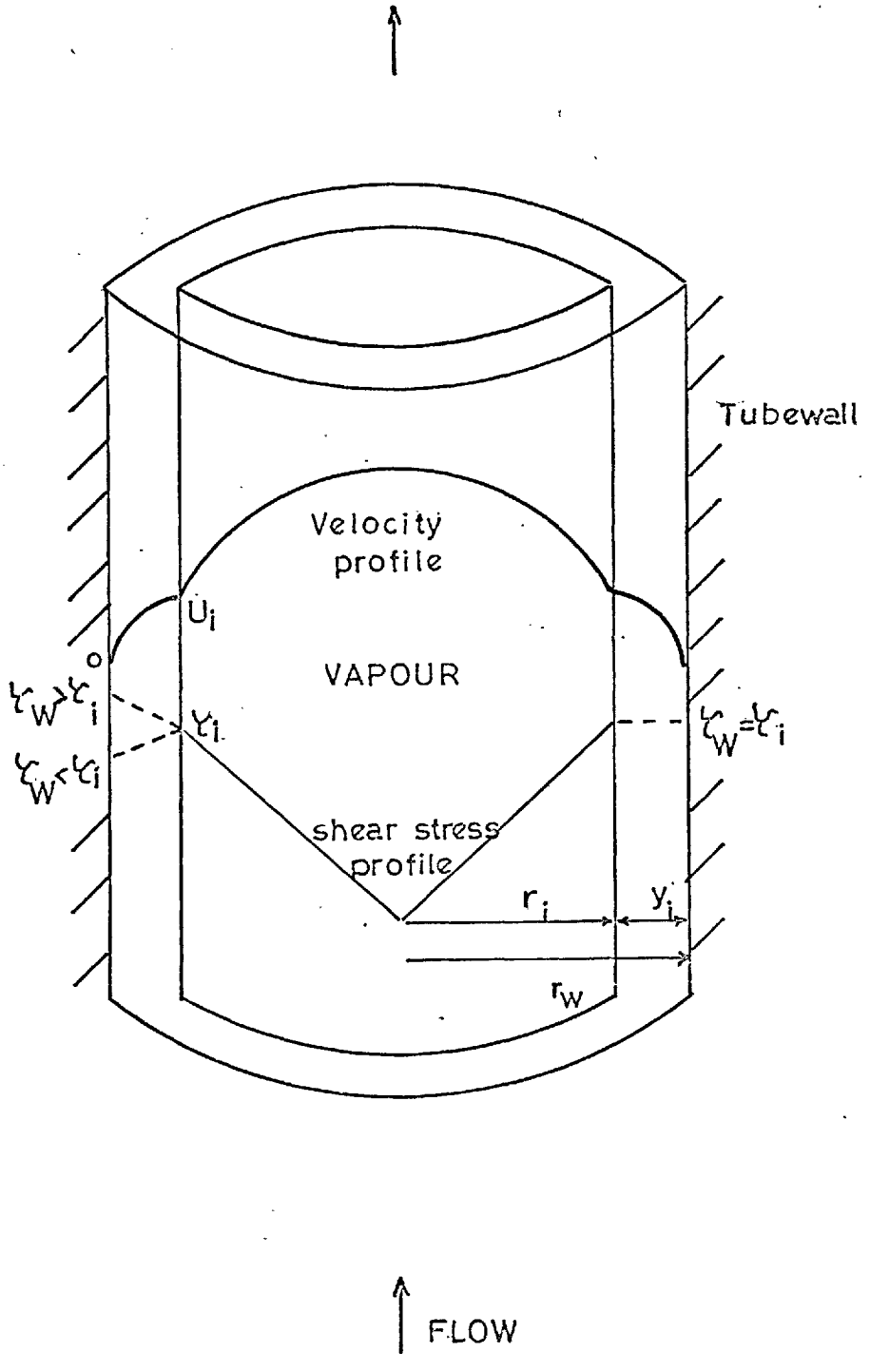
$$\frac{dP_{aV}}{dz} = \frac{G_V^2}{R_V^2 \rho_V} \left(2 \frac{d}{dz} (\ln G_V) - \frac{1}{R_V} \frac{dR_V}{dz}\right) - u_{iR_V} \frac{G_V}{dz} \frac{d}{dz} (\ln G_V) \quad (T\ 1.4)$$

and for the entrained liquid

$$\frac{dP_{ae}}{dz} = \frac{SU_V G_e}{R_V} \left(\frac{d}{dz}(\ln G_V) + \frac{d}{dz}(\ln G_e) + \frac{d}{dz}(\ln S) - \frac{1}{R_V} \frac{dR_V}{dz}\right) - \frac{G_e U_i}{R_V} \frac{d}{dz} (\ln G_e)$$

(T 1.5)

FIG T1·1



Analytical Model of Annular Flow

S is related to the impact pressure of the entrained droplets by the expression

$$P_I = \frac{G_V^2}{R_V^2 \rho_V} \left(\frac{1}{2} K^2 + \alpha S K x_V\right) \quad . \quad . \quad . \quad . \quad . \quad (T\ 1.6)$$

where

S = drop velocity / local vapour velocity

α = constant depending on the behaviour of the drops in the vicinity of the probe which can have values between $\frac{1}{2}$ and 2.

$$x_V = \frac{G_e}{G_V} R_V$$

In this present analysis K was put equal to the value for turbulent flow of 1.14 and the value of S was derived from equation T 1.6 as follows

for $\alpha S \geq 1$ $\quad S = 1$

for $\alpha S < 1$ $\quad S = \alpha S$

Mantzouranis assumed that the Von Karman velocity profile represents the condition in the liquid. Von Karman recognised three velocity regions :

Laminar sub-layer $0 < y^+ < 5$; $u^+ = y^+$ . . (T 1.7)

buffer layer $5 < y^+ < 30$; $u^+ = 5 \ln y^+ - 3.05$. (T 1.8)

turbulent layer $30 < y^+ < \infty$; $u^+ = 2.5 \ln y^+ + 5.5$. (T 1.9)

where $y^+ = \frac{\rho u^* y}{\mu}$; $u^+ = \frac{\Pi}{u^*}$ and $u^* = \sqrt{\frac{\tau_W}{\rho_L}}$

If U is the velocity of a liquid passing through an element of area dA then the mass flow

$$W = \int_{y_1}^{y_2} U dA \quad . \quad . \quad . \quad . \quad . \quad . \quad . \quad (T\ 1.10)$$

Converting equation (T1.10) to universal parameters and substituting $u^+ = f(y^+)$

from equations (T 1.7), (T 1.8) and (T 1.9), gives on integration :

<u>laminar</u>; $W_l^+ = \frac{1}{2}(y_2^+)^2 - \frac{1}{3Re^*}(y_2^+)^3$ . . (T 1.11)

<u>Buffer</u>; $W_b^+ = 5y_2^+ (\ln y_2^+ - 1.61) - \frac{2.5(y_2^+)^2}{Re^*} (\ln y_2^+ - 1.11) - \frac{31.25}{Re^*}$

(T 1.12)

<u>Turbulent</u>; $W_t^+ = 2.5y_2^+(\ln y_2^+ + 1.2) - \frac{1.25(y_2^+)^2}{Re^*} (\ln y_2^+ + 1.7) + \frac{5739}{Re^*} - 345$

(T 1.13)

Use of these equations in conjunction with the force balances, enables an estimate of the film thickness, y_i, to be obtained.

T.2 Sliding Velocity of Bubble

The four forces acting in the system which will be considered in this analysis are shown in Fig.T 2.1.

Viscous Drag Force on Hemispherical Bubble :

$$F_D = \frac{C_D}{2} (U_L - U_b)^2 \frac{\pi R_b^2}{2} \quad . \quad . \quad . \quad . \quad . \quad . \quad (T\ 2.1)$$

where PEEBLES and GARBER (75) show that

$$C_D \approx \frac{22}{Re} \quad . \quad . \quad . \quad . \quad . \quad . \quad (T\ 2.2)$$

for a bubble in uniform motion with

$$Re = \frac{2R_b}{2^{1/3}} \frac{\rho_L (U_L - U_b)}{\mu_L} \quad . \quad . \quad . \quad . \quad . \quad . \quad (T\ 2.3)$$

for a hemispherical bubble.

Therefore

$$F_D = \frac{11 \times 2^{1/3}}{4} \mu_L (U_L - U_b) \pi R_b \quad . \quad . \quad . \quad . \quad (T\ 2.4)$$

Buoyancy force on hemispherical bubble :

$$F_B = \frac{2}{3} \pi R_b^3 (\rho_L - \rho_V) g \quad . \quad . \quad . \quad . \quad (T\ 2.5)$$

Inertial force on hemispherical bubble :

$$F_I = \pi R_b^2 \rho_L (U_b \dot{R}_b + U_b \frac{\dot{R}_b}{3} - \dot{U}_L R_b - U_L \dot{R}_b) \quad . \quad . \quad (4.31)$$

where U_L may be considered uniform for y^+ 30.

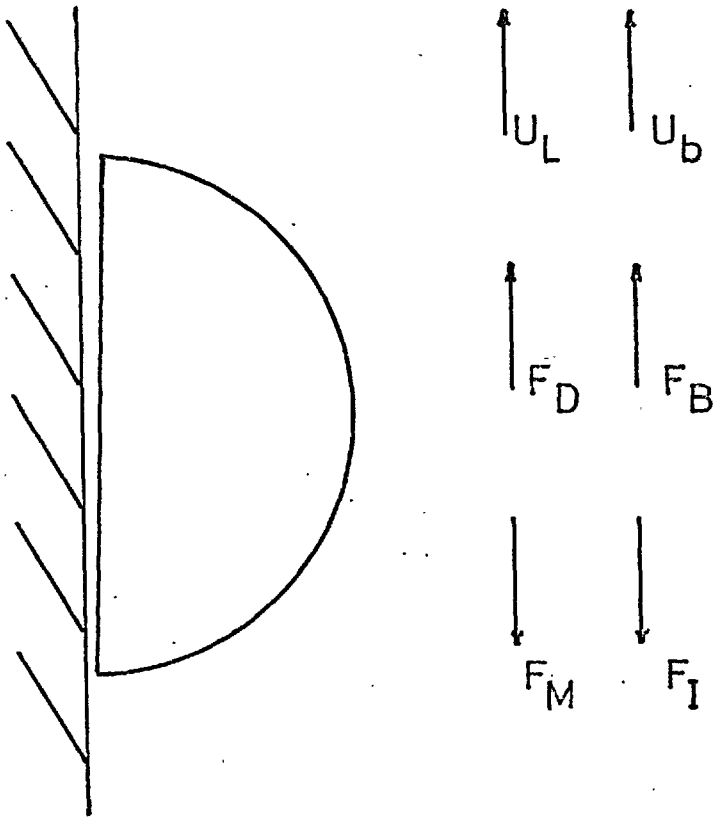
Rate of Change of Momentum of Bubble

$$F_M = \frac{d}{dt} (\rho_V \frac{2}{3} \pi R_b^3 U_b) \quad . \quad . \quad . \quad (T\ 2.6)$$

Bubble Velocity

It is assumed that the velocity of the bubble changes so that the four forces given by equations (T 2.4), (T 2.5), (4.31) and (T 2.6) remain in equilibrium, so that

FIG T2·1



Forces Acting On Sliding Bubble

$$F_M + F_I = F_B + F_D \quad \cdots \quad (T\ 2.7)$$

Substituting the appropriate expressions for the forces into equation (T 2.7) and rearranging yields the following differential expression

$$\frac{dU_b}{dt} + U_b \frac{3}{(2\rho_V + \rho_L)t}\left(\frac{(2\rho_V + \rho_L)}{2} + \frac{11 \times 2^{1/3}}{4}\sqrt{\frac{\mu_L}{A^2}}\right) = \frac{3}{(2\rho_V + \rho_L)} \times$$

$$\left(\frac{\rho_L U_L}{2t} + \frac{2}{3}(\rho_L - \rho_V)g + \frac{11 \times 2^{1/3}}{4} \times \sqrt{\frac{\mu_L U_L}{A^2}}\right) \quad \cdots \quad (T\ 2.8)$$

which integrates to give the following expression for U_b:

$$U_b = \left(\frac{3}{2\rho_V + \rho_L}\right)\left(\frac{\rho_L U_L}{2K} + \frac{2}{3}\left(\frac{\rho_L - \rho_V}{(K+1)}\right)gt + \frac{11 \times 2^{1/3}}{4A^2}\sqrt{\frac{\mu_2 U_L}{K}}\right) + \frac{C}{t^K}$$

$$\cdots \quad (T\ 2.9)$$

where C = constant of integration

$$K = \frac{3}{(2\rho_V + \rho_L)}\left(\frac{(2\rho_V + \rho_L)}{2} + \frac{11 \times 2^{1/3}}{4}\sqrt{\frac{\mu_L}{A^2}}\right) \quad \cdots \quad (T\ 2.10)$$

From data of Gunther at 10 f/s for water

$$R_b = 0.026 \text{ in}$$

$$t = 3 \times 10^{-4} \text{ s}$$

$$A = 0.0346 \text{ m/s}^{\frac{1}{2}}$$

$$U_L = 10 \text{ f/s}$$

$$U_b = 8 \text{ f/s}$$

and assuming $\rho_L \gg \rho_V$ K of equation (T 2.10) can be reduced to

$$K = \frac{3}{2} \quad (T\ 2.11)$$

and the expression for U_b becomes

$$U_b = U_L + \frac{C}{t^{3/2}} \quad \cdots \quad (T2.12)$$

For Gunther's data

$$C \simeq -10^{-5}$$

and $$U_b = U_L - \frac{10^{-5}}{t^{3/2}} \qquad \text{(T 2.13)}$$

Equation (T 2.13) shows that a bubble will accelerate rapidly during the early part of its growth but that its velocity will change only slowly as the bubble approaches its departure size.

Computational

Block diagrams describing the computer programmes used to analyse the experimental data and theory are presented. The derived point data along the test column are presented in Table A2 and the predicted critical heat fluxes from the Gambill and Von Glahn correlations are presented in Table A1. The film thickness data (Table 7.2) was obtained using a technique similar to that presented by BACKHURST (2).

C.1 Analysis of Experimental Data

The programme calculates the appropriate values to test the Von Glahn (C 1.3) and Gambill (C 1.1) correlations, the tube wall temperature, stream temperature, stream pressure, quality, nucleation temperature, point heat transfer coefficient (Equation 7.1) and the predicted heat transfer coefficient using the Dittus-Boelter equation with the Guerrieri-Talty correction factor. (Section 2.3)

The following equations are referred to in the block diagram (C.1)

$$QTOT = \sum_{i=1}^{i=13} q_i \qquad \text{(C 1.1)}$$

$$HF = q_i / A_{HT} \qquad \text{(C 1.2)}$$

$$X_i = \frac{T_o}{T_s} + QT\emptyset T_{i+1} / (T_\varepsilon C_p G_T) - 1 \qquad \text{(C 1.3)}$$

$$T_{nuc} = T_W - \frac{q \times 10^{-6}}{HT\ k_L} \qquad \text{(C 1.4)}$$

C.2 Analysis of Bubble Growth Rate

For solution of equation :

$$\dot{R} = \frac{k_L(T_W - T_b)}{2\pi\rho_V \lambda R_b^2} \int_0^{\pi} \int_0^{R_b} \frac{r}{\xi} \, dr \, d \qquad \text{(4.42)}$$

defining

$$DFUN = \left(\delta_0^2 - \frac{2k_L}{\rho_L \lambda} (T_W - T_S) \frac{R_b}{V_b} \left(\left(1 - \frac{r^2 \sin^2 \Psi}{R_b^2}\right)^{\frac{1}{2}} - \frac{r}{R_b} \cos \Psi \right) \right)^{\frac{1}{2}} \quad \ldots \quad (C\ 2.1)$$

as derived from equation (4.36) on integration and substitution of equation (4.47)

C.2.1 Subroutine DUBINT

To integrate a function in the form

$$\int_{Y_1}^{Y_2} \int_{X_1}^{X_2} DFUN(X,Y)\, dX\, dY \quad \ldots \quad (C\ 2.2)$$

Arguments used are :

X1, X2, XR, SIMP, Y1, Y2, YNR, DFUN

where

XR = number of intervals in range of X (even)

YNR = number of intervals in range of Y (even)

SIMP = integration subroutine C 2.2.

C.2.2 Subroutine SIMP

To integrate a function in the form

$$\int_{X_2}^{X_1} DFUN(X,Y)\, dX \quad \ldots \quad (C\ 2.3)$$

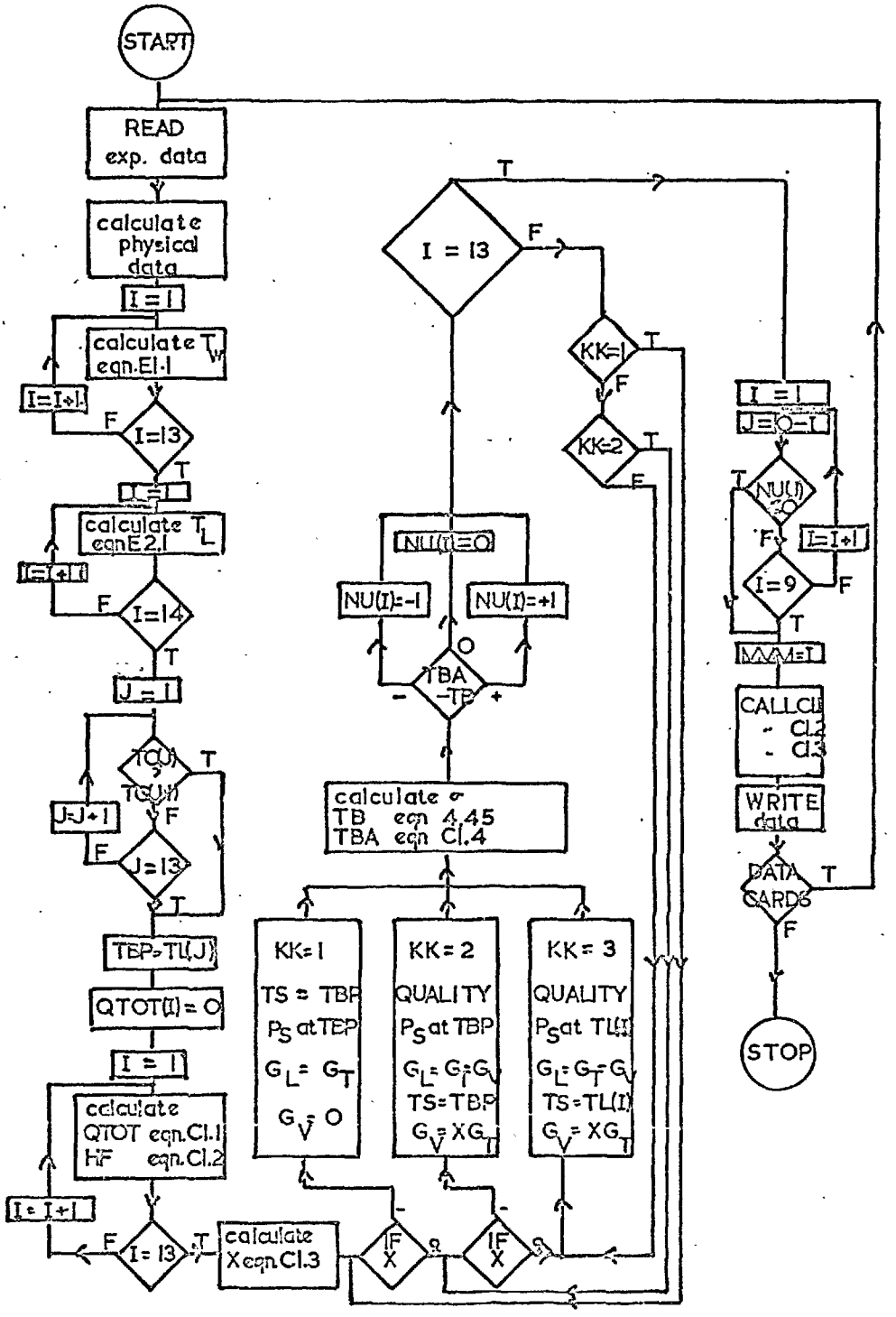
for a given value of Y.

Arguments used are :

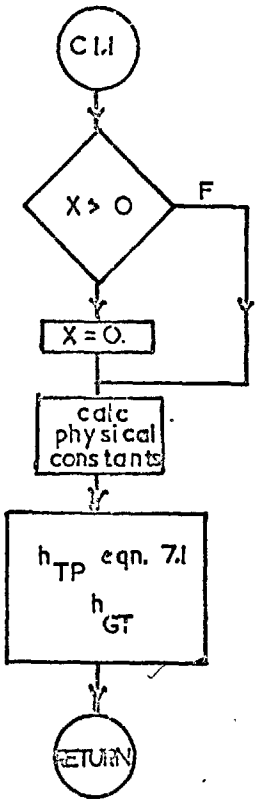
X1, X2, NR, Y, DFUN

NR = number of intervals in range of X (even)

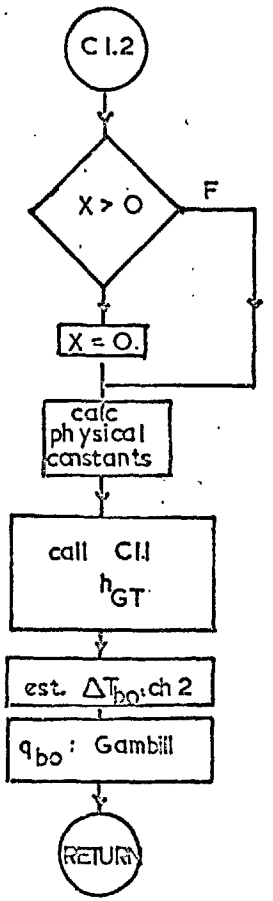
C1 Analysis Of Experimental Data



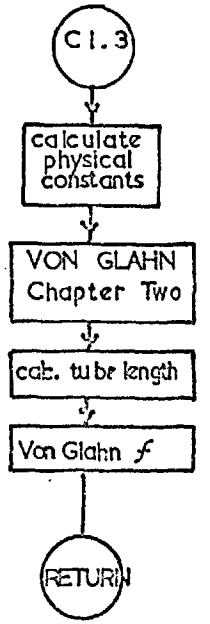
GUERRIERI-TALTY



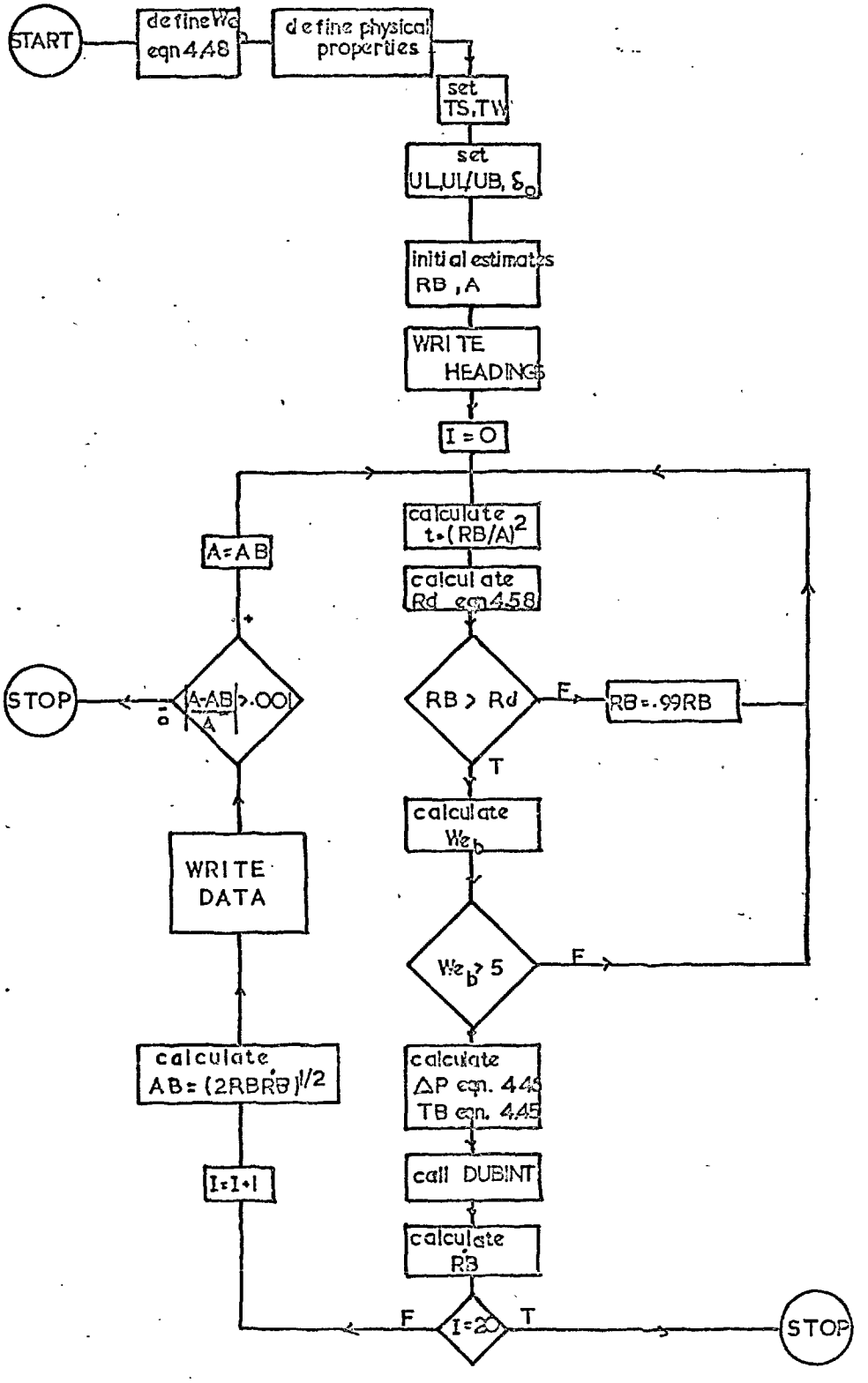
GAMBILL



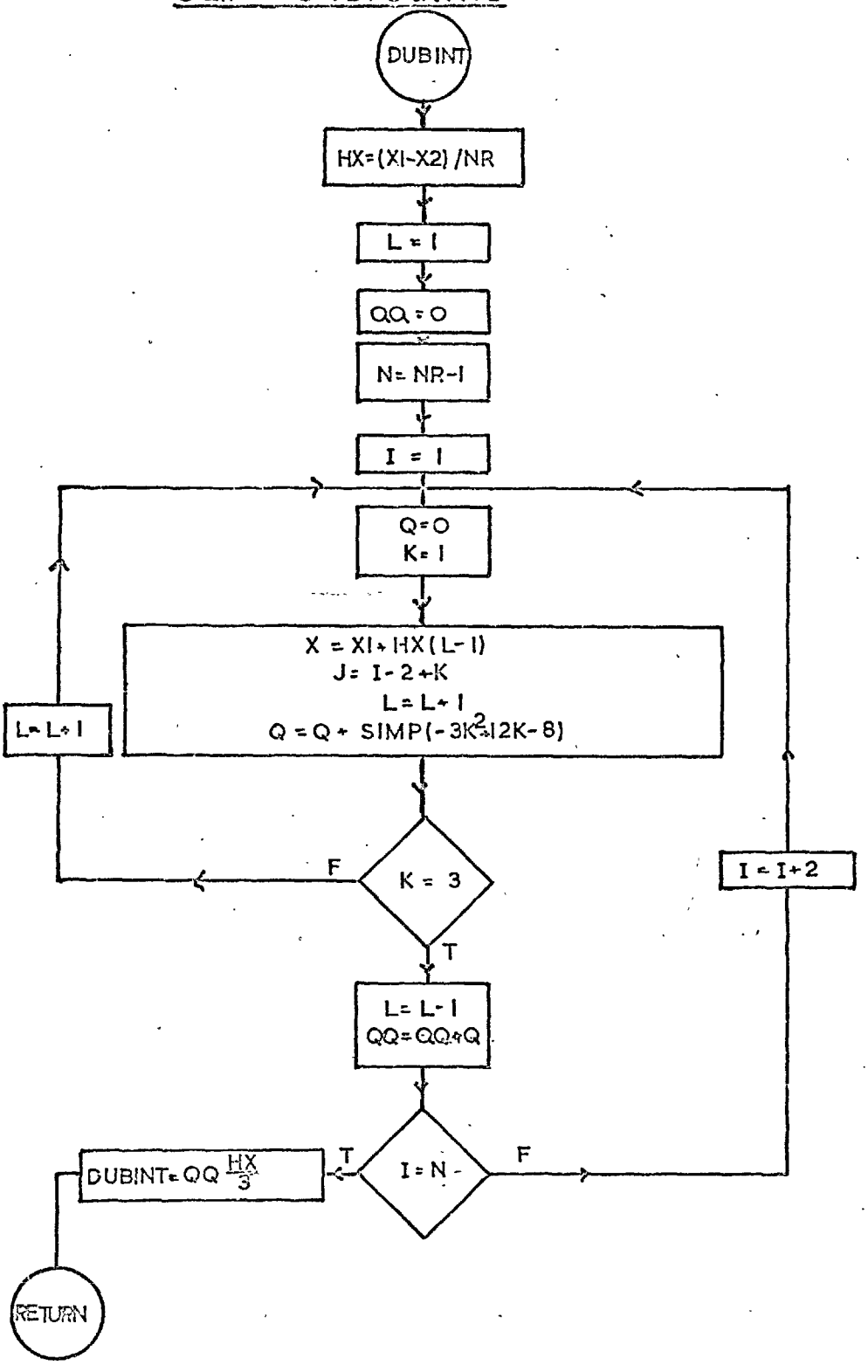
VON GLAHN



C2 Analysis Of Bubble Growth



C2.1 Subroutine



C2.2 Subroutine

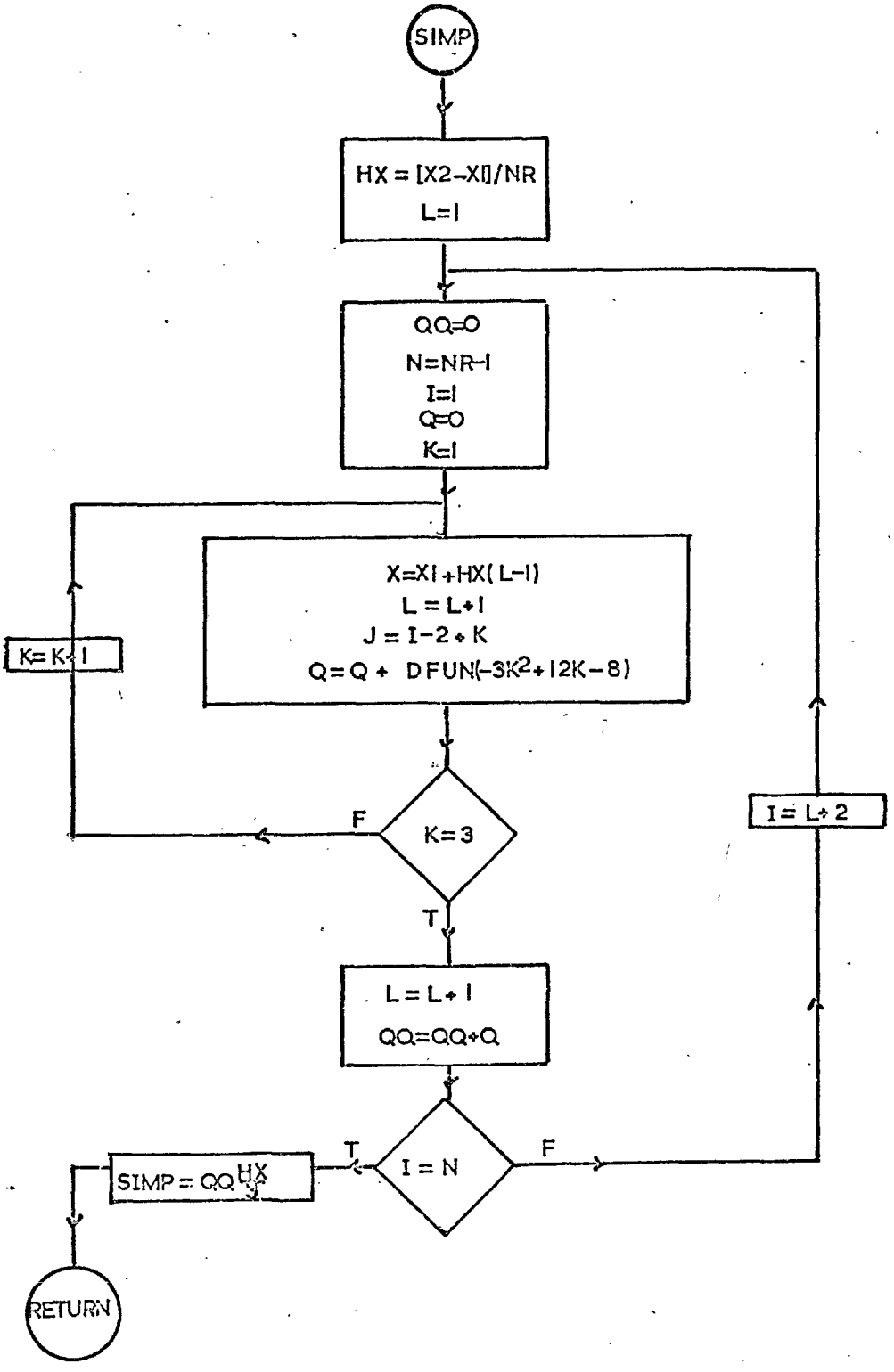


TABLE A1 DATA FROM BURNOUT CORRELATIONS

Run No.	Gambill Prediction Heat Flux (W/m^2) x 10^{-6}			Von Glahn Correlation X			function 'f' x10^5		
	10	12	13	10	12	13	10	12	13
511	0.442	0.441	0.441	0.27	0.82	0.83	0.57	0.45	0.40
512	0.447	0.446	0.446	0.71	0.82	0.82	0.59	0.47	0.42
513	0.442	0.442	0.441	0.74	0.85	0.85	0.57	0.45	0.41
411	0.450	0.449	0.448	0.63	0.77	0.78	0.59	0.46	0.42
412	0.448	0.447	0.447	0.66	0.78	0.79	0.59	0.46	0.42
413	0.448	0.447	0.447	0.67	0.80	0.80	0.59	0.46	0.42
311	0.450	0.450	0.450	0.54	0.70	0.73	0.59	0.46	0.42
312	0.451	0.450	0.450	0.58	0.74	0.77	0.59	0.46	0.42
313	0.451	0.450	0.449	0.59	0.75	0.76	0.59	0.47	0.42
211	0.447	0.447	0.446	0.44	0.68	0.70	0.59	0.47	0.42
212	0.449	0.449	0.449	0.46	0.67	0.70	0.60	0.47	0.42
213	0.449	0.449	0.449	0.48	0.66	0.70	0.60	0.47	0.42
111	0.443	0.445	0.445	0.47	0.75	0.75	0.55	0.43	0.39
112	0.444	0.445	0.445	0.44	0.71	0.72	0.57	0.45	0.41
113	0.443	0.443	0.443	0.44	0.74	0.74	0.55	0.43	0.39
521	0.516	0.514	0.513	0.55	0.60	0.62	1.18	0.93	0.84
522	0.512	0.510	0.510	0.58	0.63	0.65	1.14	0.90	0.81
523	0.516	0.514	0.513	0.57	0.62	0.64	1.18	0.93	0.84
421	0.519	0.518	0.517	0.49	0.57	0.60	1.19	0.94	0.85
422	0.516	0.514	0.513	0.51	0.59	0.60	1.18	0.93	0.84
423	0.519	0.517	0.517	0.53	0.60	0.62	1.18	0.93	0.83
321	0.512	0.511	0.510	0.42	0.52	0.54	1.21	0.96	0.86
322	0.513	0.512	0.511	0.42	0.53	0.54	1.21	0.96	0.86
323	0.516	0.514	0.514	0.44	0.55	0.58	1.19	0.94	0.85
221	0.506	0.505	0.505	0.36	0.50	0.50	1.21	0.96	0.86
222	0.497	0.497	0.497	0.35	0.49.	0.51	1.16	0.91	0.82
223	0.504	0.503	0.503	0.37	0.52	0.52	1.17	0.93	0.83
121	0.487	0.489	0.489	0.29	0.46	0.46	1.15	0.91	0.82
122	0.488	0.489	0.489	0.29	0.45	0.45	1.15	0.91	0.82
123	0.483	0.485	0.484	0.28	0.44	0.44	1.15	0.91	0.82
431	0.569	0.568	0.568	0.42	0.47	0.49	1.83	1.44	1.30
432	0.574	0.573	0.572	0.44	0.49	0.51	1.83	1.44	1.30
433	0.576	0.574	0.573	0.45	0.50	0.52	1.83	1.44	1.30
331	0.570	0.568	0.567	0.40	0.50	0.50	1.85	1.46	1.32
332	0.562	0.561	0.560	0.36	0.44	0.44	1.85	1.46	1.32
333	0.566	0.564	0.564	0.39	0.49	0.48	1.83	1.44	1.30
231	0.545	0.544	0.544	0.32	0.42	0.43	1.78	1.41	1.27
232	0.545	0.545	0.544	0.32	0.42	0.43	1.78	1.41	1.27
233	0.519	0.520	0.520	0.23	0.33	0.33	1.85	1.46	1.32
131	0.511	0.513	0.513	0.25	0.35	0.35	1.74	1.37	1.23
132	0.511	0.513	0.513	0.26	0.35	0.35	1.74	1.37	1.23
133	0.512	0.513	0.513	0.25	0.35	0.35	1.74	1.37	1.23

TABLE A2

Table A2 presents the following point data:-

$qx10^{-6}$ W/m^2 : nett heat input to each section.

T_W ^oC : corrected tube wall temperature.

T_L ^oC : tube core temperature.

P_V bars : core pressure calculated from T_L.

X : quality at exit to each section.

T_i ^oC : superheat required to initiate boiling.

T_{ie} ^oC : estimated superheat at each section obtained from the relationship

$$T_{ie} = T_W - \frac{q \times y_c}{k_L}$$

where $y_c = 1/\mu m$ (see experimental section)

Nu : used to indicate nucleation

If $T_{ie} - T_i$ is positive then Nu = +1 (nucleation),

if $T_{ie} - T_i$ is negative then Nu = -1 (no nucleation).

$h_{GT}x10^{-4}$ $W/m^2\ ^oC$: Guerrieri-Talty estimate of heat transfer coefficient.

$h_{exp}x10^{-4}$ $W/m^2\ ^oC$: calculated heat transfer coefficient from point data using the relationship

$$h_{exp} = \frac{q}{T_W - T_L}$$

N.B.

In some earlier runs T_L (travelling thermocouple) was measured using the variable reference junction of T_W. These values can be differentiated from those where a reference junction at 0.0 ^oC was used since they are quoted to only one place of decimals and are accurate to $\pm$ 0.6 ^oC. The values obtained using 0.0 ^oC as a reference are quoted to two places.

TABLE A2 (cont.)

Run No. 511

Separator Pressure 1.858 bars Inlet Temp. 49.7 °C

Tube Section	$q \times 10^{-6}$ W/m^2	T_W °C	T_L °C	P_V bars	$W_L \times 10^2$ Kg/s	X	T_i °C	T_{ie} °C	Nu	$h_{GT} \times 10^{-4}$ W/m^2/°C	$h_{exp} \times 10^{-4}$ W/m^2/°C
1	.0512	74.5	50.2	1.930	3.65	-.16	83.9	73.7	-1	-	-
2	.0512	78.1	56.0	1.930	3.65	-.04	83.3	77.3	-1	-	-
3	.0512	79.6	64.0	1.930	3.52	.036	82.5	78.8	-1	.071	.329
4	.0512	81.5	67.6	1.930	3.32	.091	82.2	80.7	-1	.101	.367
5	.0512	81.3	68.1	1.930	3.12	.147	82.1	80.5	-1	.119	.388
6	.0512	81.3	68.3	1.930	2.91	.202	82.1	80.5	-1	.132	.392
7	.0512	79.1	68.2	1.928	2.71	.258	82.1	78.3	-1	.141	.472
8	.0512	78.1	68.2	1.924	2.51	.314	82.0	77.3	-1	.148	.514
9	.0933	85.4	68.1	1.918	2.13	.416	81.9	84.0	+1	.156	.539
10	.2615	103.0	67.7	1.897	1.09	.701	81.7	99.1	+1	.148	.740
11	.0	70.2	67.4	1.879	1.09	.702	81.5	70.2	-1	.148	-
12	.0	67.6	67.3	1.876	1.09	.703	81.4	67.6	-1	.148	-
13	.0	67.3	67.2	1.873	1.09	.703	81.4	67.3	-1	.148	-

Run No. 512

Separator Pressure 1.888 bars Inlet Temp. 49.7 °C

Tube Section	$q \times 10^{-6}$ W/m^2	T_W °C	T_L °C	P_V bars	$W_L \times 10^2$ Kg/s	X	T_i °C	T_{ie} °C	Nu	$h_{GT} \times 10^{-4}$ W/m^2/°C	$h_{exp} \times 10^{-4}$ W/m^2/°C
1	.0587	75.3	50.3	1.940	3.82	-.15	84.0	74.4	-1	-	-
2	.0587	78.8	58.1	1.940	3.82	-.02	83.2	78.0	-1	-	-
3	.0587	80.2	65.3	1.940	3.63	.050	82.5	79.3	-1	.084	.392
4	.0587	82.4	68.0	1.940	3.40	.111	82.3	81.5	-1	.112	.408
5	.0587	82.6	68.4	1.940	3.17	.172	82.2	81.7	-1	.130	.413
6	.0587	83.1	68.4	1.940	2.93	.232	82.2	82.2	+1	.142	.400
7	.0587	79.9	68.4	1.940	2.70	.293	82.2	79.0	-1	.152	.511
8	.0464	78.1	68.3	1.932	2.51	.342	82.1	77.4	-1	.157	.473
9	.0464	81.5	68.3	1.931	2.33	.390	82.1	80.8	-1	.161	.350
10	.2768	103.6	68.0	1.914	1.23	.678	81.9	99.4	+1	.156	.777
11	.0	70.7	67.7	1.896	1.22	.680	81.7	70.7	-1	.156	-
12	.0	67.9	67.6	1.895	1.22	.680	81.7	67.9	-1	.156	-
13	.0	67.8	67.5	1.889	1.22	.681	81.6	67.8	-1	.156	-

TABLE A.2(cont.)

Run No. 513

Separator Pressure 1.852 bars Inlet Temp. 49.7 °C

Tube Section	$qx10^{-6}$ W/m^2	T_W °C	T_L °C	P_V bars	$W_L x10^2$ Kg/s	X	T_i °C	T_{ie} °C	Nu	$h_{GT} x10^{-4}$ W/m^2/°C	$h_{exp} x10^{-4}$ W/m^2/°C
1	.0687	74.1	50.4	1.968	3.70	-.13	84.4	73.1	-1	-	.289
2	.0687	78.8	60.2	1.968	3.66	.011	83.4	77.8	-1	.046	.369
3	.0687	79.5	66.8	1.968	3.39	.085	82.7	78.4	-1	.099	.542
4	.0687	81.9	68.0	1.968	3.12	.158	82.6	80.9	-1	.123	.493
5	.0687	82.0	68.3	1.968	2.85	.231	82.6	81.0	-1	.139	.502
6	.0687	81.3	68.5	1.968	2.57	.305	82.6	80.2	-1	.149	.535
7	.0307	77.4	68.5	1.968	2.45	.338	82.6	76.9	-1	.153	.345
8	.0307	76.3	68.9	1.968	2.33	.371	82.5	75.8	-1	.155	.422
9	.0307	77.2	68.6	1.947	2.20	.406	82.3	76.7	-1	.157	.356
10	.2801	103.9	67.5	1.889	1.07	.710	81.6	99.7	+1	.149	.770
11	.0	69.7	67.3	1.877	1.07	.711	81.4	69.7	-1	.149	-
12	.0	67.5	67.3	1.877	1.07	.711	81.4	67.5	-1	.149	-
13	.0	67.2	67.2	1.873	1.07	.712	81.4	67.2	-1	.149	-

Run No. 411

Separator Pressure 1.870 bars Inlet Temp. 49.7 °C

Tube Section	$qx10^{-6}$ W/m^2	T_W °C	T_V °C	P_V bars	$W_L x10^2$ Kg/s	X	T_i °C	T_{ie} °C	Nu	$h_{GT} x10^{-4}$ W/m^2/°C	$h_{exp} x10^{-4}$ W/m^2/°C
1	.0395	70.9	50.3	1.920	3.79	-.18	83.7	70.3	-1	-	.191
2	.0395	74.9	53.5	1.920	3.79	-.10	83.4	74.3	-1	-	.184
3	.0395	77.1	60.5	1.920	3.79	-.01	82.7	76.5	-1	-	.239
4	.0395	79.2	65.7	1.920	3.65	.035	82.2	78.6	-1	.073	.293
5	.0395	80.1	67.4	1.920	3.50	.077	82.0	79.5	-1	.097	.316
6	.0395	79.8	67.9	1.920	3.34	.118	82.0	79.2	-1	.114	.332
7	.0395	78.3	68.0	1.920	3.19	.159	82.0	77.7	-1	.126	.383
8	.0395	77.8	68.1	1.920	3.03	.200	82.0	77.2	-1	.135	.406
9	.0935	86.4	68.1	1.920	2.66	.298	82.0	85.0	+1	.151	.510
10	.2825	106.7	67.9	1.908	1.54	.594	82.0	102.5	+1	.161	.727
11	.0	70.5	67.6	1.894	1.53	.595	81.6	70.5	-1	.161	-
12	.0	67.6	67.5	1.890	1.53	.595	81.6	67.6	-1	.161	-
13	.0	67.3	67.4	1.883	1.53	.596	81.5	67.3	-1	.161	-

TABLE A2 (cont.)

Run No. 412

Separator Pressure 1.853 bars Inlet Temp. 49.5 °C

Tube Section	$q \times 10^{-6}$ W/m^2	T_W °C	T_L °C	P_V bars	$W_L \times 10^2$ Kg/s	X	T_i °C	T_{ie} °C	Nu	$h_{GT} \times 10^{-4}$ W/m^2/°C	$h_{exp} \times 10^{-4}$ W/m^2/°C
1	.0452	70.4	50.1	1.913	3.79	-.17	83.7	69.7	-1	-	-
2	.0452	75.1	55.7	1.913	3.79	-.07	83.1	74.5	-1	-	-
3	.0452	76.1	62.4	1.913	3.75	.012	82.4	75.4	-1	.047	.329
4	.0452	78.8	66.8	1.913	3.57	.059	82.0	78.1	-1	.088	.376
5	.0452	79.7	67.7	1.913	3.39	.106	81.9	79.1	-1	.109	.375
6	.0452	78.1	67.9	1.913	3.21	.153	81.9	77.4	-1	.124	.445
7	.0452	77.3	68.0	1.913	3.03	.200	81.9	76.6	-1	.136	.485
8	.0466	76.1	67.9	1.910	2.84	.249	81.8	75.4	-1	.144	.467
9	.0466	78.6	67.8	1.906	2.66	.298	81.8	77.9	-1	.151	.433
10	.3095	104.7	67.6	1.890	1.43	.622	81.6	100.0	+1	.160	.833
11	.0	69.8	67.4	1.879	1.43	.623	81.5	69.8	-1	.160	-
12	.0	68.1	67.3	1.876	1.43	.624	81.4	68.1	-1	.160	-
13	.0	68.1	67.2	1.870	1.42	.624	81.4	68.1	-1	.160	-

Run No. 413

Separator Pressure 1.847 bars Inlet Temp. 49.5 °C

Tube Section	$q \times 10^{-6}$ W/m^2	T_W °C	T_L °C	P_V bars	$W_L \times 10^2$ Kg/s	X	T_i °C	T_{ie} °C	Nu	$h_{GT} \times 10^{-4}$ W/m^2/°C	$h_{exp} \times 10^{-4}$ W/m^2/°C
1	.0529	71.1	50.0	1.923	3.79	-.16	83.8	70.3	-1	-	-
2	.0529	76.2	56.9	1.923	3.79	-.04	83.1	75.4	-1	-	-
3	.0529	76.8	63.9	1.923	3.66	.034	82.4	76.1	-1	.072	.408
4	.0529	79.9	67.4	1.923	3.45	.089	82.1	79.1	-1	.103	.422
5	.0529	80.8	67.9	1.923	3.24	.145	82.0	80.0	-1	.122	.411
6	.0529	78.9	67.1	1.923	3.03	.200	82.0	78.1	-1	.135	.411
7	.0307	75.8	68.1	1.923	2.91	.232	82.0	75.3	-1	.141	.400
8	.0307	74.5	68.1	1.920	2.79	.264	82.0	74.1	-1	.147	.477
9	.0307	76.6	68.0	1.913	2.66	.297	81.9	76.1	-1	.151	.357
10	.3181	109.5	67.7	1.896	1.40	.630	81.7	104.7	+1	.159	.759
11	.0	70.5	67.5	1.887	1.40	.631	81.6	70.5	-1	.159	-
12	.0	67.5	67.4	1.884	1.40	.631	81.5	67.5	-1	.159	-
13	.0	67.3	67.4	1.883	1.40	.631	81.5	67.3	-1	.159	-

TABLE A2 (cont.)

Run No. 311

Separator Pressure 1.858 bars Inlet Temp. 49.7 °C

Tube Section	$q \times 10^{-6}$ W/m^2	T_W °C	T_V °C	P_V bars	$W_L \times 10^2$ Kg/s	X	T_i °C	T_{ie} °C	Nu	$h_{GT} \times 10^{-4}$ W/m^2/°C	$h_{exp} \times 10^{-4}$ W/m^2/°C
1	.0279	68.2	50.2	1.889	3.79	-.20	83.3	67.8	-1	-	-
2	.0279	73.1	51.3	1.889	3.79	-.14	83.2	72.7	-1	-	-
3	.0279	75.2	58.0	1.889	3.79	-.08	82.6	74.7	-1	-	-
4	.0279	77.0	62.1	1.889	3.79	-.02	82.1	76.6	-1	-	-
5	.0279	78.1	65.3	1.889	3.71	.020	81.8	77.6	-1	.058	.219
6	.0279	78.3	67.0	1.889	3.60	.049	81.6	77.8	-1	.082	.248
7	.0279	77.0	67.4	1.889	3.49	.047	81.6	76.6	-1	.098	.290
8	.0279	76.0	67.5	1.889	3.38	.107	81.6	75.6	-1	.110	.327
9	.0935	85.8	67.5	1.889	3.01	.204	81.6	84.4	+1	.136	.512
10	.2610	105.8	67.5	1.888	1.98	.476	81.6	101.8	+1	.163	.682
11	.0	70.8	67.3	1.877	1.98	.478	81.5	70.8	-1	.163	-
12	.0	67.5	67.2	1.870	1.98	.478	81.4	67.5	-1	.163	-
13	.0	67.3	67.2	1.870	1.98	.478	81.4	67.3	-1	.163	-

Run No. 312

Separator Pressure 1.857 bars Inlet Temp. 49.8 °C

Tube Section	$q \times 10^{-6}$ W/m^2	T_W °C	T_V °C	P_V bars	$W_L \times 10^2$ Kg/s	X	T_i °C	T_{ie} °C	Nu	$h_{GT} \times 10^{-4}$ W/m^2/°C	$h_{exp} \times 10^{-4}$ W/m^2/°C
1	.0318	69.4	50.3	1.929	3.79	-.20	83.9	68.9	-1	-	-
2	.0318	73.4	52.0	1.929	3.79	-.13	83.7	72.9	-1	-	-
3	.0318	76.1	58.8	1.929	3.79	-.06	83.0	75.6	-1	-	-
4	.0318	78.1	63.4	1.929	3.78	.003	82.6	77.7	-1	.026	.216
5	.0318	79.2	66.7	1.929	3.65	.036	82.2	78.7	-1	.073	.254
6	.0318	78.8	67.9	1.929	3.53	.069	82.1	78.3	-1	.094	.291
7	.0318	77.2	68.1	1.929	3.40	.102	82.1	76.7	-1	.108	.352
8	.0464	77.3	68.2	1.929	3.22	.151	82.1	76.6	-1	.124	.515
9	.0464	80.3	68.2	1.929	3.03	.199	82.1	79.5	-1	.135	.387
10	.3130	111.8	68.1	1.922	1.79	.526	82.0	107.1	+1	.163	.716
11	.0	71.0	68.0	1.915	1.79	.527	81.9	71.0	-1	.163	-
12	.0	67.5	67.8	1.905	1.79	.528	81.8	67.5	-1	.163	-
13	.0	67.3	67.7	1.897	1.78	.529	81.7	67.3	-1	.163	-

TABLE A2 (cont.)

Run No. 313

Separator Pressure 1.841 bars Inlet Temp. 49.6 °C

Tube Section	$q \times 10^{-6}$ W/m^2	T_W °C	T_V °C	P_V bars	$W_L \times 10^2$ Kg/s	X	T_i °C	T_{ie} °C	Nu	$h_{GT} \times 10^{-4}$ W/m^2/°C	$h_{exp} \times 10^{-4}$ W/m^2/°C
1	.0372	73.4	50.2	1.898	3.83	-.19	83.4	72.9	-1	-	-
2	.0372	74.7	54.1	1.898	3.83	-.11	83.1	74.1	-1	-	-
3	.0372	78.3	60.2	1.898	3.83	-.03	82.5	77.7	-1	-	-
4	.0372	79.5	65.3	1.898	3.73	.026	81.9	79.0	-1	.065	.261
5	.0372	79.8	67.1	1.898	3.58	.065	81.8	79.2	-1	.092	.295
6	.0372	79.5	67.5	1.898	3.43	.103	81.7	79.0	-1	.109	.310
7	.0307	77.1	67.6	1.898	3.31	.135	81.7	76.6	-1	.120	.324
8	.0307	76.3	67.6	1.898	3.19	.166	81.7	75.9	-1	.129	.353
9	.0307	79.3	67.7	1.898	3.07	.198	81.7	78.9	-1	.136	.263
10	.3280	112.0	67.6	1.892	1.77	.537	81.6	107.0	+1	.164	.738
11	.0	70.5	67.4	1.879	1.77	.538	81.5	70.4	-1	.164	-
12	.0	67.2	67.3	1.878	1.77	.538	81.5	67.2	-1	.164	-
13	.0	66.8	67.2	1.872	1.77	.539	81.4	66.8	-1	.164	-

Run No. 211

Separator Pressure 1.864 bars Inlet Temp. 49.6 °C

Tube Section	$q \times 10^{-6}$ W/m^2	T_W °C	T_V °C	P_V bars	$W_L \times 10^2$ Kg/s	X	T_i °C	T_{ie} °C	Nu	$h_{GT} \times 10^{-4}$ W/m^2/°C	$h_{exp} \times 10^{-4}$ W/m^2/°C
1	.0163	64.6	50.2	1.869	3.83	-.23	83.1	64.4	-1	-	-
2	.0163	68.4	51.0	1.869	3.83	-.19	83.0	68.1	-1	-	-
3	.0163	69.6	53.6	1.869	3.83	-.16	82.7	69.3	-1	-	-
4	.0163	71.5	56.6	1.869	3.83	-.12	82.4	71.3	-1	-	-
5	.0163	72.8	59.0	1.869	3.83	-.08	82.2	72.6	-1	-	-
6	.0163	73.8	61.4	1.869	3.83	-.05	81.9	73.5	-1	-	-
7	.0163	73.1	63.6	1.869	3.83	-.01	81.7	72.9	-1	-	-
8	.0163	72.8	65.2	1.869	3.79	.011	81.6	72.6	-1	.045	.212
9	.0935	83.1	66.4	1.869	3.42	.107	81.4	81.6	+1	.111	.560
10	.2576	102.6	67.1	1.869	2.41	.372	81.4	98.7	+1	.160	.725
11	.0	70.6	67.2	1.869	2.41	.372	81.4	70.6	-1	.160	-
12	.0	67.4	67.1	1.868	2.40	.372	81.3	67.4	-1	.160	-
13	.0	67.3	67.0	1.861	2.40	.373	81.3	67.3	-1	.160	-

TABLE A2 (cont.)

Run No. 212

Separator Pressure 1.869 bars Inlet Temp. 49.8 °C

Tube Section	$q \times 10^{-6}$ W/m^2	T_W °C	T_V °C	P_V bars	$W_L \times 10^2$ Kg/s	X	T_i °C	T_{ie} °C	Nu	$h_{GT} \times 10^{-4}$ W/m^2/°C	$h_{exp} \times 10^{-4}$ W/m^2/°C
1	.0185	66.6	50.4	1.892	3.85	-.22	83.3	66.3	-1	-	-
2	.0185	69.5	51.2	1.892	3.85	-.18	83.3	69.3	-1	-	-
3	.0185	71.9	54.5	1.892	3.85	-.14	82.9	71.6	-1	-	-
4	.0185	73.9	57.6	1.892	3.85	-.10	82.6	73.6	-1	-	-
5	.0185	75.7	60.4	1.892	3.85	-.06	82.3	75.4	-1	-	-
6	.0185	76.4	63.1	1.892	3.85	-.02	82.1	76.2	-1	-	-
7	.0185	75.8	65.1	1.892	3.82	.008	81.9	75.5	-1	.041	.172
8	.0464	77.2	66.5	1.892	3.63	.056	81.7	76.4	-1	.087	.435
9	.0464	79.5	67.4	1.892	3.45	.103	81.7	78.8	-1	.110	.383
10	.2861	107.1	67.6	1.892	2.32	.397	81.6	102.8	+1	.162	.723
11	.0	70.8	67.6	1.892	2.32	.397	81.6	70.8	-1	.162	-
12	.0	67.8	67.5	1.889	2.32	.397	81.6	67.8	-1	.162	-
13	.0	67.4	67.5	1.886	2.32	.397	81.6	67.4	-1	.162	-

Run No. 213

Separator Pressure 1.869 bars Inlet Temp. 49.8 °C

Tube Section	$q \times 10^{-6}$ W/m^2	T_W °C	T_V °C	P_V bars	$W_L \times 10^2$ Kg/s	X	T_i °C	T_{ie} °C	Nu	$h_{GT} \times 10^{-4}$ W/m^2/°C	$h_{exp} \times 10^{-4}$ W/m^2/°C
1	.0216	67.7	50.4	1.888	3.85	-.22	83.3	67.3	-1	-	-
2	.0216	70.6	51.2	1.888	3.85	-.17	83.2	70.3	-1	-	-
3	.0216	73.6	55.7	1.888	3.85	-.12	82.8	73.3	-1	-	-
4	.0216	75.8	59.3	1.888	3.85	-.08	82.4	75.5	-1	-	-
5	.0216	77.9	62.4	1.888	3.85	-.03	82.1	77.6	-1	-	-
6	.0216	78.1	65.3	1.888	3.82	.009	81.8	77.7	-1	.042	.170
7	.0309	77.4	66.7	1.888	3.69	.040	81.7	76.9	-1	.077	.289
8	.0309	76.0	67.3	1.888	3.57	.072	81.6	75.5	-1	.096	.355
9	.0309	76.9	67.4	1.888	3.45	.104	81.6	76.4	-1	.110	.327
10	.3023	108.4	67.5	1.888	2.26	.414	81.6	103.8	+1	.163	.739
11	.0	70.3	67.5	1.888	2.26	.414	81.6	70.3	-1	.163	-
12	.0	67.7	67.4	1.884	2.26	.414	81.5	67.7	-1	.163	-
13	.0	67.5	67.4	1.879	2.25	.414	81.5	67.5	-1	.163	-

TABLE A2 (cont.)

Run No. 111

Separator Pressure 1.909 bars Inlet Temp. 50.1 °C

Tube Section	$q \times 10^{-6}$ W/m^2	T_W °C	T_V °C	P_V bars	$W_L \times 10^2$ Kg/s	X	T_i °C	T_{ie} °C	Nu	$h_{GT} \times 10^{-4}$ W/m^2/°C	$h_{exp} \times 10^{-4}$ W/m^2/°C
1	.0044	60.8	50.9	1.920	3.55	-.25	83.7	60.8	-1	-	-
2	.0044	67.8	51.0	1.920	3.55	-.24	83.7	67.7	-1	-	-
3	.0044	70.7	51.5	1.920	3.55	-.23	83.6	70.6	-1	-	-
4	.0044	72.6	51.9	1.920	3.55	-.22	83.6	72.5	-1	-	-
5	.0044	71.1	52.3	1.920	3.55	-.21	83.5	71.1	-1	-	-
6	.0044	69.0	52.5	1.920	3.55	-.20	83.5	68.9	-1	-	-
7	.0044	67.8	53.0	1.920	3.55	-.19	83.5	67.7	-1	-	-
8	.0044	67.8	53.9	1.920	3.55	-.18	83.4	67.7	-1	-	-
9	.0935	81.4	55.2	1.920	3.49	.017	83.3	80.0	-1	.053	.356
10	.3418	118.2	67.2	1.920	2.14	.397	82.1	113.0	+1	.152	.670
11	.0	71.3	68.1	1.920	2.14	.397	82.0	71.3	-1	.152	-
12	.0	68.2	67.9	1.908	2.14	.398	81.8	68.2	-1	.152	-
13	.0	67.9	67.8	1.905	2.14	.399	81.8	67.9	-1	.152	-

Run No. 112

Separator Pressure 1.904 bars Inlet Temp. 50.0 °C

Tube Section	$q \times 10^{-6}$ W/m^2	T_W °C	T_V °C	P_V bars	$W_L \times 10^2$ Kg/s	X	T_i °C	T_{ie} °C	Nu	$h_{GT} \times 10^{-4}$ W/m^2/°C	$h_{exp} \times 10^{-4}$ W/m^2/°C
1	.0052	62.0	50.7	1.910	3.69	-.25	83.6	61.9	-1	-	-
2	.0052	68.0	50.9	1.910	3.69	-.24	83.5	67.9	-1	-	-
3	.0052	70.1	51.4	1.910	3.69	-.23	83.5	70.0	-1	-	-
4	.0052	69.7	51.9	1.910	3.69	-.22	83.4	69.7	-1	-	-
5	.0052	69.1	52.5	1.910	3.69	-.21	83.4	69.0	-1	-	-
6	.0052	69.1	53.3	1.910	3.69	-.19	83.3	69.0	-1	-	-
7	.0052	68.8	54.0	1.910	3.69	-.18	83.2	68.7	-1	-	-
8	.0464	75.8	55.0	1.910	3.69	-.08	83.1	75.1	-1	-	-
9	.0464	79.4	62.5	1.910	3.65	.012	82.4	68.7	-1	.047	.275
10	.3222	116.6	67.3	1.910	2.38	.357	81.9	111.9	+1	.154	.654
11	.0	71.1	67.9	1.910	2.38	.357	81.8	71.1	-1	.154	-
12	.0	68.0	67.8	1.902	2.37	.357	81.8	68.0	-1	.154	-
13	.0	67.6	67.7	1.900	2.37	.358	81.7	67.6	-1	.154	-

TABLE A2 (cont.)

Run No. 113

Separator Pressure 1.914 bars Inlet Temp. 50.2 °C

Tube Section	$q \times 10^{-6}$ W/m^2	T_W °C	T_V °C	P_V bars	$W_L \times 10^2$ Kg/s	X	T_i °C	T_{ie} °C	Nu	$h_{GT} \times 10^{-4}$ W/m^2/°C	$h_{exp} \times 10^{-4}$ W/m^2/°C
1	.0061	64.0	50.8	1.913	3.55	-.25	83.6	63.9	-1	-	-
2	.0061	70.8	50.2	1.913	3.55	-.23	83.6	70.7	-1	-	-
3	.0061	73.8	51.7	1.913	3.55	-.22	83.5	73.7	-1	-	-
4	.0061	71.9	52.1	1.913	3.55	-.21	83.5	71.8	-1	-	-
5	.0061	70.5	52.9	1.913	3.55	-.18	83.5	70.4	-1	-	-
6	.0061	71.0	53.8	1.913	3.55	-.18	83.3	70.9	-1	-	-
7	.0309	77.8	54.7	1.913	3.55	-.10	83.2	77.3	-1	-	-
8	.0309	77.0	59.6	1.913	3.55	-.03	82.7	76.6	-1	-	-
9	.0309	77.3	64.2	1.913	3.49	.019	82.3	76.9	-1	.054	.235
10	.3102	114.3	67.6	1.913	2.26	.364	81.9	109.6	+1	.150	.664
11	.0	71.1	68.0	1.913	2.26	.364	81.9	71.1	-1	.150	-
12	.0	68.3	67.9	1.907	2.26	.364	81.8	68.3	-1	.150	-
13	.0	68.0	67.7	1.901	2.26	.365	81.7	68.0	-1	.150	-

Run No. 521

Separator Pressure 1.864 bars Inlet Temp. 49.7 °C

Tube Section	$q \times 10^{-6}$ W/m^2	T_W °C	T_V °C	P_V bars	$W_L \times 10^2$ Kg/s	X	T_i °C	T_{ie} °C	Nu	$h_{GT} \times 10^{-4}$ W/m^2/°C	$h_{exp} \times 10^{-4}$ W/m^2/°C
1	.1035	81.1	50.4	2.010	7.59	-.18	84.9	79.6	-1	-	-
2	.1035	84.3	56.3	2.010	7.59	-.07	84.3	82.7	-1	-	-
3	.1035	84.6	64.8	2.010	7.42	.021	83.5	83.1	-1	.104	.521
4	.1035	87.2	68.9	2.010	7.01	.075	83.1	85.6	+1	.168	.568
5	.1035	87.3	69.7	2.010	6.60	.130	83.1	85.9	+1	.204	.589
6	.1035	86.1	69.4	1.992	6.18	.186	82.8	84.5	+1	.230	.619
7	.1035	84.1	69.2	1.983	5.76	.241	82.7	82.5	-1	.249	.695
8	.1035	82.1	68.9	1.968	5.33	.297	82.5	80.5	-1	.263	.788
9	.1876	92.7	68.6	1.946	4.57	.397	82.3	89.8	+1	.278	.779
10	.1800	110.1	68.2	1.929	3.85	.493	82.1	107.4	+1	.284	.430
11	.0	70.1	67.9	1.908	3.83	.495	81.8	70.1	-1	.284	-
12	.0	67.9	67.6	1.894	3.82	.496	81.7	67.9	-1	.284	-
13	.0	67.4	67.3	1.875	3.80	.498	81.4	67.4	-1	.285	-

TABLE A2 (cont.)

Run No. 522

Separator Pressure 1.845 bars Inlet Temp. 49.8 °C

Tube Section	$q \times 10^{-6}$ W/m^2	T_W °C	T_V °C	P_V bars	$W_L \times 10^2$ Kg/s	X	T_i °C	T_{ie} °C	Nu	$h_{GT} \times 10^{-4}$ W/m^2/°C	$h_{exp} \times 10^{-4}$ W/m^2/°C
1	.1181	79.8	50.3	1.997	7.35	-.15	84.6	78.0	-1	-	-
2	.1181	83.9	57.4	1.997	7.35	-.02	84.0	82.2	-1	-	-
3	.1181	84.2	65.9	1.997	6.97	.052	83.2	82.4	-1	.143	.648
4	.1181	87.1	68.9	1.997	6.50	.116	82.9	85.3	+1	.192	.648
5	.1181	89.1	69.4	1.997	6.03	.180	82.9	87.3	+1	.222	.601
6	.1181	88.8	69.4	1.996	5.56	.244	82.9	87.0	+1	.243	.610
7	.1181	86.0	69.1	1.978	5.08	.309	82.7	84.2	+1	.259	.702
8	.0935	83.1	68.9	1.968	4.70	.361	82.5	81.7	-1	.267	.658
9	.0935	86.4	68.6	1.950	4.31	.413	82.3	85.0	+1	.273	.526
10	.2247	111.4	68.2	1.929	3.41	.536	82.1	108.0	+1	.277	.521
11	.0	70.2	67.8	1.905	3.39	.539	81.8	70.2	-1	.277	-
12	.0	67.5	67.9	1.892	3.38	.540	81.6	67.5	-1	.277	-
13	.0	67.2	67.4	1.882	3.37	.541	81.5	67.2	-1	.277	-

Run No. 523

Separator Pressure 1.829 bars Inlet Temp. 49.6 °C

Tube Section	$q \times 10^{-6}$ W/m^2	T_W °C	T_V °C	P_V bars	$W_L \times 10^2$ Kg/s	X	T_i °C	T_{ie} °C	Nu	$h_{GT} \times 10^{-4}$ W/m^2/°C	$h_{exp} \times 10^{-4}$ W/m^2/°C
1	.1377	81.1	50.3	2.002	7.62	-.14	84.8	78.9	-1	-	-
2	.1377	85.0	59.2	2.002	7.60	.003	84.0	82.9	-1	.045	.533
3	.1377	84.6	67.6	2.002	7.05	.074	83.1	82.5	-1	.168	.812
4	.1377	87.9	69.5	2.002	6.50	.146	83.0	85.9	+1	.213	.747
5	.1377	91.6	69.5	2.002	5.96	.218	82.9	89.5	+1	.242	.624
6	.1377	89.5	69.3	1.987	5.40	.291	82.8	87.4	+1	.262	.681
7	.0621	89.9	69.0	1.972	5.14	.325	82.6	80.0	-1	.269	.523
8	.0621	79.9	68.8	1.960	4.88	.359	82.4	78.9	-1	.275	.558
9	.0621	82.5	68.5	1.945	4.63	.393	82.3	81.5	-1	.279	.446
10	.2552	112.8	68.0	1.916	3.59	.528	81.9	109.0	+1	.285	.569
11	.0	70.4	67.6	1.893	3.58	.531	81.4	70.4	-1	.285	-
12	.0	67.2	67.3	1.877	3.56	.532	81.5	67.2	-1	.285	-
13	.0	66.8	67.1	1.866	3.55	.533	81.3	66.8	-1	.285	-

TABLE A2 (cont.)

Run No. 421

Separator Pressure 1.946 bars Inlet Temp. 50.1 °C

Tube Section	$qx10^{-6}$ W/m^2	T_W °C	T_L °C	P_V bars	$W_L x10^2$ Kg/s	X	T_i °C	T_{ie} °C	Nu	$h_{GT} x10^{-4}$ W/m^2/°C	$h_{exp} x10^{-4}$ W/m^2/°C
1	.0788	81.9	-	2.058	7.69	-.21	-	79.6	+1	-	-
2	.0788	86.1	-	2.058	7.69	-.13	-	84.9	+1	-	-
3	.0788	86.5	-	2.058	7.69	-.04	-	85.3	+1	-	-
4	.0788	86.2	-	2.058	7.55	.019	-	85.0	+1	.105	-
5	.0788	89.5	-	2.058	7.27	.059	-	88.3	+1	.165	-
6	.0788	88.3	70.50	2.058	6.92	.100	76.2	87.1	+1	.188	.443
7	.0788	84.9	70.35	2.049	6.60	.142	76.1	83.7	+1	.213	.540
8	.0788	83.4	70.25	2.042	6.28	.184	76.0	82.2	+1	.232	.596
9	.1878	93.9	70.10	2.034	5.53	.281	75.9	91.1	+1	.262	.787
10	.2574	115.2	68.55	2.003	4.48	.481	75.4	111.3	+1	.233	.564
11	.0	70.5	68.20	1.981	4.46	.420	75.1	70.5	-1	.283	-
12	.0	67.4	68.00	1.970	4.45	.421	74.9	67.4	-1	.283	-
13	.0	67.7	67.80	1.958	4.44	.422	74.8	67.7	-1	.283	-

Run No. 422

Separator Pressure 1.941 bars Inlet Temp. 50.2 °C

Tube Section	$qx10^{-6}$ W/m^2	T_W °C	T_L °C	P_V bars	$W_L x10^2$ Kg/s	X	T_i °C	T_{ie} °C	Nu	$h_{GT} x10^{-4}$ W/m^2/°C	$h_{exp} x10^{-4}$ W/m^2/°C
1	.0910	79.9	50.6	1.996	7.59	-.18	84.7	78.6	-1	-	.310
2	.0910	83.4	55.3	1.996	7.59	-.09	84.3	82.1	-1	-	.323
3	.0910	83.9	63.3	1.996	7.55	.005	83.5	82.5	-1	.057	.442
4	.0910	86.0	68.0	1.996	7.19	.052	83.0	84.6	+1	.147	.507
5	.0910	86.1	68.3	1.996	6.83	.100	82.9	84.7	+1	.186	.541
6	.0910	84.9	69.4	1.996	6.47	.147	82.9	83.5	+1	.214	.587
7	.0910	83.0	69.2	1.984	6.10	.197	82.7	81.6	-1	.234	.659
8	.0935	81.6	69.0	1.972	5.71	.247	82.6	80.2	-1	.251	.740
9	.0935	85.1	68.8	1.959	5.33	.297	82.4	83.7	+1	.263	.572
10	.2890	119.1	68.5	1.942	4.17	.450	82.2	114.7	+1	.282	.571
11	.0	70.8	68.0	1.914	4.15	.453	81.9	70.8	-1	.283	-
12	.0	67.8	67.7	1.901	4.14	.454	81.7	67.8	-1	.283	-
13	.0	67.3	67.5	1.886	4.13	.456	81.6	67.3	-1	.283	-

TABLE A2 (cont.)

Run No. 423

Separator Pressure 1.952 bars Inlet Temp. 50.5 °C

Tube Section	$q \times 10^{-6}$ W/m^2	T_W °C	T_L °C	P_V bars	$W_L \times 10^2$ Kg/s	X	T_i °C	T_{ie} °C	Nu	$h_{GT} \times 10^{-4}$ W/m^2/°C	$h_{exp} \times 10^{-4}$ W/m^2/°C
1	.1057	83.0	-	2.071	7.59	-.17	-	81.4	-1	-	-
2	.1057	87.4	-	2.071	7.59	-.06	-	85.8	-1	-	-
3	.1057	85.9	-	2.071	7.42	.023	-	86.1	-1	.113	-
4	.1057	87.7	-	2.071	6.99	.078	-	86.1	-1	.181	-
5	.1057	89.9	-	2.071	6.57	.134	-	88.3	-1	.220	-
6	.1057	88.4	70.70	2.071	6.15	.189	83.7	86.8	+1	.231	.597
7	.0623	82.8	70.50	2.058	5.89	.223	83.6	81.8	-1	.243	.507
8	.0623	80.2	70.30	2.047	5.64	.257	83.7	79.3	-1	.253	.628
9	.0623	84.4	70.15	2.037	5.38	.291	83.4	83.4	+1	.261	.438
10	.3184	125.5	69.70	2.013	4.10	.460	83.1	120.7	+1	.283	.571
11	.0	71.1	69.20	1.981	4.07	.463	82.7	71.1	-1	.283	-
12	.0	67.7	68.90	1.967	4.06	.465	82.5	67.7	-1	.283	-
13	.0	67.3	68.80	1.960	4.06	.466	82.4	67.3	-1	.283	-

Run No. 321

Separator Pressure 1.853 bars Inlet Temp. 49.5 °C

Tube Section	$q \times 10^{-6}$ W/m^2	T_W °C	T_L °C	P_V bars	$W_L \times 10^2$ Kg/s	X	T_i °C	T_{ie} °C	Nu	$h_{GT} \times 10^{-4}$ W/m^2/°C	$h_{exp} \times 10^{-4}$
1	.0559	73.1	50.0	1.946	7.81	-.22	84.1	72.2	-1	-	.243
2	.0559	78.9	51.6	1.946	7.81	-.16	83.9	78.0	-1	-	.205
3	.0559	75.6	55.7	1.946	7.81	-.10	83.5	74.8	-1	-	.281
4	.0559	82.2	61.5	1.946	7.81	-.04	83.0	81.3	-1	-	.271
5	.0559	83.1	65.5	1.946	7.76	.007	82.6	82.3	-1	.069	.317
6	.0559	83.0	67.8	1.946	7.54	.036	82.3	82.2	-1	.130	.368
7	.0559	80.4	68.4	1.946	7.31	.064	82.3	79.5	-1	.162	.468
8	.0559	80.4	68.5	1.946	7.09	.092	82.3	79.5	-1	.186	.473
9	.1876	87.8	68.5	1.944	6.35	.188	82.2	84.9	+1	.237	.974
10	.2968	110.9	68.2	1.927	5.16	.340	82.0	106.5	+1	.278	.694
11	.0	70.7	67.8	1.905	5.13	.342	81.8	70.7	-1	.278	-
12	.0	67.7	67.5	1.890	5.13	.344	81.6	67.7	-1	.279	-
13	.0	67.2	67.4	1.882	5.12	.345	81.5	67.2	-1	.279	-

TABLE A2 (cont.)

Run No. 322

Separator Pressure 1.863 bars Inlet Temp. 49.8 °C

Tube Section	$q \times 10^{-6}$ W/m^2	T_W °C	T_L °C	P_V bars	$W_L \times 10^2$ Kg/s	X	T_i °C	T_{ie} °C	Nu	$h_{GT} \times 10^{-4}$ W/m^2/°C	$h_{exp} \times 10^{-4}$ W/m^2/°C
1	.0641	74.3	50.3	1.972	7.81	-.21	84.4	73.3	-1	-	.267
2	.0641	79.9	52.1	1.972	7.81	-.14	84.2	78.9	-1	-	.231
3	.0641	81.7	58.1	1.972	7.81	-.08	83.7	80.7	-1	-	.272
4	.0641	83.0	63.5	1.972	7.81	-.01	83.1	82.0	-1	-	.329
5	.0641	83.6	67.3	1.972	7.60	.027	82.6	82.6	-1	.116	.393
6	.0641	83.8	68.8	1.972	7.35	.059	82.6	82.8	+1	.157	.427
7	.0641	81.1	69.0	1.972	7.10	.092	82.6	80.1	-1	.185	.532
8	.0937	82.3	68.9	1.969	6.72	.140	82.5	80.9	-1	.215	.702
9	.0937	82.6	68.9	1.964	6.35	.188	82.5	81.2	-1	.237	.682
10	.3066	112.6	68.6	1.946	5.12	.345	82.3	107.9	+1	.278	.696
11	.0	70.8	68.2	1.924	5.10	.348	82.0	70.8	-1	.279	-
12	.0	67.9	67.9	1.910	5.08	.349	81.8	67.9	-1	.279	-
13	.0	67.5	67.7	1.897	5.07	.351	81.7	67.5	-1	.280	-

Run No. 323

Separator Pressure 1.936 bars Inlet Temp. 50.0 °C

Tube Section	$q \times 10^{-6}$ W/m^2	T_W °C	T_L °C	P_V bars	$W_L \times 10^2$ Kg/s	X	T_i °C	T_{ie} °C	Nu	$h_{GT} \times 10^{-4}$ W/m^2/°C	$h_{exp} \times 10^{-4}$ W/m^2/°C
1	.0737	81.4	-	2.041	7.70	-.21	-	80.3	-1	-	-
2	.0737	85.3	-	2.041	7.70	-.13	-	84.1	-1	-	-
3	.0737	96.3	-	2.041	7.70	-.06	-	85.2	-1	-	-
4	.0737	86.5	-	2.041	7.63	.009	-	85.4	-1	.079	-
5	.0737	88.6	-	2.041	7.34	.047	-	87.5	-1	.151	-
6	.0737	87.4	70.20	2.041	7.04	.085	83.4	86.2	+1	.178	.430
7	.0621	83.3	70.20	2.040	6.79	.118	83.4	82.3	-1	.200	.474
8	.0621	82.1	70.10	2.034	6.54	.150	83.3	81.2	-1	.217	.517
9	.0621	85.8	69.90	2.023	6.29	.184	83.2	84.9	+1	.232	.390
10	.3418	122.7	69.60	2.008	4.92	.362	83.0	117.5	+1	.277	.645
11	.0	70.8	69.00	1.973	4.89	.365	82.6	70.9	-1	.278	-
12	.0	67.3	68.75	1.958	4.88	.367	82.4	67.3	-1	.278	-
13	.0	66.9	68.55	1.945	4.86	.368	82.3	66.9	-1	.278	-

TABLE A2 (cont.)

Run No. 221

Separator Pressure 1.936 bars Inlet Temp. 50.0 °C

Tube Section	$q \times 10^{-6}$ W/m^2	T_W °C	T_L °C	P_V bars	$W_L \times 10^2$ Kg/s	X	T_i °C	T_{ie} °C	Nu	$h_{GT} \times 10^{-4}$ W/m^2/°C	$h_{exp} \times 10^{-4}$ W/m^2/°C
1	.0327	73.6	-	1.989	7.59	-.24	-	73.1	-1	-	-
2	.0327	77.6	-	1.989	7.59	-.21	-	77.1	-1	-	-
3	.0327	77.9	-	1.989	7.59	-.17	-	77.4	-1	-	-
4	.0327	79.0	-	1.989	7.59	-.14	-	78.5	-1	-	-
5	.0327	79.8	-	1.989	7.59	-.10	-	79.3	-1	-	-
6	.0327	79.6	-	1.989	7.59	-.07	-	79.1	-1	-	-
7	.0327	79.1	-	1.989	7.59	-.03	-	78.6	-1	-	-
8	.0327	77.9	-	1.989	7.59	.000	-	77.4	-1	.021	-
9	.1878	95.2	69.00	1.989	6.84	.098	82.8	92.4	+1	.186	.716
10	.3527	126.0	69.30	1.989	5.44	.283	82.8	120.6	+1	.260	.622
11	.0	71.3	68.85	1.963	5.42	.286	82.5	71.3	-1	.260	-
12	.0	68.0	68.70	1.953	5.41	.287	82.4	68.0	-1	.261	-
13	.0	67.9	68.55	1.947	5.41	.287	82.3	67.9	-1	.261	-

Run No. 222

Separator Pressure 1.847 bars Inlet Temp. 49.6 °C

Tube Section	$q \times 10^{-6}$ W/m^2	T_W °C	T_L °C	P_V bars	$W_L \times 10^2$ Kg/s	X	T_i °C	T_{ie} °C	Nu	$h_{GT} \times 10^{-4}$ W/m^2/°C	$h_{exp} \times 10^{-4}$ W/m^2/°C
1	.0372	72.3	50.1	1.915	7.46	-.23	83.7	71.8	-1	-	.167
2	.0372	76.5	51.0	1.915	7.46	-.19	83.6	76.0	-1	-	.145
3	.0372	78.9	52.7	1.915	7.46	-.15	83.4	78.4	-1	-	.142
4	.0372	79.9	55.0	1.915	7.46	-.11	83.2	79.3	-1	-	.150
5	.0372	81.6	59.0	1.915	7.46	-.06	82.8	81.0	-1	-	.165
6	.0372	81.3	62.4	1.915	7.46	-.02	82.5	80.8	-1	-	.196
7	.0372	79.2	65.4	1.915	7.40	.009	82.2	78.7	-1	.072	.270
8	.0935	80.4	67.3	1.915	7.03	.058	82.0	79.0	-1	.151	.715
9	.0935	85.3	68.0	1.915	6.66	.108	81.9	83.9	+1	.189	.541
10	.2906	109.1	68.0	1.914	5.51	.262	81.9	104.7	+1	.252	.707
11	.0	69.8	67.7	1.899	5.50	.263	81.7	69.8	-1	.252	-
12	.0	67.5	67.5	1.888	5.49	.265	81.6	67.5	-1	.253	-
13	.0	67.1	67.7	1.897	5.49	.264	81.7	67.1	-1	.252	-

TABLE 42 (cont.)

Run No. 223

Separator Pressure 1.936 bars Inlet Temp. 50.0°C

Tube section	$qx10^{-6}$ W/m^2	T_W °C	T_L °C	P_V bars	$W_L x10^2$ Kg/s	X	T_i °C	T_{ie} °C	Nu	$h_{GT} x10^{-4}$ W/m^2/°C	$h_{exp} x10^{-4}$ W/m^2/°C
1	.0440	76.3	-	1.996	7.57	-.23	-	75.6	-1	-	-
2	.0440	82.3	-	1.996	7.57	-.19	-	81.7	-1	-	-
3	.0440	84.0	-	1.996	7.57	-.14	-	83.4	-1	-	-
4	.0440	90.1	-	1.996	7.57	-.09	-	89.5	-1	-	-
5	.0440	87.4	-	1.996	7.57	-.04	-	86.7	-1	-	-
6	.0440	84.7	-	1.996	7.56	.001	-	84.0	-1	.031	-
7	.0623	82.3	69.15	1.996	7.32	.034	82.9	81.4	-1	.123	.474
8	.0623	80.2	69.45	1.996	7.07	.066	82.9	79.2	-1	.160	.579
9	.0623	84.1	69.40	1.994	6.82	.099	82.8	83.2	+1	.185	.423
10	.3382	125.6	69.30	1.989	5.47	.277	82.8	120.5	+1	.258	.601
11	.0	70.7	68.90	1.965	5.45	.280	82.5	70.7	-1	.259	-
12	.0	67.2	68.75	1.956	5.45	.281	82.4	67.2	-1	.259	-
13	.0	66.9	68.55	1.946	5.44	.282	82.3	66.9	-1	.259	-

Run No. 121

Separator Pressure 1.930 bars Inlet Temp. 51.0 °C

Tube Section	$qx10^{-6}$ W/m^2	T_W °C	T_L °C	P_V bars	$W_L x10^2$ Kg/s	X	T_i °C	T_{ie} °C	Nu	$h_{GT} x10^{-4}$ W/m^2/°C	$h_{exp} x10^{-4}$ W/m^2/°C
1	.0854	63.0	-	1.957	7.45	-.25	-	62.9	-1	-	-
2	.0854	68.1	-	1.957	7.45	-.24	-	68.0	-1	-	-
3	.0854	69.3	-	1.957	7.45	-.23	-	69.2	-1	-	-
4	.0854	70.5	-	1.957	7.45	-.22	-	70.3	-1	-	-
5	.0854	71.6	-	1.957	7.45	-.21	-	71.4	-1	-	-
6	.0854	72.8	-	1.957	7.45	-.20	-	72.6	-1	-	-
7	.0854	73.1	-	1.957	7.45	-.19	-	72.9	-1	-	-
8	.0854	73.7	-	1.957	7.45	-.18	-	73.6	-1	-	-
9	.1878	92.4	57.25	1.957	7.37	.011	83.5	89.5	+1	.080	.535
10	.3600	129.2	67.80	1.957	5.94	.202	82.5	123.8	+1	.234	.586
11	.0	71.4	68.75	1.957	5.94	.202	82.4	71.4	-1	.233	-
12	.0	67.8	68.55	1.946	5.93	.204	82.4	67.8	-1	.234	-
13	.0	67.5	68.40	1.938	5.93	.204	82.3	67.5	-1	.234	-

TABLE A2 (cont.)

Run No. 122

Separator Pressure 1.927 bars Inlet Temp. 50.9 °C

Tube Section	$q \times 10^{-6}$ W/m^2	T_W °C	T_L °C	P_V bars	$W_L \times 10^2$ Kg/s	X	T_i °C	T_{ie} °C	Nu	$h_{GT} \times 10^{-4}$ W/m^2/°C	$h_{exp} \times 10^{-4}$ W/m^2/°C
1	.0098	64.9	-	1.948	7.45	-.25	-	64.8	-1	-	-
2	.0098	70.8	-	1.948	7.45	-.24	-	70.7	-1	-	-
3	.0098	72.1	-	1.948	7.45	-.23	-	72.0	-1	-	-
4	.0098	73.8	-	1.948	7.45	-.22	-	73.7	-1	-	-
5	.0098	74,7	-	1.948	7.45	-.20	-	74.6	-1	-	-
6	.0098	75.4	-	1.948	7.45	-.19	-	75.2	-1	-	-
7	.0098	75.4	-	1.948	7.45	-.18	-	75.2	-1	-	-
8	.0937	82.4	-	1.948	7.45	-.08	-	81.0	-1	-	-
9	.0937	86.5	63.90	1.948	7.37	.011	82.8	85.1	+1	.080	.415
10	.3600	130.6	68.20	1.948	5.94	.203	82.4	125.2	+1	.234	.577
11	.0	71.5	68.60	1.948	5.94	.203	82.3	71.5	-1	.233	-
12	.0	67.4	68.50	1.942	5.94	.203	82.2	67.4	-1	.234	-
13	.0	67.1	68.35	1.933	5.93	.204	82.1	67.1	-1	.234	-

Run No. 123

Separator Pressure 1.930 bars Inlet Temp. 50.0 °C

Tube Section	$q \times 10^{-6}$ W/m^2	T_W °C	T_L °C	P_V bars	$W_L \times 10^2$ Kg/s	X	T_i °C	T_{ie} °C	Nu	$h_{GT} \times 10^{-4}$ W/m^2/°C	$h_{exp} \times 10^{-4}$ W/m^2/°C
1	.0116	66.7	—	1.935	7.45	-.26	-	66.5	-1	-	-
2	.0116	73.0	-	1.935	7.45	-.24	-	72.8	-1	-	-
3	.0116	74.4	-	1.935	7.45	-.23	-	74.2	-1	-	-
4	.0116	73.9	-	1.935	7.45	-.22	-	73.7	-1	-	-
5	.0116	74.4	-	1.935	7.45	-.20	-	74.2	-1	-	-
6	.0116	76.0	-	1.935	7.45	-.19	-	75.8	-1	-	-
7	.0623	83.4	-	1.935	7.45	-.12	-	82.4	-1	-	-
8	.0623	81.4	-	1.935	7.45	-.05	-	80.4	-1	-	-
9	.0623	83.2	64.90	1.935	7.40	.007	82.5	82.2	-1	.066	.341
10	.3293	123.7	67.85	1.935	6.10	.182	82.2	118.7	+1	.226	.590
11	.0	70.8	68.20	1.935	6.10	.182	82.2	70.8	-1	.226	-
12	.0	67.5	68.35	1.935	6.10	.182	82.1	67.5	-1	.226	-
13	.0	67.4	68.30	1.932	6.09	.182	82.1	67.4	-1	.226	-

TABLE A2 (cont.)

Run No. 431

Separator Pressure 1.943 bars Inlet Temp. 46.7 °C

Tube Section	$q \times 10^{-6}$ W/m^2	T_W °C	T_L °C	P_V bars	$W_L \times 10^2$ Kg/s	X	T_i °C	T_{ie} °C	Nu	$h_{GT} \times 10^{-4}$ W/m^2/°C	$h_{exp} \times 10^{-4}$ W/m^2/°C
1	.1457	89.4	-	2.090	11.80	-.24	-	87.2	-1	-	-
2	.1457	91.7	-	2.090	11.80	-.15	-	89.5	-1	-	-
3	.1457	90.2	-	2.090	11.80	-.05	-	88.0	-1	-	-
4	.0	75.8	-	2.090	11.80	-.05	-	75.8	-1	-	-
5	.1457	92.0	-	2.090	11.52	.024	-	89.7	-1	-	-
6	.1457	92.8	71.05	2.090	10.94	.073	84.0	90.6	+1	.236	.670
7	.1457	90.8	71.05	2.090	10.36	.122	84.0	88.6	+1	.285	.737
8	.1457	88.8	70.60	2.065	9.74	.174	83.7	86.6	+1	.321	.801
9	.2726	112.0	70.20	2.039	8.62	.269	83.4	107.8	+1	.365	.653
10	.1420	101.0	69.50	1.999	8.01	.321	82.9	98.9	+1	.381	.450
11	.0	69.4	69.2	1.981	7.99	.323	82.7	69.4	-1	.381	-
12	.0	67.5	68.90	1.967	7.97	.325	82.5	67.5	-1	.382	-
13	.0	66.9	68.7	1.953	7.95	.326	82.4	66.9	-1	.382	-

Run No. 432

Separator Pressure 1.961 bars Inlet Temp. 45.8 °C

Tube Section	$q \times 10^{-6}$ W/m^2	T_W °C	T_L °C	P_V bars	$W_L \times 10^2$ Kg/s	X	T_i °C	T_{ie} °C	Nu	$h_{GT} \times 10^{-4}$ W/m^2/°C	$h_{exp} \times 10^{-4}$ W/m^2/°C
1	.1700	91.4	-	2.149	11.80	-.25	-	88.8	-1	-	-
2	.1700	99.9	-	2.149	11.80	-.14	-	97.3	-1	-	-
3	.1700	91.5	-	2.149	11.80	-.03	-	76.8	-1	-	-
4	.0	76.8	-	2.149	11.80	-.03	-	88.9	-1	-	-
5	.1700	94.4	-	2.149	11.29	.044	-	91.8	-1	.206	-
6	.1700	94.0	72.05	2.149	10.61	.101	84.7	91.4	+1	.265	.774
7	.1700	93.0	71.65	2.127	9.90	.161	84.4	90.4	+1	.312	.798
8	.1407	90.3	71.10	2.093	9.29	.213	84.0	88.2	+1	.341	.732
9	.1407	95.1	70.75	1.072	8.71	.262	83.8	93.0	+1	.362	.578
10	.2303	118.1	70.20	2.040	7.75	.343	83.4	114.6	+1	.386	.481
11	.0	70.1	69.70	2.013	7.71	.346	83.1	70.1	-1	.387	-
12	.0	67.7	69.35	1.991	7.69	.349	82.8	67.7	-1	.387	-
13	.0	67.5	69.10	1.976	7.67	.350	82.6	67.5	-1	.388	-

TABLE A2 (cont.)

Run No. 433

Separator Pressure 1.953 bars Inlet Temp. 45.8 °C

Tube Section	$q \times 10^{-6}$ W/m^2	T_W °C	T_L °C	P_V bars	$W_L \times 10^2$ Kg/s	X	T_i °C	T_{ie} °C	Nu	$h_{GT} \times 10^{-4}$ W/m^2/°C	$h_{exp} \times 10^{-4}$ W/m^2/°C
1	.2042	93.1	-	2.157	11.80	-.23	-	90.0	-1	-	-
2	.2042	95.0	-	2.157	11.80	-.10	-	91.9	-1	-	-
3	.2042	92.8	-	2.157	11.57	.020	-	89.7	-1	.151	-
4	.0	77.0	-	2.157	11.57	.020	-	77.0	-1	.151	-
5	.2042	96.4	-	2.157	10.75	.089	-	93.3	-1	.270	-
6	.2042	96.0	72.15	2.157	9.93	.158	84.8	92.9	+1	.309	.856
7	.0937	86.7	71.65	2.127	9.52	.193	84.4	85.3	+1	.331	.622
8	.0937	85.5	71.20	2.101	9.11	.228	84.1	84.0	-1	.348	.659
9	.0937	89.5	70.85	2.078	8.71	.262	83.8	88.1	+1	.362	.501
10	.2696	124.3	70.20	2.039	7.59	.357	83.4	120.2	+1	.389	.498
11	.0	70.4	69.60	2.006	7.55	.360	83.0	70.4	-1	.390	-
12	.0	67.7	69.30	1.987	7.53	.362	82.8	66.7	-1	.390	-
13	.0	67.3	68.90	1.966	7.50	.365	82.5	67.2	-1	.391	-

Run No. 331

Separator Pressure 1.912 bars Inlet Temp. 46.0

Tube Section	$q \times 10^{-6}$ W/m^2	T_W °C	T_L °C	P_V bars	$W_L \times 10^2$ Kg/s	X	T_i °C	T_{ie} °C	Nu	$h_{GT} \times 10^{-4}$ W/m^2/°C	$h_{exp} \times 10^{-4}$ W/m^2/°C
1	.1072	81.7	-	2.051	11.95	-.27	-	80.1	-1	-	-
2	.1072	89.5	-	2.051	11.95	-.20	-	87.8	-1	-	-
3	.1072	89.2	-	2.051	11.95	-.13	-	87.6	-1	-	-
4	.1072	72.7	-	2.051	11.95	-.06	-	71.1	-1	-	-
5	.1072	92.4	-	2.051	11.88	.006	-	90.8	-1	.092	-
6	.1072	91.0	-	2.051	11.46	.041	-	89.3	-1	.203	-
7	.1072	87.5	70.10	2.051	11.03	.077	83.6	85.9	+1	.243	.616
8	.1072	84.2	70.40	2.051	10.60	.113	83.5	82.6	-1	.279	.773
9	.2812	104.7	70.15	2.038	9.47	.208	83.4	100.4	+1	.342	.815
10	.2859	120.2	69.55	2.004	8.29	.306	83.0	115.8	+1	.381	.565
11	.0	70.1	68.95	1.968	8.24	.310	82.6	70.1	-1	.382	-
12	.0	67.4	68.50	1.943	8.21	.313	82.2	67.4	-1	.383	-
13	.0	66.8	68.30	1.931	8.19	.314	82.1	66.8	-1	.384	-

TABLE A2 (cont.)

Run No. 332

Separator Pressure 1.844 bars Inlet Temp. 49.9 °C

Tube Section	$q \times 10^{-6}$ W/m^2	T_W °C	T_L °C	P_V bars	$W_L \times 10^2$ Kg/s	X	T_{si} °C	T_{ie} °C	Nu	$h_{GT} \times 10^{-4}$ W/m^2/°C	$h_{exp} \times 10^{-4}$ W/m^2/°C
1	.0957	78.8	50.3	2.025	11.95	-.22	85.1	77.3	-1	-	-
2	.0957	83.8	51.9	2.025	11.95	-.16	85.0	82.3	-1	-	-
3	.0957	83.0	56.2	2.025	11.95	-.09	84.6	81.6	-1	-	-
4	.0957	86.3	62.1	2.025	11.95	-.03	84.0	84.8	+1	-	-
5	.0957	87.8	66.9	2.025	11.74	.017	83.5	86.3	+1	.137	.459
6	.0957	87.3	69.4	2.025	11.36	.049	83.3	85.9	+1	.205	.534
7	.0957	84.4	69.9	2.025	10.98	.081	83.2	83.0	-1	.248	.662
8	.1402	84.6	69.8	2.018	10.41	.128	83.1	82.5	-1	.293	.946
9	.1402	88.7	69.4	1.996	9.83	.178	82.9	86.6	+1	.326	.726
10	.2764	111.3	68.9	1.963	8.69	.273	82.5	107.1	+1	.370	.652
11	.0	70.9	68.2	1.926	8.64	.277	82.0	70.8	-1	.372	-
12	.0	68.0	68.0	1.918	8.63	.278	81.9	68.0	-1	.372	-
13	.0	67.4	67.7	1.898	8.60	.280	81.7	67.4	-1	.373	-

Run No. 333

Separator Pressure 1.953 bars Inlet Temp. 46.0 °C

Tube Section	$q \times 10^{-6}$ W/m^2	T_W °C	T_L °C	P_V bars	$W_L \times 10^2$ Kg/s	X	T_i °C	T_{ie} °C	Nu	$h_{GT} \times 10^{-4}$ W/m^2/°C	$h_{exp} \times 10^{-4}$ W/m^2/°C
1	.1495	89.4	-	2.116	11.80	-.26	-	87.2	-1	-	-
2	.1495	91.9	-	2.116	11.80	-.16	-	89.7	-1	-	-
3	.1495	90.4	-	2.116	11.80	-.06	-	88.1	-1	-	-
4	.0	75.8	-	2.116	11.80	-.06	-	75.8	-1	-	-
5	.1495	92.4	69.65	2.116	11.55	.021	84.5	90.1	+1	.146	.658
6	.1495	93.0	71.50	2.116	10.95	.072	84.3	90.7	+1	.234	.696
7	.0937	86.9	71.50	2.116	10.58	.103	84.3	85.5	+1	.268	.608
8	.0937	84.9	71.20	2.098	10.18	.137	84.1	83.5	-1	.296	.683
9	.0937	89.9	70.85	2.079	9.78	.171	83.9	88.5	+1	.319	.491
10	.3328	128.2	70.35	2.049	8.42	.286	83.5	123.2	+1	.370	.575
11	.0	70.9	69.65	2.008	8.37	.291	83.0	70.9	-1	.372	-
12	.0	67.7	69.20	1.984	8.34	.293	82.7	67.7	-1	.373	-
13	.0	67.4	68.90	1.965	8.31	.296	82.5	67.4	-1	.374	-

TABLE A2 (cont.)

Run No. 231

Separator Pressure 1.925 bars Inlet Temp. 46.0 °C

Tube Section	$qx10^{-6}$ W/m^2	T_W °C	T_L °C	P_V bars	$W_L x10^2$ Kg/s	X	T_i °C	T_{ie} °C	Nu	$h_{GT} x10^{-4}$ W/m^2/°C	$h_{exp} x10^{-4}$ W/m^2/°C
1	.0661	81.9	-	2.010	11.50	-.29	-	81.0	-1	-	-
2	.0661	88.7	-	2.010	11.50	-.25	-	87.7	-1	-	-
3	.0661	90.0	-	2.010	11.50	-.20	-	89.0	-1	-	-
4	.0	72.0	-	2.010	11.50	-.20	-	72.0	-1	-	-
5	.0661	90.2	-	2.010	11.50	-.15	-	89.2	-1	-	-
6	.0661	91.2	-	2.010	11.50	-.11	-	90.2	+1	-	-
7	.0661	86.8	-	2.010	11.50	-.06	-	85.8	-1	-	-
8	.0661	84.6	-	2.010	11.50	-.01	-	83.6	-1	-	-
9	.2817	108.2	69.10	2.010	10.47	.090	83.1	103.9	+1	.250	.721
10	.3600	132.5	69.70	2.010	9.04	.214	83.0	127.1	+1	.335	.573
11	.0	71.4	68.95	1.968	8.99	.219	82.5	71.4	-1	.338	-
12	.0	67.9	68.60	1.948	8.96	.221	82.3	67.9	-1	.339	-
13	.0	67.4	68.35	1.933	8.94	.223	82.1	67.4	-1	.340	-

Run No. 232

Separator Pressure 1.940 bars Inlet Temp. 46.0 °C

Tube Section	$qx10^{-6}$ W/m^2	T_W °C	T_L °C	P_V bars	$W_L X10^2$ Kg/s	X	T_i °C	T_{ie} °C	Nu	$h_{GT} x10^{-4}$ W/m^2/°C	$h_{exp} x10^{-4}$ W/m^2/°C
1	.0772	83.9	-	2.029	11.50	-.29	-	82.7	-1	-	-
2	.0772	90.4	-	2.029	11.50	-.24	-	89.2	-1	-	-
3	.0772	91.2	-	2.029	11.50	-.18	-	90.1	-1	-	-
4	.0	73.1	-	2.029	11.50	-.18	-	73.1	-1	-	-
5	.0772	91.5	-	2.029	11.50	-.13	-	90.4	-1	-	-
6	.0772	70.8	-	2.029	11.50	-.07	-	69.6	-1	-	-
7	.0772	87.2	-	2.029	11.50	-.02	-	86.1	-1	-	-
8	.1409	88.6	68.90	2.029	11.05	.039	83.4	86.5	+1	.182	.715
9	.1409	95.6	70.00	2.029	10.49	.087	83.3	93.4	+1	.247	.551
10	.3600	133.8	69.85	2.019	9.05	.213	83.2	128.3	+1	.335	.563
11	.0	71.0	69.15	1.980	9.00	.217	82.7	71.0	-1	.337	-
12	.0	67.6	68.85	1.963	8.98	.219	82.5	67.6	-1	.338	-
13	.0	67.0	68.60	1.950	8.96	.221	82.3	67.0	-1	.339	-

TABLE A2 (cont.)

Run No. 233

Separator Pressure 1.875 bars Inlet Temp. 49.8 °C

Tube Section	$q \times 10^{-6}$ W/m^2	T_W °C	T_L °C	P_V bars	$W_L \times 10^2$ Kg/s	X	T_i °C	T_{ie} °C	Nu	$h_{GT} \times 10^{-4}$ W/m^2/°C	$h_{exp} \times 10^{-4}$ W/m^2/°C
1	.0387	71.9	50.2	1.950	11.95	-.25	84.2	71.3	-1	-	-
2	.0387	76.5	50.8	1.950	11.95	-.22	84.1	75.9	-1	-	-
3	.0387	78.3	52.3	1.950	11.95	-.19	83.9	77.8	-1	-	-
4	.0387	80.2	54.2	1.950	11.95	-.17	83.8	79.6	-1	-	-
5	.0387	80.4	55.8	1.950	11.95	-.14	83.6	79.8	-1	-	-
6	.0387	82.1	57.8	1.950	11.95	-.12	83.4	81.5	-1	-	-
7	.0937	83.9	59.3	1.950	11.95	-.05	83.3	82.5	-1	-	-
8	.0937	82.8	63.6	1.950	11.87	.006	82.8	81.4	-1	.092	.488
9	.0937	83.3	67.7	1.950	11.50	.037	82.4	81.8	-1	.185	.601
10	.2736	110.0	68.6	1.950	10.42	.128	82.3	105.8	+1	.293	.661
11	.0	70.6	68.3	1.934	10.40	.130	82.1	70.7	-1	.295	-
12	.0	68.1	68.1	1.920	10.38	.132	82.0	68.1	-1	.296	-
13	.0	67.7	67.8	1.906	10.36	.133	81.8	67.7	-1	.297	-

Run No. 131

Separator Pressure 1.854 bars Inlet Temp. 49.4 °C

Tube Section	$q \times 10^{-6}$ W/m^2	T_W °C	T_L °C	P_V bars	$W_L \times 10^2$ Kg/s	X	T_i °C	T_{ie} °C	Nu	$h_{GT} \times 10^{-4}$ W/m^2/°C	$h_{exp} \times 10^{-4}$ W/m^2/°C
1	.0387	71.5	49.8	1.928	11.95	-.25	83.9	70.9	-1	-	-
2	.0387	76.1	50.4	1.928	11.95	-.22	83.8	75.6	-1	-	-
3	.0387	78.0	51.9	1.928	11.95	-.20	83.7	77.4	-1	-	-
4	.0387	79.8	53.8	1.928	11.95	-.17	83.5	79.2	-1	-	-
5	.0387	78.0	55.4	1.928	11.95	-.14	83.3	79.4	-1	-	-
6	.0387	81.7	57.4	1.928	11.95	-.12	83.1	81.1	-1	-	-
7	.0937	83.5	58.9	1.928	11.95	-.05	83.0	82.1	-1	-	-
8	.0937	82.4	63.2	1.928	11.88	.006	82.6	81.0	-1	.091	.487
9	.0937	82.6	67.3	1.928	11.81	.048	82.3	78.4	-1	.266	.179
10	.2736	110.1	68.2	1.928	10.79	.097	82.1	110.1	+1	.265	1.788
11	.0	70.3	68.0	1.913	10.79	.099	81.9	70.3	-1	.267	-
12	.0	67.8	67.7	1.899	10.75	.100	81.7	67.8	-1	.269	-
13	.0	67.3	67.4	1.885	10.73	.102	81.6	67.3	-1	.271	-

TABLE A2 (cont.)

Run No. 132

Separator Pressure 1.930 bars Inlet Temp. 46.0 °C

Tube Section	$q \times 10^{-6}$ W/m^2	T_W °C	T_L °C	P_V bars	$W_L \times 10^2$ Kg/s	X	T_i °C	T_{ie} °C	Nu	$h_{GT} \times 10^{-4}$ W/m^2/°C	$h_{exp} \times 10^{-4}$ W/m^2/°C
1	.0294	75.3	-	1.961	11.20	-.31	-	74.9	-1	-	-
2	.0294	80.6	-	1.961	11.20	-.29	-	80.1	-1	-	-
3	.0294	79.9	-	1.961	11.20	-.27	-	79.5	-1	-	-
4	.0	64.2	-	1.961	11.20	-.27	-	64.2	-1	-	-
5	.0294	84.2	-	1.961	11.20	-.25	-	83.7	-1	-	-
6	.0294	83.7	-	1.961	11.20	-.22	-	83.3	-1	-	-
7	.0294	79.6	-	1.961	11.20	-.20	-	79.2	-1	-	-
8	.1409	88.2	-	1.961	11.20	-.10	-	86.1	-1	-	-
9	.1409	95.7	-	1.961	11.19	.001	-	93.5	+1	.046	.141
10	.3600	133.2	68.30	1.961	9.76	.128	82.5	127.8	+1	.279	.554
11	.0	71.4	68.80	1.961	9.76	.128	82.5	71.4	-1	.278	-
12	.0	67.6	68.55	1.947	9.74	.130	82.3	67.6	-1	.280	-
13	.0	67.2	68.40	1.937	9.73	.131	82.2	67.2	-1	.281	-

Run No. 133

Separator Pressure 1.935 bars Inlet Temp. 46.0

Tube Section	$q \times 10^{-6}$ W/m^2	T_W °C	T_L °C	P_V bars	$W_L \times 10^2$ Kg/s	X	T_i °C	T_{ie} °C	Nu	$h_{GT} \times 10^{-4}$ W/m^2/°C	$h_{exp} \times 10^{-4}$ W/m^2/°C
1	.0354	75.0	-	1.963	11.20	-.31	-	74.4	-1	-	-
2	.0354	80.4	-	1.963	11.20	-.28	-	79.9	-1	-	-
3	.0354	81.4	-	1.963	11.20	-.26	-	80.9	-1	-	-
4	.0	65.2	-	1.963	11.20	-.26	-	65.3	-1	-	-
5	.0354	83.1	-	1.963	11.20	-.23	-	82.6	-1	-	-
6	.0354	83.7	-	1.963	11.20	-.20	-	83.2	-1	-	-
7	.0937	87.8	-	1.963	11.20	-.16	-	86.4	-1	-	-
8	.0937	84.8	-	1.963	11.20	-.07	-	83.4	-1	-	-
9	.0937	91.2	-	1.963	11.19	-001	-	89.8	-1	-	-
10	.3600	129.4	68.55	1.963	9.76	.128	74.8	123.9	+1	-	-
11	.0	70.7	68.85	1.963	9.76	.128	74.8	70.7	-1	-	-
12	.0	67.4	67.65	1.951	9.75	.130	74.6	67.4	-1	-	-
13	.0	67.0	68.35	1.935	9.73	.132	74.4	67.0	-1	-	-

REFERENCES

1 Mantzouranis, B.G., Ph.D. Thesis, London University (1959).

2 Backhurst, J.E., Ph.D. Thesis, London University (1965).

3 Rohsenow, W.M., 'Developments in Heat Transfer' p.234, Edward Arnold, (1964).

4 Bell, D.W., Nucl. Sci. Eng. 7, 245 (1960).

5 Bergles, A.E., R.F. Lopina, M.P. Fiori, Trans ASME Series C, 89 (1), 69, (1967).

6 Lowdermilk, W.H., C.D. Lanzo, B.L. Siegel, NACA TN-4382 (1958).

7 Tippetts, F.E., Trans ASME Series C 86, 12 (1964).

8 Hewitt, G.F., H.A. Kearsley, P.M.C. Lacey, D.J. Pulling, AERE-R374 (1963) Atomic Energy Research Establishment, Harwell.

9 Fiori, M.P., A.E. Bergles, M.I.T. report no. DSR 70281-56 (1968).

10 Macbeth, R.V., AEEW-R358 (1964) Atomic Energy Establishment, Winfrith.

11 Gunther, F.C., Trans ASME 73, 115 (1951).

12 Von Glahn, U.H., NASA TN D-1285 (1962).

13 Gambill, W.R., CEP Symp. Series 59 (41), 71 (1963).

14 Sonnemann, G., Nucl. Sci. Eng. 5, 242 (1959).

15 Guerrieri, S.A., R.D. Talty, CEP Symp. Series 52 (18), 69 (1956).

16 Rohsenow, N.M., H.Y. Choi, 'Heat Mass and Momentum Transfer', pp211-236 Prentice Hall, N.J. (1961).

17 Kirby, G.J., R. Staniforth, J.H. Kinneir, AEEW-R281 (1965), Atomic Energy Establishment, Winfrith.

18 Bennett, A.W., G.F. Hewitt, H.A. Kearsey, R.K.F. Keeys, P.M.C. Lacey, AERE-R4874 (1965). Atomic Energy Research Establishment, Harwell.

19 Isbin, H.S., R. Vanderwater, H. Fauske, S. Singh. Trans ASME Series C 83, 149 (1961).

20 Goldmann, K.H., H. Firstenberg, C. Lombardi, Trans ASME Series C 83, 158 (1961).

21 Topper, L., Trans ASME, Series C 85, 284 (1963).

22 Stein, R.P. et al, U.S. Atomic Energy Commission Report NYO- 9844 Vol.1: Re (21).

23 Cousins, L.B., G.F. Hewitt, AERE-R5657 (1968). Atomic Energy Research Establishment, Harwell.

24 Becker, K.M., A.I. Ch.E.Jo. 9, 216 (1963).

25 Tippetts, F.E., Trans ASME, Serier C 86, 23 (1964).

26 Jens, W.H., P.A. Lottes, ANL-4627 (1951) : Re (14).

27 Hewitt, G.F., P.M.C. Lacey, Int.Jo. Heat Mass Trans. 8,781 (1965).

28 Bankoff, S.U., CEP Symp. Series 57 (32), 156 (1961).

29 Todreas, N.E., W.M. Rohsenow. MIT. Tech. Rep. No. 9843-37 (1965).

30 Waters. E.D., J.K. Anderson, W.L. Thorpe, J.M. Batch, CEP Symp. Series 61 (57), 230, (1965).

31 Bennett, A.W., G.F. Hewitt, H.A. Kearsey, R.K.F. Keeys, D.J. Pulling, AERE-R 5076 (1966). Atomic Energy Research Establishment, Harwell.

32 Bernath, L., CEP Symp. Series 56 (30), 95 (1960).

33 Tong, L.S., H.B. Currin, P.S. Larsen, O.G. Smith, CEP Symp. Series 62 (64), 35 (1966).

34 Strenge, P.H., A. Orell, J.W. Westwater, A.I.Ch.E.Jo. 7, 578 (1961).

35 Plesset, M.S., Zwick, J.Applied Phys. 23, 95 (1952).

36 Forster, H.K., N. Zuber, A.I.Ch.E.J. 1, 531 (1955).

37 Jakob, M., W. Fritz, Forsch. Gebiete Ingenieurw. 2, 435, (1931)

38 Griffith, P., 'Developments in Heat Transfer' ed. by W.M. Rohsenow, pp261-292 Edward Arnold (1964).

39 Hamburger, L.G., Int.Jo. Heat Mass Trans. 8, 1369 (1965).

40 Zuber, N., Int.Jo. Heat Mass Trans. 2, 83 (1961)

41 Han, C.Y., P. Griffith, Int.Jo. Heat Mass Trans. 8, 887 (1965).

42 Susumu Kotake, Int.Jo. Heat Mass Trans. 9, 711 (1966).

43 Moore, F.D., R.B. Mesler, A.I.Ch.E.Jo. 7, 620 (1961).

44 Snyder, N.R., O.K. Edwards, Memo 20-1371, JPL, June 14-15 (1956), p.38.

45 Edwards, D.K., MS Thesis, University of California, (1956).

46 Hendricks, R.C., R.R. Sharp, NASA TN D-2290 (April 1964).

47 Lloyd, A.J.P., D.Phil. Thesis, Cambridge University (1967).

48 Bankoff, S.G., J.P. Mason, A.I.Ch.E.Jo. 8, 30 (1962).

49 Bankoff, S.G., A.I.Ch.E.Jo. 8, 63 (1962).

50 Bergles, A.E., W.M. Rohsenow, Trans ASME Series C 86, 365 (1964).

51 Han, C.Y., P. Griffith, Eng.Proj.Lab.Rept.No. 7673-19 M.I.T. (1962)

52 Kenning, D.B.R., M.G. Cooper, Paper II, presented at Symp. Boiling Heat Transfer, I.M.E., Manchester University (September 1965).

53 Sato, T., Matsumur A.H., Bull Japan Soc. Mech. Engs. 7, 392 (1964).

54 Davis, E.J., G.H. Anderson, A.I.Ch.E.Jo. 12, 774 (1966).

55 Chandrasekhar, T.S., 'Hydrodynamic and Hydromagnetic Stability' p10, Oxford University Press, (1961),

56 Alves, G.E., Chem. Eng. Progress 50, 449 (1954).

57 Wicks, M., A.E. Dukler, A.I.Ch.E.Jo. 6, 463 (1960).

58 Gill, L.E., G.F. Hewitt, J.W. Hitchon, P.M.C. Lacey, Chem. Eng. Sci. 19, 665 (1964).

59 Sullivan, S.L., B.W. Hardy, C.D. Holland, A.I.Ch.E.Jo. 10, 848 (1964).

60 Lamb, H., 'Hydrodynamics' Chapter 5. 4 edition, Cambridge University Press (1916).

61 Johnson M.A., J. Javier de la Pena, R.B. Mesler, CEP Symp. Series 62 (64) 1 (1966).

62 Koumoutsos, N., R. Moissis, A. Spyridonos, Trans ASME Series C, 90, 223 (1968).

63 Levy, S., Int Jo. Heat Mass Trans. 10, 951 (1967).

64 Corty, C., A.S. Foust, CEP Symp. Series 51 (17). 1, (1955).

65 Bankoff, S.G., CEP Symp. Series 55 (29), 87, (1959).

66 Clark, H.B., P.S. Strenge, J.W. Westwater, CEP Symp. Series 55 (29), 103 (1959).

67 Hewitt, G.F., H.A. Kearsey, P.H.C. Lacey, D.J. Pulling, AERE R 4864 (1964) Atomic Energy Research Est. Harwell.

68 Gill, L.E., G.F. Hewitt, Chem. Eng. Sci. 26, 71 (1965).

69 Gill, L.E., G.F. Hewitt, J.W. Hitchon, Chem. Eng. Sci. 18, 525 (1963).

70 Paleev, I.I., B.S. Filippovich, Int. Jo. Heat Mass Trans. 9, 1089, (1966).

71 Truong Quang Minh, I. Huyghe, Symposium on Two-Phase Flow, Exeter, Paper 62, June 1965.

72 Lamb, H., 'Hydrodynamics' p19. 4 edition Cambridge University Press (1916).

73 Hall-Taylor, N., G.F. Hewitt, P.M.C. Lacey, Chem. Eng. Sci. 18, 537 (1963).

74 Levy, S., Int Jo. Heat Mass Transfer 9 (3), 171, (1966).

75 Peebles, F.N., H.J.Garber, Chem. Eng. Progress 49, 88 (1953).

76 Anderson, G.H., G.G. Haselden, B.G. Mantzouranis, Chem. Eng. Sci. 17, 751 (1962).

77 Dussourd, J.L., A.H. Shapiro, Heat Transfer and Fluid Mechanics Institute, University of California, Los Angeles (June 23-25, 1955).